DEVELOPMENT AND EVALUATION OF AROMATIC POLYAMIDE-IMIDE MEMBRANES FOR H_2S AND CO_2 SEPARATIONS FROM NATURAL GAS

A Dissertation
Presented to
The Academic Faculty

by

Justin Vaughn

In Partial Fulfillment
of the Requirements for the Degree
Doctor of Philosophy in the
School of Chemical and Biomolecular Engineering

Georgia Institute of Technology
May 2013

DEVELOPMENT AND EVALUATION OF AROMATIC POLYAMIDE-IMIDE MEMBRANES FOR CO_2 AND H_2S SEPARATIONS FROM NATURAL GAS

Approved by:

Dr. William Koros, Advisor
School of Chemical and Biomolecular Engineering
Georgia Institute of Technology

Dr. Amyn Teja
School of Chemical and Biomolecular Engineering
Georgia Institute of Technology

Dr. David Bucknall
School of Materials Science and Engineering
Georgia Institute of Technology

Dr. Krista Walton
School of Chemical and Biomolecular Engineering
Georgia Institute of Technology

Dr. Carson Meredith
School of Chemical and Biomolecular Engineering
Georgia Institute of Technology

Date Approved: 20.February.2012

I have not failed. I have just found 10,000 ways that do not work.

-Thomas A. Edison

This dissertation is dedicated to my parents, Jeff and Kathi Vaughn. Without their loving support, both emotionally and perhaps more important, financially, I would absolutely without a doubt not be where I am today.

ACKNOWLEDGEMENTS

First and foremost, this project would not have been possible without the generous funding provided by The King Abdullah University of Science and Technology Global Research Partnership (KAUST-GRP), Award #KUS-I1-011-21.

Now I shall move on to the many memorable people who have made an impact on me during my graduate school experience. Let me start by saying the last four years of my life have been a roller coaster ride to say the least, filled with many highs as well as some lows. I have learned and grown more, both as a chemical engineer and as a person, in the last 4 years than I have in the last 23 years of my life. With that, a tremendous amount of gratitude is owed to my advisor, Dr. William Koros. I am almost certain that I will never find another person more dedicated to their craft than he is. His enthusiasm and tenacity for scientific discovery are second to none, and I'm sure I'm not alone when saying it was inspiring at times. He was also willing to take on a simple chemistry major such as myself, which definitely shocked me at the time. Beyond just the field of membrane science, Dr. Koros has taught me that life is about "selling yourself," even if you believe that what you have to offer isn't so exciting. Also, no matter how busy he was, he was always willing to put in whatever amount of time and effort was necessary for his students. For this, I will be forever grateful.

I would also like to thank my committee members, Dr. Bucknall, Dr. Meredith, Dr. Teja and Dr. Walton for your valuable input and willingness to serve on my committee during the important steps of my PhD education.

As cliché as it sounds, I could literally go on for pages thanking and talking about all of the various people who have influenced me during my graduate school tenure. In an effort to save from writing a novel, I will try to keep this concise, but in case you haven't noticed from the rest of this dissertation; my writing is probably anything but. I would like to start with Dr. JR Johnson for putting up with me over the last four years, for consistently reminding me of my inferior chemistry degree, for being jealous that he didn't go to Ohio State, and in general having an answer for every question or problem that I encountered. Along with JR, Dr. Oguz Karvan designed and built the majority of the H_2S lab. A sincere amount of gratitude is owed to the two of you. Exceptional engineers the both of you are, but perhaps it was the general conversations—both academic and non—that were the most memorable.

An order of thanks is owed to all Koros group members, past and present. Specifically, Dr. Ryan Adams for "showing me the ropes" when I first joined the group; Dr. Jong Suk Lee for

teaching me how to conquer the enigma that is the density gradient column as well as for being a friend who was always up for coffee, cooking me tasty Korean food, and sharing a good laugh; Dr. Dhaval Bhandari for solid professional and friendly advice, and finally Dr. Ryan Lively for pleasant research as well as non-research related conversation, because let's admit it, we don't think about research 100% of the time while we are in lab. You have all been good colleagues and more importantly friends. I hope to maintain contact over the years.

My fellow classmates in the Koros group were also quite influential during my work. Dr. Meha Rungta and Dr. Liren Xu, who although our research projects were very different, were good citizens of the group who were able to share research ideas and humorous discussion. Dr. Canghai Ma, who had the highly sought after privilege of sharing an office with me over the last year, was a good office-mate who was willing to put up with my general office shenanigans. Dr. Vinod Babu, who had the extra special privilege of sharing the same office space as me throughout our entire Koros group tenure, was a good classmate, officemate, and friend. Thanks for putting up with my antics, my terrible sense of humor and music choices, and generally keeping me on the politically correct side of the spectrum. I would also like to mention and thank Brian Kraftschick and Carine Kuete Achoundong, who worked alongside me on the H_2S projects, for sharing of data, general discussions about such wacky H_2S behavior, and for your willingness to sacrifice lab equipment during the latter parts of my work so that I could finish on time. Other Koros group members who deserve mentioning are Stephen Burgess for DMA measurements as well as just being a good person and group member, and Stephanie Li for being a friend, listener to my general gripes and complaints about research, and for lending me batteries.

It would be remiss of me not to mention my regular Red Brick Brewery crew, Jonathon 'T' Rubin, Stephanie Didas and Ryan Clairemont, who were always up for Friday brewery tours. Jonathon was also lucky enough to live in the same house as me for four years. Thanks for providing me with many a late night and tremendously fruitful discussion, dinner leftovers, late night Sunday trips to the grocery store, and various biking adventures. Josh Thompson, who is a colleague as well as a friend, also deserves a 'shout out.' Let us not forget the times you Jonathon and I had while living at 784 Penn Avenue. Those times are neither here nor there. And no, I'm not forgetting you Erin Redmond. When research got the best of us, Erin was always up for commiserating and debating whether graduate school was the right choice for us. Oh yea, Mr. William Archie, thanks for Sunday dinners and being a good friend outside of Georgia Tech throughout my time here in graduate school. I am thankful to have met all of you and know that I have made friends for life.

Last but certainly not least, an extraordinary amount of debt and gratitude is owed to my parents, Jeff and Kathi Vaughn. Without your financial and emotional support, I can without a doubt say I would not be here nor be the man that I am today. The two of you have sacrificed more for me than I can ever hope to repay. I could not have asked for better parents, and hope that one day I can repay even a shred of it back to you. And how could I forget my brother, Josh Vaughn, who probably understands me more than anyone on this planet. Thanks for the fun and memorable summer trips while I was here in Atlanta.

Hopefully I've mentioned everyone, and I am sincerely sorry if I forgot you. It has been a wild four years and I thoroughly look forward to what life will bring me next. Godspeed, and bring it on real-world!

TABLE OF CONTENTS

LIST OF TABLES

LIST OF FIGURES

SUMMARY

Over the past decade, membrane based gas separations have gained traction in industry as an attractive alternative to traditional thermally based separations due to their potential to offer lower operational and capital expenditures, greater ease of operation and lower environmental impact. As membrane research evolves, new state-of-the-art membrane materials as well as processes utilizing membranes will likely be developed. Therefore, their incorporation into existing thermally based units as a debottlenecking step or as a stand-alone separation unit is expected to become increasingly more common. Specifically for natural gas, utilization of smaller, more remote natural gas wells will require the use of less equipment intensive and more flexible separation technologies, which precludes the use of traditional, more capital and equipment intensive thermally based units.

The use of membranes is, however, not without challenges. Perhaps the most important hurdle to overcome in membrane development for natural gas purification is the ability to maintain high efficiency in the presence of harsh feed components such as CO_2 and H_2S, both of which can swell and plasticize polymer membranes. Additionally, as this project demonstrates, achievement of similarly high selectivity for *both* CO_2 and H_2S is challenged by the different governing factors that control their transport through polymeric membranes. However, as others have suggested and shown, as well as what is demonstrated in this project, when CO_2 is the primary contaminant of interest, maintaining high CO_2/CH_4 efficiency appears to be more important in relation to product loss in the downstream. This work focuses on a class of fluorinated, glassy polyamide-imides which show high plasticization resistance *without* the need for covalent crosslinking. Membranes formed from various polyamide-imide materials show high mixed gas selectivities with adequate productivities when subjected to feed conditions

that more closely resemble those that may be encountered in a real natural gas well. The results of this project highlight the polyamide-imide family as a promising platform for future membrane material development for materials aimed at aggressive natural gas purifications due to their ability to maintain high selectivities under aggressive feed conditions without the need for extensive stabilization methods.

CHAPTER 1

INTRODUCTION AND MOTIVATION

1.1. Natural Gas Production

As the world's population continues to increase, so too will the need for additional sources of energy. Total worldwide energy consumption is expected to grow from 505 quadrillion Btu to 770 quadrillion Btu by the year 2035 [1], equating to a 53% increase in total energy usage. This growing trend, coupled with governmental legislation and policies demanding more efficient energy technologies and lower CO_2 emissions has thrust natural gas into the spotlight. As demonstrated in Figure 1.1, coal continues to be the primary source of atmospheric CO_2 emissions. Natural gas, with its lower CO_2 emissions and increased thermal efficiency, has become the fastest growing fossil fuel, and its consumption is projected to increase by 52% through the year 2035. Additionally, since the early 90s, new technologies such as horizontal drilling have allowed companies to access wells that were previously considered unreachable. Because of these reasons, total worldwide natural gas consumption is predicted to bypass coal, as shown in figure 1.2, primarily for use in electricity generation and as an industrial fuel.

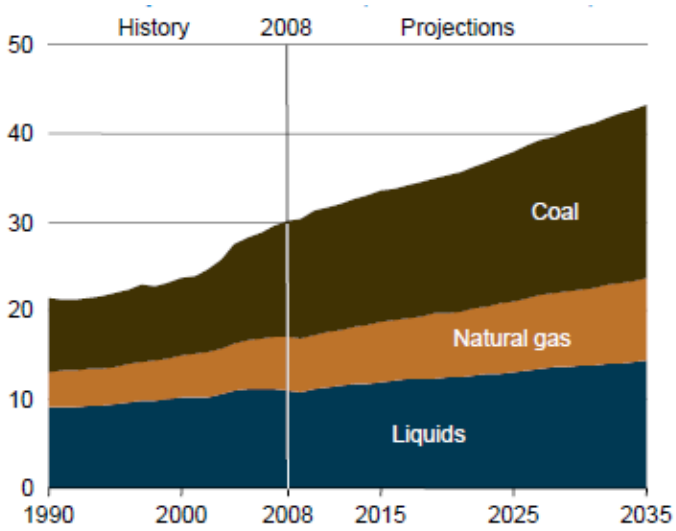

Figure 1.1: World energy-related carbon dioxide emissions by fuel (billion metric tons), 1990-2035 [1].

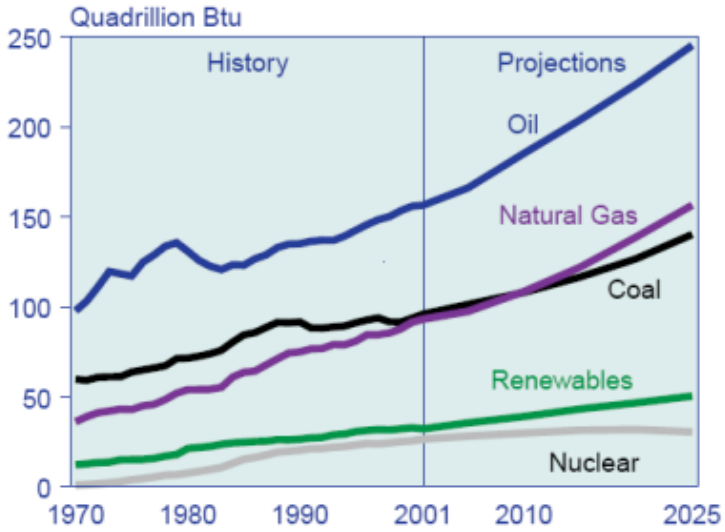

Figure 1.2: Current and projected fuel consumption by type of fuel, in quadrillion Btu [2].

While natural gas is composed primarily of CH_4, a number of other components can exist in an underground gas well. Table 1.1 shows the typical composition of a natural gas

well, although the exact type and concentration of each component will vary considerably depending on geographical location.

Table 1.1: Typical composition found in U.S. natural gas wells [3].

Component	Concentration (mol %)
CH_4	60-90%
CO_2	<1- 40%
H_2S	<4 ppm - 5%
C_{2+}	0-20%
Inerts (N_2, Ne, He)	Trace

Despite an increased thermal efficiency and cleaner burning benefits of natural gas, almost all natural gas requires pretreatment before transmission of the product gas, CH_4, to the consumer. The light hydrocarbons and heavier liquid components (C_{3+}) have value in other markets and are usually removed and sold for other applications. The greater challenge lies in removal of the contaminant gases, CO_2 and H_2S, which are known as acid gases because they can combine with water to corrode pipelines and machinery. Carbon dioxide is also non-flammable and thus reduces the heating value of the gas, and H_2S is highly toxic and corrosive in the absence of water. Therefore, these acid gases must be removed as far upstream as possible before transmission of the gas into the pipeline. The EPA has set the upper limits for CO_2 and H_2S levels in the product stream as < 2% and < 4 ppm, respectively [3,6,4]. Although CO_2 is usually in the range from 1-40% as reported in Table 1.1, it can be considerably higher, such as in enhanced oil

recovery (EOR), where its concentration can be as high as 90% [6]. Thus, the removal of these acid gases constitutes a key process in natural gas production and is in fact the largest industrial gas separation operation [4] . Natural gas that is contaminated with both CO_2 and H_2S above acceptable limits is usually referred to as “acid gas.” When only H_2S is present in the gas-well beyond the EPA’s specifications, the gas is known as “sour gas,” and the removal of these contaminants is referred to as natural gas “sweetening.”

The removal of acid gases is traditionally accomplished through amine absorption or cryogenic distillation. In amine absorption, the process stream is passed through large absorption columns which contain an aqueous amine solution, usually monoethanolamine or diethanolamine [7] . While these technologies offer proven and capable performance, they are not without problems. The absorption process generally involves large thermal swings which are necessary to regenerate the spent amine solution. It also requires constant monitoring and can lead to maintenance issues as well as significant operating expenses [4]. The amount of absorbent solvent scales with the amount of acid gas in the process stream, thus a significant volume of absorbent coupled with large, thick –walled absorption vessels can contribute to significant capital expenditures. The large absorption towers are also ill-suited for remote locations, environments where many future natural gas wells are expected to be located. Finally, the spent solvent can be corrosive and itself presents disposal issues. Hence, it is apparent that newer, more energy efficient and reliable technologies for natural gas separations are needed.

1.2. Membrane Separations

The commercial use of gas separation membranes did not develop until the 1970s, where until then they remained more of an intellectual curiosity. In 1831, Mitchell was the first to demonstrate the concept of membrane permselectivity when he observed faster CO_2 transport rates than H_2 through natural rubber [6-8]. In 1866, Thomas Graham postulated the mechanism of gas transport as having both a thermodynamic and kinetic factor, which lead to the well-established solution diffusion model. It wasn't until the 1960s that membranes, even for liquid feeds, became industrially attractive when Loeb and Sourijajan produced the first asymmetric membrane, which allowed them to achieve fluxes 10X higher than what was previously shown with symmetric materials. This landmark achievement in membrane science was a key factor in the later development of membranes in the 1970s as an alternative to thermal methods for industrial gas separations.

Because the membrane based gas separation is driven by the large partial pressure differential that occurs naturally due to the high gas well-head pressures (>800 psia), membrane separations have the potential to be much lower in energy consumption compared to amine technologies. Also, the small, modular form of membrane units make them ideal for use in remote locations where it would be impractical to install absorption columns. A typical membrane scaffold compared to an absorption column is shown in Figure 1.3.

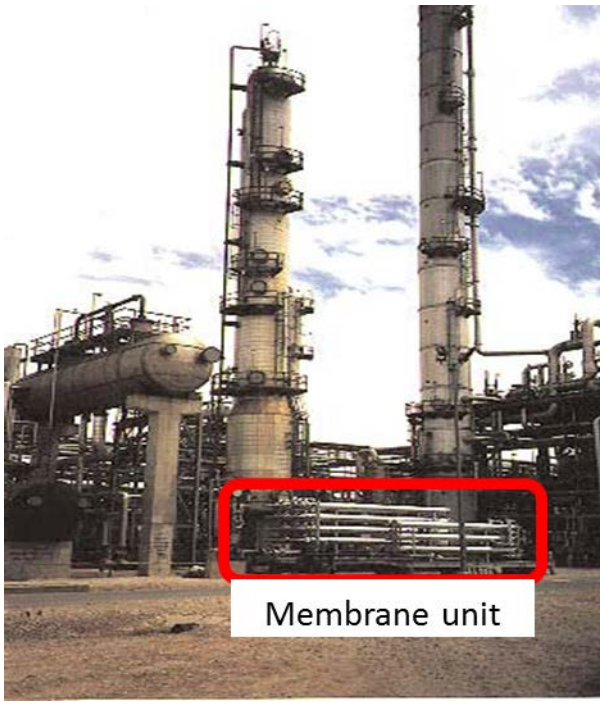

Figure 1.3: Membrane separation units shown next to an amine absorption tower. *Picture courtesy of Medal L.P.*

Additionally, membrane's small, modular form allows for easier scale-up and retrofitting into existing amine separation units.

Despite these potential advantages that membranes offer over distillation and amine technologies, their performance tends to show limits as has been described by an upper-bound tradeoff [9, 10], as depicted in Figure 1.4.

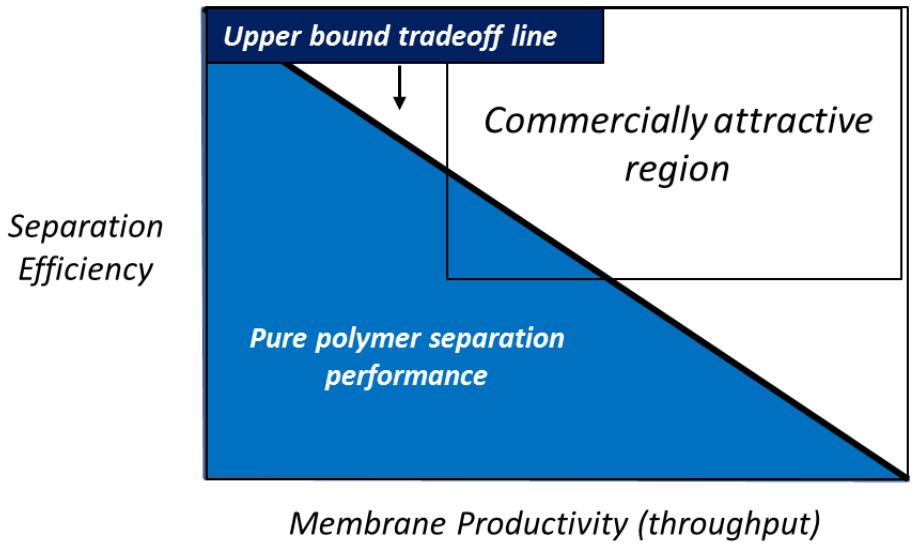

Figure 1.4: Depiction of membrane performance tradeoff for polymer materials.

Because the separation of gases by a membrane relies mainly on size differences between a gas pair, the higher the productivity or throughput of a particular membrane material, the lower is the difference in transport rates of the gases and thus selectivity tends to decline. This has resulted in an upper bound performance tradeoff for a given gas pair for which no economically processible materials exist with productivities and efficiencies that exceed the upper bound. The basis of this tradeoff is described empirically by Robeson and theoretically by Freeman [11-12]. Commercially attractive materials must offer both high efficiency (selectivity) as well as productivity (throughput). For CO_2/CH_4, a number of polymers, such as polyimides, have been extensively researched over the past decade. Many of these materials show performances near or on the upper-bound, however, they tend to suffer significant performance declines under harsh processing environments, such as those encountered in a natural gas well.

For certain separations involving polar or condensable gases, the ability of a membrane to perform near the upper bound is challenged by penetrant induced

plasticization, whereby highly soluble components swell the polymer chains, leading to increased fluxes of both gases and reduced ability of the membrane to perform size discrimination. This concept will be further discussed in Chapter 2. Membrane plasticization is especially relevant in natural gas separations, where CO_2 and H_2S, both of which are highly condensable, can swell the polymer chains at low partial pressures. For example, CA becomes plasticized at CO_2 partial pressures above 200 psia, leading to severely reduced CO_2/CH_4 selectivity. Plasticization is not unique to CA, and in fact, most pure polymers, especially polyimides which have not been stabilized by chemical or thermal methods tend to swell near 200 psia CO_2 partial pressure. In practice, natural gas wells can reach pressures as high as 1000 psia with CO_2 concentrations above 40%. Hence, without additional processing steps to stabilize the membrane, polymeric materials are limited to low pressures and concentrations of acid gases. The various methods to control plasticization will be discussed in detail in chapter 2.

1.3. H_2S Removal from Natural Gas

While the previous discussion on membrane separations applies to both CO_2 and H_2S, most of the trends and phenomena discussed were based on research and observations made from CO_2 removal from natural gas. Very little work has been done academically to demonstrate the efficacy of membranes for the removal of H_2S from natural gas. This is due to the high toxicity of H_2S and the stringent safety requirements that must be followed when working with it. Additionally, cellulose acetate (CA), which is the current industrial standard polymeric membrane material, along with other glassy, CO_2 selective materials generally show low H_2S selectivities over CH_4. As such,

membrane development for H_2S removal has focused on rubbery polymers at low feed pressures. Bhide and Stern have reported a number of rubbery polymers with H_2S/CH_4 selectivities that are more than double that of their corresponding CO_2/CH_4 selectivities [13–15]. On the other hand, they also showed glassy polymers with CO_2/CH_4 selectivities that are much higher than their corresponding H_2S/CH_4 selectivity. They suggested that no single material exists that shows similarly high selectivities toward *both* CO_2 and H_2S. The fundamental reasons for this discrepancy in selectivities stem from different factors that govern the transport of the two gases and the different selectivity mechanisms between rubbery and glassy materials. These differences will be discussed in Chapter 2. Still another challenge exists with membrane based H_2S removal, which is H_2S's ability to plasticize polymer membranes at even lower partial pressures than CO_2. Because H_2S is polar and more condensable than CO_2, its solubility in membranes is generally much higher than CO_2, which can lead to plasticization at low feed pressures. However, some authors have suggested and shown that the separation of condensable gases from light gases using rubbery polymers, such as hydrocarbon gases from H_2, can actually be enhanced by plasticization [16]. Such a phenomenon again stems from differences in the separation mechanisms between rubbery and glassy polymers. This plasticization enhanced selectivity could be extended to the separation of H_2S from CH_4 using rubbery polymers. Thus, plasticization, which tends to reduce the separation efficiency of CO_2 from natural gas using glassy polymers may actually enhance the removal efficiency of H_2S in rubbery polymers. Because of the above complex issues, research towards the simultaneous removal of both acid gases from natural gas has been limited.

It may seem intuitive that one simply use glassy, CO_2 selective polymers for a binary CO_2/CH_4 separation, and rubbery polymers for a binary H_2S/CH_4 separation. Many natural gas wells, however, contain a mixture of *both* CO_2 and H_2S [4]. Therefore, a membrane separation unit should have both H_2S and CO_2 selective elements in series, or one single element that is selective toward both. The type of membrane material used, rubbery or glassy, will depend on the feed and processing conditions. Hao et al. simulated different configurations of H_2S selective membranes, CO_2 selective membranes, and both types of membranes in series. They concluded that a single membrane that is more selective towards the contaminant gas of highest feed concentration resulted in the lowest processing cost [17].

Baker et al. compared the separation costs of a traditional DEA absorption unit to a membrane/SulfaTreat® hybrid separation unit, with the membrane unit being comprised of a rubbery polymer [4]. In this situation, the rubbery membrane acted as a bulk separation unit, with the final H_2S polishing step to bring it's concentration below 4 ppm being accomplished by a SulfaTreat® fixed bed absorption unit. Particularly when the total feed flow rate was between 2 and 5 MMscfd, the membrane/ SulfaTreat® hybrid unit resulted in both lower capital and operating cost when the feed was composed of H_2S and CO_2 in the range of 0.05-5% and 3-20%, respectively. It is important to note that the CO_2 concentration in their study was relatively closer to its pipeline specification of 2%. The moderate CO_2/CH_4 selectivity of the rubber was therefore able to reduce its concentration to the required specification. In the same work, Baker suggested that when CO_2 concentration was higher than 25%, the rubbery materials used for their membrane hybrid unit would *not be able to* bring the CO_2 concentration down to pipeline grade

without vastly over processing the feed. They conjectured that in such a case, a more CO_2 selective material, such as CA, should be used in series with the rubbery material.

Regardless of the type of material used, it is unlikely that membranes alone could be used to bring the concentration of both gases down to pipeline grade. Membranes *can*, however, be used as a bulk separation unit to reduce the concentration of acid gases. The final polishing step could be accomplished through an absorption unit as demonstrated by Baker et al. A lower acid gas concentration being fed to the amine polishing unit could significantly reduce both the capital and operating cost of such a unit, since these costs tend to scale with the concentration of acid gases. Furthermore, as Hao et al. discussed, one single membrane that is more selective toward the contaminant gas in highest concentration may lead to lower processing costs than having two or more membrane units in series. Since most natural gas wells in the U.S. contain CO_2 in higher concentration than H_2S [6, 17, 18], a single membrane element comprised of a glassy polymer with high CO_2/CH_4 selectivity and moderate H_2S/CH_4 selectivity, such as CA, may be suitable for this type of separation. Although the performance of CA membranes is proven and well understood, total capital and operating costs could be further reduced using membranes with higher CO_2/CH_4 selectivities. Such higher selectivities could result in lower CH_4 loss, which is a main driver of operating costs. Additionally, CA's performance at CO_2 pressures above 200 psia becomes significantly reduced. Thus, there may be an avenue for the use of membranes, specifically glassy materials, for the removal of both H_2S and CO_2 from natural gas. As noted, an overwhelming majority of research for H_2S removal has focused on rubbery polymers. As such, there exists significant room for the characterization and development of glassy membranes for H_2S

removal. Moreover, evaluation of these materials towards the simultaneous separation of CO_2 and H_2S under industrially relevant conditions is important. Also, as noted, such work has received only minor attention academically. Therefore, the goal of this project is to not only develop and characterize H_2S transport through glassy polymers, but to bridge the gap between H_2S selective materials on one end of the spectrum and CO_2 selective materials on the other end. These materials will also be evaluated towards the simultaneous CO_2 *and* H_2S separation from natural gas, which will be referred to as a total acid gas separation.

Based on the above discussion, the overarching goal of this work is to fundamentally characterize and compare H_2S transport through glassy and rubbery polymers, and to assess the separation performance of said materials towards the simultaneous separation of CO_2 and H_2S from natural gas under industrially relevant conditions.

1.4. Research Objectives

(1) Synthesis and development of polyamide-imide dense film membranes and evaluation of their CO_2 and H_2S separation properties

Understanding the structure/property relationships that govern the transport of gases and membrane selectivity is crucial for future work aimed at improving the separation properties. An initial polyamide-imide, which has been described in the literature, will be synthesized. This material has adapted an amide bond, which imparts interchain hydrogen bonding and acts to physically crosslink the polymer chains, to a high performance polyimide which is otherwise susceptible to plasticization.

Therefore, this class of materials has the potential to combine good productivity and efficiency with high plasticization resistance. The CO_2 and H_2S transport properties will be evaluated, and based on these results, new materials with enhanced separation properties will be synthesized.

(2) Fundamental characterization of CO_2 and H_2S transport through both glassy and rubbery polymer materials

As previously mentioned, because selectivity in glassy and rubbery polymers is based on different factors, glassy materials generally show high CO_2/CH_4 selectivities but low H_2S/CH_4 selectivities, while rubbery polymers show the opposite trend. This objective aims to determine the governing factors that control the transport H_2S through both types of materials and how these differences are reflected through the selectivities that rubbers and glasses show for H_2S over CH_4. The goal will be to determine the underlying reasons for the opposite selectivity trends shown for both types of materials, and suggest methods for improving the H_2S/CH_4 selectivity in glassy polymers. In conjunction with objective 1, this objective will provide fundamental insight into the transport of H_2S through polymeric materials, and provide valuable information for future efforts aimed at material development for acid gas purification.

(3) Evaluation of the total acid gas separation performance of glassy and rubbery polymer membranes under realistic, aggressive feed conditions

Because real natural gas wells reach pressures above 800 psia, the true separation performance cannot be adequately evaluated using single gas, low pressure testing. Non-ideal effects such as membrane plasticization can cause significant performance reductions. It is therefore necessary to test materials under mixed gas, high pressure conditions. Because glassy polymers are more CO_2 selective, it is hypothesized that they will show higher total acid gas selectivities in conditions where CO_2 concentration is higher than H_2S. Conversely, the more H_2S selective rubbery materials are expected to show higher total acid gas selectivities when H_2S concentration is greater than CO_2. Additionally, phenomenon such as plasticization enhanced selectivity in rubbery polymers will be evaluated to determine its effect on the CO_2/CH4 selectivity. The end goal of this objective is to determine concentration ranges where glassy polymers have potential to offer better separation performance than rubbery polymers for natural gas purification.

1.5. Dissertation Overview

Chapter 2 will discuss the differences between glassy and rubbery polymers and the fundamentals behind gas transport through dense polymer materials. Relevant membrane phenomena, such as plasticization and the methods for controlling it will also be discussed. Chapter 3 will explain the experimental aspects, such as polymer synthesis and the measurement of gas permeability and sorption. Chapter 4 and 5 will report on the effects of thermal annealing on the initial polymer as well as discuss modifications to the

polymer backbone aimed at improving upon the H_2S transport and selectivity. Chapter 6 will focus on the fundamental transport characterization of H_2S and CO_2 through glassy and rubbery polymer materials, and chapter 7 will be devoted to high pressure, ternary mixed gas permeability testing. The final chapter will discuss recommendations for future work.

1.6. **References**

[1] K. A. Smith et al., *International Energy Outlook 2011, DOE/EIA-0484*, Energy Information Administration, (2011).

[2] J. Staub et al., *International Energy Outlook 2009, DOE/EIA-0484(2009)*, Energy Information Administration, (2011).

[3] R. W. Baker, "Future Directions of Membrane Gas Separation Technology," Industrial and Engineering Chemistry Research, **41**, 1393-1411, (2002).

[4] R. W. Baker and K. Lokhandwala, "Natural Gas Processing with Membranes: An Overview," *Industrial & Engineering Chemistry Research*, **47** (7), 2109-2121, (2008).

[5] K. Amo et al., "Low-Quality Natural Gas Sulfur Removal / Recovery, Final Report," *Membrane Technology and Research, Inc.*, (1998).

[6] A. Tabe-Mohammadi, "A Review of the Applications of Membrane Separation Technology in Natural Gas Treatment," *Separation Science and Technology*, 34:10, 2095-2111, (2007).

[7] J. K. Ward, "Crosslinkable Mixed Matrix Membranes For The Purification of Natural Gas, *PhD Dissertation*, Georgia Institute of Technology, Atlanta, Georgia, (2010).

[8] W.J. Koros and R.T. Chern, "Separation of Gaseous Mixtures Using Polymer Membranes," *Handbook of Separation Process Technology, 862-963, (John Wiley & Sons, Inc., New York, 1987).*

[9] L.M. Robeson, "Polymer membranes for gas separation," *Current Opinion in Solid State and Materials Science*, **4** (6), 549-552, (1999).

[10] L. M. Robeson, “The upper bound revisited,” *Journal of Membrane Science*, **320**, (1–2), 390-400, (2008).

[11] B. D. Freeman, “Basis of Permeability/Selectivity Tradeoff Relations in Polymeric Gas Separation Membranes,” *Macromolecules*, **32**, 375-380, (1999).

[12] L. Robeson, “Correlation of separation factor versus permeability for polymeric membranes,” *Journal of Membrane Science*, **62** (2), 165-185, (1991).

[13] G. Chatterjee, A.A. Houde, S.A. Stern, "Poly(ether urethane) and poly(ether urethane urea) membranes with high H_2S/CH_4 selectivity, *Journal of Membrane Science*, **135**, 99-106, (1997).

[14] B.D. Bhide, S.A. Stern, “Membrane processes for the removal of acid gases from natural gas. I. Process configurations and optimization of operating conditions,” *Journal of Membrane Science*, **81** (3), 209-237, (1993).

[15] B. Bhide, A. Voskericyan, S.A. Stern, “Hybrid processes for the removal of acid gases from natural gas,” *Journal of Membrane Science*, **140** (1), 27-49, (1998).

[16] H. Lin, E. Van Wagner, B. D. Freeman, L. G. Toy, R. P. Gupta, “Plasticization-enhanced hydrogen purification using polymeric membranes,” *Science,* **311**, 5761, 639-42, (2006).

[17] J. Hao, P. A. Rice, S. A. Stern, “Upgrading low-quality natural gas with H_2S-and CO_2-selective polymer membranes. Part I. Process design and economics of membrane stages without recycle streams,” *Journal of Membrane Science*, **209**, 177-206, (2002).

CHAPTER 2

BACKGROUND AND THEORY

2.1. Polymeric Membranes for Gas Separations

There are many ways to classify polymers, however, for transport purposes, the molecular motions and packing structure of the polymer matrix can be classified as being either glassy or rubbery depending on the proximity of the polymer's glass transition temperature (T_g) to the operating temperature of interest [1]. The T_g of rubbers is below the operating temperature, and as such, they consist of densely packed polymer chains with a high degree of rotational and vibrational mobility that occurs due to long range, cooperative motions of the polymer chain segments. These molecular motions, which are thermally activated, create transient fluctuations in interchain spacing, which result in the formation of short-term "pockets" of free volume for which gas sorption and diffusion can occur. The time that the size and size distribution of these packets remains fixed is very short, and no net change in the intersegmental chain spacing occurs. Consequently, gas flux through rubbery polymers tends to be higher than glassy polymers, and their size discriminating capabilities are low. Rubbery polymers can be described as a highly viscous, high molecular weight liquid. Their backbone typically consists of long repeat units of flexible functional groups such as (–CH_2-), (-O-), (–COO-) and (-NH-). The latter three increase polarity and contribute to high solubility of polar, condensable molecules [2]. Glassy polymers, on the other hand, are below the T_g, and as a result, contain rigid polymer chains that are essentially "frozen" into a non-equilibrium conformation [3]. The glassy polymer chains lack sufficient mobility to relax to their most thermodynamically

favorable conformation. Such low mobility creates molecular scale packing defects or excess free volume microvoids which are “frozen” into the glassy matrix. This can be conceptualized in the specific volume vs. temperature diagram shown in figure 2.1.

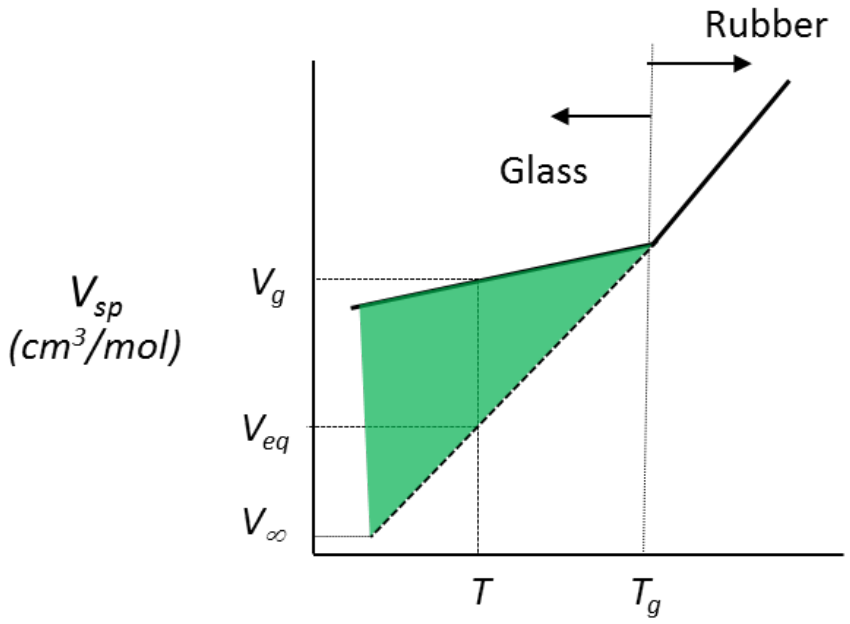

Figure 2.1: Specific volume dependence on temperature. Figure adapted from [1].

The specific volume of the glassy polymer matrix, V_g, is greater than V_{eq}, the specific volume of the hypothetical rubbery polymer at that temperature. The difference between the experimental specific volume and the hypothetical specific volume is the excess free volume that is trapped into the rigid glassy matrix. Localized, non-cooperative thermally activated oscillations along the polymer backbone contribute to a more defined distribution of intersegmental spacing and free volume, giving glassy polymers their ability to distinguish gas molecules based on size and shape [1]. The amount of excess free volume will depend on the rate of quenching below the T_g [4–6]; the slower the

cooling rate, the more time the chains have to relax to their thermodymically favored conformation. In the limit of infinite cooling, no glassy microvoids would form, and the specific volume of the glass would equal that of the hypothetical rubbery volume [1]. The specific volume of the hypothetical rubber is depicted as V_∞ in figure 2.1. The separation characteristics of polymer membranes are determined by chain mobility, intersegmental chain spacing, free volume within the polymer matrix, and distributions of the latter two. Physicochemical interactions between penetrant gas and the polymer also play a role, although to a smaller extent in glassy polymers. Thus, gas transport in rubbery and glassy polymers is governed by physical and physiochemical factors, the extent of each factor being different between the two types of polymers. Such factors give rise to different selectivities for CO_2 and H_2S over CH_4 in rubbers and glasses, and these differences will be further discussed in section 2.5 and chapter 6.

2.2. Gas Transport through Non-porous Media

2.2.1. General Transport Theory

The transport of gases in non-porous materials is described by a solution-diffusion mechanism [7–9], where gas molecules sorb in the upstream, high pressure side of the membrane, followed by activated diffusion through the membrane and desorption at the downstream, low pressure side. This mechanism of membrane-based gas transport is represented in figure 2.2.

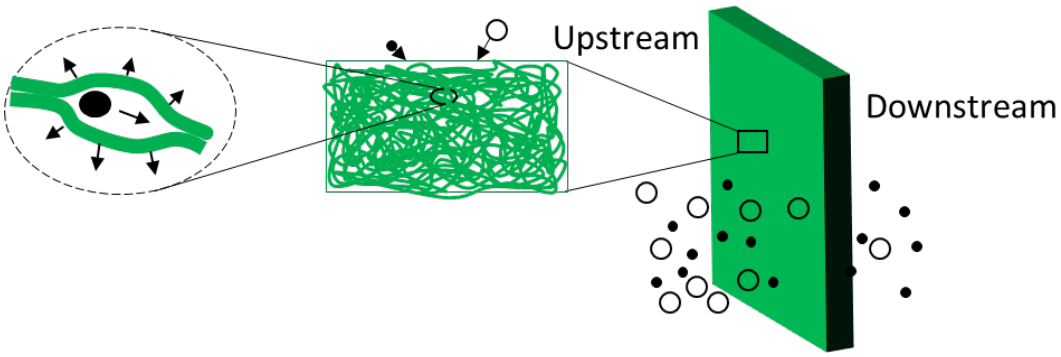

Figure 2.2: Schematic representation of gas dissolution and transport via the solution-diffusion mechanism. Schematic adapted from [9].

The driving force for mass transport occurs due to a thermodynamic activity difference across the membrane, which leads to a concentration difference, thus gas diffusion occurs in the direction of decreasing activity [1]. In general, transport favors the smaller penetrant with greater mobility. Hence, most membranes are selective for the smaller gas. However, deviations can arise, such as in the case of highly condensable hydrocarbon gases in rubbery polymers, which have been shown to be selective toward the more larger, more soluble penetrant [10, 11]. In fact, solubility is the primary factor in determining transport differences in rubber polymers. This will be discussed further in section 2.2.2.

Gas solubility is usually quantified by a sorption coefficient or capacity, and is defined as the concentration in cc(STP)/(cc·polymer) normalized by the penetrant partial pressure in contact with the membrane.

$$S_i = \frac{C_i}{p_i} \tag{2.1}$$

S is a measure of how much penetrant can be accommodated in the polymer matrix per unit volume of the matrix and per unit pressure [1].

Gas diffusion is described by a sequence of random “hops”, where the gas molecule is envisioned to jump from one sorption site within the polymer matrix to another [12]. This process is depicted in figure 2.3.

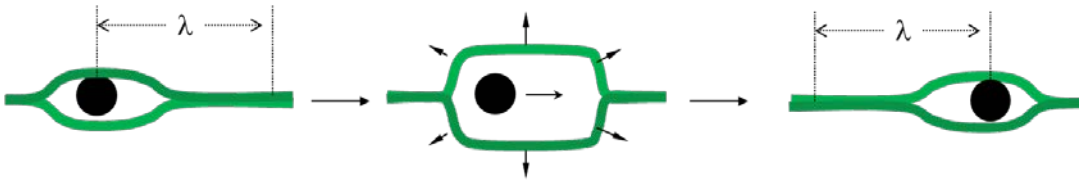

Figure 2.3: Depiction of activated diffusion process.

In order to execute a diffusion jump, a gap of sufficient size must be created in the adjacent polymer chains. These transient gaps occur due to random, thermally activated motions of the polymer chains. The diffusion coefficient can be expressed as a function of the jump length, λ_i, and frequency, f_i, of gap openings. This relation is given in Equation 2.2 [13]:

$$D_i = \frac{\lambda_i^2 \cdot f_i}{6} \tag{2.2}$$

The size and frequency of gap openings depends on many factors, some of which are intrinsic to the polymer material, such as polymer chain stiffness and intersegmental

spacing, while some are due to operating conditions such as temperature, concentration and nature of the penetrant gas. Nearby gas molecules can influence the creation of a gap opening, and high activity penetrants can alter the polymer chain packing distribution.

In both glassy and rubber polymers, diffusion is normally described by Fick's first law [1]:

$$J_i = -D_i \frac{\partial C_i}{\partial x} \tag{2.3}$$

where J_i is the flux of the gas in cc(STP)/(cm2*s), *Di* is the diffusivity in cm^2/s, C_i is the local penetrant concentration and *x* is the coordinate direction of flux in the membrane in cm. The diffusion coefficient of a penetrant tends to depend on its local concentration. Because a concentration gradient exists across the membrane, an average diffusion coefficient is generally used as follows [7, 8]:

$$\bar{D}_i = \frac{\int_{C_{i,d}}^{C_{i,up}} D_i(C)dc}{C_{i,up} - C_{i,down}} \tag{2.4}$$

$\bar{D}_i$ is concentration averaged diffusivity in cm^2/s, *Ci,up* and *Ci,d* are the penetrant concentrations on the high and low-pressure sides of the membrane respectively. Substituting equation 2.4 into 2.3 and separating the variables gives:

$$\int_0^l Ji \cdot dx = -\bar{D}_i \int_{C_{i,up}}^{C_{i,d}} dC \tag{2.5}$$

Under steady-state conditions of constant flux, equation 2.5 can be integrated to give 2.6:

$$J_i = \bar{D}_i \cdot \frac{[C_{i,up} - C_{i,d}]}{l} \tag{2.6}$$

l is the membrane thickness in cm. Substituting Equation 2.1 into 2.6 gives:

$$J_i = \frac{\bar{D}_i}{l} \cdot [S \cdot p_{i,up} - S \cdot p_{i,d}] \tag{2.7}$$

$p_{i,up}$ and $p_{i,d}$ are the upstream and downstream penetrant partial pressures. Similar to the diffusion coefficient, an average sorption coefficient, given by Equation 2.8, is used due to a concentration gradient existing across the membrane [8].

$$\bar{S}_i = \frac{C_{i,up} - C_{i,d}}{\Delta p_i} \tag{2.8}$$

Inserting Equation 2.8 into 2.7 gives:

$$\frac{J_i \cdot l}{\Delta p_i} = \bar{D}_i \times \bar{S}_i \tag{2.9}$$

To account for non-ideal gas phase effects, a partial fugacity difference, Δf_i, is often used instead of a partial pressure difference.

The flux of a penetrant gas through the membrane is most often characterized by a permeability coefficient, which for permanent gases and all practical purposes is pressure

independent. The permeability coefficient, or gas permeability, is defined as the flux of penetrant *i* normalized by its partial pressure or fugacity difference across the membrane, as well as the membrane thickness, *l*, as given in equation 2.10.

$$P_i = \frac{flux_i}{\Delta p_i / l} \tag{2.10}$$

As can be seen in Equation 2.9, the permeability can be described by the product of the sorption and diffusion coefficients. Hence, the permeability of a penetrant gas as well as the selectivity of a membrane is governed by both physiochemical interactions as well as penetrant mobility differences.

The efficiency of a membrane is described by a selectivity factor. The ideal selectivity factor, which is simply the ratio of the single gas permeability coefficients as shown in Equation 2.11, describes the intrinsic separation capabilities of a material for a gas pair.

$$\alpha^*_{i/j} = \frac{P_i}{P_j} \tag{2.11}$$

P_i and P_j are the permeability coefficients of the fast and slow gases, respectively. In accordance with equation 2.9, the ideal selectivity can be divided into the product of a mobility and solubility selectivity:

$$\alpha^*_{A/B} = \left[\frac{D_A}{D_B}\right] \times \left[\frac{S_A}{S_B}\right] \tag{2.12}$$

The solubility selectivity is controlled by polymer-penetrant physiochemical interactions, while the diffusion selectivity is controlled by how frequently, on a time averaged basis, a hole of sufficient volume appears next to a penetrant gas [1].

For mixed gas feeds, the selectivity factor is given by the ratios of the mole fractions of the fast gas to the slow gas in the permeate and feed streams, respectively.

$$\alpha_{A/B} = \frac{\left[y_A / y_B\right]_{permeate}}{\left[y_A / y_B\right]_{feed}} \tag{2.13}$$

When the pressure in the downstream side of the membrane is very low relative to the upstream side, as is the case for the permeation experiments in this project, the mixed gas selectivity factor is equal to the ratio of the individual permeability coefficients of the fast to slow gas.

2.2.2. Transport in Rubbery Polymers

Transport in rubbery polymers is phenomenologically more simple than in glassy polymers. For materials above their glass transition temperatures, the sorption of penetrant gases into the polymer matrix is analogous to gas dissolution into a liquid, where Henry's Law is used to describe the linear concentration vs. pressure relationship, and absorbed gas molecules are said to be in a "dissolved" state. Henry's Law for gas *ab*sorption is given mathematically in Equation 2.14 and depicted graphically in figure 2.4.

$$C_i = k_{D,i} \cdot p_i \tag{2.14}$$

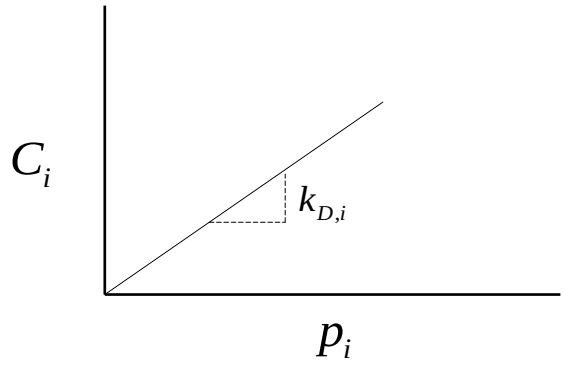

Figure 2.4: Concentration vs. pressure isotherm for Henry's Law type sorption in materials above their glass transition temperature.

$k_{D,i}$ usually refers to the Henry's Law coefficient, given by the slope of the concentration vs. pressure isotherm, and describes the ease to which the polymer chains can open up to accommodate a penetrant gas molecule [3]. p_i is the penetrant partial pressure in contact with the membrane. Because rubbery materials are in a state of packing equilibrium, no permanent excess free volume microvoids exist. Outside of polymer chain swelling, the sorption coefficient in Equation 2.1 in rubbery materials is constant and is equal to the Henry's Law coefficient in Equation 2.14.

The flux of a gas molecule in a rubbery polymer is envisioned to occur by moving from one "dissolved" point to another "dissolved" point. Because all the sorption environments are the same in a rubbery matrix, the diffusion coefficient is also constant in non-swelling conditions, and is described as $D_{D,i}$, where subscript "*D*" refers to a "dissolved" environment. In the absence of swelling, the permeability in rubbery polymers is constant and described by Equation 2.15.

$$P_i = D_{D,i} \cdot S_i = D_{D,i} \cdot k_{D,i} \tag{2.15}$$

For highly sorbing gases or vapors, penetrant concentration may deviate significantly from Henry's Law [7]. In this case, sorption can be described using the Flory-Huggins equation:

$$\ln a = \ln \phi + (1-\phi) + \chi(1-\phi)^2 \tag{2.16}$$

a is the penetrant activity, ϕ is the volume fraction of penetrant dissolved in the polymer, and χ is the Flory-Huggins interaction parameter. Under such conditions, the diffusion coefficient also increases significantly with penetrant concentration.

As discussed in section 2.1, rubbery polymers have weak size sieving capabilities due to a high degree of chain mobility. Figure 2.5 compares O_2 and N_2 diffusivities and diffusion selectivities for a series of rubbery and glassy polymers.

A)

Polymer	$D_{O_2} \times 10^8$ (cm^2/sec)	$\frac{D_{O_2}}{D_{N_2}}$
Butyl rubber	8.1	1.8
LDPE[a] (density = 0.914 g/cm^3)	46	1.4
Polychloroprene	43	1.5
Polybutadiene	150	1.4
Natural rubber	158	1.4
Gutta percha	70	1.4
Poly(dimethyl butadiene)	14	1.8
Polyoxymethylene	3.7	1.7

[a] Low density poly(ethylene).
Data from Stannett [65].

B)

Polymer	$D_{O_2} \times 10^8$ (cm^2/sec)	$\frac{D_{O_2}}{D_{N_2}}$	Pressure (atm)
Polycarbonate[a]	5.1	3.1	1
Tetramethyl polycarbonate[a]	8.1	3.8	1
Polysufone[b]	4.4	3.6	5
Tetramethyl polysulfone[b]	8.0	3.8	5
Polystyrene[c]	16.5	3.3	1
Polyphenylene oxide[d]	21.5	3.2	1.5
Polyphenylene sulfide[d]	1.13	3.0	1.5

[a] Data from Muruganandam *et al.* [89].
[b] Data from McHattie *et al.* [43].
[c] Data from Puleo *et al.* [112].
[d] Data from Aguilar-Vega and Paul [113].

Figure 2.5: Diffusion coefficients and diffusion selectivities for a series of rubbery **A)** and glassy **B)** polymers. Figured adapted from [7].

The diffusivities are much higher, and in some cases orders of magnitude higher in rubbery materials versus glassy polymers. Such low size discrimination in rubbers means their selectivity mechanism is governed mainly by solubility differences between a gas pair. Thus, applications involving the removal of condensable components from non-condensable components, such as organic vapors from air may benefit from the use of a rubbery rather than glassy material. In such a situation, penetrant solubility is high enough that the larger, more condensable gas shows higher permeable than the smaller, more permanent gas [14].

2.2.3. Transport in Glassy Polymers

The transport and separation property differences between rubbery and glassy polymers stem from the non-equilibrium nature of glassy materials. As discussed at the beginning of this chapter, the sharp decrease in thermal expansion coefficient in glasses as the T_g is traversed creates molecular scale packing defects. As a result, two different sorption environments exist within a glassy polymer matrix. This is illustrated in figure 2.6.

Figure 2.6: Schematic of dual sorption environments in glassy polymers.

The Langmuir environment is associated with non-equilibrium, molecular scale intersegmental packing defects which are fixed in the glassy state. The concentration in this environment is noted by C_H, where subscript "*H*" stands for hole, as this sorption mechanism is often referred to as "hole-filling" to describe gas molecules *adsorbing* into pre-existing free-volume pockets. The Henry's environment is analogous to sorption domains in rubbers, where densely packed polymer chains are in packing equilibrium. Sorption in this environment involves dilation of the polymer matrix, and scales linearly with penetrant partial pressure as described a Henry's Law relation. As in rubbers, the concentration of penetrant *absorbed* into this environment is given by C_D.

As a consequence of the "frozen" in packing defects, a simple Henry's Law model fails to describe concentration vs. pressure behavior in glassy polymers. Instead, isotherms which are concave to the pressure axis are usually observed. This behavior is depicted in figure 2.7-B.

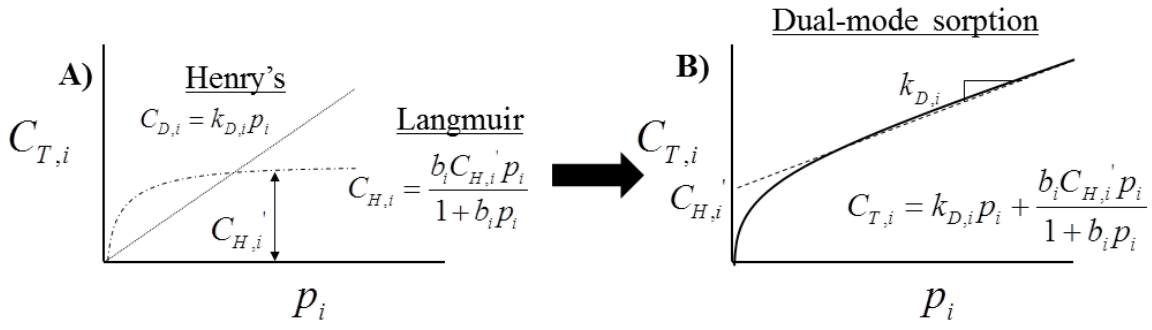

Figure 2.7: A) Individualized Henry's and Langmuir sorption isotherms and **B)** typical concentration vs. pressure behavior observed in glassy polymers as a result of the summation of the two environments.

$k_{D,i}$ is the Henry's Law coefficient as described in section 2.2.2. The Langmuir capacity constant, C_H', in cc(STP)/(ccpolymer), represents the maximum concentration of penetrant gas which can *ad*sorb into the finite number of excess free volume microvoids. It can be estimated by extrapolating the linear portion of the dual-mode sorption isotherm to the pressure axis. b is the Langmuir affinity constant in $psia^{-1}$ and represents the ratio of the sorption and desorption rate constants, respectively. Thus, the affinity constant is a measure of the tendency of a gas to adsorb into the Langmuir microcavities. The two sorption environments are described by dual-mode sorption theory in glassy polymers [3]. Hence, the total concentration of penetrant gas inside the glassy matrix is a sum of the concentrations, which exist in local equilibrium, of the two individual environments.

The Langmuir capacity is related to the proximity of the temperature to the polymer T_g [1]. The higher the T_g and the further away the operating temperature is from it, the less energy the polymer chains have to relax to an equilibrium state. As the temperature approaches the T_g, the free volume microvoids tend to relax out by a diffusive mechanism. Higher T_g generally correlates with increased C_H', and so higher T_g materials generally accommodate higher concentrations of penetrant gas. Because these sorption sites are finite in number, they become saturated as penetrant partial pressure increases and sorption then occurs predominantly in the Henry's environment. This is depicted in figure 2.7-B, where the concentration isotherm becomes linear in accordance with gas dissolution described by Henry's Law. In general, gas sorption in glasses is higher than in rubbers, especially at low pressures, due to the existence of non-equilibrium excess free volume microvoids.

The previous discussion dealt with the equilibrium portion of the dual-mode sorption theory. Vieth and Sladek developed a model to describe diffusion in glassy polymers with the idea that penetrants in the two different sorption sites have different intrinsic diffusional mobilities [15, 16]. The model originally postulated that penetrant sorbed in glassy microvoids were completely immobilized and did not contribute to the diffusive flux. Therefore, only penetrants dissolved in the equilibrium portions were mobile and contributed to the overall flux. This assumption was later relaxed by Petropoulous, and subsequent NMR and transport studies led to the observation that penetrants sorbed into the two distinct environments have different diffusive mobilities. This led to development of the partial immobilization model, which envisioned that only a fraction of penetrants adsorbed into the Langmuir sites contribute to the overall diffusive flux. According to this assumption, the total penetrant flux can be expressed by an extension of Fick's First Law to account for diffusion from both sorbed populations, and is given in Equation 2.17 [1, 17]:

$$J_T = -D_D \frac{\partial C_D}{\partial x} - D_H \frac{\partial C_H}{\partial x} \tag{2.17}$$

D_D and D_H are the diffusion coefficients in the dissolved and Langmuir mode, respectively, in cm^2/s. Koros and Paul [1, 18] formulated a more convenient, equivalent expression by assuming that the total penetrant concentration can be divided into a mobile part with diffusivity D and concentration Cm, while the remaining concentration $C - Cm$ is completely immobilized. Furthermore, all the gas associated with C_D as well as

a fraction F of the gas associated with C_H is included in Cm, with the remaining C_H, 1-$1-F$, being completely immobile. This leads to a modification of Equation 2.17:

$$J_T = -D\frac{\partial C_m}{\partial x} \tag{2.18}$$

where

$$C_m = C_D + FC_H \tag{2.19}$$

$F = D_H / D_D$ and is a measure of the relative mobilities of penetrant adsorbed into holes to that dissolved in the equilibrium region. Based on this formulation, the partial immobilization model for the permeability is given by:

$$P = k_D D_D \left[1 + \frac{KF}{1+bp}\right] \tag{2.19}$$

where

$$K = \frac{C_H' b}{k_D} \tag{2.20}$$

p is the penetrant partial pressure, k_D, b, C_H', and F are as previously defined. Depending on the value of F, the permeability may be suppressed due to a lower D_{eff} as a result of increased penetrant immobilization in the Langmuir sites. Figure 2.8 demonstrates the effect of F on permeability vs. pressure behavior in glassy polymers.

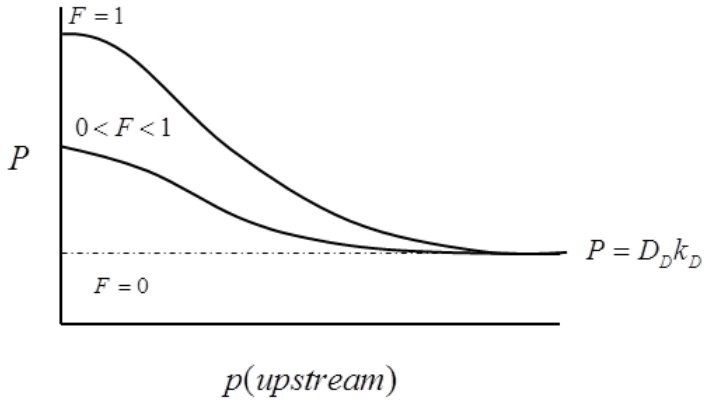

Figure 2.8: Effect of F on permeability in glassy polymers.

As F decreases, the mobility of penetrants in the Langmuir sites to dissolved sites decreases, which reduces the permeability. In the limit when molecules sorbed into Langmuir sites have no mobility, the permeability becomes independent of penetrant pressure and permeation flux is due solely to contributions from penetrants in dissolved regions. Similar to the sorption coefficient, saturation of the Langmuir sorption sites causes the permeability to decrease with increasing pressure as depicted in Figure 2.8, eventually reaching the asymptotic limit when all diffusion jumps and additional sorption occurs from dissolved penetrant.

2.2.4. Temperature Dependence of Transport Parameters

The dual-mode sorption and permeation models are phenomenological in nature. Additional quantum and statistical mechanical based methods to describe gas diffusion on a molecular level all involve formation of an activated state that must be created prior to gas permeation. The activated states and thus the temperature dependence of the permeation and diffusion coefficients take the form of an Arrhenius expression.

$$D = D_o \exp(\frac{-E_D}{RT}) \tag{2.21}$$

$$P = P_o \exp(\frac{-E_P}{RT}) \tag{2.22}$$

D_o and P_o are the preexponential factors, E_D and E_P are the diffusion and apparent permeation activation energies. Similarly, the temperature dependence on the sorption coefficient is given by the Van't Hoff expression.

$$S = S_o \exp(\frac{-\Delta H_S}{RT}) \tag{2.23}$$

S_o is the preexponential factor and ΔH_S is the enthalpy of sorption, which consists of two factors:

$$\Delta H_S = \Delta H_{cond} + \Delta H_{mix} \tag{2.24}$$

ΔH_{cond} is the enthalpy of condensation, and is opposite in sign to the enthalpy of vaporization. ΔH_{mix} is the enthalpy change of mixing a penetrant with the polymer matrix. Thus, sorption consists of two steps [19]: 1.) "condensation" of the penetrant to liquid-like density and 2.) mixing of penetrant gas with the polymer chains. The "condensation" term is negative for most gases, while the mixing term can be positive or negative depending on the work input required to create space in the polymer chains to

accommodate a penetrant molecule. Polymer-penetrant interactions will also affect the enthalpy of mixing. For most gases, the enthalpy of condensation dominates and the overall enthalpy change is exothermic, especially for condensable gases in glassy polymers, where molecular scale spaces within the polymer chains are preexisting. In such circumstances, sorption decreases with temperature. Highly supercritical gases such as H_2 and He have very low ΔH_{cond} and weak interactions with the polymer. In this situation, the enthalpy of sorption becomes slightly positive and gas sorption increases with temperature [7]. It follows from Equation 2.9 that the activation energy for permeation then is the sum of the contributions from the enthalpy change of sorption and activation energy of diffusion, as given in 2.24.

$$E_P = E_D + \Delta H_S \tag{2.24}$$

Gas diffusivity generally shows a greater dependence on temperature, i.e. $E_D > \left|\Delta H_S\right|$ and E_P increases with temperature. Diffusion activation energy is positive and increases with molecular size because larger, thermally activated gaps must be created to execute a diffusion jump.

2.3. Non-Ideal Transport Effects

2.3.1. Plasticization

The selective separation of high activity, condensable gases in glassy polymers is challenged by membrane plasticization. This occurs when highly condensable gases reach a certain concentration in the polymer membrane, leading to physical swelling of

the polymer chains and increases in segmental mobility [20–23]. The plasticization pressure is the point at which the permeability vs. pressure isotherm reaches a minimum, after which the permeability begins to increase with penetrant pressure as illustrated in Figure 2.9:

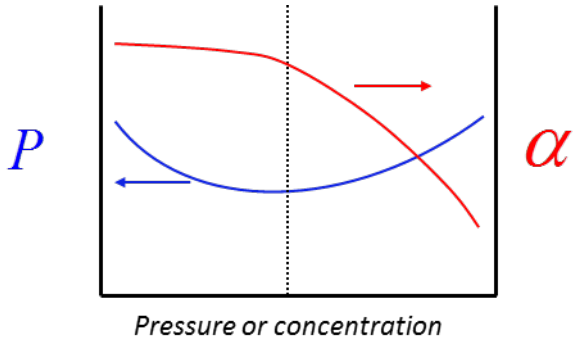

Figure 2.9: Schematic of permeability and selectivity vs. pressure showing the effect of plasticization.

The enhancement of segmental mobility results in a loss of size and shape discrimination, leading to increased penetrant diffusivities. The greatest increase occurs for the larger penetrant, therefore, significant selectivity reductions usually follow plasticization. Glassy polymers are most susceptible to plasticization since their microsctructure is in a non-equilibrium conformation. Penetrant induced swelling can cause permanent alterations to the local packing environment. Because their selectivity relies mainly on diffusion differences, increases in chain mobility can significantly reduce their overall permselectivity. Rubbery polymers, which normally have low mobility selectivities, are not affected by chain swelling to the same extent as glassy polymers. In fact, their permselectivity can be enhanced by plasticization. This can occur because gas sorption increases with the enhancement in polymer free volume that can accompany penetrant

induced swelling. Under such conditions, the sorption coefficient of the more soluble gas will increase to a greater extent than the less soluble one. This can increase sorption selectivity and compensate for any small loss in diffusion selectivity, therefore, overall permselectivity can be enhanced [11]. Hydrogen sulfide and carbon dioxide, both of which are highly condensable and polar/polarizable, can plasticize polymer membranes at low partial pressures, making the issue of plasticization especially relevant in membrane based natural gas purification. The methods for stabilizing glassy polymers against plasticization will be discussed in section 2.5.

2.3.2. Competitive sorption

Another factor that can reduce selectivity in a multi-component feed, relative to pure gas, is competitive sorption. This happens when penetrants compete for the fixed number of Langmuir sorption sites in glassy polymers [24]. This reduces permeability of the more soluble component by suppression of its Langmuir sorption term. The effect of multiple components on the sorption of component *i* can be described by an extension to the dual-mode concentration model given in Figure 2.7. As can be seen in Equation 2.24, the Langmuir affinity constants of all components are included in the denominator of the Langmuir concentration term for component *i*. This reduces the total concentration of penetrant *i* as the partial pressure of the other components increases. Competitive sorption will also affect the permeability, and this can be predicted by an extension of the dual-mode partial immobilization model, and is given by Equation 2.25.

$$C_{T,i} = k_{D,i} p_i + \frac{C_{H,i}' b_i p_i}{1 + \sum_{i=1}^{n} (bp)_i} \tag{2.24}$$

$$P_i = k_{D,i} D_{D,i} \cdot \left(1 + \frac{F_i K_i}{1 + \sum_{i=1}^{n} (bp)_i} \right) \tag{2.25}$$

n is the number of components in the mixture.

2.4. Challenges Associated with the Simultaneous Removal of CO_2 and H_2S

As previously mentioned, glassy polymers are primarily diffusion selective. Their selectivity for a gas pair increases as the size difference between the two gases increases. Rubbery polymers are selective based almost exclusively on solubility differences. Differences in diffusivity have only a minor effect on a rubbery polymer's permselectivity. The size differences of the gases, as measured by kinetic diameter, are given in Figure 2.10 along with condensability differences as inferred by penetrant critical temperature.

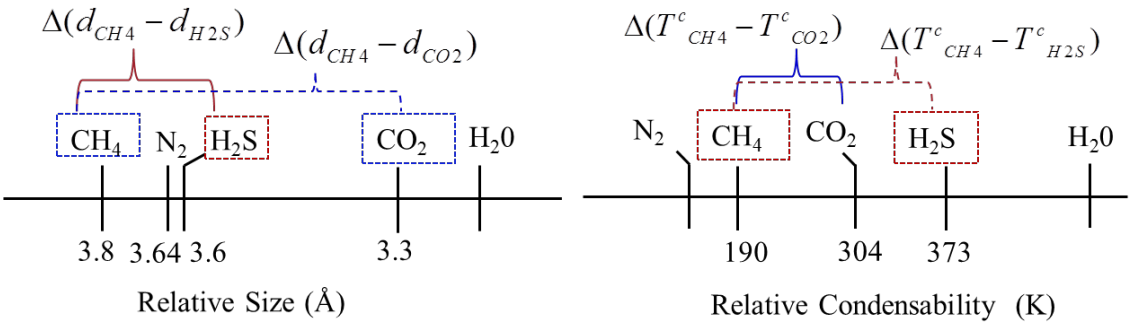

Figure 2.10: Kinetic diameter and condensability differences for various gases.

As shown in Figure 2.10, the kinetic diameter difference between CO_2 and CH_4 is 0.5 compared to 0.2 Å for H_2S and CH_4. On the other hand, the difference in condensability between CO_2 and CH_4 is 114 vs. 184 K for H_2S and CH_4. Hence, glassy polymers have been used predominantly for CO_2/CH_4 separations due to their ability to provide high diffusion selectivity and moderate sorption selectivity. Because of a smaller size difference between H_2S and CH_4 and glassy polymers' generally low sorption selectivity, rubbery polymers offer higher H_2S/CH_4 selectivities. The trends in permeability and permselectivity for these gases are shown in Table 2.1. As can be observed, glassy polymers have high CO_2/CH_4 selectivities and low H_2S/CH_4 selectivities, while the opposite trend occurs in rubbery polymers.

Table 2.1: Typical CO_2 and H_2S permeabilities and permselectivities in rubbery and glassy polymers. Values are based on mixed gas literature values [2, 25–27] and pure gas data collected in our lab. *Additional H_2S data was contributed by B. Kraftschick and C. Kuete in the Koros group.*

	P_{H2S} (Barrer)	P_{CO2} (Barrer)	$\alpha_{H2S/CH4}$	$\alpha_{CO2/CH4}$
Typical rubbery polymer	150-650	11-15	35-50	8-10
Typical Glassy polymer	3-20	20-350	10-15	30-60

In our lab, it has been observed that the H_2S/CH_4 permselectivity in most high CO_2/CH_4 performance glasses is never greater than 20. This is due to unexpectedly low and sometimes reversed H_2S/CH_4 diffusion selectivities along with only moderate H_2S/CH_4 sorption selectivity. Therefore, H_2S solubility must be increased in order to increase the H_2S/CH_4 permselectivity. This can be done through incorporation of polar functional groups, which may also increase CO_2 solubility. However, as will be discussed in chapter 5 and 6, increases in H_2S solubility can increase susceptibility to plasticization, which would presumably reduce the size sieving dependent CO_2/CH_4 permselectivity. Additionally, functional groups which have been shown to provide favorable solubility interactions with H_2S, such as repeat units of $(–O\text{-}CH_2\text{-})_n$ and $(\text{-}COOR\text{-})_n$, tend to enhance chain flexibility, which could reduce the CO_2/CH_4 mobility selectivity. These issues contribute to the challenge of designing materials with similarly high CO_2 and H_2S selectivities, which has hindered development of glassy polymers for H_2S/CH_4 separations. However, as discussed in chapter 1, H_2S/CH_4 permselectivity may not need to be as high as CO_2/CH_4 permselectivity because CO_2 is usually present in much higher concentrations relative to H_2S. Under such conditions, high CO_2/CH_4 selective glassy

polymers can act as a bulk removal step, which would reduce CO_2 and H_2S concentration prior to an amine based downstream polishing step. To compare the total selectivity for CO_2 and H_2S relative to CH_4, it is useful to define a "total acid gas" selectivity, which is given in Equation 2.26.

$$\alpha_{TAG}^{*} = \frac{\left(P_{CO2} + P_{H2S}\right)}{P_{CH4}} \tag{2.26}$$

P_{CO2}, P_{H2S} and P_{CH4} are the pure or mixed gas permeability coefficients. The subscript "*TAG*" refers to "total acid gas." Table 2.2 compares total acid gas selectivity factors between rubbery and glassy polymers. Although the binary CO_2/CH_4 and H_2S/CH_4 selectivities are essentially opposite in rubbers and glasses as shown in Table 2.1, the two materials show similar total acid gas selectivities. However, the permeation driving forces for CO_2 and H_2S will be different when their upstream partial pressures are not equal. In this case, their relative fluxes will also be different. Therefore, it is more useful to compare rubbery and glassy polymers using a separation factor similar to that given in Equation 2.13. A penetrant driving force "corrected" total acid gas separation factor is then given by equation 2.27:

$$SF_{TAG} = \left(\frac{y_{CO2} + y_{H2S}}{y_{CH4}}\right)_{permeate} \Big/ \left(\frac{y_{CO2} + y_{H2S}}{y_{CH4}}\right)_{feed} \tag{2.27}$$

y_{CO2}, y_{CH4}, and y_{H2S} are the mole fractions. Using equation 2.27, the relative fluxes of a hypothetical ternary gas stream can be estimated from pure gas permeabilities. The estimated total acid gas selectivities estimated from pure gas measurements for a range of glassy polymers used in our lab are tabulated in Table 2.2. "H_2S lean" represents a feed consisting of higher CO_2 concentration relative to H_2S, while "H_2S rich" stands for higher H_2S concentration relative to CO_2. We can therefore estimate how differences in H_2S and CO_2 driving forces affect the separation performance of rubbers and glasses.

The H_2S lean feed used to estimate SF_{TAG} for the glasses in Table 2.2 is composed of 5/20/75%, and the H_2S rich feed is comprised of 20/10/70% $H_2S/CO_2/CH_4$ respectively. An upstream feed pressure of 200 psia was used in the calculation. For the rubbery polymers, mixed gas data at 145 psia was adapted from Stern et al. [2]. In their work, the H_2S lean feed is composed of 1.3/28/70.1% $H_2S/CO_2/CH_4$, while the H_2S rich feed is composed of 12.5/18/69.4% $H_2S/CO_2/CH_4$. Although they did not use a feed composition where H_2S concentration was higher than CO_2, we can still demonstrate the effect that increasing H_2S concentration has on the total acid gas separation factor.

Table 2.2: Total acid gas ideal selectivity and penetrant driving force corrected total acid gas separation factors for rubbery and glassy polymers. *The estimated selectivity factors for glassy polymers are based on pure gas permeability data from materials tested in the Koros lab.*

	α_{TAG}*	SF_{TAG} H_2S Lean	SF_{TAG} H_2S rich
Typical rubbery polymer	20-90	7-35	15-40
Typical Glassy polymer	40-65	35-45	19-30

Equation 2.27 provides a more meaningful comparison between rubbery and glassy polymers under similar feed conditions. As predicted, the values in Table 2.2 suggest glassy polymers will be more selective when CO_2 concentration is higher than H_2S, while rubbers have higher total selectivity when H_2S concentration is greater than CO_2. In other words, when CO_2 concentration is higher than H_2S, glassy polymers will permeate more CO_2 and H_2S molecules with lower CH_4 loss in the downstream than rubbers allow. Additionally, glassy polymers can be more easily fabricated into hollow fiber morphology, which may give them additional advantages over rubbery polymers. Although the values in Table 2.2 are hypothetical and based on pure gas, ideal conditions, they do suggest that glassy polymers may have higher total selectivities relative to rubbers when subjected to natural gas streams containing low H_2S levels relative to CO_2, as is the case in most conventional gas wells. It is important to note that the SF_{TAG} is partial pressure dependent, thus it only provides a meaningful comparison of materials under similar feed conditions. Thus, an important objective in this thesis will involve testing this total acid gas selectivity hypothesis by comparing the separation performance of rubbers and glasses under varying ternary mixed gas feeds at pressures up to 1000 psia. These conditions more accurately reflect those that might be encountered at a real natural gas well-head and thus provide a better separation performance indicator for the two types of materials. This will be the subject of chapter 7.

2.5. Methods for Controlling Plasticization

Because many glassy polymers tend to plasticize near 200 psia CO_2 partial pressure, additional functionalization of the membrane is necessary in order to provide a stable and efficient separation of CO_2 and H_2S from natural gas. Crosslinking is one of the most commonly used methods for controlling swelling and plasticization in polymer membranes. Kita et al. crosslinked benzophenone containing polyimides using UV irradiation and saw significant improvements in permselectivity [28]. Wright et al. used similar photo-induced crosslinking on polyacrylate and dihydroxybenzophenone based polymers [29]. Although improvements in selectivity were observed, in both cases, permeability was reduced due to tighter chain packing and increased rigidity.

Staudt-Bickel and Koros [30] developed a covalent crosslinking method as a post-treatment step for 6FDA based polyimides containing diaminobenzoic acid (DABA), which involves reacting the free carboxylic acid group of DABA with ethylene glycol as illustrated below.

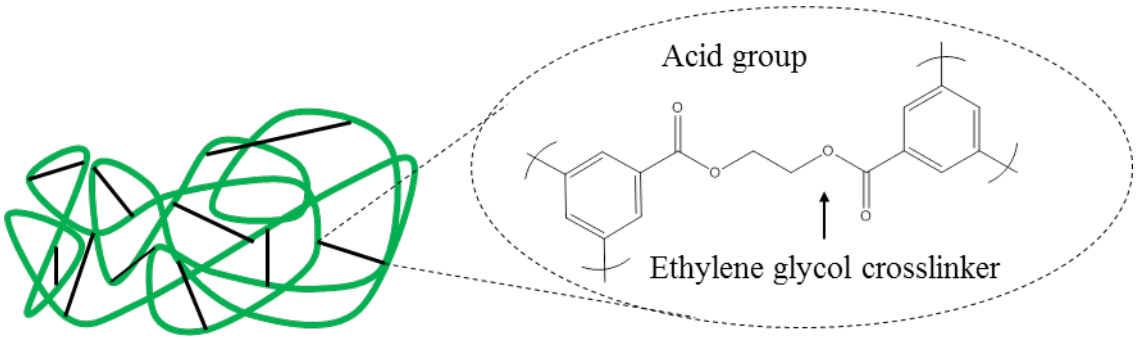

Figure 2.11: Schematic of covalent crosslinking in diaminobenzoic acid containing polyimides.

They showed increased selectivity along with an unexpected increase in permeability, which presumably occurred due to the crosslinking agent "propping" open the polymer

chains. Wind et al. used the same technique on 6FDA based copolyimides containing DABA as the crosslinkable diamine and various other diamines such as 6FpDA and DAM. They also studied the effect of different crosslinkers such as butylene glycol, cyclohexanedimethanol, and benzenedimethanol on the plasticization and separation properties. An increase in plasticization resistance was confirmed by extending the plasticization pressure of the crosslinked polyimides to upwards of 550 pure CO_2 pressure [30, 31]. In the above cited works involving crosslinking polyimides, it was shown that plasticization is suppressed by controlling chain mobility in the Henry's region, since controlling polymer matrix dilation involved in penetrant sorption was crucial in suppressing excessive chain swelling [21, 32]. Covalent crosslinking has been extensively researched by many past members of the Koros group who successfully applied it to both zeolite based mixed matrix membranes [33] as well as hollow-fiber membranes [34].

Another common method for stabilizing membranes against plasticization involves heating the membrane to high temperatures. Specifically for polyimides, which contain alternating electron rich and poor segments, higher temperatures impart increased chain mobility, which allows electron poor regions to overlap electron rich regions on adjacent chains. These intermolecular overlaps form dipole-dipole type interactions known as charge transfer complexes (CTC) or pi-pi stacking complexes. These interactions tend to reduce segmental mobility of the polymer chains. As illustrated in figure 2.12, carbonyl groups can withdraw electron density away from the central imide ring through both electronic conjugation and inductive effects [35, 36].

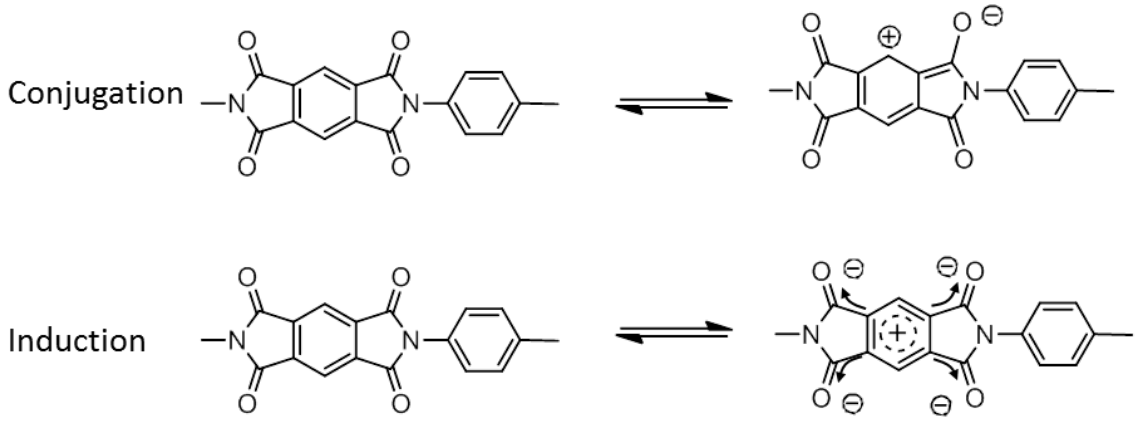

Figure 2.12: Mechanisms of electron withdrawal from the central imide ring in polyimides.

The pi-electron cloud on the neighboring diamine can act as an electron donor. In order for intermolecular charge transfer to form, close, parallel overlap of adjacent chains must occur. A presumed configuration of polymer chains forming CTCs is depicted in figure 2.13.

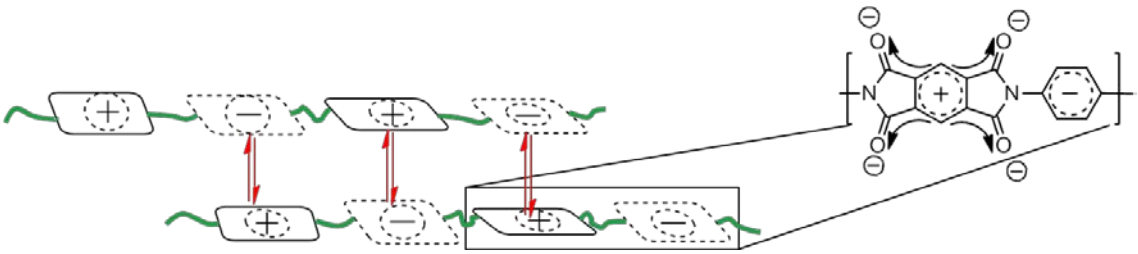

Figure 2.13: Presumed chain packing configuration of adjacent polymer chains undergoing CTC formation.

CTCs increase plasticization resistance in a similar manner as covalent crosslinking, however, because close overlap of chain segments is required, CTC formation often results in densification and large decreases in permeability. Wessling et al. showed CO_2 permeability reductions of almost 50% after annealing Matrimid® at 350°C for 30

minutes [37]. Although plasticization resistance was suppressed, the high temperatures (> T_g) required and permeability losses are undesirable for commercial applications.

Polyamide-imides are a relatively novel class of polymer membrane materials for natural gas purification. These materials combine the imide functionality, which can form CTCs, with interchain hydrogen bonding capability from the amide bond. The hydrogen bonding interactions can act as physical crosslinks, as depicted in figure 2.14, between adjacent chains without the extra processing steps involved in covalent crosslinking.

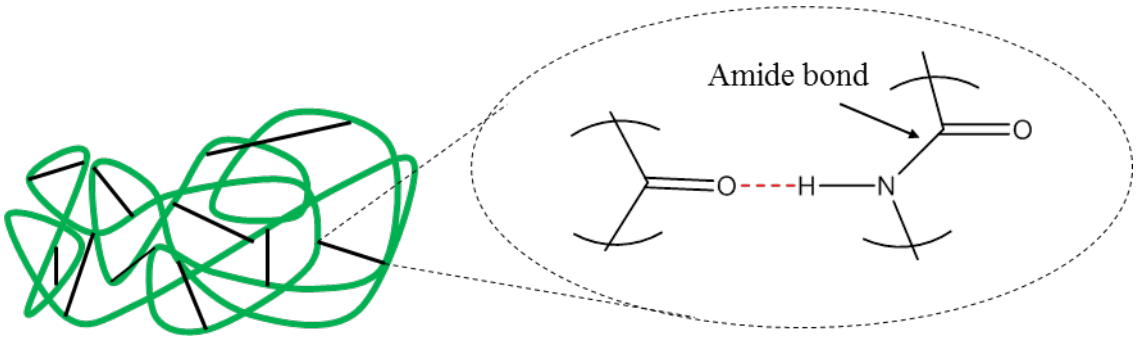

Figure 2.14: Proposed interchain hydrogen bonding interactions in polyamide-imides.

Kosuri and Koros demonstrated the intrinsic plasticization resistance in these materials using Torlon®, a commercially available polyamide-imide. They subjected hollow fiber Torlon® membranes to a 90/10 CO_2/CH_4 feed stream up to 1200 psia and observed a modest permselectivity reduction from 50 to 39 [38]. Moreover, the CO_2/CH_4 selectivity was stable at 1250 psia for up to 6 days, indicating that no glassy relaxations indicative of penetrant induced plasticization occurred. Despite its robust nature, permeabilities

through Torlon® are very low due to a high degree of chain packing, bringing into question the practicality of Torlon® for natural gas separations.

Fritsch et al. synthesized polyamide-imides with increased permeability by incorporating packing inhibiting groups such as hexafluoro (-CF_3-) and pendent methyl groups into the amide-imide backbone [39]. The later work by Nagel et al. provides a thorough correlation of the transport properties with polymer free volume for a large number of 6FDA based polyamide-imides [40]. They showed permeabilities as high as 56 Barrers and permselectivities as high as 67 for polyamide-imides composed of asymmetric 6FDA as the dianhydride, 6FpDA as the diamine, and various isomers of amino-benzoic acid, which connects the diamine to the dianhydride. Neither plasticization resistance nor mixed gas separation performance were studied, however, in either of the above cited works.

The goal of this project is therefore to study the separation properties of 6FDA based polyamide-imides for the simultaneous separation of CO_2 and H_2S from natural gas under realistic, well-head conditions. In addition to polyamide-imide's intrinsically high plasticization resistance, the amide bond may contribute to favorable H_2S solubility interactions and thus contribute to higher H_2S/CH_4 permselectivity. The base structure for this project is shown in Figure 2.15, with **R** varying depending on the diamine used in the polyamidization reaction. This structure was chosen because it showed the highest combination of permeability and selectivity in the work by Fritsch et al. [40] for the CO_2/CH_4 case when 6FpDA was used as the diamine. New materials based on this structure will be synthesized by varying the diamine structure, and the subsequent effect on the transport properties will be discussed.

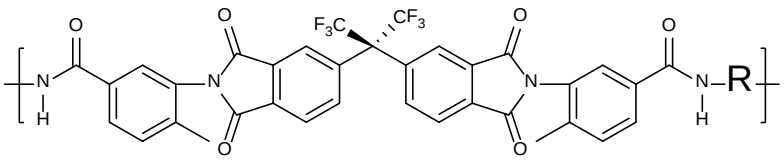

Figure 2.15: Base structure of polyamide-imide used in this work. R is varied by the diamine.

2.6. References

[1] R.E. Kesting and A.K. Fritzsche, *Polymeric Gas Separation Membranes*, (John Wiley & Sons, Inc., New York, 1993).

[2] G. Chatterjee, A.A. Houde, S.A. Stern, "Poly(ether urethane) and poly(ether urethane urea) membranes with high H_2S/CH_4 selectivity," *Journal of Membrane Science*, **135**, 99-106, (1997).

[3] S. Kanehashi and K. Nagai, "Analysis of dual-mode model parameters for gas sorption in glassy polymers," *Journal of Membrane Science*, **253** (1–2), 117-138, (2005).

[4] Y. Tsujita, H. Hachisuka, T. Imai, A. Takizawa, T. Kinoshita, "Solubility and permeability of quenched poly (2,6-dimethyl phenyleneoxide) with various microvoids," *Journal of Membrane Science*, **60** (1), 103-111, (1991).

[5] H. Hachisuka, H. Takizawa, Y. Tsujita, A. Takizawa, T. Kinoshita, "Gas transport properties in polycarbonate films with various unrelaxed volumes," *Polymer*, **32** (13), 2382-2386, (1991).

[6] H. Hachisuka, Y. Tsujita, A. Takizawa, T. Kinoshita, "Gas transport properties of annealed polyimide films," *Journal of Polymer Science Part B: Polymer Physics*, **29 (**1), 11-16, (1991).

[7] K. Ghosal and B. D. Freeman, "Gas separation using polymer membranes: an overview," *Polymers for Advanced Technologies*, **5 (**11), 673-697, (1994).

[8] W.J. Koros and R.T. Chern, *Handbook of Separation Process Principles*, 862-896, (John Wiley & Sons Inc., New York, 1987).

[9] W. J. Koros and G. K. Fleming, "Membrane-based gas separation," *Journal of Membrane Science*, **83** (1), 1-80, (1993).

[10] Y. Yampolskii, "Polymeric Gas Separation Membranes," *Macromolecules*, **45** (8), 3298-3311, (2012).

[11] H. Lin, E. Van Wagner, B. D. Freeman, L. G. Toy, R. P. Gupta, "Plasticization-enhanced hydrogen purification using polymeric membranes," *Science*, **311** (5761), 639-42, (2006).

[12] W. J. Koros, M. R. Coleman, and D. R. B. Walker, "Controlled Permeability Polymer Membranes," *Annual Review of Materials Science*, **22** (1), 47-89, (1992).

[13] W.J. Koros and W. Madden, "Transport Properties in Polymers," Encyclopedia of Polymer Science and Technology, 3rd Edition, **12**, 292-381, (John Wiley & Sons Inc., 2004).

[14] R. W. Baker, N. Yoshioka, J. M. Mohr, A. J. Khan, "Separation of organic vapors from air," *Journal of Membrane Science*, **31**, (2–3), 259-271, (1987).

[15] W.R. Vieth, J.M. Howell, J.M. Hsieh, "Dual Sorption Theory," *Journal of Membrane Science*, **1**, 177-220, (1976).

[16] H. L. Frisch,"Sorption and transport in glassy polymers-a review," *Polymer Engineering and Science*, **20**, (1), 2-13, (1980).

[17] V. Stannett, "The Transport of Gases in Synthetic Polymeric Membranes-An Historic Perspective," *Journal of Membrane Science*, **3**, 97-115, (1978).

[18] D. R. Paul and W. J. Koros, "Effect of partially immobilizing sorption on permeability and the diffusion time lag," *Journal of Polymer Science: Polymer Physics Edition*, **14** (4), 675-685, (1976).

[19] T. C. Merkel, V. Bondar, K. Nagai, and B. D. Freeman, "Hydrocarbon and Perfluorocarbon Gas Sorption in Poly(dimethylsiloxane), Poly(1-trimethylsilyl-1-propyne), and Copolymers of Tetrafluoroethylene and 2,2-Bis(trifluoromethyl)-4,5- difluoro-1,3-dioxole," *Macromolecules*, **32**, (2), 370-374, (1999).

[20] J. D. Wind, S. M. Sirard, D. R. Paul, P. F. Green, K. P. Johnston, W. J. Koros, "Carbon Dioxide-Induced Plasticization of Polyimide Membranes: Pseudo-Equilibrium Relationships of Diffusion, Sorption, and Swelling," *Macromolecules*, **36** (17), 6433-6441, (2003).

[21] M. Wessling, H. Strathmann, A. Bos, and I. G. M. Punt, "CO_2 -induced plasticization phenomena in glassy polymers," *Journal of Membrane Science,* **155**, 67-78, (1999).

[22] A.F. Ismail and W. Lorna, "Penetrant-induced plasticization phenomenon in glassy polymers for gas separation membrane," *Separation and Purification Technology*, **27 (**3), 173-194, (2002).

[23] M. Wessling, I. Huisman, T. V. D. Boomgaard, C. A. Smolders, "Time-dependent permeation of carbon dioxide through a polyimide membrane above the plasticization pressure," *Journal of Applied Polymer Science*, **58** (11), 1959-1966, (1995).

[24] T. Visser, G. Koops, M. Wessling, "On the subtle balance between competitive sorption and plasticization effects in asymmetric hollow fiber gas separation membranes," *Journal of Membrane Science*, **252** (1–2), 265-277, (2005).

[25] J. Hao, P. A. Rice, S. A. Stern, "Upgrading low-quality natural gas with H_2S- and CO_2-selective polymer membranes Part I . Process design and economics of membrane stages without recycle streams," *Journal of Membrane Science*, **209,** 177-206, (2002).

[26] J. Hao, P. A. Rice, S.A. Stern, "Upgrading low-quality natural gas with H_2S- and CO_2-selective polymer membranes Part II. Process design, economics, and sensitivity study of membrane stages with recycle streams," *Journal of Membrane Science*, **320**, (1–2), 108-122, (2008).

[27] T. Mohammadi, M. T. Moghadam, M. Saeidi, M. Mahdyarfar, "Acid Gas Permeation Behavior Through Poly (Ester Urethane Urea) Membrane," *Industrial and Engineering Chemistry Research*, **47,** 7361-7367, (2008).

[28] H. Kita, T. Inada, K. Tanaka, K. Okamoto, "Effect of photocrosslinking on permeability and permselectivity of gases through benzophenone-containing polyimide," *Journal of Membrane Science*, **87**, (1–2), 139-147, (1994).

[29] C. T. Wright and D. R. Paul, "Gas sorption and transport in UV-irradiated polyarylate copolymers based on tetramethyl bisphenol-A and dihydroxybenzophenone," *Journal of Membrane Science*, **124**, (2), 161-174, (1997).

[30] J. D. Wind, C. Staudt-Bickel, D. R. Paul, W. J. Koros, "Solid-State Covalent Cross-Linking of Polyimide Membranes for Carbon Dioxide Plasticization Reduction," *Macromolecules*, **36**, (6), 1882-1888, (2003).

[31] J. D. Wind, C. Staudt-Bickel, D. R. Paul, W. J. Koros, "The Effects of Crosslinking Chemistry on CO_2 Plasticization of Polyimide Gas Separation Membranes," *Industrial & Engineering Chemistry Research*, **41**, (24), 6139-6148, (2002).

[32] J.D. Wind et al., "Carbon Dioxide-induced Plasticization of Polyimide Membranes: Pseudo-Equilibrium Relationships of Diffusion, Sorption, and Swelling," *Macromolecules*, **36,** 6433-6431, (2003).

[33] J.K. Ward, "Crosslinkable Mixed Matrix Membranes For the Purification of Natural Gas," *PhD Dissertation*, Georgia Institute of Technology, Atlanta, Georgia, (2009).

[34] I.C. Omole, "Crosslinked Polyimide Hollow Fiber Membranes for Aggressive Natural Gas Feed Streams," *PhD Dissertation*, Georgia Institute of Technology, Atlanta Georgia, (2008).

[35] R.A. Dine-Hart and W.W. Wright, "A Study of Some Properties of Aromatic Imides," *Die Makromolekulare Chemie*, **143** (3583), 189-206, (1971).

[36] M. Hasegawa et al., "Photophysical processes in aromatic polyimides. Studies with model compounds," *Journal of Polymer Science Part B: Polymer Physics*, **31** (11), 1617-1625, (1993).

[37] A. Bos, I. G. M. Pünt, M. Wessling, H. Strathmann, "Plasticization-resistant glassy polyimide membranes for CO_2/CO_4 separations," *Separation and Purification Technology*, **14** (1–3), 27-39, (1998).

[38] M. R. Kosuri and W. J. Koros, "Defect-free asymmetric hollow fiber membranes from Torlon®, a polyamide–imide polymer, for high-pressure CO_2 separations," *Journal of Membrane Science*, **320**, (1–2), 65-72, (2008).

[39] D. Fritsch and N. Avella, "Synthesis and properties of highly gas permeable poly(amide-imide)s," *Macromolecular Chemistry and Physics*, **197** (2), 701-714, (1996).

CHAPTER 3

MATERIALS AND METHODS

3.1. Materials

3.1.1. Glassy Polymers

The polyamide-imides (PAIs) used in this study were synthesized by a two-reaction sequence originally described by Fritsch and Avella [1]. In the first reaction, the intermediate diacid, which contains the diimide functionality, was formed by reacting 2 equivalents of 3-amino-4-methylbenzoic acid (3ABA) (Sigma Aldrich, St. Louis, MO.) with 6FDA (2,2'-bis [3,4-dicarboxyphenyl] hexafluoropropane dianhydride (Alfa Aesar, Ward Hill, MA.). Thermal imidization utilizing temperatures between 160 and 200°C was used to induce ring closure. The water formed was distilled off through azeotropy with xylene or dichlorobenzene. This reaction is shown in figure 3.1-A. Prior to the reaction, both monomers were dried in a vacuum oven under 30 mmHg reduced pressure for 16-18 hours. Temperatures of 90°C and 120°C were used for 3ABA and 6FDA respectively.

The diacid, 6FDA-3ABA, was purified through multiple recrystallizations in ethanol. A single recrystallization step was insufficient in removing unreacted 3ABA, which was indicated by a reddish tint on the isolated 6FDA-3ABA solid. High purity of the intermediate diacid is essential for one-to-one stoichiometry in the subsequent polymerization reaction, which in turn is necessary for high molecular weight. 6FDA-3ABA purity was determined qualitatively by the absence of a red tint in 6FDA-3ABA, resulting in a pure, flaky white solid. Upon isolating and drying the recrystallized

monomer through vacuum filtration in a fume hood for at least 3 hours, the product was heated at 210°C for 24 hours to complete imidization. This reaction method allows for the synthesis of one large pot of diacid precursor, so that a variety of polymers differing only by the diamine forming the tail-tail connection can be synthesized.

The second reaction, which is shown in Figure 3.1-B, involved reacting 6FDA-3ABA with one equivalent of a diamine through direct polycondensation as reported by Yamazaki [2]. The diamines used in this work include: 4,4′-(hexafluoroisopropylidene) dianiline (6FpDA), 2,4-diamino mesitylene (DAM), and 2,3,5,6-tetramethyl-1,4-phenylenediamine (TmPDA). All diamines were obtained from Sigma Aldrich. The structure of the diamines and the names of their corresponding polymers are given in Table 3.1. The diamines were chosen because poly*imides* containing them have shown very high permeabilities due to inhibited chain packing. Additional reasons for utilizing these diamines will be discussed in detail in Chapters 4 and 5. Reaction times of 6-12 hours were used for the polycondensation reaction, and temperatures between 120-130°C were found to give polymers with good molecular weight. Total solid concentration was typically between 20-22% in NMP. 6F-PAI-3, composed of 2,3,5,6-tetramethylphenylenediamine, became crosslinked in solution during the polymerization reaction. Lower solid concentrations (15-17%) and temperatures (~115°C) were used to prevent this undesired side-reaction. The product polymer was precipitated, blended (2x), and boiled (2x) in fresh methanol. The solid was isolated by vacuum filtration and air dried in a fume hood for 3 hours followed by heating in a vacuum oven at 150°C for 24 hours under 30 mmHg reduced pressure. Molecular weight, as determined by gel permeation chromatography, was approximately 50-60 kDa.

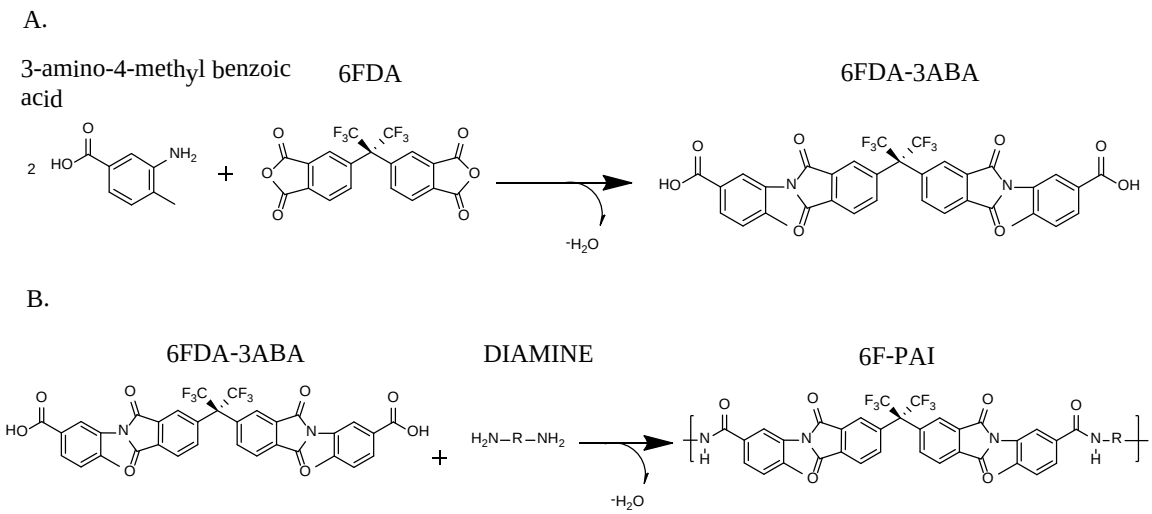

Figure 3.1: Reaction sequence for 6FDA based polyamide-imides (6F-PAIs).

Table 3.1: Structures of diamines and polyamide-imides used in this work.

	R=	Polymer/Diamine
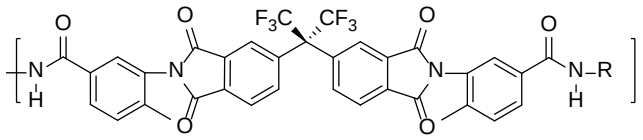	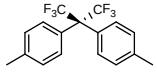	6F-PAI-1/6FpDA
		6F-PAI-2/DAM
		6F-PAI-3/TmPDA
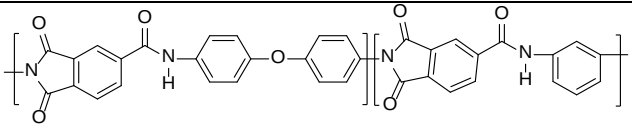	Torlon® 4000T	

Torlon® 4000T, which is also shown in table 3.1, was purchased from Solvay Advanced Polymers (Alpharetta, GA.).

Glassy poly*imides* 6FDA-6FpDA and 6FDA-6IpDA were synthesized using either chemical or thermal imidization by past members of the Koros group. 6FDA-DAM polyimide was purchased from Akron Polymer Systems, Inc. (Akron, OH.).

3.1.2. Rubbery Polymers

Pebax® SA01 MV 3000, a polyether-amide block copolymer, was chosen as a representative highly H_2S selective rubbery polymer. The exact chemical structures of Pebax® polymers are proprietary, however, they are very similar to the poly(ether urethane) urea shown in figure 3.2 [3]. These rubbery materials consist of alternating "hard" segments of amide bonds with "soft" segments comprised of flexible ether linkages. In this work, Pebax® was purchased from Arkema Inc. Technical Polymers.

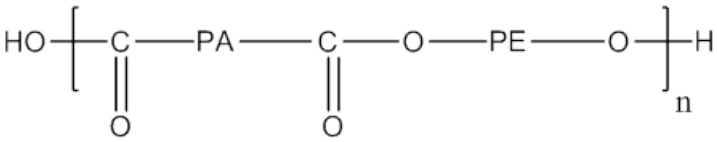

Figure 3.2: General polyamide-polyether structure related to Pebax®-type polymers.

3.2. Membrane Fabrication

3.2.1. Formation of Dense Film Membranes

Although hollow-fiber morphology is the industrially preferred geometry, it is more convenient to prepare and study the intrinsic properties of dense film membranes when developing new materials. Because the polyamide-imides investigated in this project are new and/or their separation properties have not been well characterized, dense film morphology is used exclusively throughout the duration of this work.

Dense film membranes were fabricated using a solution-casting technique. Solid polymer was completely dissolved in sufficient solvent and spread over a clean glass plate using a stainless steel doctoring blade with approximately 125-380 μm clearance. A concentration of 18-25% (w/w) solid was used, depending on the Mw of the polymer.

6F-PAI-1 and all poly*imides* were cast using tetrahydrofuran (THF), (99.9% anhydrous, Sigma Aldrich), as the solvent. The glass plate was treated with Glasscad 18™ (Geleste Inc.) to increase hydrophobicity of the casting surface, which eased the removal of the vitrified polymer film. All casting equipment was placed inside a polyethylene glove bag (Glass-col LLC, Terre Haute, IN) which was purged with N_2 and saturated with THF vapors for at least 3 hours prior to film casting. Casting in a solvent vapor rich environment slows down the rate of solvent evaporation and produces smoother films. The freshly cast membrane was allowed to vitrified for 12 hours before removing from the glove bag, followed by annealing in a vacuum oven at 200°C for 24 hours under 30 mmHg reduced pressure. A slow cooling rate of over 6 hours was used to return the oven to room temperature.

The casting procedure for 6F-PAI-2, 3 and Torlon® was modified due to insolubility in THF and other low boiling solvents. Instead, dimethyl formamide (DMF), (99.9% anhydrous, Sigma Aldrich), was used. Furthermore, an untreated glass plate was implemented for these three materials due to a de-wetting effect, where immediately upon casting, the polymer solution self-arranged into discontinuous pools on the glass surface when drawn onto Siliclad™ treated plates. This is likely due to slightly higher hydrophilicity in these lower fluorinated materials. Because of DMF's low volatility, a glove bag was not used. Immediately after drawing the polymer solution, the glass plate

with the freshly cast polymer film was placed on top of a 120°C heating element for 3 hours, which was sufficient for vitrification into a solid film that could be peeled off of the plate. The polymer film was then soaked in a methanol bath for 12-16 hours, dried under ambient conditions for 3 hours, and annealed in a vacuum oven at 220°C for 24 hours under 30 mmHg reduced pressure. Up to 5% or more residual DMF was found in polymer films that were not solvent exchanged, which could significantly affect the transport properties. After solvent exchanging, less than 0.5% residual DMF existed in the membranes. Residual solvent content was checked using thermogravimetric analysis, which will be described in section 3.3.4.1.

Because Pebax® is insoluble in most solvents at room temperature, the solid polymer and solvent, N-methyl pyrrolidone (NMP, Sigma Aldrich, 99.9% anhydrous), was heated to approximately 150°C in order to form a viscous and homogenous polymer solution of approximately 30% solid (w/w). The solution was then immediately drawn onto a room temperature, untreated glass plate. The drawn film vitrified quickly as the temperature decreased, and a solid polymer film could be obtained within a few moments after casting. The plate with the polymer film was then placed on top of a 120°C heating element for 3 hours in order to evaporate most of the remaining NMP, followed by drying in a vacuum oven at 110°C under 30 mmHg reduced pressure for 2 days. Less than 1% residual NMP remained in the films after this drying procedure, which was confirmed by TGA.

3.2.2. Membrane Masking

An approximately 1 inch diameter membrane sample, devoid of any defects such as visible pinholes, was cut from the larger polymer film and sandwiched between two annular pieces of aluminum tape. The inner and outer diameters of the tape were approximately 0.5 and 1.75 inches respectively. The sandwiched polymer film was then placed into an in-house designed stainless steel permeation cell and sealed by another annular piece of aluminum tape with inner and outer diameter larger than the diameters of the two sandwich pieces. Membrane thickness was determined using an average of 10 measurements taken by a circular tipped micrometer.

Under high upstream pressures, gas can bypass the polymer membrane by traveling through the polymer-aluminum tape interface, which is pointed out in figure 3.3, thus creating a non-selective route for gas transport. To prevent this, this interface was sealed with Duralco 4525 epoxy (Cortronics Corp., Brooklyn, NY). It could also be used to mask any visible defects on the polymer film surface. The epoxy was cured at 35°C and ambient pressure for 12 hours before closing the permeation cell and loading into the permeation box. Prior to closing the cell, the upstream area available for gas flux was scanned into a personal computer and measured using Scion Image software (Scion Corp., Frederick, MD). Two rubber O-rings, both of which were larger than the outer diameter of the largest annular aluminum tape, were sandwiched between the top and bottom portions of the permeation cell to prevent leakage in and out of the cell. A picture the sandwiched polymer film before and after epoxy application is shown in figure 3.3. A depiction of a permeation cell is given in figure 3.4.

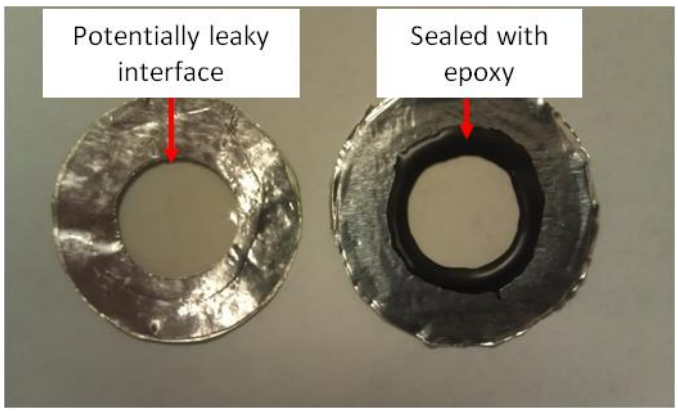

Figure 3.3: Polymer membrane "sandwich" before (left) and after epoxy (right)

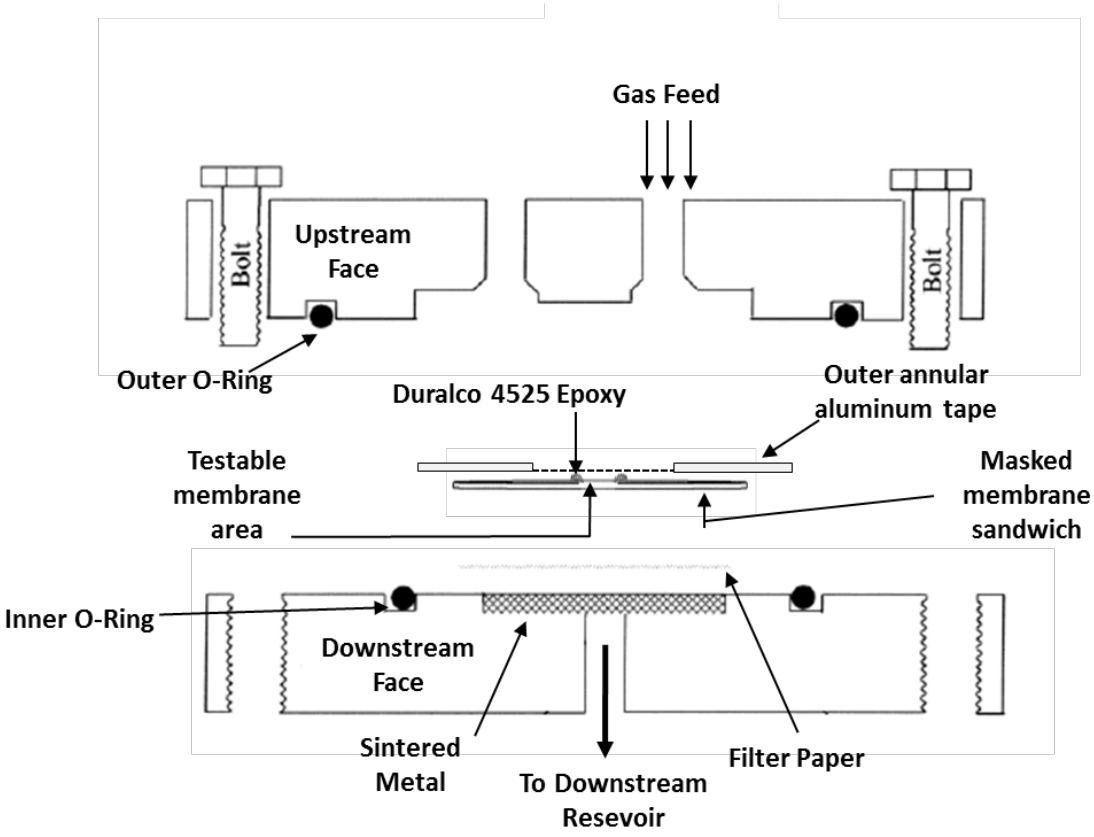

Figure 3.4: Diagram of in-house designed permeation cell used for permeation testing. Figure adapted from [4].

3.3. Membrane Characterization Techniques

3.3.1. Permeation Analysis

3.3.1.1. Permeation Equipment

Gas permeability through dense film membranes was measured using a constant volume, variable pressure apparatus [4]. With this technique, a high pressure is applied to the upstream side of the membrane, and the rate of gas transmission through the membrane is monitored by measuring the pressure rise, (*dp/dt*), in the downstream side. A basic schematic of a permeation unit is given in Figure 3.5. Although the actual design may differ considerably depending on the application, all of the essential components are shown.

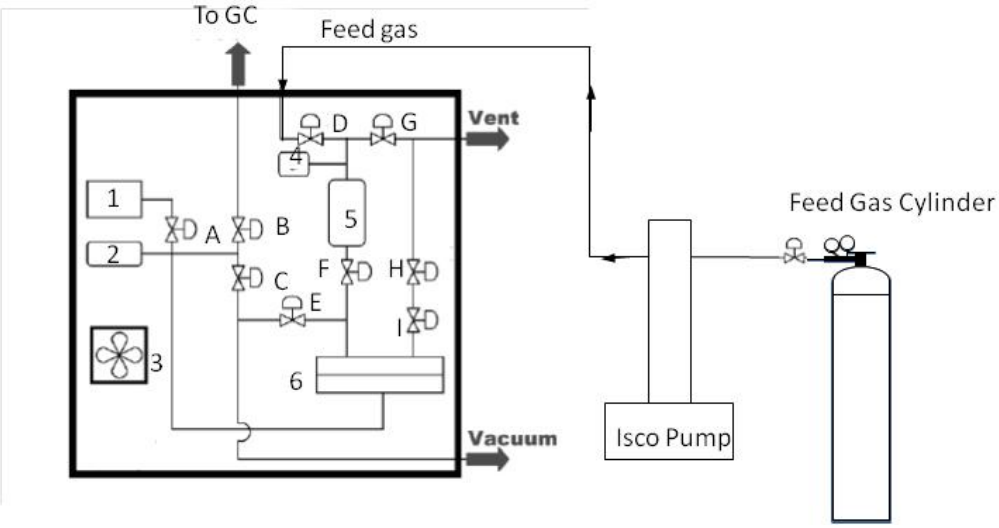

Figure 3.5: Schematic of the basic set-up of a constant volume, variable pressure permeation system. Figure adapted from [5].

The numbered components can be described as follows: (1) 10-100 torr downstream pressure transducer (MKS Instruments, Dallas, TX.) (2) downstream volume extension, (3) compact enclosure fan heater (Omega Engineering Inc., Stamford, CT.), (4) 2000 psia

upstream transducer (Honeywell, Columbus, OH.), (5) upstream volume, (6) in-house designed permeation cell. The lettered valves are as follows: (A) downstream transducer isolation valve, (B) GC isolation valve, (C) vacuum isolation valve, (D) feed input valve, (E) downstream/upstream isolation valve, (F) feed isolation valve, (G) upstream system vent valve, (H) retentate metering valve, (I) retentate shutoff valve. An Isco pump (Teledyne Isco, Lincoln, NE) was used to maintain upstream pressure during mixed gas testing or to pressurize feeds when cylinder pressure was insufficient. The system was constructed from 0.125 and 0.25 in stainless steel Swagelok® tubings and valves (Swagelok Co., Solon, OH). All connections inside the system were made by Swagelok VCR® fittings with stainless steel or nickel gaskets. The entire permeation box was insulated and maintained at 35°C.

The downstream pressure rise was measured using Labview software (National Instruments Corp., Austin, TX) installed on an external desktop computer. The output from the downstream transducer was converted to a pressure signal by the Labview program, which produced a plot of the downstream pressure rise vs. time *(dp/dt)*. The Labview code was custom written by Dr. Oguz Karvan, a past research engineer in the Koros group, specifically for permeation experiments in our lab.

3.3.1.2. Design Considerations for H_2S handling

Because H_2S is highly toxic, additional safety measures were put into place in order to safely handle it. A separate lab dedicated solely for H_2S measurements was designed by Dr. Karvan and Dr. JR Johnson and constructed by the three of us. Only qualified and trained personnel were permitted to enter the lab. Additionally, an air

purifying respirator (North half mask 7700 APR) equipped with acid gas cartridges (North by Honeywell) and a personal H_2S monitoring badge were donned whenever working in the lab.

All permeation and sorption equipment were housed within a sealed Plexiglas fume cabinet as pictured in Figure 3.6. The cabinet was connected to an overhead manifold under constant negative pressure. The manifold duct was connected to a sodium hydroxide scrubber on the roof of the building. All gas from permeation and sorption experiments was vented into the manifold duct and passed through the sodium hydroxide scrubber prior to being release to the atmosphere. Additionally, all cylinders containing H_2S were stored in highly vented fume cabinets.

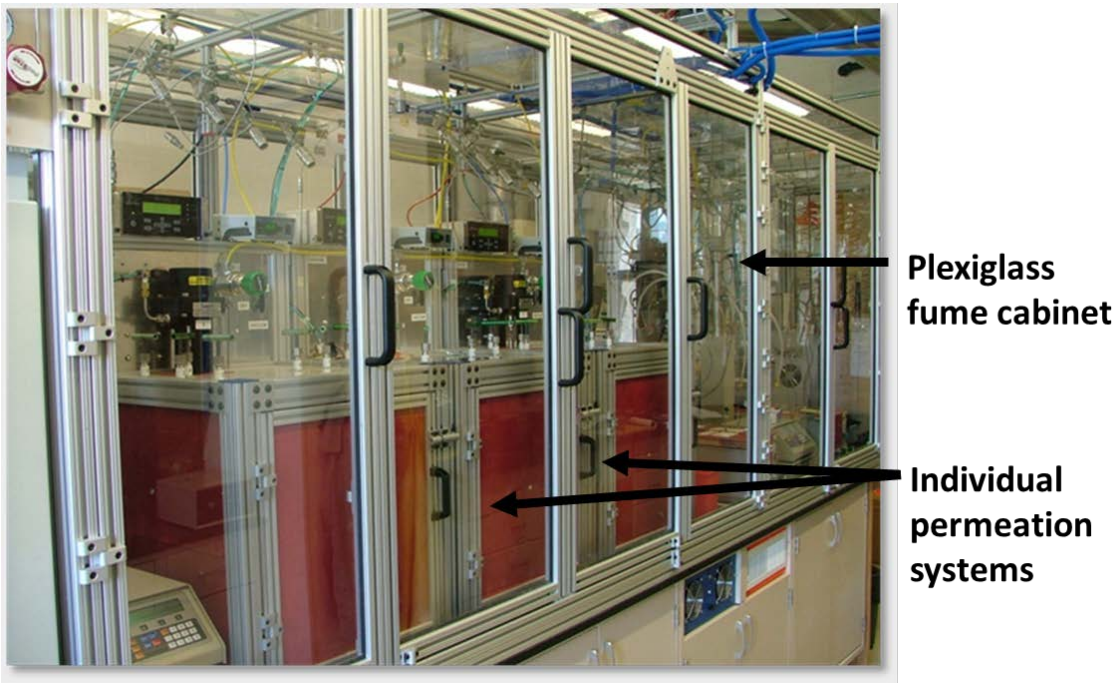

Figure 3.6: Actual picture of permeation equipment housed within the ventilated plexiglass fume cabinet.

3.3.1.3. Pure Gas Permeation Analysis

Pure gas permeation experiments were conducted as follows: 1. Load permeation cell with sample into permeation box, open valves C, E, A, and F for 18-24 hours. This procedure degasses the permeation piping system and membrane sample. 2. Close all valves and measure the leak rate into the downstream for 40-60 minutes. 3. Purge and pressurize upstream feed reservoir with desired gas. 4. Close valve C and E. 5. Open valve F and simultaneously begin collection of pressure vs. time data in the downstream volume. 5. Monitor downstream pressure rise until steady state has been reached. 6. Depressurize upstream and open valve C and E to begin degassing entire system for at least 12 hours prior to measuring the next gas.

The Swagelok connections used in the permeation and sorption systems have a minute but finite leak rate. Because the downstream pressure during permeation experiments was kept very low relative to atmospheric pressure, an influx of atmospheric gas will occur over time. Step 2 above is designed to measure the rate of this increase, which is then subtracted out from the *(dp/dt)* obtained during a permeation run. Improperly constructed systems and insufficient tightening of valves and tube connections can contribute to high leak rates. Additionally, degassing of residual gases from the membrane can also contribute to a pressure rise during leak testing. This contribution to the leak can be mitigated by sufficient degassing of the membrane as described in step 1 above. In this work, leak rates were less than or equal to $1x10^{-6}$ torr/sec, which was always less than 1% of $\left(\frac{\partial p}{\partial t}\right)$ due to the permeation flux through the membrane.The permeability was calculated using equation 3.1:

$$P = \frac{\left[\left(\partial p / \partial t\right)_{permeation} - \left(\partial p / \partial t\right)_{leak}\right] \cdot V_{DS} \cdot 22400 \cdot l}{R \cdot T \cdot area \cdot \Delta f} \tag{3.1}$$

$\left(\partial p / \partial t\right)_{permeation}$ and $\left(\partial p / \partial t\right)_{leak}$ are the downstream pressure rise contributions in *torr/s* from upstream penetrant flux and ambient leakage, respectively. V_{DS} is the downstream volume in *cc*, 22400 is the STP conversion factor, *l* is the membrane thickness in *cm*, R is the ideal gas constant, T is temperature in *K*, area is the upstream membrane area available for gas flux in cm^2, and Δf is the penetrant fugacity differential between the up and downstream. Fugacity coefficients were calculated using the Peng Robinson Equation of State, which is discussed in Appendix A. The permeability coefficient is usually expressed in units of Barrer, which are given below:

$$\left(1Barrer = \frac{cc(STP) \cdot cm}{cm^2 \cdot \Delta cmHg \cdot s}\right) \tag{3.2}$$

Upon closing valve C and opening feed valve F, a period of time exists for which no permeate accumulates in the downstream. This is shown in Figure 3.7 and referred to as the time lag.

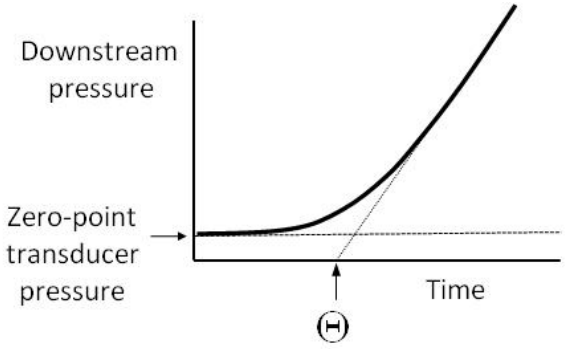

Figure 3.7: Depiction of a transient permeation experiment. The steady-state permeability is measured after 4 to 6 transient time-lags, $(4-6)\times\Theta$, have elapsed.

Theta, or Θ, is the time-lag from which the time period to reach steady-state permeability is estimated from, and is calculated by extrapolating the linear portion of *dp/dt* to the x-axis. The time lag is indicative of the time required for a penetrant to establish its steady-state concentration profile across the membrane. For permeability determination, *dp/dt* is only calculated after 4-6 steady-state time lags have been reached. Figures 3.8 and 3.9 demonstrate how the time lag changes as *dp/dt* increases until a steady-state permeation flux has been reached.

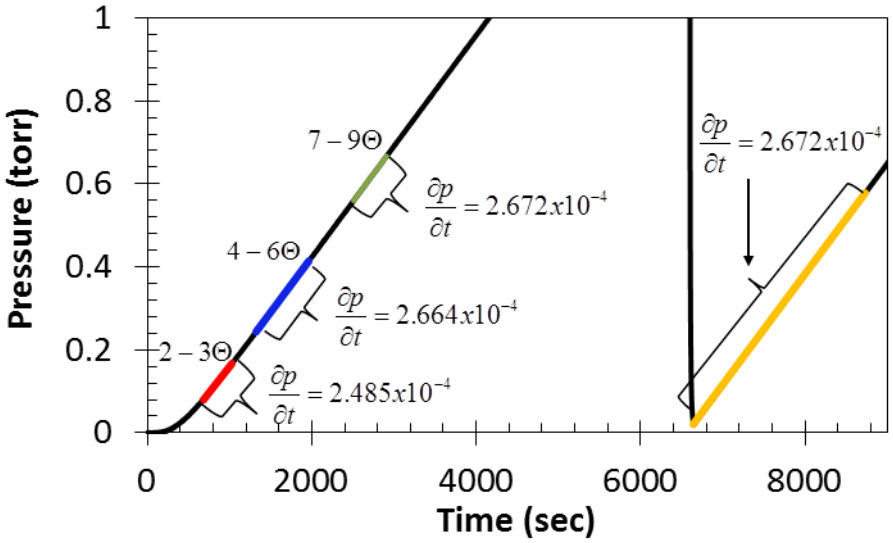

Figure 3.8: Actual *dp/dt* data from a CH_4 permeation experiment at 35 psia and 35°C in 6FDA-6FpDA.

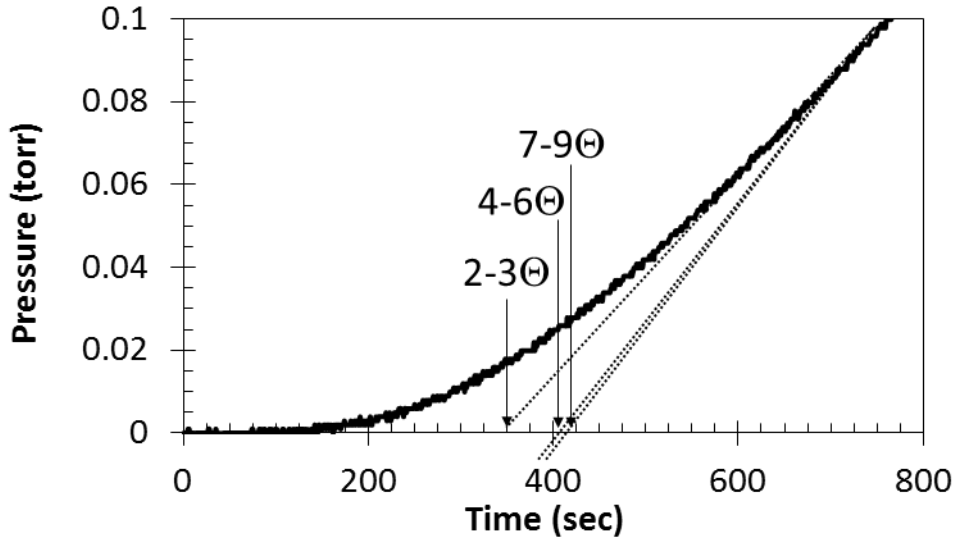

Figure 3.9: Figured 3.8 zoomed in to 0-800 seconds. Dashed lines represent extrapolations of the linear portions of *dp/dt* fit to the data at increasing multiples of Θ. The steady-state time lag increases until the steady state permeation flux, *dp/dt* is established.

As shown in Figure 3.8, the increase in *dp/dt* from 2-3Θ to 4-6Θ is approximately 7%, which equates to an increase in the CH_4 permeability of 7.5% as shown in Table 3.1.

After 7-9Θ, *dp/dt* increases by less than 1%. Accordingly, permeability increases by approximately 0.09%. Therefore, the permeability can be calculated only after a time period of at least 4-6 steady-state time-lags have passed.

Table 3.2: Transient permeation data for CH_4 in 6FDA-6FpDA at 35°C and 35 psia.

Elapsed permeation time	P_{CH4} (Barrer)	% Increase
2-3Θ	1.642	--
4-6Θ	1.765	7.5
7-9Θ	1.767	0.09

Figure 3.9 shows how the time lag increases as *dp/dt* approaches its steady-state value. One must be careful not to estimate 4-6Θ based on early *dp/dt* data, as Θ calculated from the initial linear portion of the pressure rise can underestimate the true steady-state time. In general, once the downstream pressure rise is approximately linear, the time to reach steady-state can be estimated from 10-14*x* the initial, apparent time lag. This should provide sufficient time to obtain the true time-lag. An iterative procedure can then be used to calculate the true, transient time-lag, once sufficient time has passed. To do this, *dp/dt* is fit over 4-6Θ. From the extrapolation of the linear line to the x-axis, a new value for Θ is obtained. A new *dp/dt* portion of the pressure rise can then be fit based on this new value of 4-6Θ, and the process is repeated until Θ and the permeability agree within a margin of error of less than 1%.

Another method used to confirm steady-state has been reached is to sufficiently evacuate the downstream, followed by re-accumulation of permeate. This is shown in Figure 3.9, where *dp/dt* from the second slope is identical to the steady-state *dp/dt* from the first slope. This procedure is used for both pure and mixed gas permeation to double-check the establishment of stead-state.

The diffusivity of a species is related to the time lag through the following relation [6]:

$$D_{app} = \frac{l^2}{6\Theta} \tag{3.3}$$

l^2 is the membrane thickness. Thus, using equation 2.9 from chapter 2, the permeability, apparent diffusion and sorption coefficients can be determined from a single permeation experiment.

3.3.1.4. Mixed Gas Permeation

Mixed gas permeation is fundamentally similar to single gas analysis, however, time lags are not measured in mixed gas experiments because both gases are permeating, making it difficult to distinguish between the two. Rather, steady-state permeation time is estimated from single gas time-lags as discussed in section 3.3.2.3. The permeability is measured after this time and approximately 1 hour later to verify that steady state has been reached.

During mixed experiments, valve I from figure 3.2 is opened, and a retentate stream is metered using valve H. The retentate stream is allowed to flow in order to avoid

concentration polarization, a phenomenon where the concentration of the fast gas in the boundary layer can decrease to such an extent that its permeation driving force decreases, leading to reduced flux of the fast gas relative to the slow gas and lower selectivity. To prevent this, a stage cut of 1% or less is used, where the stage cut represents the ratio of permeate to retentate flow rates.

Once the total permeation flux reaches steady-state, a pressure of 9-15 torr is allowed to accumulate in the downstream volume. Valve B is then opened, and a gas sample is sent to the GC (Varian 450, now Agilent Technologies, Santa Clara, CA.) to determine the composition of the permeated gas. Valve B is then closed and valve C is opened to evacuate the downstream volume. Valve C is closed after sufficient evacuation, and permeate gas is allowed to re-accumulate to 9-15 torr for additional sampling in the GC. The process is repeated 3 times, or as long as needed to reach a true steady state, and an average permeability is then calculated from Equation 3.4. Similar to the pure gas fugacity coefficients, fugacity coefficients for the feed gas mixtures were calculated using the procedure outlined in Appendix A.

$$P_i = \frac{\left[\left(\partial p / \partial t\right)_{total} - \left(\partial p / \partial t\right)_{leak}\right] \cdot y_{i,up} \cdot V_{DS} \cdot 22400 \cdot l}{R \cdot T \cdot area \cdot (p_{T,up} y_{i,up} \phi_{i,up} - p_{T,d} y_{i,d} \phi_{i,d})} \tag{3.4}$$

3.3.2. Gas Sorption

Pressure-decay sorption, originally described by Koros and Paul [7], was used to measure equilibrium uptake of penetrant gas in a membrane. A depiction of a pressure-decay sorption cell is shown in figure 3.10.

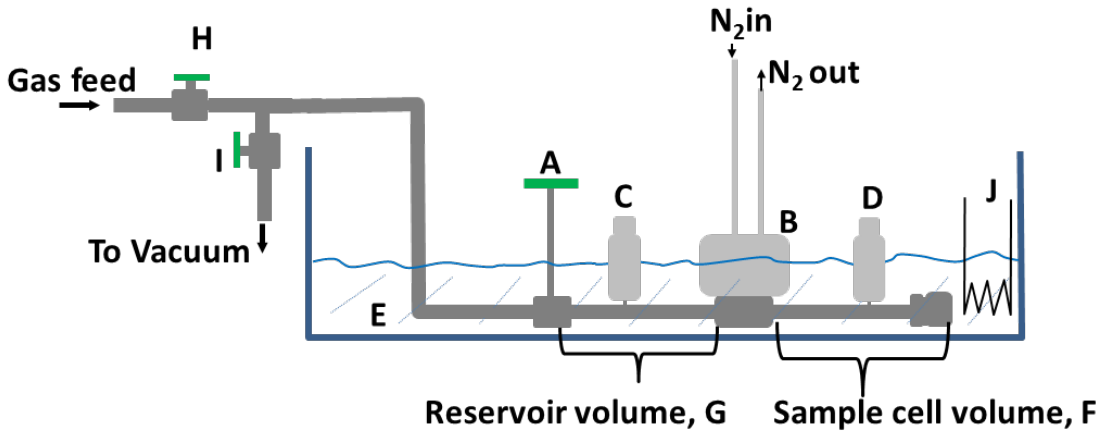

Figure 3.10: Pressure-decay cell used to measure equilibrium penetrant uptake.

A typical sorption apparatus is composed of the following essential components: A.) Reservoir isolation valve. B.) Pneumatic sample cell isolation valve. C.) 2500 psia reservoir transducer (Ametek Aerospace, Costa Mesa, CA.). D.) Sample cell transducer (Ametek Aerospace). E.) Heat transfer fluid (Duratherm, North America). F.) Sample cell volume. G.) Reservoir volume. H.) Feed isolation valve. I.) Vacuum isolation valve. J.) Heating element equipped with thermostat and circulator (Polyscience, Niles, Ill.). The entire apparatus is built from 0.25 inch stainless steel Swagelok tubing. Valve B is a pneumatic valve activated by a house N_2 supply and controlled by the Labview software, which is run on an external computer. Prior to running a sorption experiment, 0.15 to 0.5 g of polymer sample is loaded into the sample cell compartment, which consists of a 3/8

inch male Swagelok VCR® fitting. Valves A, B and I are opened, valve H is closed, and vacuum is pulled on the entire apparatus for 12-24 hours to allow for sufficient degassing. The sorption apparatus is completely submerged in heat transfer fluid and maintained at 35°C.

A sorption experiment is run by closing valve B and pressurizing the reservoir volume to a higher pressure than the sample cell, followed by an equilibration period of approximately 20 minutes. The pressure in volumes G and F are monitored during this time. Valve B is then opened and quickly closed over a 1 second interval, which doses a portion of the equilibrated gas from the reservoir volume into the sample cell volume, causing the sample cell pressure to increase. As the sample sorbs penetrant gas, the pressure in the sample cell decreases with time until equilibrium uptake is reached. This pressure decay is monitored by the Labview software, and based on the final sample cell pressure and the mole balance given in Equation 3.5, the moles of gas sorbed into the polymer can be calculated and converted to a concentration. From the equation, V_c and V_p are the sample cell and polymer volume, respectively. $p_{c,i}$, $Z_{c,i}$ and $p_{c,F}$, $Z_{c,F}$ are the initial and final equilibrated pressures and compressibility factors of the penetrant in the sample cell at those pressures. $p_{R,i}$, $Z_{R,i}$ and $p_{R,F}$, $Z_{R,F}$ are the initial and final equilibrated pressures and compressibility factors of penetrant in the reservoir volume at those pressures. R is the ideal gas constant and T is the temperature of the reservoir bath in K. The compressibility factors for CO_2, CH_4, and H_2S were also calculated from the Peng Robinson Equation of State, while for Xe and CF_4, a corresponding states relation is used. Both of these procedures are outlined in Appendix A.

$$\Delta n_p = \frac{(V_c - V_p)\cdot\left(\frac{p_{c,i}}{z_{c,i}} - \frac{p_{c,F}}{z_{c,F}}\right) + V_R \cdot \left(\frac{p_{R,i}}{z_{R,i}} - \frac{p_{R,F}}{z_{R,F}}\right)}{RT} \tag{3.5}$$

Once penetrant concentration at the equilibrated cell pressure is calculated, a higher pressure can again be introduced into the reservoir volume and the process repeated. This sequence of incrementally increasing the reservoir pressure and dosing a known quantity of that gas into the sample cell allows for the measurement of concentration uptake in the membrane vs. pressure.

3.3.3. Thermal Analysis

3.3.3.1. Thermal Gravimetric Analysis (TGA)

A thermal gravimetric analyzer (STA 409 PC Luxx, Netzsch, Burlington, MA) was used to analyze residual solvent content in annealed polymer films. A heating rate of 10°C/min was used up to 220°C and 120°C for the polyamide-imides and Pebax®, respectively. The heating compartment was purged with N_2 at 30 cc/min. TGA plots for 6F-PAI-2 and Pebax® are shown in Figures 3.11 and 3.12, respectively. For 6F-PAI-2, less than 0.6% weight loss occurs after the film is subjected to the prescribed annealing procedure. Pebax® shows essentially no weight loss throughout the entire TGA run, which ran for approximately 10 hours. These figures confirm that the annealing procedures used were sufficient in removing most residual solvent from the polymer films.

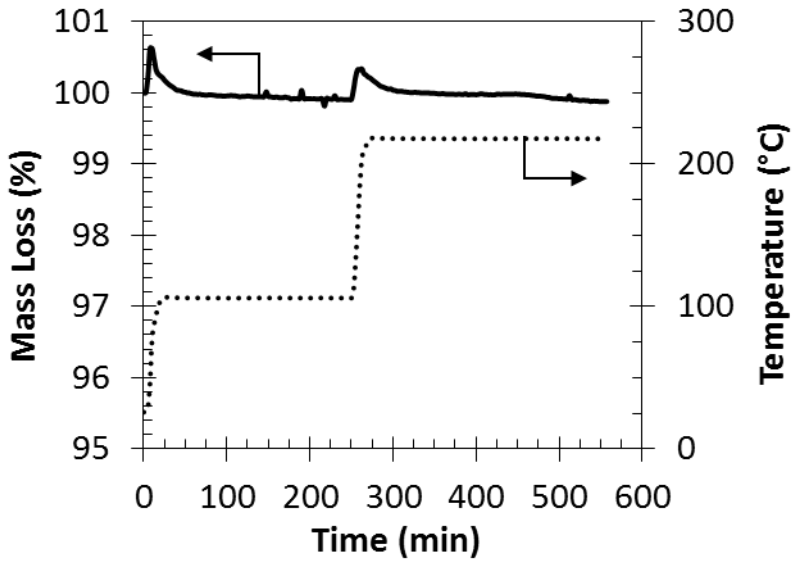

Figure 3.11: TGA plot for 6F-PAI-2 cast in DMF, solvent exchanged in MeOH for 12 hours, and annealed at 220°C for 24 hours at 30 mmHg reduced pressure. The initial increases in mass correspond to changes in buoyancy as the sample compartment heats up. The mass loss at constant temperature for both temperature holding times is within the buoyancy changes, which is less than 0.6%. Therefore, no significant residual solvent content remained in the membranes.

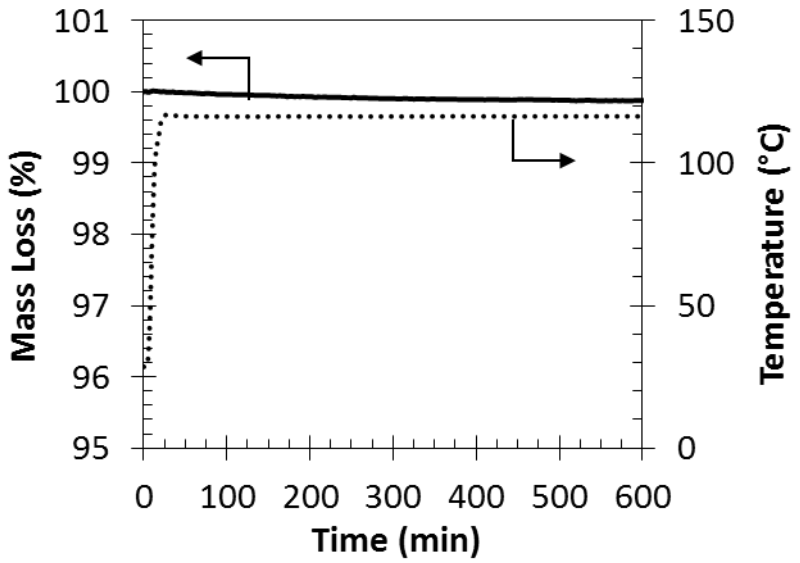

Figure 3.12: TGA plot for Pebax® cast in NMP, dried at 110°C for 3 hours at ambient pressure followed by heating at 110°C under 30 mmHg reduced pressure for 2 days.

3.3.3.2. Differential Scanning Calorimetry (DSC)

A DSC analyzer (TA instruments, New Castle, DE.) was used to measure the glass transition temperature of glassy polymer films. N_2 at 50 cc/min was used as the purge gas. The films were heated at 10°C/min from 25°C to 370°C, cooled down to 25°C and the cycle repeated. The tangent slope at the step transition of the second heating run was used to calculate the T_g.

3.3.4. FTIR-ATR Spectroscopy

Fourier transform infrared attenuated total reflectance spectroscopy (FTIR-ATR) was performed using a Bruker-Tensor 27 spectrometer (Bruker Corp. Billerica, MA.) equipped with a Harrick MVP 2 Series™ ATR (Harrick Scientific Products Inc., Pleasantville, NY.) utilizing a N_2 purge at 30 cc/min. An average of 128 scans with a resolution of 4 cm^{-1} was taken. This technique was used to confirm imide and amide bond formation in 6FDA-3ABA and final polymer structures, respectively. Bulk powder was used for 6FDA-3ABA, and dense films with thicknesses ranging from 25-50 μm were used for structure identification of the polymer membranes.

3.3.5. UV-Vis/ Microfluorescence Spectroscopy

Ultraviolet-visible spectroscopy was performed on a Beckman Coulter DU Series 700 (Beckman Coulter, Brea, CA.) general purpose spectrometer to compare differences in absorbance properties arising from *intramolecular* interactions of monomers and dilute polymer solutions. Concentrations of $1x10^{-6}$ M in DMF were used to avoid saturation of the detector.

Solid state microfluorescence spectroscopy (Horiba Scientific, Edison, NJ.) was used to study differences in *intermolecular* charge transfer formation in polymer films. A right angle configuration was used, and both excitation and emission profiles were collected.

3.3.6. X-Ray Diffraction

The amorphous structure and d-spacing of polymer films was analyzed using an X-ray diffractometer (X'pert Pro PANanalytical) using a Cu Ka radiation source of wavelength 1.5406 Å. Measurements were carried out from 4-50° using an X'celerator detector on a low background sample holder. More detail on how this technique was used to analyze the polymer membranes is discussed in chapters 4 and 5.

3.3.7. Bulk Density

In chapter 4, the densities of annealed polyamide-imides and polyimides were measured by Micromeritics Inc. (Norcross GA.) using He pycnometry. However, the densities given by this technique were substantially higher than those reported in the literature. For this reason, only the trends in density as a function of annealing temperature in chapter 4 are important.

In chapter 5, the densities of polymer films were measured by a density gradient column prepared from calcium nitrate (Sigma Aldrich) dissolved in distilled water. The values agreed closely with reported literature values. An average of at least 3 representative pieces of a polymer film was used to determine the density.

3.3.8. Gel Permeation Chromatography (GPC)

Molecular weight of synthesized polyamide-imides was determined using gel permeation chromatography in the Beckham group at Georgia Tech. Molecular weights ranged from 50-60 kDA.

3.4. References

[1] D. Fritsch and N. Avella, "Synthesis and properties of highly gas permeable poly(amide-imide)s," *Macromolecular Chemistry and Physics*, **197**, (2), 701-714, (1996).

[2] N. Yamazaki and M. Matsumoto, "Reactions of the N-Phosphonium Salts of Pyridines," *Journal of Polymer Science: Polymer Chemistry Edition*, **13**, 1373-1380, (1975).

[3] G. Chatterjee, A.A. Houde, S.A. Stern, "Polyer(ether urethane) and poly(ether urethane urea) membranes with higher H_2S/CH_4 selectivity, *Journal of Membrane Science*, 135, 99-106, (1997).

[4] S. Damle and W.J. Koros, "Permeation Equipment for High-Pressure Gas Separation Membranes," *Industrial & Engineering Chemistry Research*, **42**, (25), 6389-6395, (2003).

[5] J. K. Ward, "Crosslinkable Mixed Matrix Membranes For The Purification of Natural Gas," *PhD Dissertation*, Georgia Institute of Technology, Atlanta, Georgia, (2010).

[6] D. R. Paul and W. J. Koros, "Effect of partially immobilizing sorption on permeability and the diffusion time lag," *Journal of Polymer Science: Polymer Physics Edition*, **14**, (4), 675-685, (1976).

[7] W. J. Koros and D. R. Paul, "Design considerations for measurement of gas sorption in polymers by pressure decay," *Journal of Polymer Science: Polymer Physics Edition*, **14**, (10), 1903-1907, (1976).

[8] M.M. Abbott, J.M. Smith, H.C. Van Ness, *Introduction to Chemical Engineering Thermodynamics*, 6th Edition, (Mcgraw Hill Higher Education, 2001).

CHAPTER 4

EFFECT OF THERMAL ANNEALING ON THE BASE POLYAMIDE-IMIDE STRUCTURE: 6F-PAI-1

This chapter discusses the effects of thermal annealing on transport properties of 6F-PAI-1 dense film membranes. Charge transfer complexes (CTCs), which can form in structures containing imide moieties, are induced by thermal treatments. CTCs have been shown to affect selectivities, permeabilities, and plasticization resistance. Therefore, the goal of this chapter is to determine how CTC formation affects the polymer physical properties and subsequent transport properties in order to guide the optimization of the polyamide-imide platform for gas separation materials.

4.1. Annealing Protocol

6F-PAI-1 was originally synthesized by Fritsch and Peinemann for use as a host for nano-sized catalyst particles [1]. Only single gas permeabilities and selectivities were reported in their work, and its separation properties at elevated pressures and mixed gas conditions were not characterized prior to the start of this project.

The structure of 6F-PAI-1 is shown in figure 4.1. The analog poly*imide*, 6FDA-6FpDA (6F-6F), is also shown in the figure. The poly*imide* will be used to compare the changes to the microstructure between amide-imides and imide backbones as a function of annealing. Because 6F-6F plasticizes around 200 psia CO_2 partial pressure, it is not appropriate for aggressive natural gas purification, and its transport properties, other than

its plasticization resistance, are not discussed in this work. A detailed discussion of 6F-6F's transport properties are reported in the work by Coleman and Koros [2].

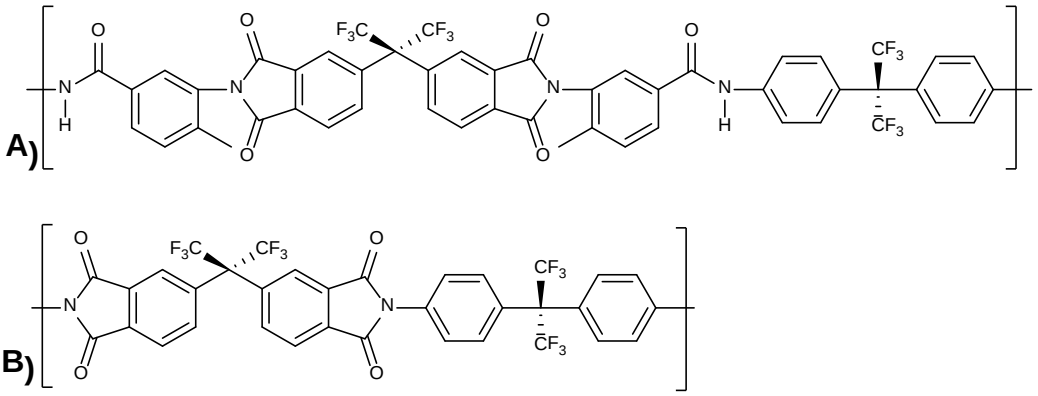

Figure 4.1: A) Structure of 6F-polyamide-imide-1 (6F-PAI-1) and **B)** Structure of 6FDA-6FpDA (6F-6F) polyimide.

Dense film membranes were prepared from THF solutions cast in a vapor saturated glovebag as described in section 3.2. Sub-T_g annealing temperatures of 150 and 200°C at 30 mmHg reduced pressure for 24 hours were chosen to study the effect of elevated *annealing temperature*, a factor which has been shown to affect CTC formation to a greater extent than annealing time at low temperature [3]. Excessively high annealing temperature, however, is undesirable, as it can increase fabrication costs and cause a collapse of the asymmetric hollow fiber morphology if the temperature approaches the polymer's T_g. For these reasons, annealing temperature, rather than time, was studied in greater detail. After the 24 hour annealing time, the temperature was cooled down to 25°C over a period of 12 hours while maintaining vacuum. An unannealed film, which was dried in a vacuum oven at room temperature for up to 2 days, was prepared as a reference. FTIR-ATR was performed on all films after annealing to confirm the absence of chemical changes during the thermal treatments. The IR spectra of 6F-PAI-1 annealed

at various temperatures are shown in Figure 4.2. Additionally, all films were soluble in THF after annealing, indicating that the changes to the polymer were physical rather than chemical in nature.

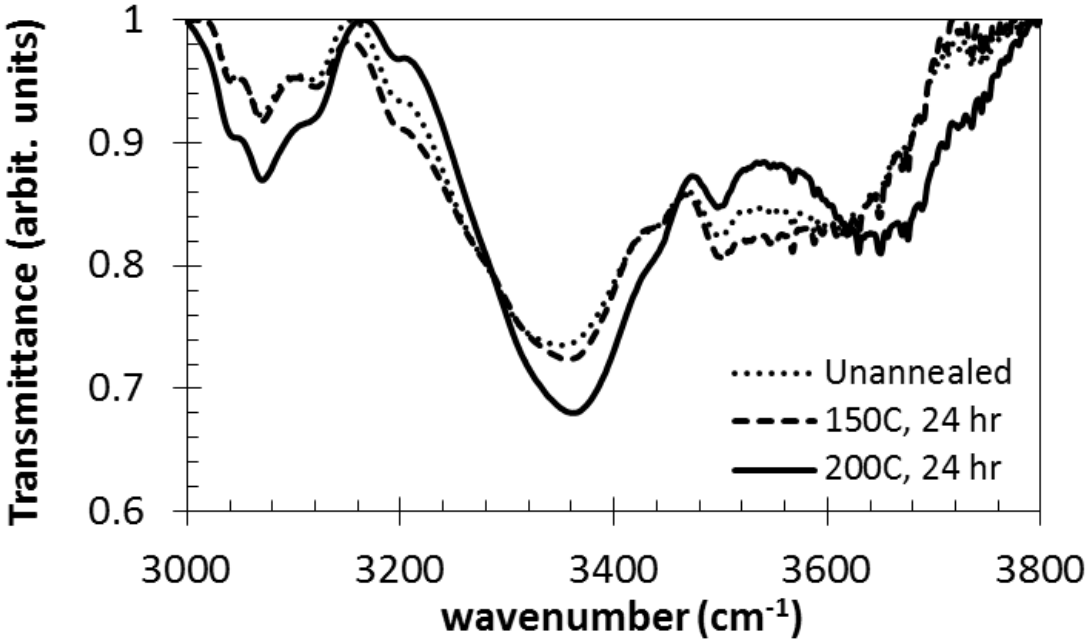

Figure 4.2: FTIR-ATR spectra in the 2000 to 4000 cm^{-1} range showing identical spectra in films annealed at different temperatures.

An examination of the broad N-H stretching frequency, which is centered around 3360 cm^{-1}, reveals interchain hydrogen bonding with the polymer matrix. "Free" N-H groups exhibit a band near 3446 cm^{-1}, which can be seen as a shoulder to the right of the broad, associated N-H stretch. The amorphous and contorted nature of the polymer packing structure is envisioned to cause a range of hydrogen bonding between N-H and C=O moieties with varying strengths, distances and geometries. Hence, the shift in peak

position of the N-H stretching frequency to below 3440 cm^{-1} indicates hydrogen bonding in the polymer.

4.2. Pure Gas Plasticization Analysis

Due to the high pressures and elevated acid gas concentrations that can occur at a natural gas wellhead, plasticization resistance is one of the most important factors to consider for polymer membranes. Due to the presence of the amide bond, polyamide-imides may offer a key advantage over more traditional, glassy polymers which usually require crosslinking for plasticization suppression. Therefore, one of the main goals of this chapter is to determine how interchain hydrogen bonding and CTC formation as a function of thermal annealing affect plasticization resistance in 6F-PAI-1.

The formation of CTCs can increase plasticization resistance by increasing intermolecular interactions between adjacent chain segments. Interchain hydrogen bonding can also stabilize against swelling and plasticization. In order to determine the extent that these two types of interactions have on plasticization resistance, preliminary pure gas CO_2 permeability vs. pressure isotherms were measured in 6F-PAI-1, and are given in Figure 4.3. More detailed mixed gas results are also subsequently presented in section 4.5. Carbon dioxide plasticization resistance is emphasized in this chapter in order to compare with other state-of-art materials, since there are essentially no studies to compare to regarding H_2S plasticization resistance in the literature. An unannealed film was used to determine if interchain hydrogen bonding without thermal annealing is sufficient for preventing plasticization. Annealing temperatures of 150 and 200°C at 24 hours were chosen to study the effect of increased annealing temperature on plasticization resistance. The permeability isotherms are shown in Figure 4.3. Data for 6F-6F annealed

at 220°C, which was adapted from the work by Wind et al. [4], is shown to compare the effect of the amide bond in 6F-PAI-1 to a more conventional *polyimide* of similar structure.

Because permeability can be time dependent after the onset of plasticization, all permeabilities were measured after 12-16 hours of permeation time at each pressure beyond the plasticization pressure. The time dependence is related to glassy-state chain relaxations that are facilitated by high penetrant concentrations. Such high sorption levels can cause an upward creep in permeability with time as the polymer chains relax. Therefore, the extent of permeability increase after the initial plasticization threshold is reached can also be used to qualitatively describe a material's stability against penetrant induced swelling.

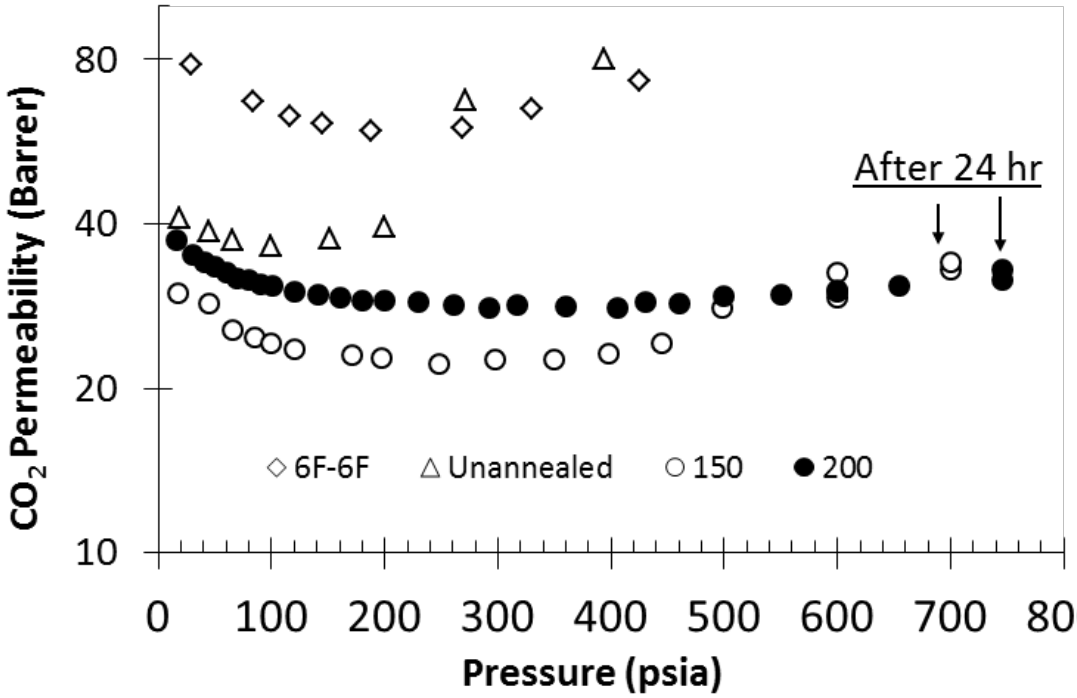

Figure 4.3: Single gas CO_2 permeability vs. pressure at 35°C. 6F-PAI-1 at various annealing conditions, *signified by triangles, filled and unfilled circles*, is compared. Data for 6F-6F annealed at 220°C for 24 hours, *represented by diamonds*, is adapted from Wind et al. [4]. The minimum in each isotherm followed by an increase in permeability represents the general plasticization pressure, or the feed pressure of CO_2 which induces plasticization.

As can be observed in Figure 4.3, unannealed 6F-PAI-1 plasticizes near 100 psia, which is lower than 6F-6F annealed at 220°C as well as 6F-PAI annealed at both 150 and 200°C. This signifies that without thermal annealing, interchain hydrogen bonding along 6F-PAI-1's backbone is not sufficient in suppressing plasticization. At room temperature, steric interactions within the polymer matrix may hinder the rigid, glassy chains from forming intermolecular CTCs. The unannealed film appears to be highly unstable against penetrant induced plasticization, and swelling occurs readily with increasing CO_2 concentration. Therefore, interchain hydrogen bonding alone does not provide adequate

stabilization against plasticization, as Figure 4.2 showed essentially no difference in the N-H stretching frequencies between the three annealing conditions. Hence, there must be additional factors, such as CTC formation, which provide additional stabilization against plasticization.

6F-PAI-1 annealed at 150°C (6F-150) shows substantially improved resistance relative to the unannealed film. For 6F-150, the plasticization pressure is not reached until approximately 350 psia. Additionally, the increase in permeability beyond this pressure is approximately 50 vs. over 100% in the unannealed film. This remarkable suppression of plasticization after annealing at 150°C can be attributed to the formation of CTCs, which will be discussed in section 4.3.1.

Increasing the annealing temperature for 6F-PAI to 200°C (6F-200) resulted in a further increase in the plasticization resistance relative to annealing at 150°C. Such higher resistance relative to 6F-150 is due to a further increase in charge transfer interactions induced by the higher annealing temperature. Sufficiently high temperatures are required to overcome steric hinderances to form CTCs. At 200°C, the polymer chains have more energy to break interactions and form new ones than they do at 150°C. For 6F-200, the plasticization pressure is extended to approximately 400 psia. This is a substantial improvement over the current industrially used materials such as CA and Matrimid®, and is similar to other high performance *crosslinked* polyimides [4, 5].

The analog polyimide, 6F-6F, which was annealed at 220°C, plasticizes near 230 psia, which is lower than 6F-PAI-1 annealed at both and 200°C. This demonstrates the inherently more stable backbone of the polyamide-imide, which is presumably due to a combination of interchain hydrogen bonding and CTC formation. Additionally, beyond

600 psia, permeability in 6F-200 increases by only 13%, which is much lower than the 30% increase shown in 6F-6F. While these results are promising, the true separation performance cannot be properly characterized from pure gas measurements, as the effect of elevated CO_2 concentration on CH_4 permeability is not shown. This can only be studied using mixed gas feeds, which will be the topic of section 4.5.

Upon closer inspection of Figure 4.3, the permeability in 6F-200 is surprisingly higher than 6F-150 at all pressures below 400 psia, where plasticization is not a significant factor for either film. Therefore, the intrinsic permeability in unplasticized 6F-200 is higher than 6F-150. As previously mentioned, thermal annealing in glassy polymers generally results in lower permeabilities due to excess free volume loss and polymer densification. A permeability increase in 6F-PAI-1 for the higher annealed film suggests that densification based physical aging *may not be the dominant response for a 200°C annealing treatment*. This hypothesis will be discussed further in the following sections.

4.3. Characterization of the Polymer Physical Structure

The polymer physical structure was analyzed in order to investigate the unusual increase in CO_2 permeability upon annealing 6F-PAI-1 at 200 relative to 150°C. It is hypothesized that the *amide-imide* backbone in 6F-PAI undergoes a significantly different transition in response to thermal annealing than does a typical polyimide. Therefore, the physical structure of the analog polyimide, 6F-6F, is also compared as a function of annealing. More simple polyimides like 6F-6F generally undergo densification based physical aging when subjected to higher annealing temperatures [6].

Hence, 6F-6F should provide a useful baseline for which to compare 6F-PAI-1 to a typical accelerated physical aging response in a material with similar structure.

4.3.1. Microfluorescence Spectroscopy

Polyimides and related materials tend to absorb UV light due to the pi electrons associated with the aromatic rings that make up their backbones. Upon excitation of a molecule by UV light to an excited state, a molecule can relax to the ground state through emission of light. This process is known as fluorescence. The distribution and relative energy states of the non-bonded and pi electrons along the polymer backbone can be affected by interactions with adjacent moieties, such as electron transfer through conjugation. Such charge transfer can change the wavelengths and intensities at which the polymer absorbs UV light. Therefore, changes in interchain interactions can be monitored through fluorescence spectroscopy.

Zhou and Koros compared fluorescence emission profiles of the Matrimid® hollow fibers annealed at various temperatures [3]. They showed increased emission intensity with thermal annealing, suggesting increased concentration of the absorbing complex in the polymer backbone. This can be rationalized through an increase in density and chain packing from excess free volume relaxation. They also observed reduced fluxes through the membrane with increased annealing temperature. No changes in emission or excitation wavelength were observed, indicating the absence of localized microstructure rearrangements in Matrimid®.

4.3.1.1. Fluorescence Excitation

Figure 4.4 compares fluorescence excitation profiles for 6F-PAI-1 and 6F-6F annealed at various temperatures.

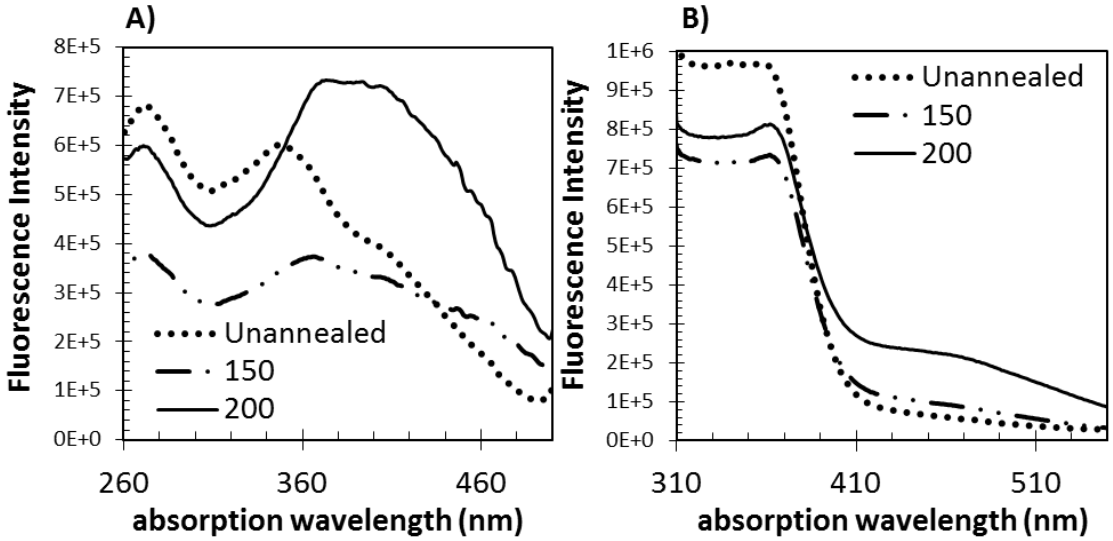

Figure 4.4: Fluorescence excitation profiles for **A)** 6F-PAI-1 and **B)** 6F-6F polyimide. 6F-PAI-1 was excited from 220-500 nm and measured at 510 nm. 6F-6F was excited from 250-600 nm and monitored at 610 nm.

It should be noted that although films of similar thickness were used between the *unannealed* and *annealed* films for 6F-PAI-1 (~45 μm), the annealed and unannealed samples were *not* taken from the same film cast. Small differences in film thicknesses between the unannealed and annealed films can result in different fluorescence intensity. Therefore, fluorescence intensity between unannealed and annealed films in 6F-PAI-1 cannot be compared on a meaningful basis; rather, only wavelengths of maximum absorption and peak shape can be compared. On the other hand, 6F-PAI-1 (150) and 6F-PAI-1 (200) *were* taken from the same film cast, therefore, their intensities can be analyzed along with their wavelengths and peak shapes. The three different annealing

conditioned films for 6F-6F were also taken from the same film cast, therefore, fluorescence intensity can also be compared between the three different annealing conditions for the analog polyimide.

The excitation profiles for annealed 6F-PAI-1 show a red-shift in the wavelength of maximum absorption, λ_{max}, compared to unannealed films. This transition indicates a change in intra or intermolecular electron conjugation along the polymer backbone occurred as a result of the thermal treatment. This change in conjugation occurs as different interchain interactions are formed due to increased polymer chain mobility during annealing. Red-shifting is most apparent when comparing unannealed to 150°C films. This is reasonable since the polymer chains have very little mobility at room temperature, and an initial thermal treatment at 150°C causes significant changes to the polymer microstructure. An increase in annealing temperature to 200°C causes a further red-shift in λ_{max} as well as increased fluorescence intensity, which indicates the formation of additional CTCs in 6F-200 relative to 6F-150.

In contrast, 6F-6F does not show any significant red-shifts or changes in the shape of the excitation bands between the three annealing conditions. Rather, only an increase in the intensity of the long wavelength emission band, centered around 460 nm, occurs. This suggests that significant changes in intermolecular interactions along 6F-6F's backbone did not occur in the annealed films with respect to the unannealed films. The density of emitting complexes is likely increasing as excess free volume decreases, as was the case with the polyimide Matrimid® shown by Zhou. Such an increase in the density of emitting complexes correlates with densification in the annealed 6F-6F films, which is confirmed by density measurements. The density and calculated free volume

will be discussed in section 4.3.2. Thus, the trends in the fluorescence spectra shown for 6F-6F are consistent with the conventional interpretation of a densification based physical aging that usually occurs in glassy polymers as a result of thermal annealing.

4.3.1.2. Fluorescence Emission

Fluorescence emission profiles were measured by exciting polymer films at the wavelength of maximum excitation intensity and measuring the subsequent emission intensity as a function of wavelength. Figure 4.5 shows emission spectra for 6F-PAI-1 and 6F-6F.

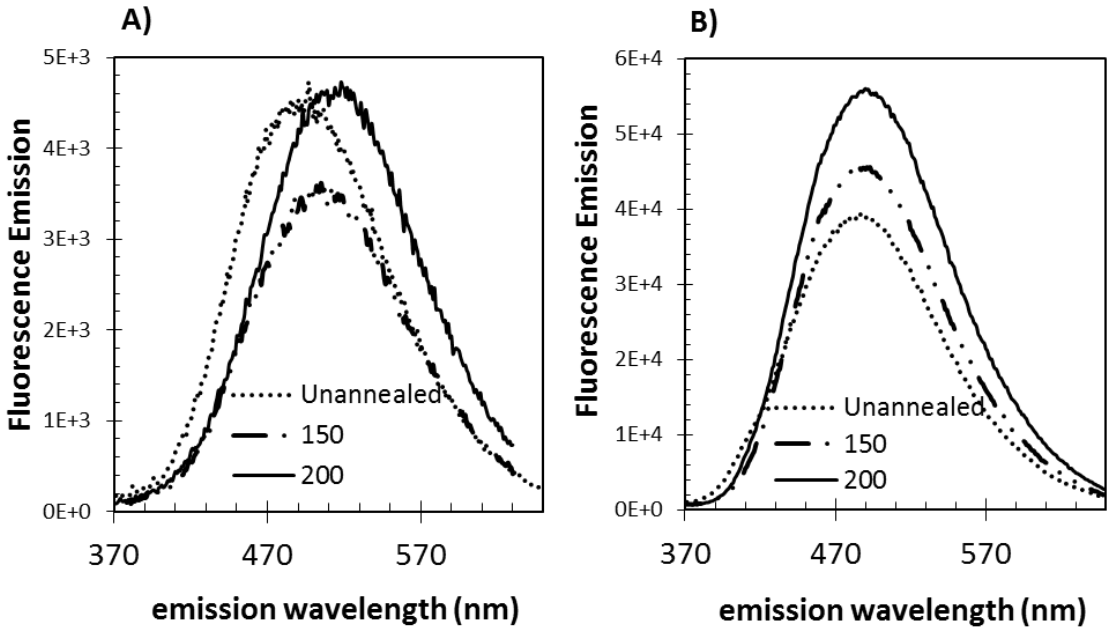

Figure 4.5: Fluorescence emission profiles for **A)** 6F-PAI-1 and **B)** 6F-6F. Emission profiles were excited at 350 nm and collected from 360 to 650 nm.

For 6F-PAI-1, red-shifting in fluorescence emission is observed for both 6F-150 and 6F-200 relative to unannealed films, indicating the formation of an excited state charge

transfer complex. In other words, electrons excited by the incident UV radiation are transferred to an adjacent acceptor moiety, lowering the energy of the excited state and increasing the emission wavelength. The 200°C annealed film shows further red-shifting in emission wavelength relative to the 150°C film. This shift is consistent with 6F-200s fluorescence excitation spectra, and suggests that additional charge transfer formation occurred with the highest annealing temperature. Therefore, additional changes to 6F-200's microstructure likely occurred relative to 6F-150.

The emission profiles for 6F-6F are consistent with their excitation spectra. No shifting in emission wavelength occurs when the films were excited at 350 nm. Instead, fluorescence intensity increases with higher annealing temperatures. Such increased intensity correlates with an increase in bulk density. Intermolecular interactions characteristic of the charge transfer band at 350 nm in 6F-6F's microstructure may simply be increasing in density instead of forming new interactions such as what was shown in 6F-PAI-1. These results highlight the differences in the microstructure evolution induced by thermal annealing between the simple imide backbone in 6F-6F and the more complex amide-imide backbone in 6F-PAI-1. Based on these results, it appears that 6F-PAI's microstructure is likely undergoing a rearrangement, rather than simply excess free volume relaxation as seems to be the case in 6F-6F.

4.3.2. X-Ray Diffraction Analysis

X-ray scattering profiles were obtained on dense film membranes to determine the effect of annealing temperature on ordering in the polymer microstructure. Figure 4.6 shows the scattering patterns for both 6F-PAI-1 and 6F-6F as a function of annealing temperature. d-spacing, which represents the average distance between the polymer

chains, was calculated from the Bragg equation given by Equation 4.1. Values for 2Theta were taken from the maximum intensity Bragg scattering peak in Figure 4.7.

$$n\lambda = 2d\sin(\theta) \tag{4.1}$$

In the equation, n is an integer, λ is the wavelength of incident x-ray beams on a lattice with planes separated by distance d, and θ is the Bragg angle.

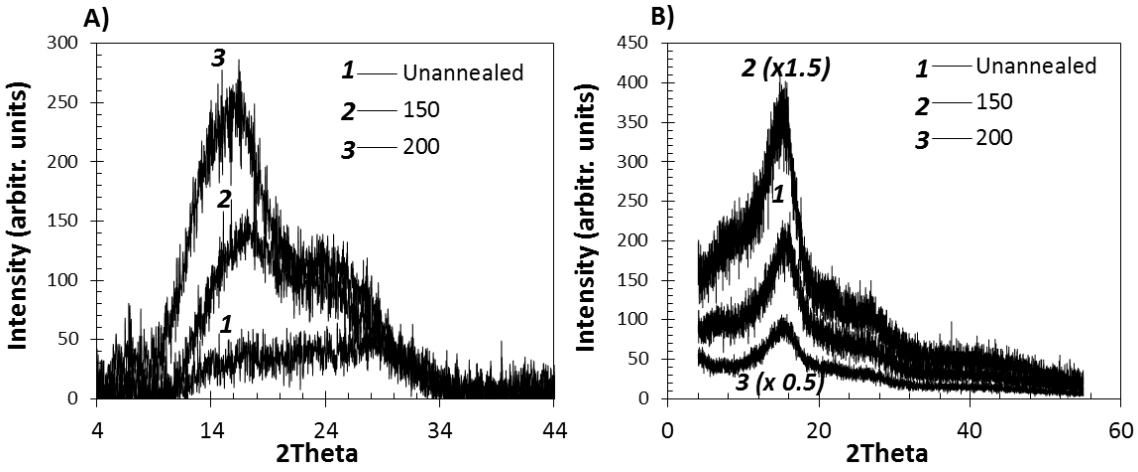

Figure 4.6: X-ray diffraction spectra for **A)** 6F-PAI-1 and **B)** 6F-6F as a function of annealing temperature.

The scattering peaks shown in Figure 4.6-A reveal a striking difference compared to 6F-6F. For 6F-PAI-1, the unannealed film appears to have much less order amongst its microstructure compared to the annealed films, as evidenced by its broad and amorphous scattering pattern. As annealing temperature is increased to 150 and then to 200°C, the scattering peaks show increased structure as well as a slight shift toward increased d-spacing with higher annealing temperatures. This indicates that the average intersegmental distance between polymer chains in 6F-PAI-1 increases with higher

annealing temperatures. Such a change is not typically observed in glassy polymers subjected to thermal treatments, as is shown in 6F-6F's spectra in Figure 4.6-B.

For 6F-6F, d-spacing is not significantly different between the films annealed at 150 and 200°C. Additionally, the shape of the scattering peaks is the same for the unannealed and annealed films. Perhaps most striking in Figure 4.6-B is the similarly shaped scattering patterns shown for the unannealed and annealed films. On the other hand, for 6F-PAI-1, the peaks for the annealed films show significantly more structure and differentiation versus the unannealed films. This indicates that microstructural "ordering" in 6F-6F does not significantly change from the thermal treatments, and is consistent with its fluorescence spectra, which suggested similar CTC formation between the three annealing treatments. On the other hand, for 6F-PAI-1, the formation of CTCs appears to result in different inter/intra molecular conjugation and interactions along the polymer main chain. The formation of new interactions apparently evolves the microstructure in 6F-PAI-1 in such a way that it becomes more "ordered" with respect to the untreated films. This is a very complex situation, and although we do not wish to speculate too much, it is useful to consider the possible significance of the various complex differences observed in the preceding characterization.

Table 4.1 compares the bulk density of polymer films, free volume, and fractional free volume for 6F-PAI-1 and 6F-6F annealed at various conditions. Fractional free volume was calculated from Equation 4.2. $\hat{V}_o$ is the occupied volume of the polymer chains that is inaccessible to penetrant gas, and is calculated from a group contribution method proposed by Bondi and described in the work by Park and Paul [7]. $\hat{V}_{sp}$ is the specific volume of the polymer and is determined from the density measurements.

$$FFV = \frac{\left(\hat{V}_{sp} - \hat{V}_{o}\right)}{\hat{V}_{sp}} \tag{4.2}$$

Table 4.1: Bulk density, fractional free volume (*FFV*), free volume (*FV*) and d-spacing for 6F-PAI-1 and 6F-6F annealed at various conditions.

Annealing condition	*ρ (g/cc)*	*FFV*	*FV (cc/mol)*	*d-spacing (Å)*
6F-PAI-1				
Unannealed	1.5845	0.07	44	--
150	1.5706	0.08	50	5.3
200	1.5570	0.09	56	5.7
6F-6F				
Unannealed	1.5744	0.10	49	*6*
150	1.6695	0.05	22	*6*
200	1.7094	0.03	12	*6*

As can be observed, the density of 6F-6F increases with increased annealing temperature, causing a reduction in its fractional free volume. This result is consistent with its fluorescence spectra, which suggested increased concentration of the emitting complexes. For 6F-PAI-1, density decreases with annealing temperature, and an increase in fractional free volume is observed. This is in direct contrast to the trend shown for the polyimide. These data, coupled with the fluorescence and XRD spectra, suggests that simple densification based physical aging cannot be used to describe the changes to the

microstructure as a result of thermal annealing. As mentioned previously, it appears that the local packing structure undergoes a rearrangement, which results in what is pictured to be an effectively "new" microstructural environment relative to the unannealed state.

The fluorescence data for 6F-PAI-1 showed red-shifting with annealing temperature, indicating increased electron conjugation, either intra or inter, throughout the polymer microstructure. In light of the comparison with 6F-6F, the most likely site for increased conjugation in 6F-PAI is around *imide* bond, as shown in Figure 4.7.

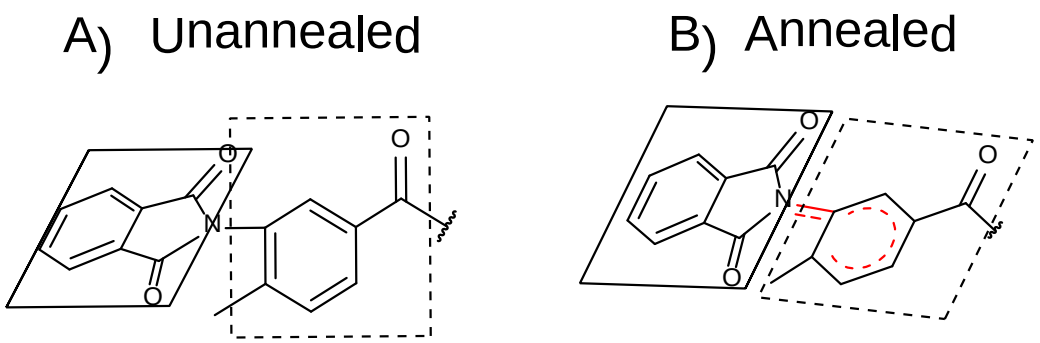

Figure 4.7: A) Imide-phenyl group (N-phenyl bond) showing low co-planarization in the unannealed state and **B)** increased N-phenyl conjugation induced by thermal annealing

In the unannealed state, the methyl group ortho to the N-C phenyl bond causes steric repulsions with the adjacent carbonyl group and inhibits planarity between the imide and phenyl planes. This would interfere with electron conjugation between the lone pair electrons associated with the imide nitrogen and the phenyl ring. During thermal annealing, increased mobility and thermal energy around this bond likely overcomes steric effects that would otherwise inhibit close parallel packing. The increased planarity would facilitate further electron conjugation across this bond, both intra and inter, as supported by the fluorescence data. The now more planar conformation would promote

overlap of electron rich and poor segments between adjacent polymer chains as CTC formation is envisioned to occur. The XRD patterns in Figure 4.6-A support the idea of increased parallel chain stacking, which would increase the long-rang ordering in the polymer microstructure as discussed in Chapter 2.

The diamine moiety in 6F-PAI-1, 6FpDA, is not envisioned to be responsible for an increase in either intra or intermolecular conjugation. This hypothesis can be rationalized by a comparison to the analog polyimide. In 6F-6F, the diamine 6FpDA forms the *imide* bond with 6FDA dianhydride. It is likely that intermolecular CTC formation, as envisioned to occur through pi-pi stacking, would arise from the stacking of the aromatic rings of 6FpDA over the imide segments of 6FDA. However, the bulky CF_3 groups probably hinder this arrangement. As such, the chain packing structure in 6F-6F is not significantly changed by thermal annealing. This is supported by the similar fluorescence and XRD patterns shown previously. Therefore, if a more ordered packing structure were forming in 6F-PAI-1, as suggested by the XRD patterns, the pi-pi stacking complexes are more likely to occur between the benzoic acid phenyl ring and the imide moiety of 6FDA dianhydride.

For 6F-PAI-1, as conjugation over the N-phenyl bond is increased and the polymer backbone becomes more planar, the polymer microstructure is envisioned to arrange itself in a “new” configuration similar to that shown in Figure 4.8. The arrows indicate intermolecular CTC sites.

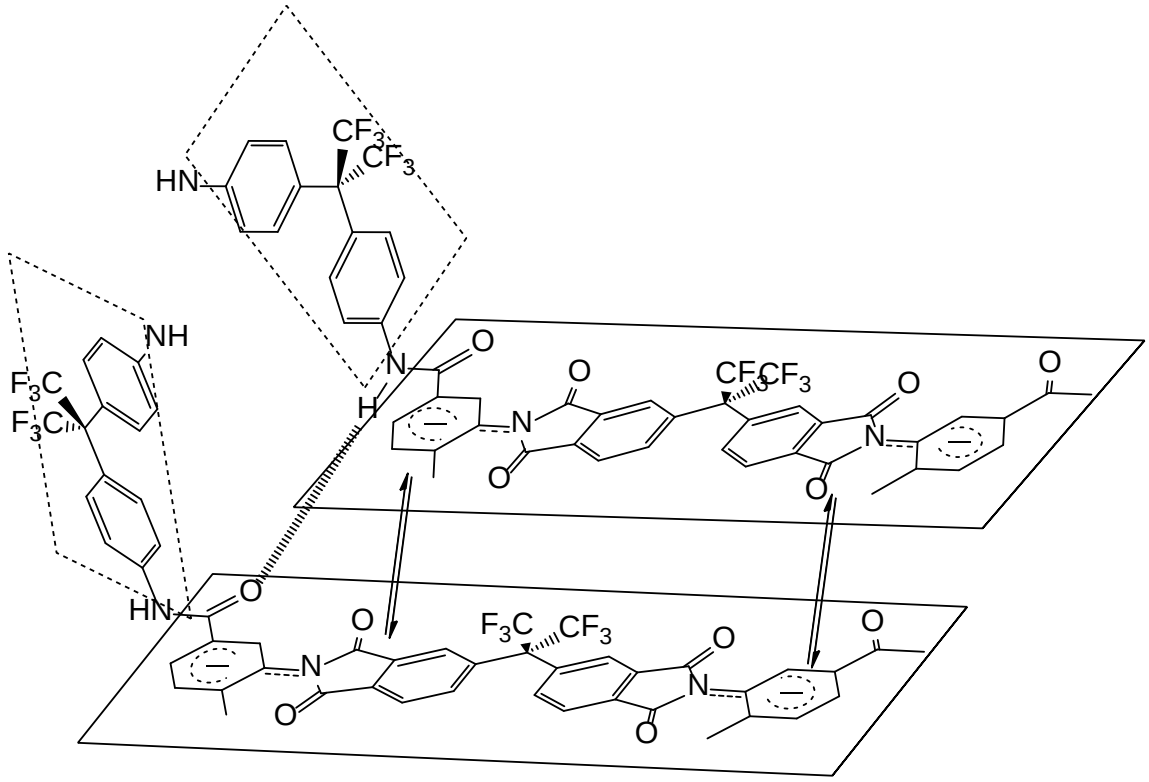

Figure 4.8: Proposed microstructure configuration of a repeat unit of 6F-PAI-1, induced by thermal annealing. The arrows indicate the electron rich and poor segments forming pi-pi stacking complexes, or CTCs.

It is hypothesized that the "new" microstructure depicted in Figure 4.8, which could only be formed from high temperature annealing, forms an "ordered-disordered" state, where the intermolecular charge transfer regions form through pi-pi stacking of the benzoic acid moiety over the imide ring of the dianhydride. This thermally-induced conformation forms what is now an effectively different microstructural environment between the annealed and unannealed films, where different intermolecular interactions form with different free volume spaces. The packing inhibiting diamine, with the bulky CF_3 groups, likely becomes the 'new' Langmuir sorption modes, where the size and distribution of such holes is different between the three different annealing conditions. Because they are flexible, molecules adsorbed into these domains have increased

mobility. This is shown by an increase in Langmuir diffusivity for both CO_2 and CH_4, which will be discussed in section 4.4. Annealing at 200 relative to 150°C enhanced this conformational change even further, increasing the N-phenyl conjugation as evidenced by red shifting of in the fluorescence excitation and emission wavelengths. At this elevated temperature, greater CTC formation occurred as co-planarity in the polymer backbone increased relative to the 150°C treatment.

Because CTCs require close overlap of specific regions on the polymer backbone, their formation likely involves various movements and rearrangements of the polymer chains in order for such interactions to form. In such a scenario, the free volume and excess free volume distribution may be changing in a complex manner, instead of simply decreasing as is likely the case in the simple polyimide analog. Together, these changes may have induced the formation of a 'new' microstructural environment that gives rise to the increase in permeability for the 200°C annealed film, and may help to explain the unusual increase in fractional free volume and d-spacing in 6F-PAI-1 with annealing. Positron annihilation spectroscopy would be an extremely valuable tool for free volume examination. Additionally, dynamic mechanical analysis (DMA) is a useful technique to probe localized chain mobilities, such as the flipping motion of a phenyl ring along its axis. If CTC formation in 6F-PAI did in fact form between the benzoic acid phenyl ring, rotation mobility would be suppressed. DMA may be able to detect such changes in localized motions along the polymer chains as a function of annealing. In summary, an increase in CTCs occurred with the increased annealing temperatures, resulting in what appears to be structure rearrangement, rather than densification.

4.4. Characterization of Single Gas Transport Properties

4.4.1. Single Gas Permeation

The single gas permeabilities and permselectivities for 6F-PAI-1 annealed under various conditions are given in Table 4.2. Based on the very low CO_2 plasticization resistance shown for the unannealed film, as well H_2S's greater ability to plasticize membranes compared to CO_2, H_2S was not measured in unannealed 6F-PAI or 6F-150. In this chapter, H_2S permeability and selectivity over CH_4 are reported for 6F-200 as a reference, and based on these results, modifications to the polymer will be proposed, while the actual modifications and transport results will be the topic of chapter 5.

Table 4.2: Single-gas transport properties in 6F-PAI-1 at 35°C and 65 psia. H_2S permeability was measured at 35 psia to prevent plasticization.

Annealing condition	P_{CO2}	P_{CH4}	P_{H2S}	P_{CO2}/P_{CH4} *(Ideal Permselectivity)*	P_{H2S}/P_{CH4} *(Ideal Permselectivity)*
unannealed	37	1.2	-	31	-
150°C	27	0.55	-	55	-
200°C	30	0.75	6.4	43	8.5

Two important trends can be observed in Table 4.2: (1) compared to unannealed films, selectivity increased and permeabilities decreased for films annealed at 150°C, and (2) a higher annealing temperature of 200°C increased but at the sacrifice of CO_2/CH_4 selectivity. The first trend is often observed in other glassy materials subjected to thermal annealing, and is indicative of excess free volume relaxation [8]. Here, the term excess is used to signify glassy-state, microvoid packing defects, which can relax out by

accelerated physical aging induced by thermal annealing. As discussed in Chapter 2, the non-equilibrium state of glassy polymers ages toward a densified, equilibrium state. This thermodynamically driven process tends to cause the excess free volume microvoids to relax and diffuse out of the polymer matrix via process called free-volume diffusion and lattice contraction [9]. Consequently, the transport properties in glassy polymers are highly dependent on processing conditions and thermal history. *Excess* free volume relaxation in 6F-150 relative to the unannealed film is further suggested by the CO_2 sorption trends, which are discussed in the next section.

On the other hand, the trend discussed in (2) is not indicative of densification based physical aging as normally observed in simple polyimides [3, 5, 6]. Rather, the surprising increase in CO_2 and CH_4 permeability suggests some unusual rearrangement of the polymer microstructure as discussed in the previous section. The following sections on the sorption and diffusivities help to decouple the effects of such rearrangement on the equilibrium and kinetic aspects of penetrant permeability.

4.4.2. Single Gas Sorption

Equilibrium penetrant concentration in the membranes vs. pressure was measured for CH_4, CO_2, and H_2S at 35°C using a pressure-decay technique. Figure 4.9 shows the equilibrium sorption isotherms for all three annealing conditions. Solid lines represent dual-mode model fits to the experimental data. In general, good agreement between model fits and experimental data was obtained as can be observed in Figure 4.9. Hydrogen sulfide was not measured in the unannealed film due to swelling at low H_2S pressures.

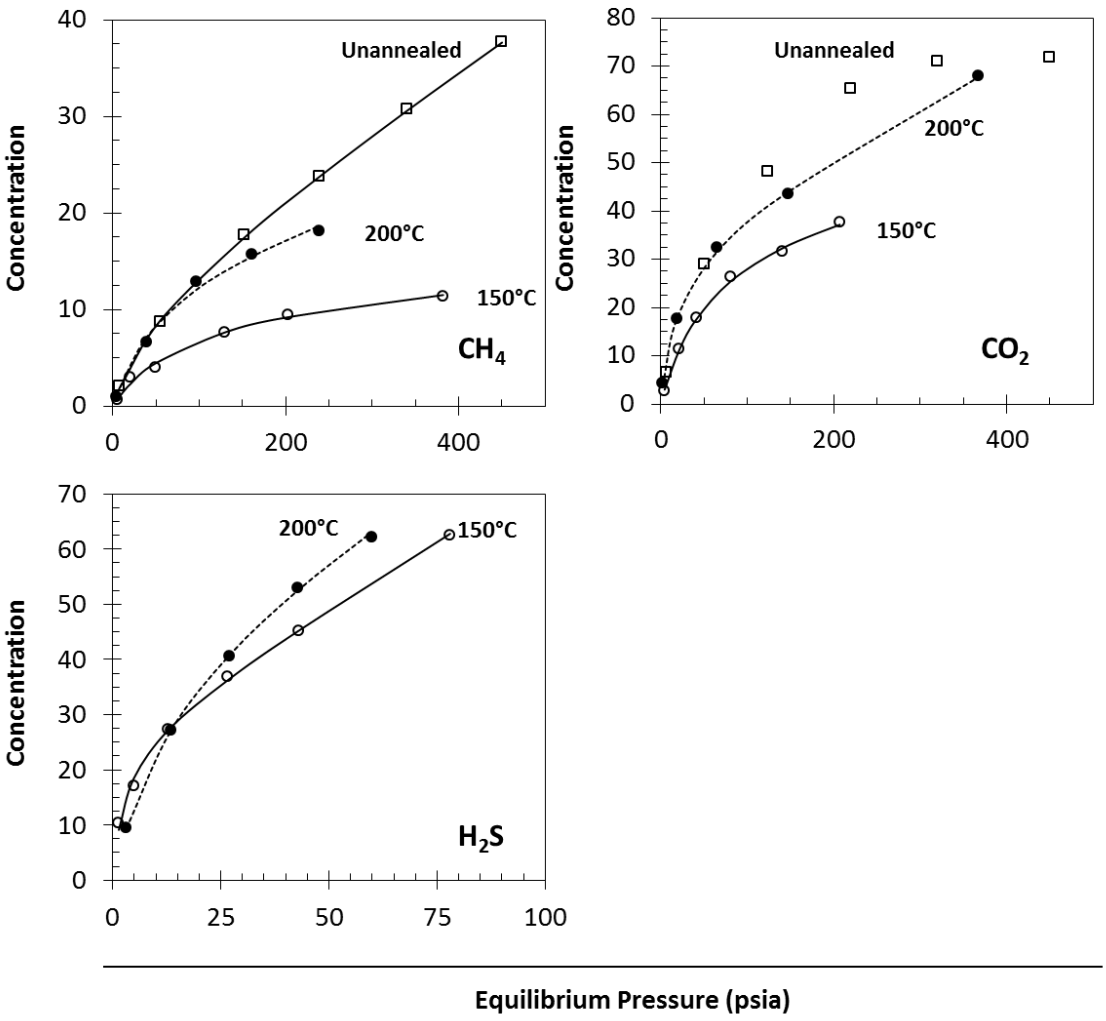

Figure 4.9: Penetrant concentration vs. pressure plots for CH_4, CO_2 and H_2S for films annealed at 150 and 200°C for 24 hours as well as an unannealed film.
*Dual-mode predictions for CO_2 in the unannealed film could not be obtained accurately due to the lower curvature in the concentration versus pressure isotherm.
H_2S was not measured in the unannealed film due to membrane swelling at low pressures.
Units of concentration are cc(STP)/cc(polymer)

As can be observed in Figure 4.9, both CO_2 and CH_4 sorption capacity are the highest in the unannealed film. This is due to a greater amount of unrelaxed, or excess free volume,

which is interpreted based on the intersection of the short, high-pressure linear portion of CO_2's isotherm with the y-axis. A considerably larger amount of unrelaxed free volume exists in the unannealed film for which CO_2 gains increased total sorption capacity at low pressures relative to the two thermally treated films. The Langmuir capacity for CH_4 does not appear to be significantly affected, which may be due to its low affinity for sorption into these sites.

A comparison between 6F-150 and 6F-200 reveals an increase in sorption capacity for all gases in films annealed at 200 relative to 150°C. As shown previously in figure 4.2, degradation or crosslinking of the polymer backbone did not occur as a result of the thermal treatments. Hence, higher sorption in the 200°C annealed films is likely the result of increased total free volume or free volume distribution, and is consistent with the density and predicted fractional free volume that was shown previously. Such a trend differs from sorption trends observed in simple polyimides undergoing accelerated physical aging. Madden et al. observed reduced hydrocarbon sorption after annealing Matrimid® at increased temperatures [11], which was shown to be due mostly to reduced sorption in the Langmuir environments. The sorption trends in Figure 4.3 are not consistent with such a simple mechanism, however.

The dual-mode framework was used to further analyze the changes in sorption capacity. Dual-mode parameters for CH_4, CO_2, and H_2S are given in Table 4.3.

Table 4.3: Dual-mode model parameters for unannealed and films annealed at 150 and 200°C for 24 hours.

Dual-mode parameters at 35°C			
Unannealed	k_D (cc(STP)/cc*psia)	b ($psia^{-1}$)	C_H' (cc(STP)/cc)
CH_4	6.7×10^{-2}	2.1×10^{-2}	9.7
*CO_2	--	--	--
150°C	k_D (cc(STP)/cc*psia)	b ($psia^{-1}$)	C_H' (cc(STP)/cc)
CH_4	$(1.2 \pm 0.92) \times 10^{-2}$	$(1.3 \pm 0.21) \times 10^{-2}$	12 ± 0.96
CO_2	$(4.0 \pm 0.91) \times 10^{-2}$	$(6.2 \pm 2.1) \times 10^{-2}$	38 ± 3.2
H_2S	0.5	0.4	25
200°C	k_D (cc(STP)/cc*psia)	b ($psia^{-1}$)	C_H' (cc(STP)/cc)
CH_4	$(4.8 \pm 2.6) \times 10^{-2}$	$(5.5 \pm 5.3) \times 10^{-2}$	9.2 ± 8.2
CO_2	$(18 \pm 8.8) \times 10^{-2}$	$(5.7 \pm 0.56) \times 10^{-2}$	30 ± 1.1
H_2S	0.44 ± 0.12	$(4.7 \pm 3.6) \times 10^{-2}$	36 ± 6.0

As shown in table 4.3, an unexpected increase in the Henry's Law coefficient for CO_2 and CH_4 occurred in films annealed at 200 relative to 150°C. The Henry's Law coefficient, k_D for H_2S, is not affected to a significant extent by the higher annealing temperature. This may be due to higher polarity in H_2S, whose sorption depends more on physiochemical interactions with the polymer than simply free volume within the matrix, as is mostly the case for CO_2 and CH_4. Such a phenomena will be discussed in Chapter 6. The Henry's Law parameter has been shown to depend on both penetrant condensability

and size. Merkel et al. showed that when k_D is normalized for penetrant condensability, it decreases with penetrant critical volume [12]. Therefore, the increase in k_D for CO_2 and CH_4 shown in Table 4.3 may be due to increased ability for these penetrants to fit into the equilibrium packing regions. A "new" Henry's region, which can accommodate more penetrant relative to the unannealed film, presumably formed as a result of thermal annealing. The increases in d-spacing and free volume for the annealed films support this trend.

It should be pointed out that the considerable standard deviation in the dual-mode parameters may be due to differences in the molecular weight between various batches of synthesized polymer. Especially for the batches produced at the beginning of this work, molecular weight tended to be slightly lower than later batches. Therefore, the transport properties between these various batches may be associated with a significant amount of variance even for films annealed under the same annealing conditions, and so we do not wish to over-interpret the parameters given in Table 4.3. Nevertheless, the two most consistent trends that were observed are as follows: (1) sorption capacity decreased comparing unannealed to annealed films, and (2) k_D *increased* in the 200°C annealing condition relative to 150°C. The first trend is due to the more conventional excess or glassy-state microvoid free volume relaxation, as apparent in the CO_2 sorption isotherms in Figure 4.9, and is consistent with what is generally observed upon accelerated physical aging of glassy polymers after thermal treatment at moderate temperatures.

The increase in k_D for CO_2 and CH_4 as shown in Table 4.2, as well as what can be qualitatively observed in Figure 4.9 is inconsistent with the conventional interpretation of physical aging, which envisions excess free volume to leave the polymer matrix and to

reduce hypothetical, non-equilibrium packing defects. The densified regions, probed by the Henry's Law parameter, are usually minimally affected because these regions are idealized as being in a state of thermodynamic packing equilibrium. Therefore, an increase in k_D is likely caused by a "new" equilibrium sorption environment with different *total* free volume than the unannealed films. This different total free volume is in addition to the glassy-state non-equilibrium packing defects, and is reflected by higher total free volume in Table 4.1. Madden et al. also observed an increase in k_D for thermally annealed Matrimid®, and attributed it to a changed microstructure as a result of thermal annealing [11]. Nevertheless, the increase in CO_2 and CH_4 permeability for the 200°C annealing condition relative to 150°C can be partially attributed to higher sorption capacity as a result of increased Henry's Law sorption.

Suffice it to say, many of the simple trends often observed with annealing a simple, purely imide backbone are not seen in this complex class of polyamide-imide (PAI) materials. Like the complementary XRD and spectroscopy results, the data show the PAI materials to be quite complex in their nature.

4.4.3. Single Gas Diffusion

Pure gas diffusivities were calculated from the time-lag method as outlined in Chapter 3, and are given in Table 4.4.

Table 4.4: Pure gas diffusivities and diffusion selectivities at 35°C and ~18psia. Units of the diffusion coefficient are cm^2/s.

Annealing condition	D_{CO2} $(x10^8)$	D_{CH4} $(x10^8)$	D_{H2S} $(x10^8)$	D_{CO2}/D_{CH4} *(Ideal Permselectivity)*	D_{H2S}/D_{CH4} *(Ideal Permselectivity)*
unannealed	4.0	0.51	-	7.8	-
150°C	1.2 ± 0.041	$(14 \pm 0.5)x10^{-2}$	-	8.8 ± 0.44	-
200°C	1.7 ± 0.18	$(17 \pm 2.0)x10^{-2}$	0.18	10 ± 1.6	0.91

A significant decrease in both CO_2 and CH_4 diffusivity can be observed when comparing unannealed 6F-PAI-1 to 6F-150 and 6F-200. This is likely caused by excess free volume relaxation in the annealed films as a result of the highly non-equilibrium state of the unannealed film. However, it may also reflect CTC formation effects and microstructure rearrangements discussed in the previous sections. For films annealed at 200°C, both CO_2 and CH_4 diffusivity increase with respect to 6F-150. The CO_2/CH_4 diffusion selectivity is essentially unchanged when considering the standard deviation. This increase in diffusivity is rather surprising. However, the sorption and density data indicated increased free volume in 6F-200. This would also result in increased diffusivities. Presumably because CTC formation usually results in reduced chain mobility from increased interchain interactions, diffusion selectivity was preserved in 6F-200.

To further elucidate the changes in CO_2 and CH_4 permeability and diffusivity upon elevated annealing temperature, the Henry's and Langmuir diffusivities were calculated for these two penetrants by fitting a plot of pure gas permeability vs. $1/(1+bf)$, as shown in Figure 4.10, to the dual-mode partial immobilization model as discussed in

chapter 2. The y-intercept of this plot is equal to $k_D D_D$ and the slope equal to FK. Dual-mode sorption parameters were taken from Table 4.3.

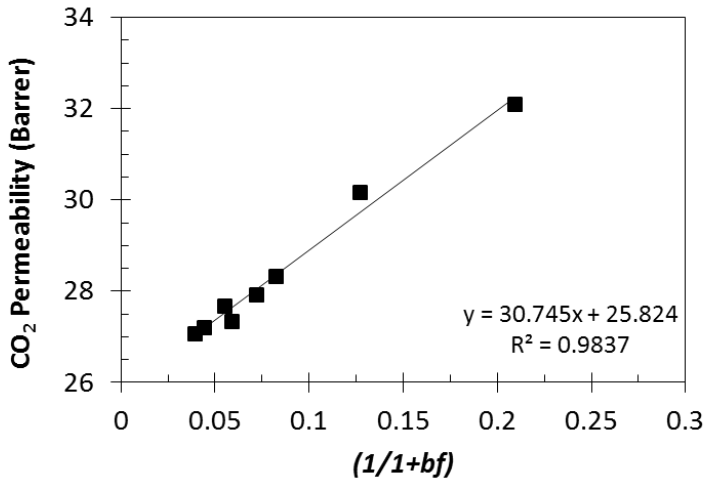

Figure 4.10: Plot of CO_2 permeability in 6F-PAI-1 vs. 1/(1+*bf*) for the 200°C annealed film. *f* is the penetrant fugacity in psia.

Table 4.5: Langmuir and Henry's diffusion coefficients for CH_4 and CO_2 in 6F-PAI-1 annealed at 150 and 200°C.
Units of diffusion coefficient are cm^2/s.

	D_D ($x10^8$)	D_H ($x10^8$)	F
CH_4			
150°C	1.40	0.039	0.029
200°C	0.54	0.075	0.14
CO_2			
150°C	17	0.66	0.038
200°C	5.5	0.88	0.16

D_D, D_H, and F for CO_2 and CH_4 are compared as a function of annealing temperature in Table 4.5. A decrease in D_D for both penetrants can be observed in the film annealed at 200°C. To the contrary, D_H increases for both CO_2 and CH_4. This leads to an increase in the mobility factor, F, for the 6F-200 relative to 6F-150. Reductions in D_D can be explained by the formation of intermolecular CTCs and close, parallel chain packing as was pictured in Figure 4.8. On the other hand, the increase in D_H as shown in Table 4.5 is not as intuitive. While not wanting to speculate to extensively, as was discussed in section 4.3.2, it is hypothesized that the "new" Langmuir environments, formed between the bulky but flexible 6FpDA moieties, could increase the mobility of penetrants sorbed into these environments. At ~20 psia, where the diffusion coefficients were measured, sorption tends to occur more in the Langmuir sorption sites, as these sites have yet to become saturated. A lower mobility factor for 6F-150 for both penetrants suggests that the effective diffusion coefficient may be lower due to increased penetrant immobilization in these microvoids. The increase in F for 6F-200 suggests that molecules sorbed into these microvoids have increased mobility, thereby increasing the effective diffusivity for CO_2 and CH_4 in 6F-200 relative to 6F-150.

In summary, because D_D decreased but D_H increased, simple densification based physical aging does not appear sufficient in describing the changes to the polymer microstructure upon thermal annealing. It has been said by other researchers that the formation of CTCs changes the local packing environment in such a way that it resembles a new material [11]. Such a picture seems reasonable considering the trends in the sorption capacity and the local diffusion coefficients shown in the previous discussion.

4.5. Mixed Gas Permeation

4.5.1. 50/50 CO_2/CH_4

200°C was chosen as the annealing temperature for mixed gas testing because it showed the highest plasticization resistance. Annealing times of 2 and 24 hours are compared. Because neither long annealing temperatures or times are desirable, it is advantageous to determine how annealing time affects the mixed gas performance. Figures 4.11 and 4.12 show the mixed gas CO_2 and CH_4 permeabilities along with CO_2/CH_4 permselectivity up to ~1000 psia for both annealing times at 200°C.

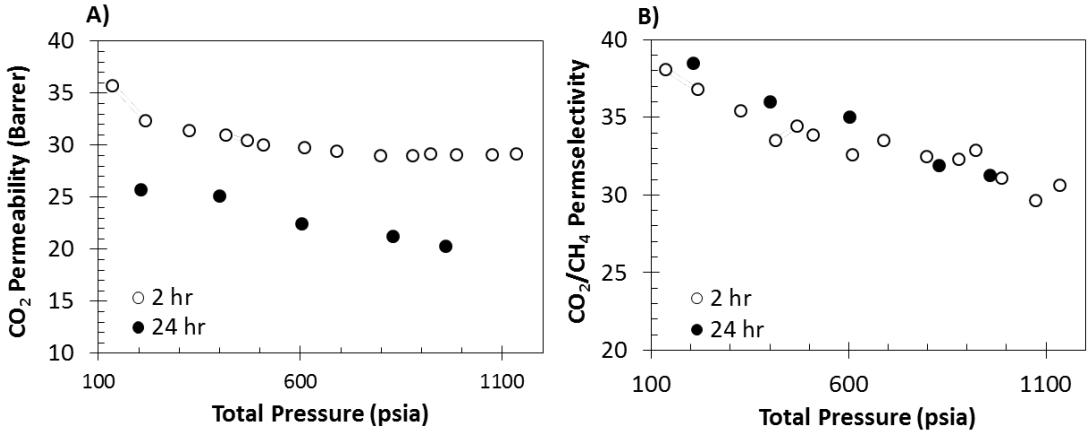

Figure 4.11: A) CO_2 permeability and **B)** CO_2/CH_4 permselectivity at 35°C using a 50/50 CO_2/CH_4 feed stream. Annealing times of 2 and 24 hours at 200°C are compared.

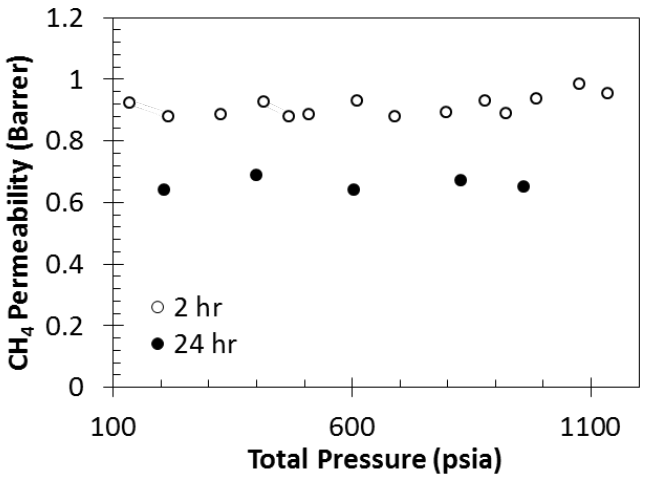

Figure 4.12: CH_4 permeability vs. pressure at 35°C for films annealed at 200°C for 2 (open circles) and 24 hours (closed circles). The feed stream was composed of 50/50 CO_2/CH_4.

Both annealing times were sufficient for stabilizing the membranes against plasticization. This is confirmed by a constant CH_4 permeability throughout the entire pressure range. CO_2 permeability decreases with feed pressure for both annealing conditions, and is due to filling of the Langmuir microvoids at higher pressures. The decreasing CO_2 permeability reduces the selectivity as well, however, even at 1000 psia total feed pressure, both films held a CO_2/CH_4 selectivity of ~30, which represents a substantial improvement over conventional uncrosslinked materials such as CA and Matrimid®.

As an additional measure of 6F-PAI-1's stability against CO_2 induced plasticization, the 24 hour annealed film that was exposed to the 50/50 CO_2/CH_4 feed stream up to 1000 psia was sufficiently degassed for 1 week and then repressurized with the same binary feed stream. This film is referred to as a "conditioned" film. Figure 4.13 compares the CO_2 permeability and CO_2/CH_4 permselectivity for virgin and conditioned films. The virgin film data is the same data given in Figures 4.11-4.12, and represents a membrane with no prior CO_2 exposure.

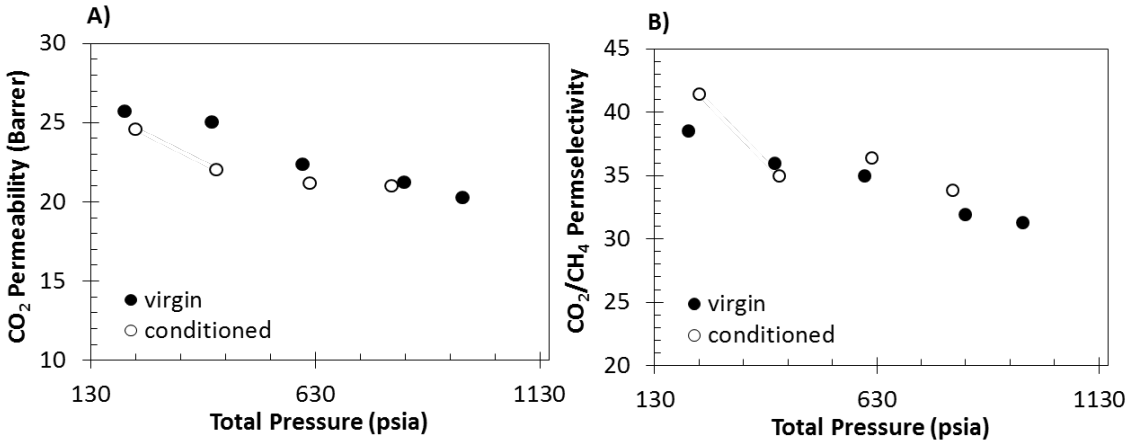

Figure 4.13: A) CO_2 permeability and **B)** CO_2/CH_4 permselectivity at 35°C for virgin (closed circles) and conditioned (open circles) films. The feed stream was composed of 50/50 CO_2/CH_4.

As can be seen in Figure 4.12, CO_2 permeability and permselectivity are essentially unaffected by exposure to high pressure CO_2 during mixed gas testing, and the transport properties of the conditioned sample closely match those of the virgin film. Thus, high levels of CO_2 sorption did not cause any permanent glassy relaxations, and the polymer matrix remained stable throughout the entire pressure range.

4.5.2. Effect of Toluene Exposure

Toluene was used as model contaminant to assess the effects of hydrocarbon exposure on the membrane. Although most natural gas streams are pretreated to remove hydrocarbons and natural gas liquids (NGL) prior to the membrane stage, it is impractical to completely remove all components [13]. Trace impurities can still break through the pretreatment train, and disruptions in the train can lead to sudden surges of hydrocarbon content in the gas stream that is to be treated by the membrane. Even minor hydrocarbon concentrations can lead to irreversible reductions in separation performance [13-14].

Hence, it is important to study the effect of such impurities in the gas stream on the separation performance.

Figure 4.14 and 4.15 show the transport properties of 6F-PAI-1 annealed at 200°C for 24 hours using a clean 50/50 CO_2/CH_4 feed and a 50/50 CO_2/CH_4 feed containing 200 ppm toluene. To determine if hydrocarbon exposure caused irreversible changes to the membrane, the film that was exposed to the toluene contaminated feed was degassed for approximately 3 days and repressurized with a clean 50/50 CO_2/CH_4 feed. Virgin film values are the same as given in Figures 4.10-4.11.

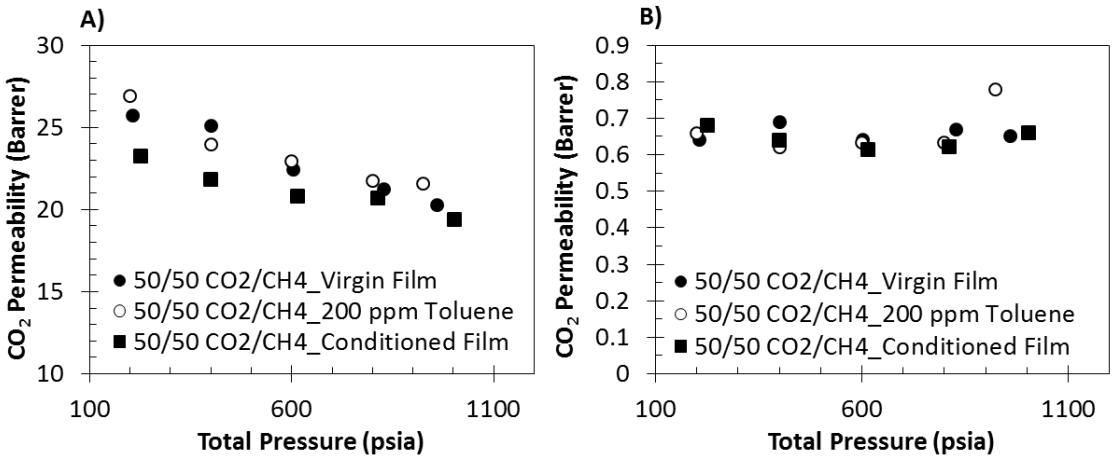

Figure 4.14: CO_2 permeability and CO_2/CH_4 permselectivity at 35°C for 6F-PAI-1 annealed at 200°C for 24 hours before, during, and after exposure to 200 ppm toluene using a 50/50 CO_2/CH_4 feed.

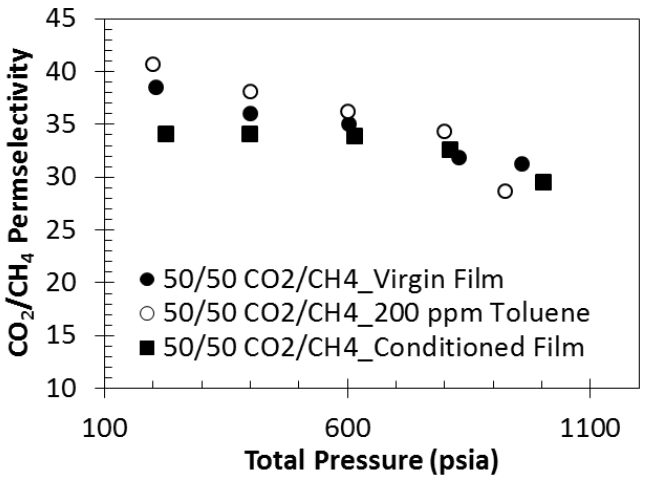

Figure 4.15: CH_4 permeability at 35°C before, during, and after exposure to 200 ppm toluene using a 50/50 CO_2/CH_4 feed stream.

Up to 800 psia total feed pressure, the permeabilities and selectivities during toluene exposure closely match those of the virgin film, thus at this concentration of toluene, exposure to the hydrocarbon has little effect on the separation performance, and a high CO_2/CH_4 selectivity of ~35 is maintained. However, beyond 800 psia, an upswing in CH_4 permeability can be observed, which causes a sudden decrease in selectivity. Although large scale, permanent changes to the polymer microstructure did not occur, as evidenced by the close matching of virgin and conditioned CH_4 permeabilities, some glassy relaxations may have occurred while in the swollen state. At low total pressures, CO_2 permeability in the conditioned film is lower than the virgin film values, which lowers the selectivity relative to the virgin film. Langmuir relaxation is further supported by the fact that only CO_2 permeability appears to be affected. At higher pressures, the virgin and conditioned values converge, and perhaps more importantly, plasticization resistance is not compromised in the toluene conditioned films.

Higher toluene concentrations should be studied for a more complete evaluation of hydrocarbon exposure to the membrane. The results in figure 4.14-4.15 show good plasticization resistance against high pressure CO_2 while in the presence of a hydrocarbon contaminant, which further demonstrates the intrinsically robust nature of the polyamide-imide backbone.

4.5.3. Effect of H_2S Exposure

As discussed in chapter 2, H_2S is a relevant contaminant in natural gas that has not been actively targeted for membrane separations because of its toxic nature. Also, its polar structure and high condensability tends to swell both uncrosslinked and crosslinked polymers at much lower partial pressures than CO_2. Such low plasticization resistance in glassy polymers is demonstrated in Figure 4.16, which shows single gas H_2S permeability vs. pressure isotherms in 6F-PAI-1, 6FDA-DAM:DABA (3:2), and 6FDA-DAM:DABA (3:2) crosslinked with propanediol. The latter two materials represent a high performance *polyimide* and its crosslinked form, materials that have shown very good permeability and selectivity for a number of gas pairs. This polymer has been developed and extensively researched by both past and current members in the Koros group [16–18].

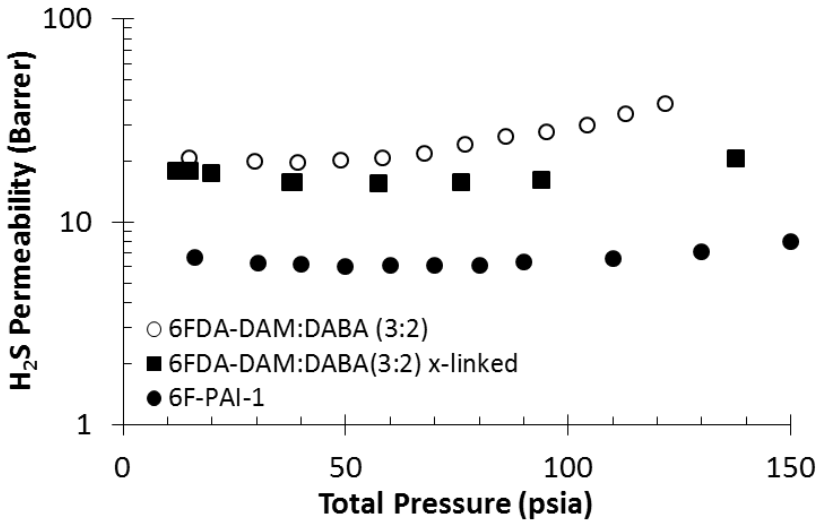

Figure 4.16: Pure gas H_2S permeability vs. pressure at 35°C for various high performance 6FDA based polyamide-imides and polyimides. Crosslinked 6FDA-DAM:DABA (3:2) is signified by "x-linked." *Polyimide data was provided by B. Kraftschick and C. Kuete in the Koros group.*

Uncrosslinked 6FDA-DAM:DABA (3:2) begins to swell near 50 psia, while the crosslinked form and 6F-PAI-1 show permeability upswing at a moderately higher pressure of around 100 psia. As is the case with CO_2, mixed gas testing is necessary to determine the effect of swelling on CH_4 permeability and selectivity of the membrane.

Figures 4.17-4.18 show CO_2, H_2S and CH_4 permeability along with their selectivities over CO_2/CH_4 and H_2S/CH_4 permselectivity for 6F-PAI-1 annealed at 200°C for 24 hours using a ternary gas stream composed of 10/20/70 $H_2S/CO_2/CH_4$. The transport properties for a 50/50 CO_2/CH_4 stream from Figures 4.10-4.11 are also shown for comparison.

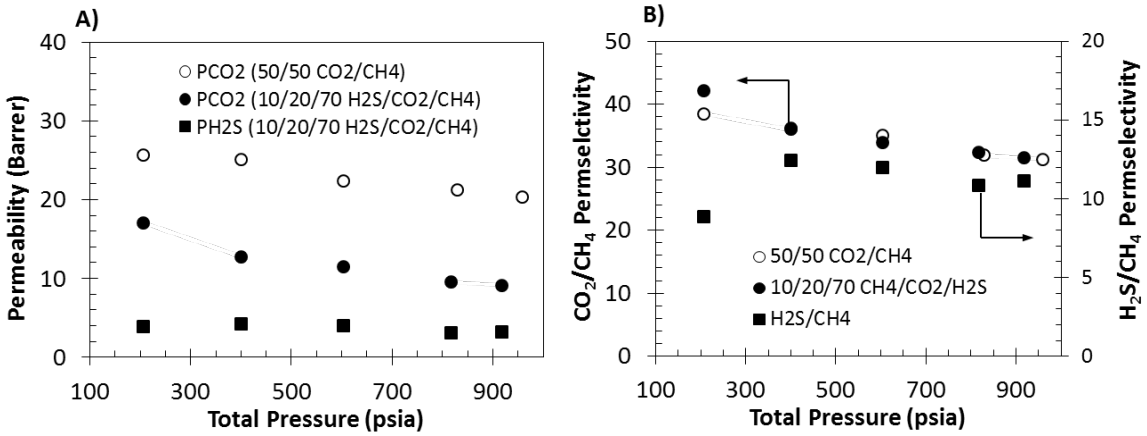

Figure 4.17: A) CO_2 and H_2S permeability and **B)** CO_2/CH_4 and H_2S/CH_4 permselectivity vs. pressure at 35°C. Open circles represent values from a 50/50 CO_2/CH_4 feed stream. Close symbols represent data from a 10/20/70 $H_2S/CO_2/CH_4$ feed stream.

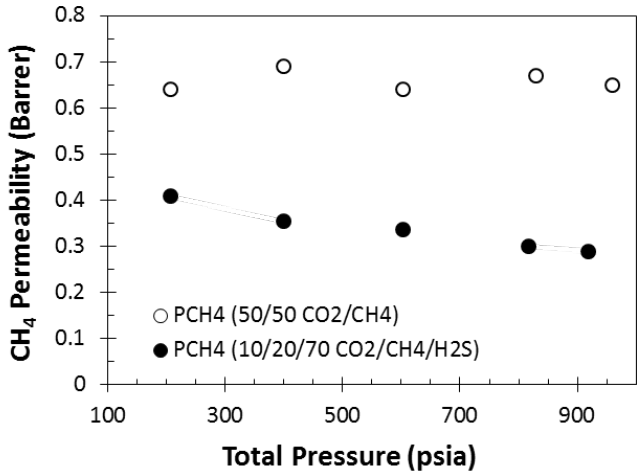

Figure 4.18: CH_4 permeability at 35°C using 50/50 CO_2/CH_4 (open symbols) and 10/20/70 $H_2S/CO_2/CH_4$ (closed symbols) feed streams.

A substantial decrease in both CO_2 and CH_4 permeability occurred in the ternary gas feed relative to a binary CO_2/CH_4 feed stream. The CO_2/CH_4 selectivity appears to be unaffected in the presence of H_2S, and the film subjected to the ternary feed still maintains a CO_2/CH_4 selectivity near 30 at 1000 psia total feed pressure. This means that both CO_2 and CH_4 permeability are affected to the same extent by the presence of H_2S,

and is likely due to H_2S outcompeting both gases for Langmuir sorption sites. Hydrogen sulfide appears to saturate its sorption equilibrium in these sites at low total pressures, which is supported by constant H_2S permeability through the entire pressure range. This effectively reduces the number of available sites for CO_2 and CH_4 sorption. Both CO_2 and CH_4 permeability decrease with pressure as they continue to fill microvoids, leading to an initial increase in H_2S/CH_4 selectivity followed by constant value of 11 up to 1000 psia. It can be said then that 6F-PAI-1 is not plasticized up to 100 psia H_2S and 200 psia CO_2, or a total of 300 psia total acid gas partial pressure. Such conditions would almost certainly plasticize uncrosslinked commercially available materials such as CA and Matrimid®.

It is interesting to note that although 6F-PAI-1 was plasticized at 100 psia H_2S in the single gas isotherm shown in Figure 4.16, it is not plasticized in the ternary gas isotherm at the same H_2S partial pressure. This is likely due to lower total H_2S concentration in the membrane exposed to the ternary feed as a result of Langmuir sorption competition with CO_2 and CH_4, and possibly lower H_2S fugacity at equivalent partial pressures in the ternary mixture. Wessling et al. [19] discussed this in detail regarding CO_2/CH_4 separations, and emphasized the importance of examining CH_4 permeability with pressure. As the permeability of the faster, more soluble component decreases with pressure from Langmuir saturation, the permselectivity will also decrease, which can mask selectivity losses in the case of increased CH_4 permeability from plasticization. Thus, it is important to evaluate CH_4 permeability during mixed gas testing.

4.6. Comparison of 6F-PAI-1 to Upper-Bound

Figure 4.19 compares 6F-PAI-1 on a Robeson type CO_2/CH_4 upper bound plot against commercially available CA and Matrimid®, as well as a number of high H_2S selective rubbery polymers reported in the literature.

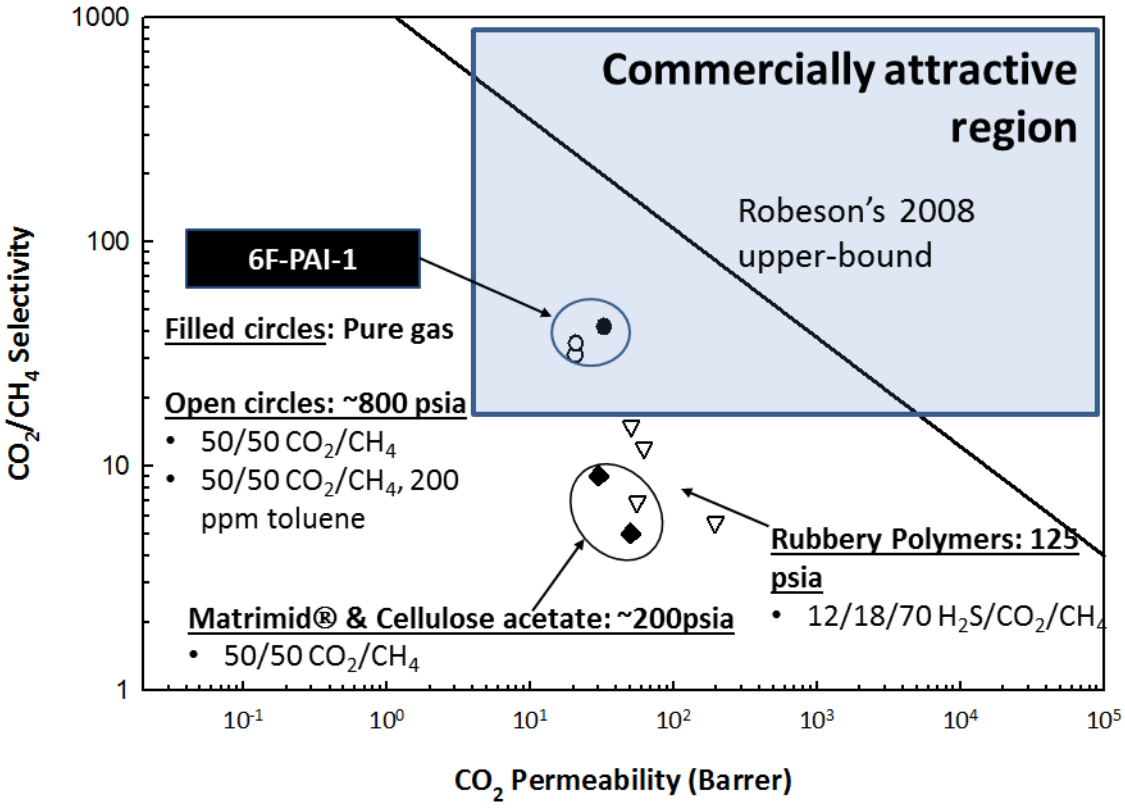

Figure 4.19: Robeson's 2008 CO_2/CH_4 upper-bound plot [18]. CA and Matrimid® data adapted from [19-20]. Rubbery polymers represent polyether urethane and polyether urethane (urea) dense film membranes from Stern et al. [21].

As can be seen in the figure, 6F-PAI-1 maintains an attractive permeability and selectivity tradeoff under highly aggressive conditions that more closely resemble those encountered at a real natural gas field. Because CA and Matrimid® are easily plasticized by CO_2, their productivity tradeoff falls away from the commercially attractive region at

higher pressures. The rubbery polyether-amide type materials show higher CO_2 permeability than the glasses, however even at low total pressures, their selectivity is below the commercially attractive region. Thus, 6F-PAI-1 has the potential to offer a selective separation for the removal of CO_2 from natural gas under aggressive conditions without the need for extensive membrane stabilization treatments.

Because an H_2S/CH_4 upper bound plot has not been established in the literature, hypothetical upper bounds were constructed for H_2S/CH_4 and for the total acid gas separation factor in order to compare glasses against rubbers. Figure 4.20 compares 6F-PAI-1 to the rubbery polymer data as referenced in Figure 4.19.

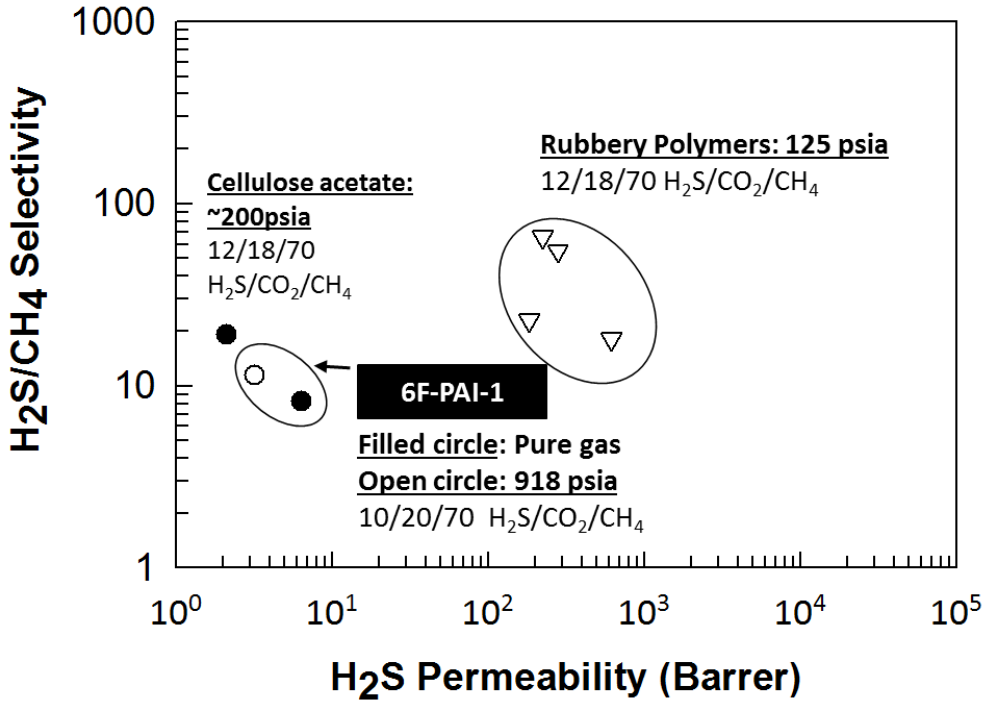

Figure 4.20: Hypothetical H_2S/CH_4 upper bound. The data for the rubbery polymers is adapted from Stern et al. [21].

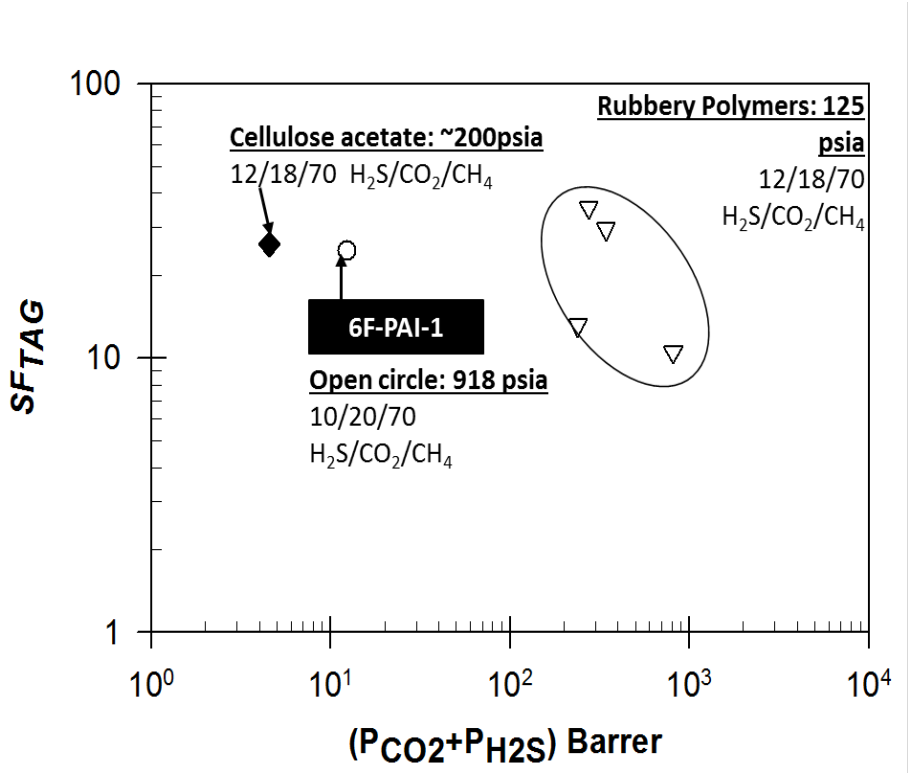

Figure 4.21: Hypothetical total acid gas upper-bound. The data for the rubbery polymers is adapted from Stern et al. [21].

As can be seen in Figure 4.20, the performance tradeoff for the H_2S/CH_4 pair in 6F-PAI-1 lies well below that of the rubbery materials. Additionally, 6F-PAI-1 only offers higher H_2S permeability compared to CA, while its H_2S/CH_4 selectivity is lower. However, using the total acid gas metric in Figure 4.21, 6F-PAI-1shows comparable *total selectivity* compared to the rubbery materials and CA, as well as higher total acid gas permeability than CA. It is important to note that the data for CA along with the rubbery polymers was measured at ~200 psia total feed pressure. These feed conditions are relatively mild compared to the testing conditions used for 6F-PAI-1, as well as those which are encountered in a real natural gas well. Thus, it will be necessary to also test the rubbers at higher feed pressures to discern the effects of elevated CO_2 and H_2S concentrations on their separation performance. This will be the subject of chapter 7.

4.7. Conclusions

The results presented in this chapter demonstrate the intrinsically high plasticization resistance of the polyamide-imide backbone when post-treated properly. This information makes this class of materials a potential alternative to covalent crosslinking for natural gas separation membranes. A combination of charger transfer formation induced from thermal annealing as well as interchain hydrogen bonding is attributed to such high intrinsic stability against plasticization. Specifically for 6F-PAI-1, thermal annealing did not result in significant permeability reductions, instead, a presumed microstructure rearrangement occurred that resulted in a slight increase in permeability with moderately high CO_2/CH_4 selectivity. Such a result cannot be explained by simple densification based physical aging that generally occurs in simple polyimides.

Figure 4.20 suggests that polyamide-imides based on 6FDA can offer a selective and robust separation in the presence of aggressive feed components without the need for extensive stabilization treatments. Moreover, the polyamide-imide backbone offers latitude for modifications to the backbone in order to develop new materials with potentially enhanced separation properties relative to 6F-PAI-1. The next chapter will discuss modifications made to the backbone of 6F-PAI-1 in order to improve the H_2S permeability and H_2S/CH_4 permselectivity

Recalling from section 4.2.3, 6F-PAI-1 showed a reversed H_2S/CH_4 diffusion selectivity of 0.91. Its permselectivity towards H_2S is thus determined entirely by solubility differences and is apparently slightly negated by the reversed mobility contribution. Based on this surprising result, modifications to the polymer backbone will

be aimed at improving H_2S permeability and selectivity by increasing H_2S sorption and opening up free volume in the polymer microstructure to move the mobility selectivity closer to 1. The next chapter will be devoted to discussing these modifications as well as the transport properties and plasticization resistance of newly synthesized polyamide-imides.

4.7. References

[1] D. Fritsch and K.-V. Peinemann, "Novel highly permselective 6F-poly(amide-imide)s as membrane host for nano-sized catalysts," *Journal of Membrane Science*, **99** (1), 29-38, (1995).

[2] M. R. Coleman and W. J. Koros, "The transport properties of polyimide isomers containing hexafluoroisopropylidene in the diamine residue," *Journal of Polymer Science Part B: Polymer Physics*, **32**, (11), 1915-1926, (1994).

[3] F. Zhou and W. J. Koros, "Study of thermal annealing on Matrimid® fiber performance in pervaporation of acetic acid and water mixtures," *Polymer*, **47** (1), 280-288, (2006).

[4] J. D. Wind, C. Staudt-Bickel, D. R. Paul, W. J. Koros, "The Effects of Crosslinking Chemistry on CO_2 Plasticization of Polyimide Gas Separation Membranes," *Industrial & Engineering Chemistry Research*, **41 (**24), 6139-6148, (2002).

[5] J. D. Wind, C. Staudt-Bickel, D. R. Paul, W. J. Koros, "Solid-State Covalent Cross-Linking of Polyimide Membranes for Carbon Dioxide Plasticization Reduction," *Macromolecules*, **36**, (6), 1882-1888, 2003.

[6] C. Fuhrman, M. Nutt, K. Vichtovonga, M. R. Coleman, "Effect of thermal hysteresis on the gas permeation properties of 6FDA-based polyimides," *Journal of Applied Polymer Science*, **91**, (2), 1174-1182, 2004.

[7] J. Y. Park and D. R. Paul, "Correlation and prediction of gas permeability in glassy polymer membrane materials via a modified free volume based group contribution method," *Journal of Membrane Science*, **125 (**1), 23-39, (1997).

[8] Y. Huang, X. Wang, and D. Paul, “Physical aging of thin glassy polymer films: Free volume interpretation,” *Journal of Membrane Science*, **277 (**1–2), 219-229, (2006).

[9] X. Duthie et al., “Thermal Treatment of Dense Polyimide Membranes,” *Journal of Polymer Science Part B: Polymer Physics*, **46**, 879-1890, (2008).

[10] K. Ghosal and B. D. Freeman, “Gas separation using polymer membranes: an overview,” *Polymers for Advanced Technologies*, **5** (11), 673-697, (1994).

[11] W. C. Madden, D. Punsalan,W. J. Koros, “Age dependent CO_2 sorption in Matrimid® asymmetric hollow fiber membranes,” *Polymer*, **46** (15), 5433-5436, (2005).

[12] T. C. Merkel, V. Bondar, K. Nagai, B. D. Freeman, “Perfluorocarbon Gases in Poly (1-trimethylsilyl-1-propyne),” *Langmuir*, **38,** 273-296, (2000).

[13] D. Q. Vu, W. J. Koros, S. J. Miller, “Effect of Condensable Impurities in CO_2/CH_4 Gas Feeds on Carbon Molecular Sieve Hollow-Fiber Membranes,” **42,** 1064-1075, (2003).

[14] J.W. Simmons, S. Kulkarni, O.M. Ekiner, "Method for separating hydrocarbon-containing gas mixtures using hydrocarbon-resistant membranes" U.S. Patent 7025804 B2, (2006).

[15] C.C. Chen, “Thermally Crosslinked Polyimide Hollow Fiber Membranes For Natural Gas Purification," *PhD Dissertation*, Georgia Institute of Technology, Atlanta, Georgia, (2011).

[16] I. C. Omole, R. T. Adams, S. J. Miller, W. J. Koros, “Effects of CO_2 on a High Performance Hollow-Fiber Membrane for Natural Gas Purification,” *Industrial & Engineering Chemistry Research*, **49 (**10), 4887-4896, (2010).

[17] J. K. Ward and W. J. Koros, “Crosslinkable mixed matrix membranes with surface modified molecular sieves for natural gas purification: II. Performance characterization under contaminated feed conditions,” *Journal of Membrane Science*, **377** (1–2), 82-88, (2011).

[18] C. Ma and W. J. Koros, “High-performance Ester-crosslinked Hollow Fiber Membranes for Natural Gas Separations,” *Journal of Membrane Science*, http://dx.doi.org/10.1016/j.memsci.2012.10.024.

[19] T. Visser, G.H. Koops, M. Wessling, "On the Subtle balance between competitive sorption and plasticization effects in asymmetric hollow fiber gas separation membranes," *Journal of Membrane Science*, **252,** 265-277, (2005).

[20] L. M. Robeson, “The upper bound revisited,” *Journal of Membrane Science*, **320**, (1–2), 390-400, (2008).

[21] A. Y. Houde, B. Krishnakumar, S. G. Charati, S.A. Stern, “Permeability of dense (homogeneous) cellulose acetate membranes to methane, carbon dioxide, and their mixtures at elevated pressures,” *Journal of Applied Polymer Science*, **62**, (13), 2181-2192, (1996).

[22] A. Bos, I. G. M. Pünt, M. Wessling, H. Strathmann, “Plasticization-resistant glassy polyimide membranes for CO_2/CO_4 separations,” *Separation and Purification Technology*, **14**, (1–3), 27-39, (1998).

[23] G. Chatterjee, A.A. Houde, S. A. Stern, “Poly(ether urethane) and poly(ether urethane urea) membranes with high H_2S/CH_4 Selectivity," *Journal of Membrane Science*, **135**, 99-106, (1997).

CHAPTER 5

EFFECT OF THE AMIDE BOND DIAMINE STRUCTURE ON THE CO_2, CH_4 AND H_2S TRANSPORT PROPERTIES

In Chapter 4, the intrinsically robust nature of the polyamide-imide backbone was demonstrated through high pressure pure and mixed gas permeation testing. This opened the door for development of new structures with the potential for enhanced permeabilities and selectivities while retaining the inherent stability against aggressive feeds. This chapter discusses the synthesis of two new polyamide-imides by varying the diamine that forms the tail-tail connection during polycondensation, and compares their transport properties to the starting material, 6F-PAI-1. Torlon®, a commercially available polyamide-imide, which is widely known for its excellent CO_2/CH_4 selectivity and high plasticization resistance is also included as a baseline for comparison. This chapter presents two new polyamide-imides with enhanced transport properties relative to Torlon® but also demonstrates the complexity of the polyamide-imide microstructure as well as the challenges associated with development of simultaneously high CO_2 and H_2S selectivity. The results of this work will provide a foundation from which to interpret the mixed gas testing results that will be presented in chapter 7.

5.1. Introduction

The permeability-selectivity comparisons of the CO_2/CH_4 and H_2S/CH_4 permselectivity, as well as the total acid gas selectivity factor showed the ability of 6F-PAI-1 to maintain good performance under highly aggressive conditions where

traditional materials such as CA and Matrimid® would tend to become plasticized. When compared using the total acid gas metric, 6F-PAI-1 showed higher permeability than CA but lower total selectivity. The diffusion and solubility data showed that H_2S/CH_4 permselectivity is governed almost entirely by solubility differences. No diffusion advantage for H_2S over CH_4 was observed, and in fact, mobility selectivity for this gas pair was less than 1. Therefore, the goal of this chapter is to modify the polymer in order to achieve higher H_2S/CH_4 selectivity through increased H_2S solubility, as well as to increase the polymer free volume in order to push the mobility selectivity closer to 1.

Several researchers have shown *polyimides* composed of diamines with bulky pendent groups ortho to the N-C imide bond result in significantly increased gas permeability with only a moderate drop in selectivity. Carbon dioxide permeabilities up to 350 and 450 Barrers have been reported in 6FDA based polyimides containing 3,5-diaminomesistylene (DAM) and 2,3,5,6-tetramethylphenylene diamine (TmPDA), respectively [1, 2]. The structures of these materials are shown in Figure 5.1.

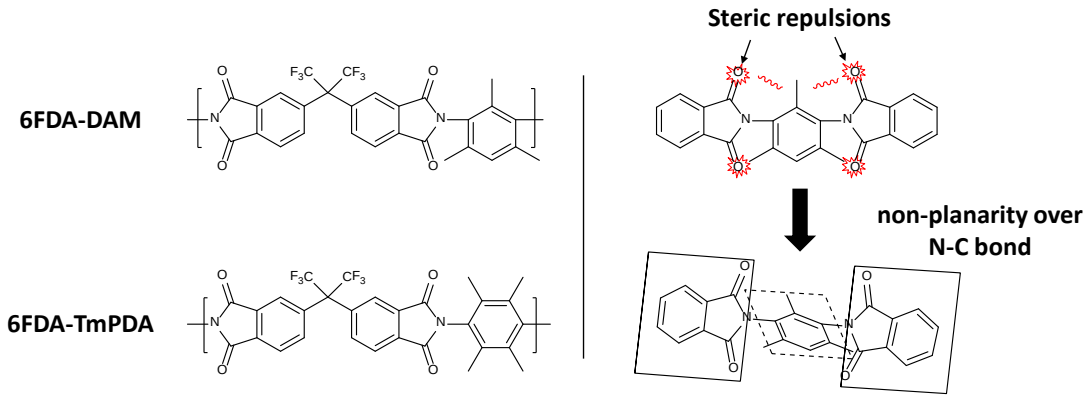

Figure 5.1: Chemical structure of 6FDA-DAM and 6FDA-TmPDA polyimides and depiction of steric interactions in 6FDA-DAM that result in a highly non-planar backbone. Similar interactions are presumed to take place around the imide bond in 6FDA-TmPDA.

Only a slight decrease in selectivity is shown in 6FDA-TmPDA relative to 6FDA-DAM despite CO_2 permeability that is almost 30% higher than the DAM analogue. The lower selectivity in 6FDA-TmPDA is presumably due to a decrease in the diffusion selectivity as a result of higher free volume.

Based on the discussion in the preceding paragraph, the diamine in 6F-PAI-1, 6FpDA, was replaced with DAM and TmPDA in an attempt to increase H_2S diffusivities. Total permselectivity was not expected to decrease since H_2S/CH_4 diffusion selectivity is already less than 1. The anticipated higher free volume in the DAM and TmPDA based *polyamide-imides*, as induced by similar steric interactions and bond dynamics depicted in Figure 5.1, was expected to bring mobility selectivity closer to 1 so that it would no longer offset H_2S's solubility advantage over CH_4. Thus, permselectivity was expected to increase partially by increasing H_2S/CH_4 diffusion selectivity closer to 1.

Work by Merkel et al. have shown interesting hydrocarbon and fluorocarbon solubility trends in various perfluorinated media [3, 4]. Additionally, they showed reduced H_2S solubility in materials containing elevated fluorine concentrations. In the case of rubbery perfluoroelastomer TFE/PMVE 49, which is based on tetrafluoroethylene, H_2S solubility was lower than CO_2. Higher CO_2 solubility was also shown in Cytop®, a high free volume, highly fluorinated glassy polymer [5]. They attributed such unusual behavior to "unfavorable" interactions between H_2S and the fluorinated polymers, however, no attempt was made to describe the nature of these interactions. Because DAM and TmPDA are non-fluorinated, H_2S solubility and thus H_2S/CH_4 permselectivity was expected to increase by substitution of fluorinated 6FpDA with non-fluorinated diamines. This strategy for simultaneously increasing permeability

and selectivity by increasing polymer free volume and penetrant solubility was cited by Freeman and coworkers as one of two methods for developing materials with a performance tradeoff closer to the upper-bound [6].

5.2. Material Development

The chemical structure of 6F-PAI-1 and the two new materials, 6F-PAI-2 and 6F-PAI-3, is given in Table 5.1. All structures were synthesized using a two-step reaction scheme as outline in chapter 3. It should be noted that the polyamide-imide backbone can also be modified by changing the amino-benzoic acid which forms the imide bond, however in this work, only the amide diamine was probed due to the easier synthetic route involved.

Table 5.1: Chemical structure of polyamide-imides synthesized in this work.

	R=	Polymer/Diamine
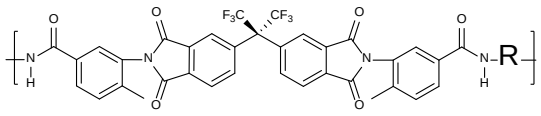 6FDA-3ABA	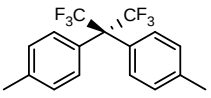	6F-PAI-1/ 6FpDA
	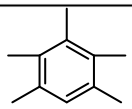	6F-PAI-2/ DAM
	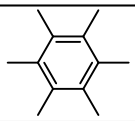	6F-PAI-3/ TmPDA

FTIR-ATR was used to confirm imide bond formation in the intermediate diacid 6FDA-3ABA as well as preservation of this bond after polycondensation. IR spectra are shown in Figure 5.2.A-D and 5.3. Symmetric and asymmetric imide stretches are shown

between 1700 and 1800 cm^{-1} in Figure 5.2 for the polymers as well as the intermediate diacid in 5.2-D. Additionally, a carbonyl stretch from the acid group of 6FDA-3ABA, which appears as a shoulder to the right of the imide peak, is shown around 1680 cm^{-1} in Figure 5.2-D and confirms formation of the intermediate diacid. Formation of the amide bond during polycondensation is supported by the amide carbonyl stretch near 1660 to 1675 cm^{-1} in Figure 5.2-A-C, as well as the amide N-H stretch centered around 3350 cm^{-1} in Figure 5.3. The broad range of wavenumbers covered by this peak is due to the N-H groups that are hydrogen bonded to varying extents, and qualitatively supports the existence of interchain hydrogen bonding.

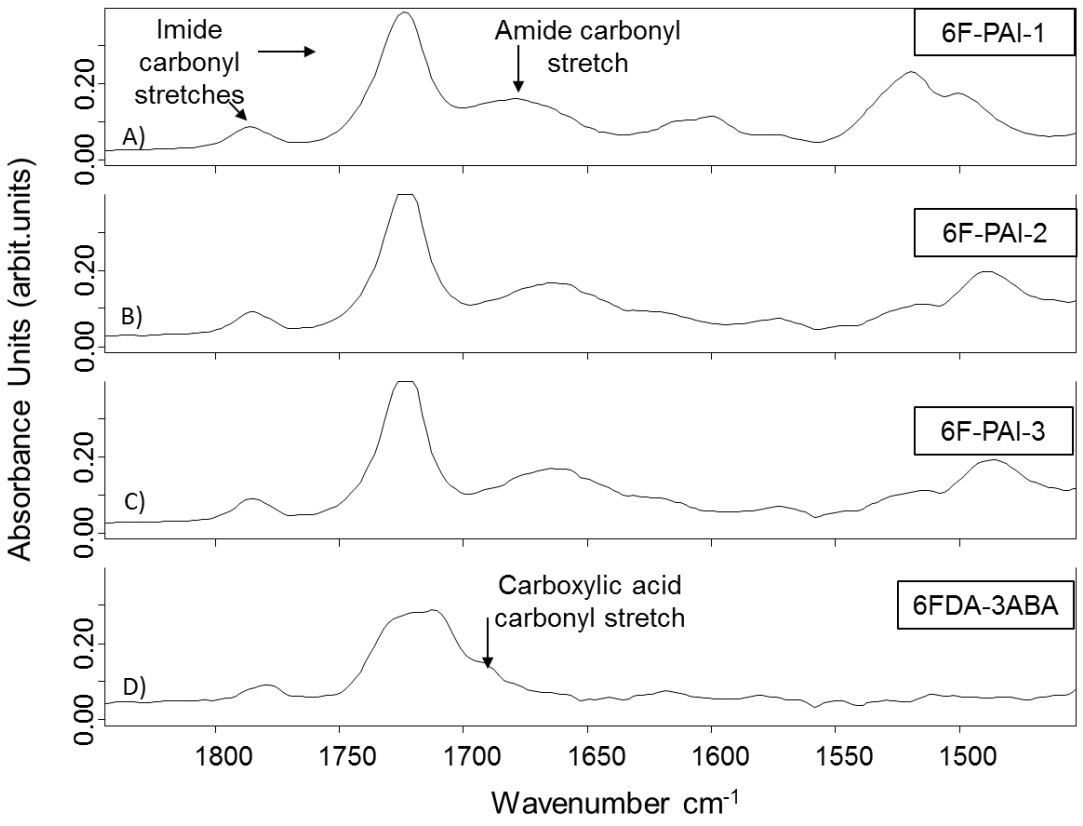

Figure 5.2-A-D: FTIR-ATR spectra for 6FDA-3ABA and 6F-PAI polymers in the 1400 to 1800 cm^{-1} range.

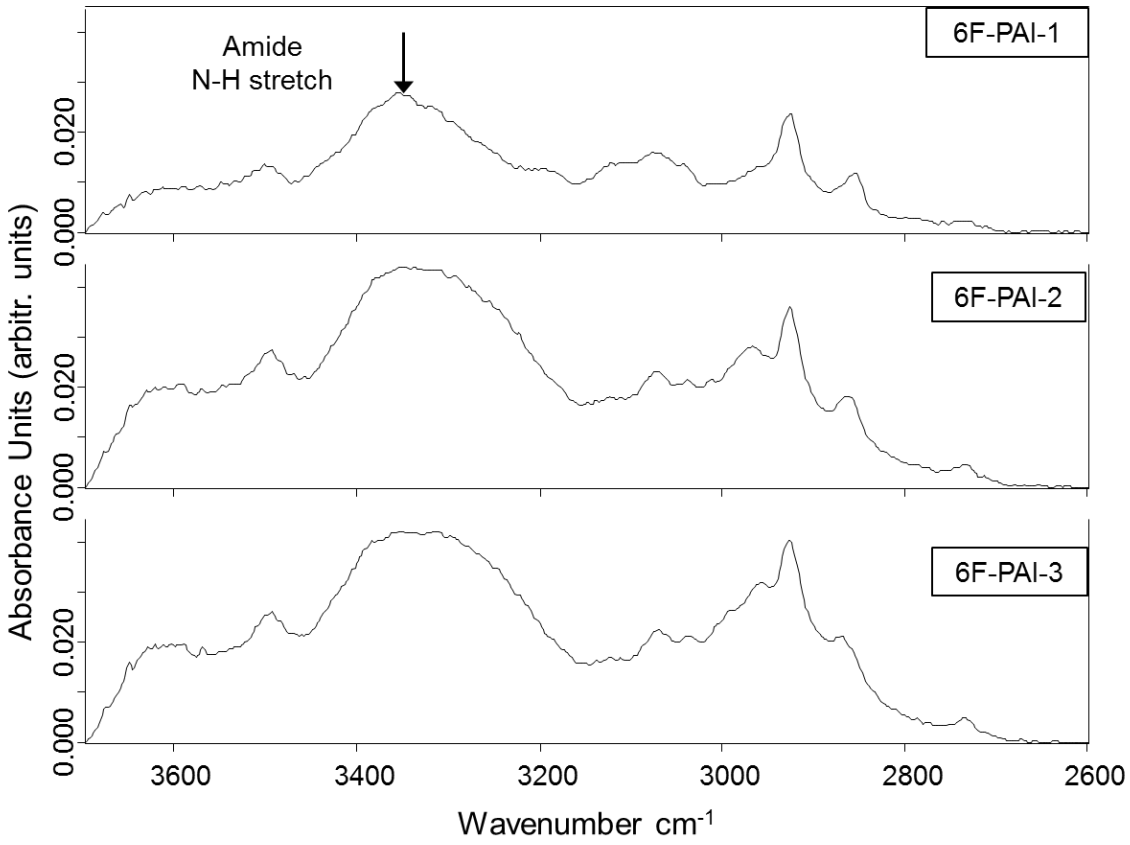

Figure 5.3: FTIR-ATR spectra for 6F-PAI polymers in the 2600 to 4000 cm^{-1} range.

5.3. Physical Structure Characterization

5.3.1. Inter/Intramolecular Charge Transfer

In this dissertation, *intramolecular* conjugation refers to electron transfer across two to three groups of bonded atoms within the same polymer chain, such as conjugation of non-bonded electrons with a phenyl ring to which the atom containing the lone pair electrons is bonded to. *Intermolecular* conjugation represents sharing of electrons, such as pi electrons of an aromatic ring or non-bonded electrons on one polymer chain with a neighboring polymer chain such as in the pi-pi stacking complexes discussed in section 2.5 of Chapter 2. It is difficult to decouple changes to intra and intermolecular

conjugation using solid state spectroscopic methods. Therefore, dilute solution state UV-Vis, which effectively "washes" out intermolecular interactions between adjacent polymer chains, is used to analyze changes in *intra*molecular charge transfer. These results are presented section 5.3.11. Solid state fluorescence spectroscopy is performed to determine changes associated with intermolecular charge transfer, and is discussed afterwards in section 5.3.1.2.

5.3.1.1. UV-Vis Spectroscopy

Differences in intrinsic *intramolecular* electron conjugation across the polymer backbone were characterized using solution state UV-Vis spectroscopy. Since 6F-PAI-1,2 and 3 differ only by the diamine forming the amide bond, differences in intramolecular conjugation most likely arise from differences in conjugation over this bond. Measurements were made in dilute solutions of DMF in order to avoid intermolecular interactions and only show differences in intrinsic conjugation across the polymer backbone.

Figure 5.4 displays UV absorption spectra for 6FDA-3ABA, 6F-PAI-1, 2 and 3, Torlon®, and the individual diamine monomers 6FpDA and DAM. TmPDA is not shown, however, it is expected to show a similar absorbance spectra as DAM.

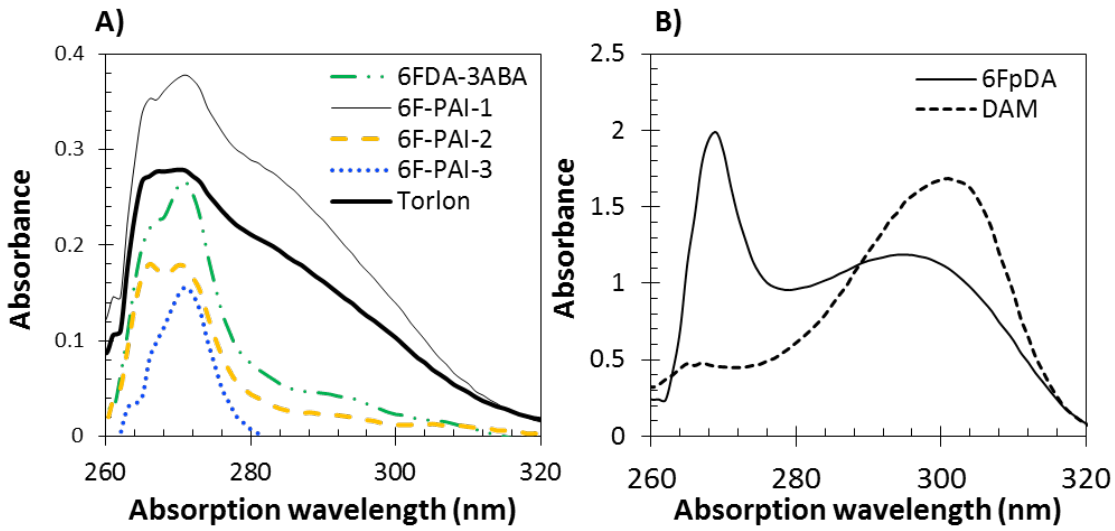

Figure 5.4: UV-Vis spectra for **A)** 6F-PAI polymers, 6FDA-3ABA and Torlon® and **B)** 6FpDA and DAM monomers.

The two absorption maxima for each plot shown in Figure 5.4-B are due to the pi electrons of the aromatic rings and non-bonded electrons of the amine nitrogen, respectively. The non-bonded electrons associated with the amine functional group can donate to the aromatic ring, which results in a red-shift in absorption wavelength. This also contributes to a broad distribution of absorption wavelengths due to varying extents of conjugation in the individual monomers. In Figure 5.4-A, 6F-PAI-2 and 3 show absorption maxima around 270 nm followed by a sharp decrease in absorption at higher wavelengths. 6F-PAI-3 does not absorb beyond 280 nm. This means that the absorption associated with the non-bonded electrons of the diamines in Figure 5.4-B is blue shifted in Figure 5.4-A, suggesting reduced conjugation of the non-bonded electrons of the nitrogen atom with the adjacent phenyl ring. The effect is much more pronounced in 6F-PAI-3, which does not absorb beyond 280 nm. Pendent methyl groups attached ortho to the amide nitrogen in DAM and TmPDA can cause steric repulsions with neighboring atoms. Such steric interactions can induce rotation of the phenyl ring and misalignment of

the pi-electron orbitals between nitrogen and the aromatic ring. In order for conjugation to occur, the pi-electron orbitals must overlap. Hence, blue shifting of the non-bonded electrons associated with nitrogen suggest rotation around this bond occurs in 6F-PAI-2 and 3 as a result of steric interactions induced by pendent methyl groups.

Because 6F-PAI-1 and Torlon® are free of such ortho pendent groups, conjugation of the lone pair electrons associated with nitrogen with the phenyl ring may occur more easily over this bond. This is supported by the shoulder peak in the absorption spectra of 6F-PAI-1 and Torlon® in Figure 5.4-A, which has a maxima near 286 and extends beyond the cutoff absorptions for 6F-PAI-2 and 3. A comparison between 6FDA-3ABA and 6F-PAI-2 reveals almost identical spectra, and further suggests no change in conjugation results from addition of DAM to form the amide bond. 6F-PAI-3 shows an absorption cutoff near 280 nm, which is the lowest cutoff wavelength shown. Facile rotation of the phenyl ring around para connected TmPDA may reduce planarity around this bond even further relative to meta connected DAM. Rotation around meta connections require the cooperative movements of neighboring groups and are thus more hindered than similar para connections.

The UV-Vis results demonstrate the effect of bulky groups ortho to rotatable bonds on the intramolecular conjugation across the polymer backbone. Due to an absence of these bulky groups in 6F-PAI-1 and Torlon® , longer wavelengths of absorption are observed, which signifies that the phenyl rings associated with such rotatable bonds are more planar with neighboring groups. Although these electronic interactions occur on a localized scale, they can have a significant impact on the physical and transport properties of the bulk material, which will be discussed in the following sections.

5.3.1.2. Solid-State Fluorescence Spectroscopy

As previously discussed in chapter 4, differences in *inter*molecular conjugation, or CTCs, can arise in the solid state due to differences in steric interactions and chain packing. These differences can manifest in the light absorption and emission properties of solid materials. Although UV-Vis can be performed on solid films, fluorescence was used instead due to the difficulty in obtaining films thin enough to avoid saturation of the UV-Vis detector.

Figure 5.5 shows fluorescence excitation A) and emission B) spectra for 6F-PAI-1-3 as well as Torlon®. Excitation spectra were also carried out on 6FDA-6FpDA and 6FDA-DAM polyimides to illustrate differences in imide and amide bond sterics, and are also shown in 5.5-A. Both *polyimides* were thermally annealed at 200°C for 24 hours, which is similar to the conditions used for the polyamide-imides. 6FDA-TmPDA was not available at the time of this work, however, its fluorescence properties are expected to be very similar to 6FDA-DAM.

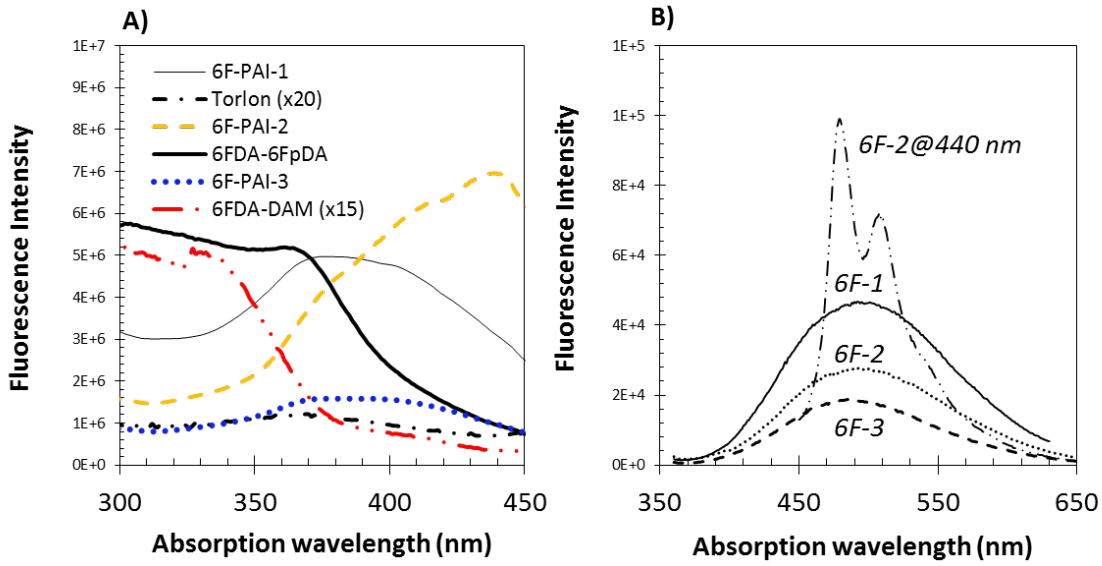

Figure 5.5: A) Fluorescence excitation spectra monitored at 500 nm and **B)** emission spectra excited at 350 nm. 6F-PAI-2 excited at 440 nm is also shown in **B)**

The excitation spectra in 5.5-A show a significant red-shift in the wavelength of maximum absorption in 6F-PAI-2, along with a change in the shape of this absorption peak. This signifies enhanced *intermolecular* CTC formation in this material relative to 6F-PAI-1 and 3, and is likely due to the meta connection in DAM. Meta connections have been shown to promote chain packing in the solid state relative to para connections [7- 9]. This was not expected to occur in the 6F-PAI series in this work due to the effect of the pendent methyl groups. Also, reduced planarity of the diamine phenyl ring around the amide bond in 6F-PAI-2, as supported in Figure 5.4, would be expected to interfere with chain packing and inhibit intermolecular CTC formation in the solid state. However, it appears that CTC formation is actually enhanced in 6F-PAI-2 relative to 6F-PAI-1 and 3. The reason for such behavior will be discussed in section 5.3.2.

For 6F-PAI-1, the longer wavelengths of UV-Vis absorption suggested increased electron conjugation and thus more planarity between phenyl rings of the diamine and the

amide bond. However, the bulky CF_3 groups along the main chain of 6F-PAI-1 likely inhibit close interaction of adjacent polymer chains that are necessary for pi-pi stacking in the solid-state. This likely contributes to lower wavelengths of fluorescence emission relative to 6F-PAI-2. For 6F-PAI-3, the UV-Vis spectra suggested that the planes of the amide bond and diamine phenyl ring of TmPDA did not overlap, thereby disrupting solid chain packing due to such non-planarity across the polymer backbone. In such a conformation, pi-pi stacking would also be hindered due to a similar effect of the bulky CF_3 groups in 6F-PAI-1. The similar bandwidth and shape of the fluorescence excitation spectra in 6F-PAI-1 and 3 suggest similar types and extents of intermolecular CTC formation. These results show that meta connections over an amide bond enhance the formation of intermolecular CTCs relative to para connected substituents bearing similar bulky substituent groups.

Fluorescence emission spectra of the polymers are shown in Figure 5.5-B. All materials show wavelengths of maximum emission around 490 nm when excited at 350 nm, confirming that the absorptions in the excitation spectra were due to a ground state CTC. The highest emission intensity, which occurs in 6F-PAI-1, is consistent with its increased absorbance intensity at 350 nm in Figure 5.5-A relative to 6F-PAI-2 and 3. 6F-PAI-2 was also excited at 440 nm, which resulted in an emission maximum shown in 5.5-B that is also centered around 490 nm, again demonstrating that the red-shift in its excitation spectra was due to the formation of a ground state CTC.

The excitation spectra in Figure 5.5-A for the analog polyimide, 6FDA-DAM, shows a blue shift in absorption maxima relative to 6FDA-6FpDA. This is due to increased steric interactions between the ortho methyl groups of DAM and nearby

carbonyl groups of 6FDA dianhydride. These steric interactions may cause cooperative reorientation of the diamine and dianhydride segments in order to reduce such interactions, leading to a repeat unit in 6FDA-DAM that is highly non-planar. These results suggest greater conformational freedom exists around the amide bond to reduce such steric repulsions, as the same diamine that increases CTCs when connecting an amide bond causes the reverse trend in CTCs when connected over an imide bond.

5.3.2. Characterization of the Physical and Thermal Properties

Table 5.2 shows the bulk density, glass transition temperature, free volume (V_f), fractional free volume (*FFV*), d-spacing, and dielectric constant (ε) for the 6F-PAI materials, Torlon®, and the analog polyimides. Free volume, fractional free volume and dielectric constant were predicted from group contribution methods [9]. d-spacing was calculated from the maximum intensity Bragg peak as shown in Figure 5.6.

Table 5.2: Physical properties of 6FDA polyamide-imides and the analog polyimides. *6FDA-DAM, 6FDA-TmPDA and Torlon data adapted Kim [10], Powell [2] and Teoh [11] et al.

Polyamide-imide	ρ (g/cc)	T_g (°C)	v_f (cc/mole)	FFV	d-spacing (Å)	ε
6F-PAI-1	1.3867	324	135	0.18	4.5	3.6
6F-PAI-2	1.3374	330	87	0.14	6.3	4.1
6F-PAI-3	1.3281	350	84	0.13	6.3	4.0
Torlon®*	1.3550	295	70	0.15	4.2	5.3
Analog Polyimides						
6FDA-6FpDA	1.4660	320	80	0.17	5.9	3.3
6FDA-DAM*	1.3342	395	79	0.19	6.3	3.4
6FDA-TmPDA*	1.3247	420	80	0.19	6.3	3.4

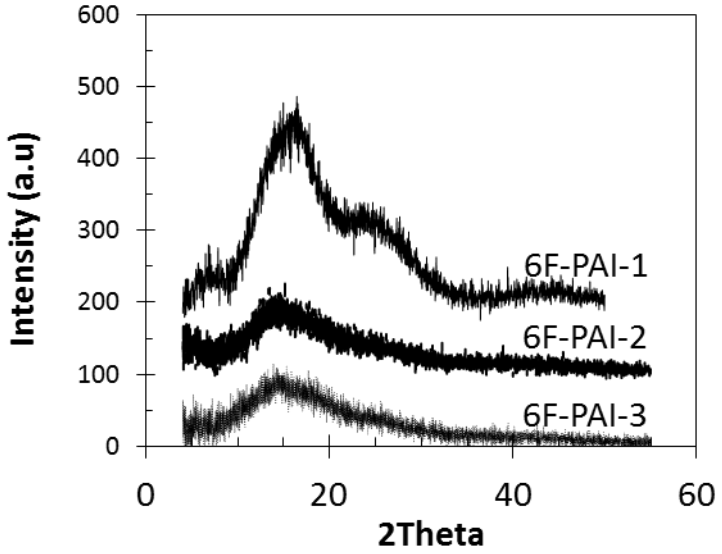

Figure 5.6: X-ray diffraction patterns for 6F-PAI polyamide-imides.

The trends in T_g shown in Table 5.2 are similar for both sets of materials. Incorporation of bulky substituents, such as pendent methyl groups, into the polymer causes an increase in T_g. Polyamide-imides and polyimides containing TmPDA show the highest T_g for both types of materials. This is due to the pendent methyl groups, which may interfere with the motions of atoms in the surrounding environment and thus increase the energy required for cooperative chain motions. Substituents bearing a kink in the central carbon atom, such as the isopropylidene carbon in 6FpDa, have increased mobility along the main chain, and materials containing such groups show the lowest T_g.

Polymer free volume and fractional free volume decrease in *polyamide-imides* containing DAM and TmPDA relative to 6FpDA, which is surprising considering an increase in free volume occurs for *polyimides* containing DAM and TmPDA relative to 6FpDA. Apparently, DAM and TmPDA increase chain packing when connected over *amide* bonds, whereas the opposite is true when connected over an *imide* bond. Although

unexpected, this trend in the polyamide-imides agrees with trends reported by Fritsch and coworkers, who observed He permeabilities that were *2x* lower in materials containing rigid and linear diamines similar to DAM and TmPDA over an amide bond compared to 6FpDA [12]. They suggested the rod-like shape of such linear diamines contributes to an increase in chain packing relative to kinked, less linear 6FpDA. In our work, the pendent ortho methyl groups associated with more linear DAM and TmPDA were expected to prevent chain packing by inducing rotation around the amide nitrogen-phenyl bond and subsequently disrupting planarity along the main chain. The UV-vis data supported this hypothesis, as longer wavelengths of absorption were observed for 6F-PAI-1 relative to 6F-PAI-2 and 3. This suggested conjugation between the amide nitrogen and the phenyl ring of DAM and TmPDA was hindered due to such non-planarity between the planes of the amide bond and phenyl ring. However, the fractional free volume and subsequent sorption and permeation data suggest that DAM and TmPDA *increased* chain packing in the solid state relative to 6FpDA connected 6F-PAI-1, while the opposite occurs in the polyimides. The discrepancy between the trends in free volume and fluorescence data between polyimides and polyamide-imides is likely due to greater conformational degrees of freedom between the imide and amide bonds. Consider Figure 5.7, which depicts the rotational degrees of freedom around the imide and amide bond.

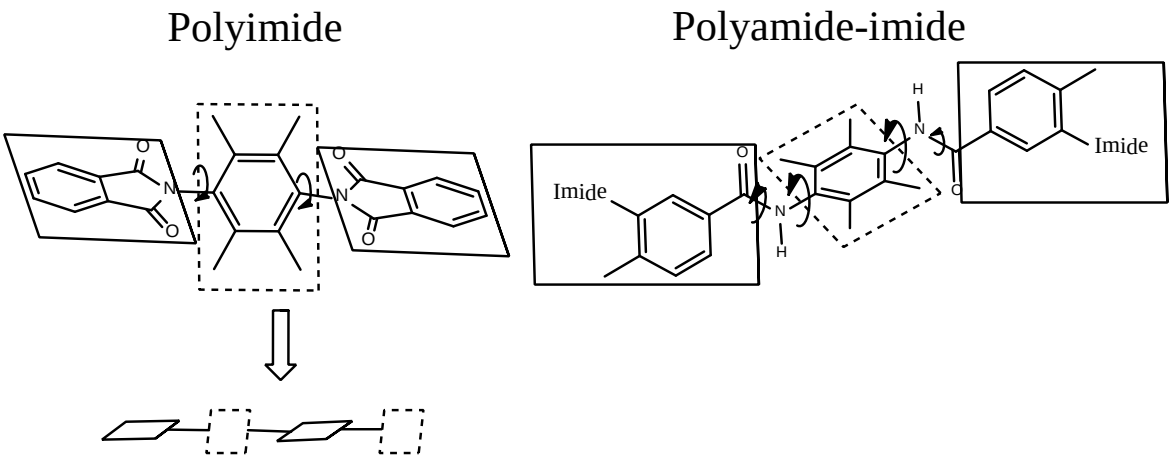

Figure 5.7: Depiction of imide and amide bond dynamics.

The only conformational degree of freedom available to reduce steric interactions between the pendent methyl groups ortho to the N-C *imide* bond is rotation of the phenyl ring so that it no longer overlaps with the planes of the dianhydride. This results in a repeating conformation of non-planar moieties across the polyimide backbone. In the amide bond, not only can phenyl ring rotation occur, but rotation around the N-C=O bond can also occur. This results in greater conformational freedom for substituents around the amide bond to reduce steric interactions. Therefore, when more linear, rod-like diamines such as DAM and TmPDA are connected over the *amide bond* as compared to kinked 6FpDA, chain packing is increased, while sterics prevent such chain packing over the *imide bond*. It appears that bulky substituents along the main chain, such as the CF_3 groups associated with 6FpDA, *hinder* chain packing over the *amide* bond to a greater extent than pendent groups such as the methyl groups associated with DAM and TmPDA. For the *polyimides*, the highly non-planar conformation induced by rotation around the

N-C imide bond is believed to *inhibit* chain packing to a greater extent than CF_3 groups along the main chain. Hence, DAM and TmPDA connected *polyimides* show *reduced* chain packing and *higher* permeabilities than their 6FpDA analog.

The calculated dielectric constants in Table 5.2 increase in 6F-PAI-2 and 3. This correlates with reduced fluorine concentration in these materials. Consequently, non-fluorinated Torlon® has the highest predicted dielectric constant. This value is related to the ability of the electrons along the polymer backbone to be distorted by an external field, or similarly, the presence of polar penetrant molecules. Higher dielectric constants are associated with increased hydrophilicity due to an increase in dipole induced-dipole interactions [13]. Because H_2S is polar, such interactions are expected to enhance its sorption. This will be discussed in more detail in section 5.4.3.

The X-ray diffraction patterns in Figure 5.6 reveal amorphous structures for all three polyamide-imides. A slight increase in d-spacing is shown in 6F-PAI-2 and 3 despite having lower predicted free volumes. An increase in d-spacing is also not consistent with 6F-PAI-2's fluorescence spectra, which suggested an increase in chain packing due to increased CTC formation. Similar inconsistencies in d-spacing and free volume in polyamide-imides were reported by Nagel et al. [7]. They measured lower d-spacing in materials with higher permeabilities. The average size of free volume holes, as measured through positron annihilation spectroscopy (PALS), was shown to be higher in the same materials with lower d-spacing. Thus d-spacing may not provide an adequate correlation with the transport properties in polyamide-imides. However, it is still quite useful in comparing the crystallinity or lack thereof in these materials.

The relatively more simple to describe polyimides show higher d-spacing in 6FDA-DAM and 6FDA-TmPDA relative to their 6FpDA analog, which is consistent with their trends in fluorescence and calculated free and fractional free volume. In summary, the different steric interactions and bond geometries around amide and imide bonds cause marked differences in chain packing when similar diamines are incorporated over such bonds. This results in drastic differences in the gas transport properties between DAM and TmPDA polyamide-imides and polyimides, which will be the topic of the remainder of this chapter.

5.4. Pure Gas Transport Characterization

5.4.1. Single Gas Permeation

While industrially attractive materials need to have both high permeability and selectivity, overall operational costs for natural gas separations can be more heavily weighted by loss of the product gas, CH_4 in the downstream [14, 15]. Therefore, membrane selectivity may be an even more important factor in determining the overall economic attractiveness of membrane process. Even more important is the ability of the membrane to maintain such high selectivity under the aggressive conditions that occur at a natural gas wellhead. However, for screening purposes, the intrinsic separation properties, as measured by pure gas experiments, are more convenient to obtain. The pure gas permeabilities and ideal selectivities for CO_2, CH_4, and H_2S are reported in Table 5.3 and 5.4, respectively. Carbon dioxide and methane data for the analogue polyimides are also shown for comparison. Hydrogen sulfide was not measured in the polyimides because of their susceptibility to plasticization. All H_2S data shown for the polyamide-imides was measured at 35 psia to prevent these effects.

Table 5.3: Pure gas permeabilities for 6F-PAI-1,2 and 3, Torlon®, and the analog polyimides. Measurements were made at 35°C and between 35-65 psia.
**Data adapted from Sridhar et al.*[1].
Permeabilities are reported in units of Barrer.

Polyamide-imide	P_{CO2}	P_{CH4}	P_{H2S}
6F-PAI-1	33	0.78	6.3
6F-PAI-2	12	0.23	2.7
6F-PAI-3	21	0.43	4.6
Torlon®	0.69	14×10^{-3}	0.19
Polyimides			
6FDA-6FpDA	46	1.5	nd
*6FDA-DAM**	350	18	nd
*6FDA-Durene**	456	28	nd

Table 5.4: Ideal permselectivities for 6F-PAI polymers, Torlon®, and the analog polyimides. Measurements were made at 35°C and between 35-65 psia.
**Data adapted from Sridhar et al*. [1].

Polyamide-imide	P_{CO2}/P_{CH4} *(Ideal Selectivity)*	P_{H2S}/P_{CH4} *(Ideal Selectivity)*
6F-PAI-1	42	8.1
6F-PAI-2	50	12
6F-PAI-3	48	11
Torlon®	49	14
Polyimides		
6FDA-6FpDA	30	nd
*6FDA-DAM**	20	nd
*6FDA-Durene**	16	nd

Consistent with lower free volume and increased chain packing that was shown in Table 5.2, permeabilities of all three gases are lower in the DAM and TmPDA connected polyamide-imides relative to their 6FpDA analogue. However, both CO_2/CH_4 and H_2S/CH_4 permselectivity are higher in 6F-PAI-2 and 3. Interestingly, CO_2/CH_4 selectivity is the same for Torlon® as it is in 6F-PAI-2 and 3, however, permeabilities in the fluorinated materials are over an order of magnitude higher. This promising result demonstrates the ability to increase permeability while preserving selectivity through incorporation of bulky groups such as CF_3 onto the polymer backbone. In fact, incorporation of such groups into the main chain of gas separation polymers has advanced the state-of-the-art for pure polymers over the past decade into a high performance, solution processible material that approaches Robeson's upper bound.

A comparison between the permeabilites and selectivities between the polyamide-imides and polyimides shown in Table 5.3 and 5.4 reveals a striking difference between the two types of materials. Substitution of 6FpDA for DAM and TmPDA in the polyimides causes the exact opposite trend in permeability and selectivity than what is shown in the polyamide-imides. Carbon dioxide and methane permeability are substantially increased in 6FDA-DAM and 6FDA-TmPDA. This can be explained by the effect of the pendent methyl groups in DAM and TmpDA, which induces rotation around the imide bond and consequently disrupts planarity across the polymer backbone. Such a conformation leads to a reduction in chain packing and increased free volume. As a consequence of lower chain packing, reduced selectivity accompanies the large increases in permeability. It would be interesting to study the effect of an additional pendent methyl group at the other ortho position of 3-aminobenzoic acid in the polyamide-imides.

This could potentially cause similar disruptions in chain packing as demonstrated in the polyimides, leading to increased gas permeabilities. However, no amino-benzoic acid monomers containing such a configuration were available at the time of this work. Other potential synthetic modifications to the 6FDA polyamide-imides will be discussed in Chapter 8.

5.4.2. Pure Gas Diffusivities

Breaking down the permeability coefficient into sorption and diffusion components can provide additional insight into the differences in free volume and polymer chain mobility between the different polymers. The sorption contribution to permeability, which will be discussed in section 5.4.3, provides information on polymer free volume and polymer-penetrant interactions within the polymer matrix, while analysis of the diffusion coefficients provides insight into both free volume and mobility of the polymer chains. Single gas diffusion coefficients were calculated from the permeation time-lag as outlined in Chapter 3, and are shown in Table 5.5.

Table 5.5: Single gas diffusivities at 35°C and 35-65 psia for 6FDA polyamide-imides and Torlon®.
Diffusion coefficients given in units of cm^2/s
All H_2S values were measured at 35 psia to prevent plasticization.

Polyamide-imide	D_{CO2} ($x10^8$)	D_{CH4} ($x10^8$)	D_{H2S} ($x10^8$)	D_{CO2}/D_{CH4}	D_{H2S}/D_{CH4}
6F-PAI-1	1.8	0.19	0.18	9.8	0.91
6F-PAI-2	1.0	0.10	0.10	9.9	0.91
6F-PAI-3	1.1	0.12	0.12	9.2	0.97
Torlon®	8.9×10^{-2}	9.8×10^{-3}	7.8×10^{-3}	9.1	0.79

As can be seen in Table 5.5, reductions in CO_2, CH_4, and H_2S permeability in 6F-PAI-2 and 3 can be partially attributed to a decrease in the penetrant diffusion coefficients. In 6F-PAI-2, CO_2 and CH_4 diffusivity decreased to the same extent, thus no significant effect on the diffusion selectivity is observed. For 6F-PAI-3, CO_2/CH_4 diffusion selectivity is only slightly lower than the original 6FpDA based material. These reductions in diffusivity are due to increased chain packing as a result of the meta connected DAM and rigid, rod-like TmPDA. Interestingly, the CO_2/CH_4 diffusion selectivity in 6F-PAI-1 is the same as 6F-PAI-2 despite 6F-PAI-1 showing diffusion coefficients that are almost double that shown in the latter material. This is again due to the effect of the bulky CF_3 groups in 6FpDA, which act to reduce chain packing while preserving rigidity. This effect is also demonstrated by comparing diffusion coefficients in all three 6F-PAI materials to Torlon®. Diffusivities in the 6FDA based materials are over an order of magnitude higher than Torlon, however, diffusion selectivities are essentially the same. Such promising results demonstrate the utility of the 6FDA dianhydride combined with rigid, packing inhibiting monomers such as 6FpDA, DAM, and TmPDA for enhancing diffusion flux while maintaining high mobility discrimination.

Contrary to the effect that was anticipated by incorporating DAM and TmPDA into backbone, H_2S/CH_4 diffusion selectivity was unchanged in 6F-PAI-2 and only marginally higher in 6F-PAI-3. Torlon®, which is non-fluorinated and has the highest calculated dielectric constant, shows the lowest H_2S/CH_4 diffusion selectivity, which is well below 1. It appears that H_2S diffusion is governed by additional factors other than its kinetic diameter. It is hypothesized that polar interactions with the polymer add an

additional energy barrier that must be overcome for H_2S to execute a diffusion jump. This may be the reason for the reversed and very low H_2S/CH_4 diffusion selectivity in Torlon®, as well as all other glassy materials shown in this work. Such complex diffusion for H_2S is in contrast to CH_4 and other non-interacting gases, whose frequency of diffusion jumps is controlled mainly by the size of a transient gap that must be created within the polymer chains. Similar anomalous behavior in diffusivity was demonstrated in CO_2 and O_2 by Wang and coworkers, who observed higher D_D values for O_2 despite having a larger kinetic diameter [16]. Testing and verification of this hypothesis regarding H_2S diffusion will be the subject of chapter 6.

5.4.3. Equilibrium Sorption Analysis

Sorption isotherms for CO_2, CH_4 and H_2S in the 6F-PAI series were measured using a pressure-decay technique as described in Chapter 3. Analysis of the sorption isotherms and subsequent dual-mode parameters provides additional insight into free volume and chain packing beyond what was predicted by simple group contribution methods given in Table 5.2. Concentration versus pressure isotherms for CH_4, CO_2, and H_2S are shown in Figures 5.8-5.10, respectively. The dual-mode sorption parameters were obtained by fitting the concentration vs. pressure isotherms to the dual-mode sorption model, and are reported in Table 5.6. In most cases, adequate fits of the experiment data to the model were obtained as demonstrated by the solid lines in the figures. For 6F-PAI-3, swelling in the H_2S isotherm beyond 100 psia made it difficult to fit the data. Swelling is signified by an upswing in the concentration isotherm that is

concave to the concentration axis. In this case, only qualitative observations on the dual-mode parameters can be made.

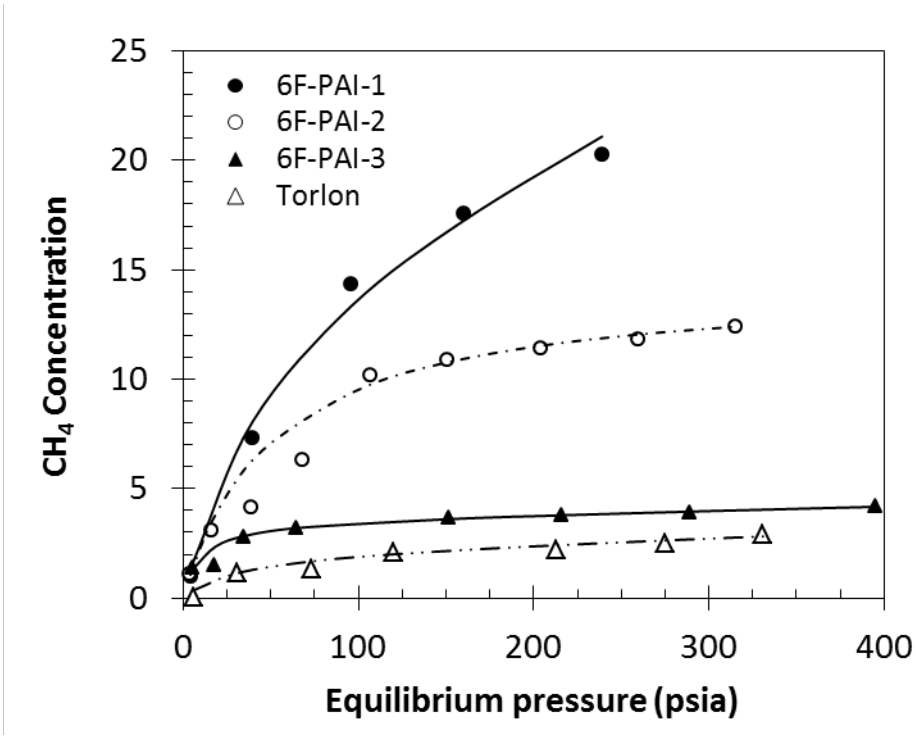

Figure 5.8: CH_4 concentration vs. pressure at 35°C for 6F-PAI-1,2 and 3 and Torlon®. *Units of concentration are cc(STP)/(cc·polymer).*

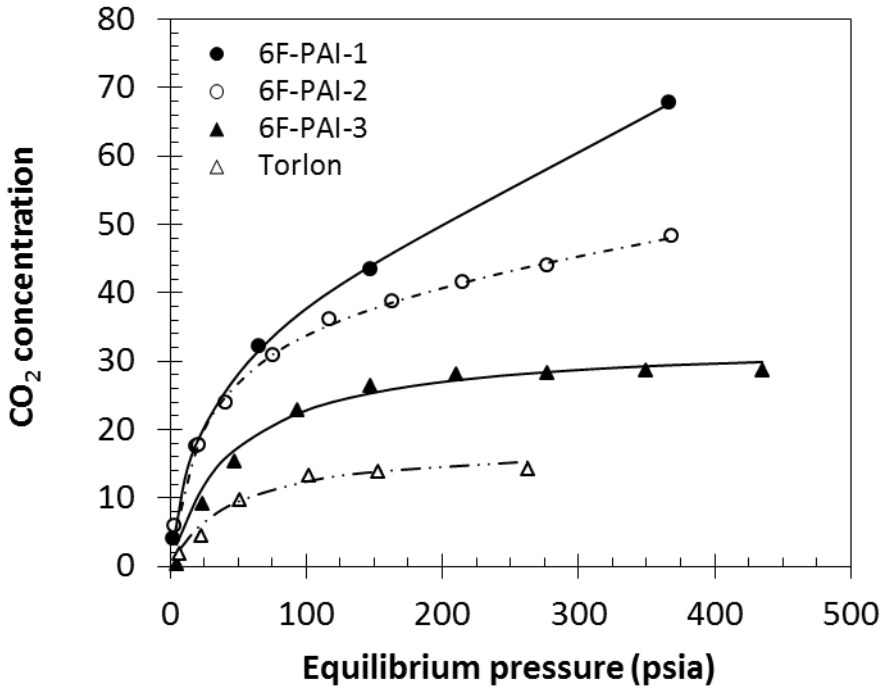

Figure 5.9: CO_2 concentration vs. pressure at 35°C for 6F-PAI-1, 2 and 3 and Torlon®. *Units of concentration are cc(STP)/(cc·polymer).*

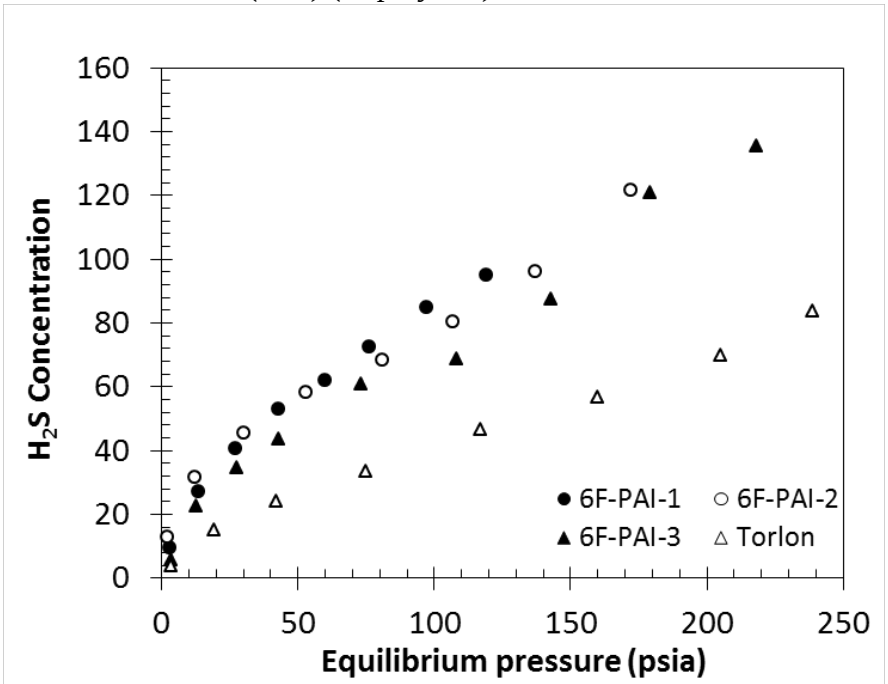

Figure 5.10: H_2S concentration vs. pressure at 35°C for 6F-PAI-1, 2 and 3 and Torlon®. *Units of concentration are cc(STP)/(cc·polymer).*

Table 5.6: Dual-mode parameters at 35°C.
*H_2S parameters were not calculated due to membrane swelling at higher pressures.
†These values were estimated manually due to the non-linear least squares fitting program assigning very low values of less than 10^{-5}.

	CO_2			CH_4			H_2S		
	k_D cc(STP)/cc·psia	C_H' cc(STP)/cc	b psia^{-1}	k_D cc(STP)/cc·psia	C_H' cc(STP)/cc	b psia^{-1}	k_D cc(STP)/cc·psia	C_H' cc(STP)/cc	b psia^{-1}
6F-PAI-1	0.12	31	0.05	0.03	15	0.02	0.53	40	0.07
6F-PAI-2	0.04	35	0.04	†3×10^{-4}	14	0.02	0.42	35	0.23
*6F-PAI-3**	†1.0×10^{-3}	35	0.02	†1.0×10^{-3}	3.5	0.10	-	-	-
Torlon®	5×10^{-4}	18	0.02	3×10^{-3}	2.1	0.03	0.28	17	0.06

Analysis of Figures 5.8 and 5.9 reveal lower CH_4 and CO_2 sorption in 6F-PAI-2 and 3 relative to 6F-PAI-1. Thus, reduced permeability in these materials can also be attributed to reduced CO_2 and CH_4 sorption capacity. The disparity in absorbed penetrant concentration is more apparent at higher pressures, and is reflected by a significantly lower Henry's Law parameter, k_D, for both CO_2 and CH_4 in the DAM and TmPDA based materials. In fact, k_D for CO_2 and CH_4 in 6F-PAI-3 as well as CH_4 in 6F-PAI-2 could only be estimated manually as the non-linear least squares fitting program assigned values to this parameter that were less than 10^{-5}. Therefore, their actual values are *not significant* beyond the fact that they are *extremely low relative* to 6F-PAI-1. This surprisingly low sorption in the idealized Henry's Law environments for 6F-PAI-3 was not anticipated based on its diffusion and permeability data presented previously. However, total free volume, as predicted in Table 5.2, was shown to be lower in 6F-PAI-3 relative to 6F-1 and 2. This reduces the space available for accommodation of a penetrant molecule, which results in reduced sorption capacity for 6F-PAI-3. The diffusion coefficients on the other hand depend on the distribution of free volume as well

as the cohesive energy density of the polymer. Enhanced CTC formation in 6F-PAI-2 likely increases the cohesive energy density and restricts polymer chain mobility, which would result in lower penetrant diffusivities. Additionally, the formation of CTCs has been shown by past researchers [17], as well as in Chapter 4 of this dissertation, to increase k_D and significantly change the local packing structure of the polymer matrix. Such phenomena may help to explain the discrepancy between diffusivity and sorption capacity in 6F-PAI-2 and 3. Furthermore, these unexpected results highlight the complex nature of polyamide-imides versus polyimides as has been the general theme of Chapters 4 and 5.

No significant trend in C_H' for CO_2 can be inferred in either of the three fluorinated materials. For 6F-PAI-3, C_H' for CH_4 is much lower relative to 6F-PAI-1 and 2. This increases the CO_2/CH_4 and H_2S/CH_4 sorption selectivity. This increase is attributed to the higher permselectivity for these gas pairs in 6F-PAI-3 relative to 6F-PAI-1. An increase in sorption selectivity for both gas pairs in 6F-PAI-2 is also the main reason for higher permselectivity.

The CO_2 and CH_4 sorption results in the previous discussion show that the structure of the diamine forming the tail-tail connection in polyamide-imides affects the "equilibrium" packed region of the microstructure to a much greater extent than the excess free volume packing defects. It can be concluded that incorporation of more linear and rigid diamines into an amide bond causes an increase in chain packing. Such an increase is significantly more pronounced in the idealized Henry's Law environments, which leads to lower sorption in the 6F-PAI-2 and 3.

A comparison of 6F-PAI-1, 2 and 3 with Torlon® reveals higher sorption capacity for all gases in the fluorinated polyamide-imides, which can be attributed to lower Langmuir capacity as well as Henry's Law type sorption in Torlon®. The more linear backbone and absence of bulky substituents in non-fluorinated Torlon® leads to a more densely packed microstructure, which in turn leads to very low penetrant sorption and diffusion. Therefore, incorporation of rigid, packing inhibiting groups such as in the 6F-PAI series can remarkably improve sorption and diffusion without sacrificing selectivity.

The H_2S isotherms in Figure 5.10 show similar H_2S concentrations in 6F-PAI-1, 2 and 3, which is interesting considering CO2 and CH4 capacity was much lower in 6F-PAI-2 and 3 compared to 6F-PAI-1. Inspection of the dual-mode parameters shows that the difference in k_D for H_2S between 6F-PAI-1 and 2 is not nearly as large as it was for CO_2 and CH_4. The Henry's parameter could not be determined for 6F-PAI-3 due to the early onset of swelling. Nevertheless, because the H_2S concentration isotherm for 6F-PAI-3 shows swelling at higher pressures, H_2S sorption in the "dissolved" modes may also be enhanced relative to the significantly reduced CO_2 and CH_4 capacity in this material. Because DAM and TmPDA are non-fluorinated, the densely packed regions of 6F-PAI-2 and 3 likely have lower fluorine concentration. Despite the increase in chain packing caused by these diamines, which is supported by a very value of k_D for CO_2 and CH_4, H_2S sorption appears to be effected by such increases in chain packing to a much lower extent than were CO_2 and CH_4. Because of this phenomena, H_2S/CH_4 solubility selectivity is increased in 6F-PAI-2 and 3 relative to 6F-PAI-1. High electronegativity in fluorine coupled with its short atomic radius reduces the ability of the surrounding valence electrons to be distorted by an external field, thus reducing polarizability around

the C-F bond. This is supported by higher dieletric constants in 6F-PAI-2 and 3, both of which have lower fluorine concentration relative to 6F-PAI-1. Hougham et al. also showed decreasing dielectric constant with increasing fluorine content in a series of polyimides with varying fluorine concentrations, and attributed this trend in part to a reduction in polarizability [13]. It is interesting to note that H_2S/CH_4 sorption selectivity was the highest in Torlon®. This is due to the combined effects of lower free volume, which reduces CH_4 sorption, and the absence of fluorine, which contributes to more favorable interactions between H_2S and the polymer. These results suggest that H_2S sorption is more dependent on physiochemical interactions with the polymer than is the sorption of CO_2 and CH_4, which depends mainly on polymer free volume. While these results are promising in that higher H_2S/CH_4 selectivity was achieved in 6F-PAI-2 and 3, the impact of this effect on the H_2S plasticization resistance and ternary mixed gas separation performance was not as favorable. Carbon dioxide and hydrogen sulfide plasticization resistances will be discussed in the next section, while the implications on the mixed gas performance will be the topic of Chapter 7.

5.4.4. Pure Gas Plasticization Analysis

5.4.4.1. Analysis of CO_2 Plasticization Resistance

Pure gas plasticization resistance provides a measure of the intrinsic stability of a material towards increasing concentrations of high activity penetrants. Figure 5.11 and shows CO_2 permeability vs. pressure isotherms at 35°C for 6F-PAI-1,2 and 3, as well as Torlon®. Similar to the procedure discussed in Chapter 4, the permeability at each

pressure beyond the plasticization pressure was measured after approximately 12 hours of elapsed permeation time.

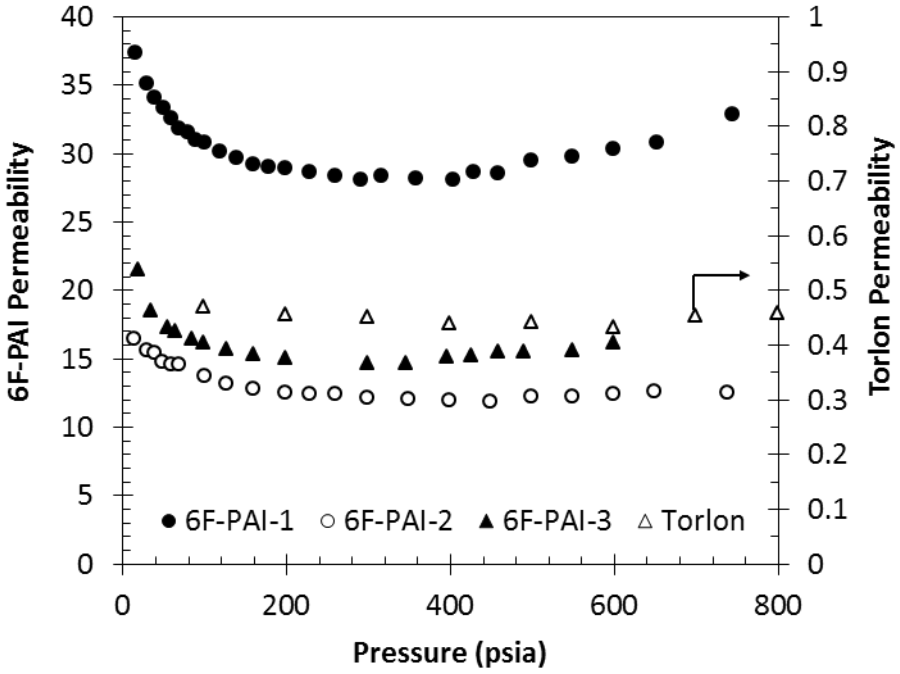

Figure 5.11: Pure gas CO_2 permeability vs. pressure isotherms at 35°C. CO_2 permeability vs. pressure in Torlon® was estimated from permeance data given in Kosuri's work [18]. A thickness of 0.55 μm was used to estimate the permeability from permeance measurements.
Units of permeability are Barrer.

It can be concluded from Figure 5.11 that all polyamide-imides show exceptionally high plasticization resistance against CO_2. Additionally, for all materials, the increase in CO_2 permeability at the highest pressure measured is less than 12% for all materials. This indicates good control against glassy relaxations induced from high concentrations of CO_2 sorbed into the membrane. These results demonstrate significant improvements in plasticization suppression over CA and Matrimid®.

Carbon dioxide concentration in 6F-PAI-3 at its plasticization pressure near 360 psia is approximately 30 cc(STP)/(cc·polymer), as inferred from the dual-mode parameters. This concentration is very close to its Langmuir capacity of 35 cc(STP)/(cc·polymer) and suggests that plasticization occurs when the Langmuir sorption sites become saturated and additional sorption takes place mainly in the densely packed regions after this point. This is also inferred by the linearity in the sorption isotherms at this pressure in Figure 5.9. In order to accommodate additional penetrant in this environment, increased space in the densely packed polymer chains must be created, which leads to swelling of the chains and an increase in permeability.

6F-PAI-1 shows plasticization beginning near 430 psia. This corresponds to a total CO_2 concentration of approximately 78 cc(STP)/(cc·polymer) and a Langmuir concentration of ~30 cc(STP)/(cc·polymer). Similar to 6F-PAI-3, the Langmuir sorption sites are essentially saturated prior to the onset of plasticization. However, in 6F-PAI-1, total CO_2 concentration is much higher than its Langmuir concentration, indicating a significant amount of penetrant is sorbed in the densely packed regions prior to plasticization. This suggests a threshold concentration must be reached in the Henry's region, rather than a total threshold concentration as others have suggested [18, 19], whereby additional penetrant can only be accommodated by dilation of the polymer chains, leading to plasticization.

6F-PAI-2 plasticizes near 450 psia. Beyond this pressure, permeability increases by only 5%, which is less than half of the increase shown in 6F-PAI-1 and 3. This higher stability is attributed to enhanced CTC formation in 6F-PAI-2 relative to 6F-PAI-1 and 3. Also, the low net permeability increase is comparable to Torlon®, whose permeability

increases by a similarly low value of 4%. Thus, the chain packing and mobility in the densely packed regions of these glassy polymers plays a critical role in the onset and evolution of plasticization at elevated CO_2 pressures.

In general, all three 6F-PAI materials represent substantial improvements over the current industrial standard CA in not only the CO_2/CH_4 permeability and selectivity, but in plasticization resistance as well. It is also important to mention that these materials did not require covalent crosslinking or excessive annealing treatments. These results are also quite promising when compared to Torlon®, and show that incorporation of rigid, packing inhibiting groups not only increase permeability while preserving selectivity, but such modifications also do not compromise plasticization suppression. Binary CO_2/CH_4 mixed gas permeation in 6F-PAI-1 was already presented in Chapter 4 and showed high selectivities at pressures near 1000 psia, as well as in the presence of toluene. The mixed gas performance of 6F-PAI-2 and 3 is expected to show similar results, and will be discussed in Chapter 7.

5.4.4.2. Analysis of H_2S Plasticization Resistance

Figure 5.12 shows H_2S permeability vs. pressure in the 6F-PAI series as well as Torlon®. As was done with CO_2 permeability, beyond the plasticization pressure, permeability at each pressure was measured after approximately 12 hours of elapsed permeation time. It should be pointed out that H_2S causes plasticization at much lower pressures than CO_2. This can be observed in Figure 5.12, where beyond 80 psia, all polymers show an upswing in H_2S permeability. This trend demonstrates the highly

aggressive nature of H_2S, which places an additional challenge on membrane development for natural gas sweetening.

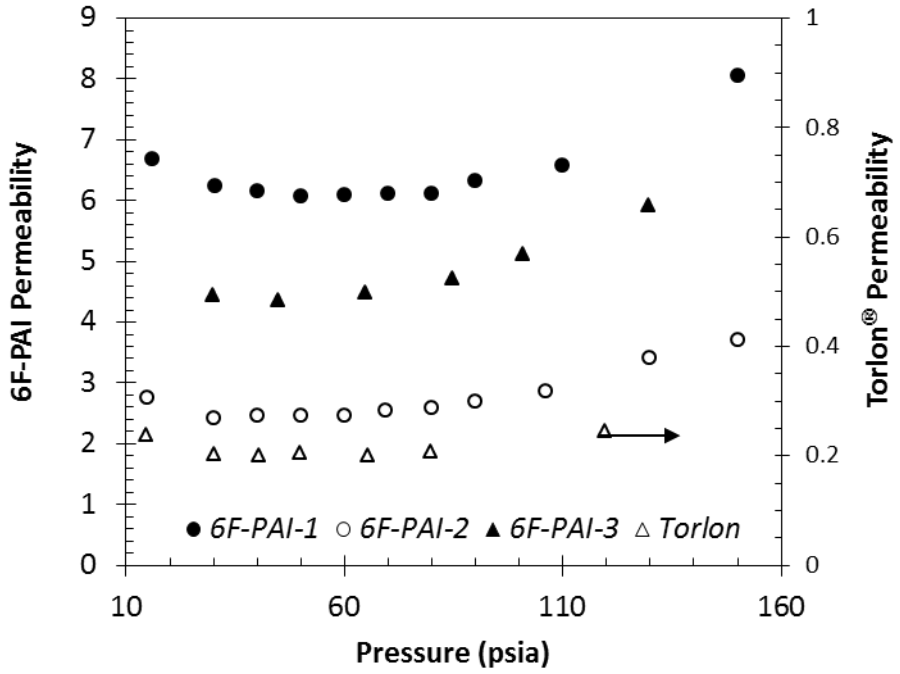

Figure 5.12: H_2S permeability isotherms at 35C for 6F-PAI polymers and Torlon®. *Units of permeability are Barrer.*

Surprisingly, H_2S plasticization resistance was reduced in 6F-PAI-2 and 3 relative to 6F-PAI-1. This is demonstrated by both lower plasticization pressure as well as a greater magnitude of permeability increase after the initial upswing in permeability. Although the differences in H_2S plasticization pressure are not as great as they were in the case of CO_2, the difference in 6F-PAI-1 and 2's mixed gas performance is drastic. Mixed gas performance will be discussed further in Chapter 7. As shown in section 5.4.3, H_2S sorption in 6F-PAI-2 and 3 was enhanced relative to 6F-PAI-1. This enhancement was more apparent in the idealized "equilibrium" packed environments, and correlates with reduced fluorine concentration associated with non-fluorinated DAM and TmPDA.

Lower fluorine concentration increases polarizability, which presumably leads to increased dipole-induced dipole interactions between H_2S and the polymer matrix. Consequently, the ability for elevated H_2S concentrations to break apart intermolecular interactions and cause chain swelling may also be increased. Perhaps even more surprising is the low H_2S plasticization resistance shown in 6F-PAI-2 and Torlon®, as both of these materials demonstrated remarkable stability against CO_2. Apparently even for materials with greater CTC formation, as is the case with 6F-PAI-2, the increase in favorable physiochemical interactions between H_2S and the polymer can increase the susceptibility of such a material towards H_2S induced swelling. The next chapter will attempt to quantify the energetics of penetrant sorption and diffusion as a function of fluorine concentration in order to better understand the trends observed in this chapter.

5.5. Conclusion

Two new 6FDA based polyamide-imides, which incorporate rigid, rod-like diaminomesistylene (DAM) and 2,3,5,6-tetramethyl-phenylene diamine (TmPDA) were synthesized via condensation polymerization reaction. These materials showed enhanced permeabilities relative to Torlon®, a high performance, commercially available polyamide-imide, without compromising permselectivity or plasticization resistance for the CO_2/CH_4 pair. A comparison of the 6FDA *polyamide-imides* to their analog *polyimides* revealed opposite trends in the effect that DAM and TmPDA have on chain packing, permeability, and selectivity. It can be concluded then that different steric interactions and polymer chain dynamics occur around amide and imide bonds.

An increase in H_2S selectivity in 6F-PAI-2 and 3 relative to the base structure, 6F-PAI-1 was achieved, and was shown to be caused by enhanced H_2S sorption in the lower fluorinated densely packed environments of 6F-PAI-2 and 3. Such higher sorption, however, increased their susceptibility to H_2S induced plasticization. On the other hand, CO_2 plasticization resistance in the DAM based polyamide-imide was as high as 450 psia, and only a minor increase in permeability of 5% beyond this pressure was observed. In the following chapter, the apparent differences between CO_2 and H_2S transport will be analyzed by measurement and analysis of the sorption and diffusion energetics.

Although H_2S plasticization pressure was reduced in 6F-PAI-2 and 3, it is unlikely that most conventional natural gas wells would contain H_2S at partial pressures as high as was used for the pure gas plasticization analysis in this chapter. In the case where H_2S concentration in the feed is low, such as 5%, even at a total feed pressure of 1000 psia, H_2S partial pressure may be below the plasticization threshold. Thus, mixed gas testing, specifically using ternary compositions of H_2S, CO_2 and CH_4 will be an important part of this project. Ternary mixed gas testing will be covered in Chapter 7.

5.6. References

[1] S. Sridhar, B. Smitha, T. M. Aminabhavi, "Separation of Carbon Dioxide from Natural Gas Mixtures through Polymeric Membranes-A Review," *Separation & Purification Reviews*, **36** (2), 113-174, (2007).

[2] C. E. Powell, X. J. Duthie, S. E. Kentish, G. G. Qiao, G. W. Stevens, "Reversible diamine cross-linking of polyimide membranes," *Journal of Membrane Science*, **291** (1–2), 199-209, (2007).

[3] T. C. Merkel, V. Bondar, K. Nagai, B. D. Freeman, "Hydrocarbon and Perfluorocarbon Gas Sorption in Poly(dimethylsiloxane), Poly(1-trimethylsilyl-1-

propyne), and Copolymers of Tetrafluoroethylene and 2,2-Bis(trifluoromethyl)-4,5- difluoro-1,3-dioxole," *Macromolecules*, **32** (2), 370-374, (1999).

[4] T. C. Merkel, V. Bondar, K. Nagai, B. D. Freeman, "Perfluorocarbon Gases in Poly (1-trimethylsilyl-1-propyne)," *Langmuir*, **38**, 273-296, (2000).

[5] T. C. Merkel and L. G. Toy, "Comparison of Hydrogen Sulfide Transport Properties in Fluorinated and Nonfluorinated Polymers," *Macromolecules*, **39** (22), 7591-7600, (2006).

[6] B. D. Freeman, "Basis of Permeability/Selectivity Tradeoff Relations in Polymeric Gas Separation Membranes," *Macromolecules*, **32,** 375-380, (1999).

[7] C. Nagel, K. Günther-Schade, D. Fritsch, T. Strunskus, F. Faupel, "Free Volume and Transport Properties in Highly Selective Polymer Membranes," *Macromolecules*, **35** (6), 2071-2077, (2002).

[8] W. J. Koros, M. R. Coleman, D. R. B. Walker, "Controlled Permeability Polymer Membranes," *Annual Review of Materials Science*, **22** (1), 47-89, (1992).

[9] D.W. Van Krevelen and K. Te Nijenhuis, *Properties of Polymers: Their Correlation with chemical Structure; their Numerical Estimation and Prediction from Additive Group Contributions*, (Elsevier, Amsterdam, The Netherlands, 1972).

[10] J. H. Kim, W. J. Koros, D. R. Paul, "Physical aging of thin 6FDA-based polyimide membranes containing carboxyl acid groups. Part I. Transport properties," *Polymer*, **47 (**9), 3094-3103, (2006).

[11] M. M. Teoh, T.-S. Chung, K. Y. Wang, M. D. Guiver, "Exploring Torlon/P84 co-polyamide-imide blended hollow fibers and their chemical cross-linking modifications for pervaporation dehydration of isopropanol," *Separation and Purification Technology*, **61** (3), 404-413, (2008).

[12] D. Fritsch and N. Avella, "Synthesis and properties of highly gas permeable poly(amide-imide)s," *Macromolecular Chemistry and Physics*, **197** (2), 701-714, (1996).

[13] G. Hougham, G. Tesoro, J. Shaw, "Synthesis and Properties of Highly Fluorinated Polyimides," *Macromolecules*, **27** (13), 3642-3649, (1994).

[14] R. W. Baker and K. Lokhandwala, "Natural Gas Processing with Membranes: An Overview," *Industrial & Engineering Chemistry Research*, **47 (**7), 2109-2121, (2008).

[15] B. D. Bhide and S. A. Stern, "Membrane processes for the removal of acid gases from natural gas. II. Effects of operating conditions , economic parameters , and membrane properties," *Journal of Membrane Science*, **81**, 239–252, (1993).

[16] R. Wang, C. Cao, T.S. Chung, "A critical review on diffusivity and the characterization of diffusivity of 6FDA–6FpDA polyimide membranes for gas separation," *Journal of Membrane Science*, **198** (2), 259-271, (2002).

[17] W. C. Madden, D. Punsalan, W. J. Koros, "Age dependent CO_2 sorption in Matrimid® asymmetric hollow fiber membranes," *Polymer*, **46** (15), 5433-5436, (2005).

[18] M. Wessling, H. Strathmann, A. Bos, I. G. M. Pu, "CO_2-induced plasticization phenomena in glassy polymers," *Journal of Membrane Science*, **155**, 67-78, (1999).

[19] M. Wessling and A. Smolders, "Dilation Kinetics of Glassy, Aromatic Polyimides Induced by Carbon Dioxide Sorption," *Journal of Polymer Science: Part B: Polymer Physics*, **33**, 1371-1384, (1995).

[20] M. Wessling and A. Smolders, "Dilation Kinetics of Glassy, Aromatic Polyimides Induced by Carbon Dioxide Sorption," *Journal of Polymer Science: Part B: Polymer Physics*, **33**, 1371-1384, (1995).

CHAPTER 6

ANALYSIS OF PERMEATION, DIFFUSION, AND SORPTION ENERGETICS

Chapters 4 and 5 demonstrated the high ideal CO_2/CH_4 permselectivity achieved in a series of 6FDA based polyamide-imides. On the other hand, a moderate H_2S/CH_4 selectivity was observed in all three polyamide-imides. It was subsequently shown that permselectivity was slightly reduced due to an unexpectedly low H_2S/CH_4 diffusion selectivity. This result is surprising considering H_2S's smaller kinetic diameter, which is the minimum zeolite window dimension which allows gas sorption of the indicated molecule to occur. Such lower diffusion relative to CH_4 suggests that H_2S diffusion is governed by additional factors beyond cohesive energy density, fractional free volume of the polymer, and kinetic diameter of the penetrant. Additionally, enhanced H_2S sorption compared to CO_2 and CH_4 in lower free volume 6F-PAI-2 and 3 further indicates that physiochemical interactions between polar H_2S and the polymer play a more important role in H_2S sorption compared to the cases for CO_2 and CH_4. The goal of this chapter is to directly determine whether higher diffusion activation energy barriers reduce H_2S's diffusion transport relative to CH_4, and if such energy correlates with increased polarizability in the polymer backbone. Additionally the effect of fluorine concentration in the polymer on H_2S sorption enthalpy will also be studied in order to elucidate the important factors that dictate the transport of H_2S in polymer membranes. From these data, the temperature dependencies of CO_2/CH_4 and H_2S/CH_4 permselectivity will be obtained, which can provide important information on membrane performance at elevated temperatures. In natural gas separations, the process stream is often heated above the dew point to prevent H_2O condensation. Therefore, knowledge of membrane

performance as a function of temperature is vital for development of an economically attractive membrane separation unit.

6.1. Theoretical Background

6.1.1 Activation Energy of Diffusion

As briefly mentioned in Chapter 2, diffusion is a thermally activated process that is characterized by an activation energy of diffusion [1]. The temperature dependence of penetrant diffusion follows an Arrhenius type expression as given in Chapter 2. Meares described this activation energy as the cohesive energy density (CED) that must be overcome between adjacent polymer chains in order create a microcavity of cylindrical volume defined by the penetrant diameter, *d*, and the average jump length, λ [2]. A depiction of this is shown in Figure 6.1.

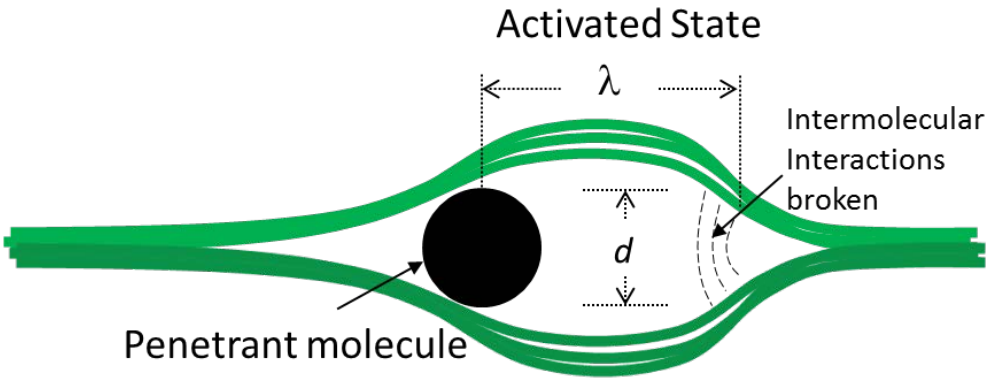

Figure 6.1: Depiction of thermally activated diffusion cavity.

The product of the cohesive energy density (CED) and volume of such a gap is equated to the diffusion activation energy, as shown in Equation 6.1. The cohesive energy density is defined as the quantity of energy per unit volume required to ideally create a void within

the polymer matrix, so it reflects the strength of intermolecular forces between closely packed polymer chains.

$$E_D = \left(\frac{\pi}{4}\right) \cdot d_k{}^2 \cdot \lambda \cdot (CED) \tag{6.1}$$

According to Equation 6.1, the activation energy, and indirectly the diffusion coefficient, depend on both the size of the penetrant as well as the physiochemical interactions between polymer chains. Smaller molecules (low d_k) in low polarity media (low CED) will diffuse faster than larger penetrants (higher d_k) in a more polar material (higher CED).

For a given material, E_D increases with penetrant size, and the magnitude of the diffusion selectivity is primarily determined by the difference in E_D between a gas pair, as is shown in Equation 6.2 where "*A*" is the fast component and "*B*" the slow component.

$$\frac{D_A}{D_B} = \frac{D_{Ao}}{D_{Bo}} \exp\left(-\frac{E_{D,A} - E_{D,B}}{RT}\right) \tag{6.2}$$

Di is the diffusion coefficient and D_{io} is the preexponential factor, which is related to the activation entropy. Pure polymer materials have very low ability to restrict vibrational and rotational degrees of freedom of different penetrants to different extents. As such, the term D_{Ao}/D_{Bo} does not play a significant role in diffusion selectivity of pure polymers. It follows that increases in temperature will be more detrimental to the diffusion selectivity in separations involving gas pairs with large size differences, and thus larger ΔE_D.

It has been postulated that E_D in certain highly interacting penetrants *also* can depend on polymer-penetrant interactions. Xu et al. observed both higher E_D and lower diffusivity in CO_2 compared to O_2, which is a surprising result considering CO_2's smaller kinetic diameter [3]. They also correlated E_D with the square of the kinetic diameter, d_K, in a series of polyamide-imides and found a strong positive correlation between E_D and d_K^2 for O_2, N_2, and CH_4. However, E_D for CO_2 was found to be rather high for its size. Costello and Koros also observed similar trends in E_D for CO_2 and O_2 in a series of polycarbonates [1]. One possible explanation may be the difficulty in estimating the effective kinetic diameter of cylindrical CO_2 compared to the lower aspect ratio O_2. The effective d_K for CO_2 is generally believed to be between its kinetic diameter of 3.3 Å and its collision diameter of 3.94 Å.

Diffusion selectivities for H_2S/CH_4 have been observed to be less than one for all polyamide-imides discussed in this dissertation. Such low selectivities are not unique to polyamide-imides, however, as even lower diffusion selectivity in polyimides 6FDA-6FpDA and 6FDA-6IpDA as well as rubbery Pebax® have been observed. The latter polyimide is very similar to the former except the CF_3 groups attached to the isopropylidene carbon in the diamine are replaced by CH_3 groups. The diffusion selectivity for H_2S/CH_4, CO_2/CH_4 and N_2/CH_4 for a number of materials are summarized in Table 6.1.

Table 6.1: Diffusion selectivity, (D_i/D_j), measured from pure gas permeation experiments at 35°C and between 30 and 40 psia.
Diffusivities were obtained by the time lag method.
d_{CH4}/d_{H2S}=3.8/3.6=1.06
d_{CH4}/d_{CO2}=3.8/3.3=1.15
d_{CH4}/d_{N2}=3.8/3.64=1.04

	H_2S/CH_4	CO_2/CH_4	N_2/CH_4
6F-PAI-1	0.90	9.8	5.9
6F-PAI-2	0.91	10	7
6F-PAI-3	0.97	9.2	5.9
Torlon®	0.78	9.1	--
6FDA-6FpDA	0.69	7.4	6.5
6FDA-6IpDA	0.75	7.7	5.1
Pebax®	0.72	1.3	--

From the above table, it is clear that H_2S has no diffusion advantage over CH_4 in any material tested in this work. Nitrogen (d_K=3.64 Å), which is larger than H_2S (d_k=3.6 Å), diffuses much faster than CH_4, which has a characteristic dimension of 3.8 Å. This typically results in N_2/CH_4 diffusion selectivities ranging from 5 to 7. As diffusivity generally correlates with kinetic diameter, larger differences in d_k usually result in higher diffusion selectivities. The ratios of d_k of the slow to fast gas for the gas pairs shown in Table 6.1 are also given in the figure caption. Because d_k^{CH4}/d_k^{H2S} is slightly greater than d_k^{CH4}/d_k^{N2}, we would expect similar if not higher diffusion selectivity for the H_2S/CH_4 pair. Mohammadi et al. measured H_2S and CH_4 permeation activation energies using mixed gases in rubbery materials *similar to Pebax®* and showed higher H_2S permeation activation energies relative to CH_4 [4]. Assuming a more negative enthalpy of sorption

for the much more condensable H_2S, E_D must be higher for H_2S if E_P is the sum of E_D and ΔH_S. As shown in Table 6.1, Pebax®, which was tested in our lab, has lower H_2S/CH_4 diffusion selectivity than most of the glassy polymers shown. Even if the effective diameter in non-spherical H_2S is larger than 3.6 Å, such a difference in the effective size between H_2S and CH_4 should be more pronounced in glassy polymers since these materials have a much higher molecular sieving capability than the highly mobile chains associated with rubbery Pebax®. Torlon® and Pebax®, both of which have the highest concentration of polar groups such as N-H and COO in the above group of polymers show lower H_2S/CH_4 diffusion selectivity than the 6FDA based polyamide-imides.

On this basis, it is hypothesized that polymer-penetrant interactions may contribute to this hindered H_2S diffusion. However, due to very unexpected and non-intuitive sorption enthalpy results obtained for the 6F-polyamide-imides, we do not believe that the trends in the subsequent diffusion activation energies for CH_4, H_2S, and CO_2 can be compared on a meaningful basis *in order to test our hypothesis* regarding such unusually low H_2S/CH_4 diffusion selectivity. As such, we do not wish to over speculate the sorption enthalpy trends between the different 6F-polyamide-imides. Instead, the sorption enthalpy data will be presented, and based on that data, a hypothesis to describe the unusual trends will be discussed and *an experiment will be performed to test it*. In the final section of this chapter, the sorption and diffusion data for two structurally similar *polyimides* will be presented. As will be shown, the trends shown in these more conventional materials (polyimides) *are consistent* with the diffusion selectivities shown in Table 6.1, therefore, the *polyimide* sorption and diffusion data will

be interpreted in order to examine the reasons behind such low H_2S/CH_4 diffusion selectivity.

6.1.2. Permeation Activation Energy and Enthalpy of Sorption

As discussed in section 2.2.4 in Chapter 2, gas sorption in polymer membranes is described by "condensation" of the gas to a liquid like density followed by mixing of the penetrant into the polymer matrix. The enthalpy change of gas sorption, which is given in Equation 6.3, consists of the change in enthalpy upon "condensation" as well as the enthalpy of mixing the liquid-like penetrant with the polymer.

$$\Delta H_S = \Delta H_C + \Delta H_{mix} \tag{6.3}$$

Note that the term "condensation" is used here loosely to describe the reduction in molar volume of the penetrant in the gas phase to a volume it would occupy prior to insertion in the actual polymer matrix. The enthalpy change associated with penetrant "condensation," ΔH_C, is generally exothermic for most gases, with the absolute magnitude of ΔH_C being larger for larger gases with higher boiling or critical temperatures [5]. The enthalpy change of mixing, ΔH_{mix}, may depend on the size of the space that is created in the polymer chains to accommodate a penetrant molecule as well as intermolecular interactions, albeit to a lesser extent outside of specific polymer-penetrant interactions. As such, ΔH_{mix} is usually endothermic (positive) due to the energy needed to create a space sufficient for penetrant insertion. For light, relatively non-polar gases such as He and H_2, ΔH_C as well as intermolecular interactions are low. Because

ΔH_{mix} is believed to be slightly positive, the total enthalpy change upon sorption of these penetrants can be an endothermic process. Consequently, gas sorption for He and H_2 tends to increase at higher temperatures. For higher molecular weight gases, $|\Delta H_C| > |\Delta H_{mix}|$, and gas sorption is an exothermic process that decreases with increased temperature. From this basis, outside of specific interactions, gas sorption in a given material generally increases with gas condensability regardless of size. However, sorption can also be affected by non-ideal polymer-penetrant interactions, which will be discussed next.

Merkel and coworkers have produced an elegant series of papers describing hydrocarbon and perfluorocarbon sorption in rubbery poly(dimethylsiloxane) (PDMS), glassy poly(1-trimethylsilyl-1-propyne) (PTMSP), and glassy copolymers based on tetrafluoroethylene [6, 7]. In general, their results demonstrated that fluorocarbon sorption in glassy hydrocarbon polymers was lower than the analog hydrocarbon penetrants, while the opposite holds true in perfluorocarbon polymers. The difference between fluorocarbon and the analog hydrocarbon penetrant sorption levels was much more apparent at higher pressures where gas sorption occurs mainly in the densely packed Henry's environments in glassy polymers. Because PDMS is devoid of non-equilibrium packing defects, the discrepancy between hydrocarbon and fluorocarbon penetrant sorption was very apparent throughout the entire pressure range studied. They also showed that a logarithmic relationship between hydrocarbon and fluorocarbon infinite dilution solubility coefficients with critical temperature existed in ultra-high free volume PTMSP, indicating gas sorption in very high free volume materials, particularly in the low pressure limit, is relatively non-discriminant of polymer-penetrant interactions,

and gas sorption depends mainly on condensability. However, in rubbery PDMS, fluorocarbon solubility fell systematically below that of their analog hydrocarbon penetrants. In the perfluoropolymers, the larger hydrocarbon solubility coefficients fell below that predicted by the best fit line of the infinite dilution sorption coefficient versus gas critical temperature. These trends suggest that in very high free volume materials, as well more moderate free volume glasses at very low pressure, gas sorption depends mainly on condensability. In lower free volume materials as well as glasses at higher penetrant partial pressures, where sorption takes place mainly in the more densely packed environments, non-ideal polymer-penetrant interactions can play a significant role in gas sorption. These observations hint at some of the issues that will be discussed later in the analysis of the two polyimides studied here.

As was shown in Chapter 5, CO_2 and CH_4 sorption was noticeably decreased in lower free volume 6F-PAI-2 and 3 relative to 6F-PAI-1, while for H_2S, sorption was very similar between all three polymers. Similar H_2S sorption in the lower free volume materials (6F-PAI-2 and 3) relative to higher free volume 6F-PAI-1 is believed to be due similar non-ideal sorption interactions between fluorine and H_2S. As was discussed in Chapter 5, Merkel and coworkers showed lower H_2S sorption relative to CO_2 in both highly fluorinated low and high free volume glassy materials, as well as highly fluorinated rubbery copolymers based on polytetrafluoroethylene (PTFE) [8]. Therefore, based on our sorption results in Chapter 5, the sorption enthalpy is expected to be lower (less exothermic) for CO_2 and CH_4 in 6F-PAI-2 and 3 relative to 6F-PAI-1 due to lower free volume in 6F-PAI-2 and 3 and higher *CED*, which should increase the energy required to create a gap between the polymer chains, thereby increasing $\left|\Delta H_{mix}\right|$.

Conversely, for H_2S, more favorable polymer-penetrant interactions due to less fluorine concentration may offset the increase in the work required for insertion of the gas into the polymer chains, thereby $|\Delta H_{mix}|$ may be lower. Thus, ΔH_S is hypothesized to become *more exothermic* for H_2S in 6F-PAI-2 and 3. A similar phenomenon is also expected to occur in polyimides 6FDA-6FpDA and 6FDA-IpDA. It would be even more interesting if ΔH_S for H_2S positively correlates with E_D in a given class of materials, which would provide strong evidence for our hindered diffusion hypothesis discussed in section 6.1.1. However, as previously mentioned, the unusual sorption enthalpies obtained in the *6F-polyamide-imides* are not consistent with the most often observed and understood relationship between sorption enthalpy and gas condensability. Therefore, the sorption enthalpies in the 6F-polyamide-imides do not correlate with our previously discussed hypothesis regarding sorption enthalpy differences in the polyamide-imides with varying fluorine concentration along the polymer backbone. Analysis of the more easy to interpret polyimides, whose sorption enthalpies are consistent with conventional wisdom, will also be used to test our hypothesis regarding fluorine concentration and enthalpy of sorption. As stated, a hypothesis and test to verify said hypothesis regarding such counter-intuitive sorption enthalpy trends in the polyamide-imides will shown.

It follows from the definition of permeability, namely $P = DS$, that the permeation activation energy is the sum of E_D and ΔH_S. For most conventional gases, including the ones tested in this dissertation, the absolute magnitude of E_D is greater than ΔH_S, and permeation is an endothermic process that increases with temperature. Larger gases with higher E_D will in turn have higher E_P, therefore, higher temperatures will be more detrimental to the permselectivity of separations relying on mobility selectivity.

6.1.3. Experimental

The temperature dependence of the solubility and permeability coefficients was determined at 40 psia over the temperature range of 30-60°C using van't Hoff and Arrhenius relationships. Gas sorption was allowed to equilibrate at a given temperature for at least 8 hours prior to measuring *S*. Equilibrium was generally reached between 5 and 6 hours, which was confirmed by comparing *S* measured after 5-6 hours with *S* measured after 8 hours. Nevertheless, 8 hours was used for equilibration at a given temperature in order to maintain consistency between each gas. Between each measurement, the entire pressure decay cell, including the membrane, was degassed and the temperature equilibrated at the next higher temperature for 12-16 hours.

For the permeability measurements, the film was not degassed between each temperature. Instead, the diffusion time lag was measured at 30°C, which was the lowest temperature studied, and once steady state permeation had been reached, the temperature was increased and allowed to equilibrate for 3 hours prior to measuring *dp/dt* at that temperature. The permeability was measured an hour later to confirm steady state temperature had been reached. The diffusion activation energy was calculated by Equation 6.4.

$$\Delta E_P = \Delta E_D + \Delta H_S \tag{6.4}$$

The measured temperature dependencies of the transport properties are only valid over the temperature range for which they were measured. The range should also be devoid of any thermal transitions in the polymer. All polymers tested in this work have T_gs well above the temperatures used in this study. A sub-T_g transition beginning around

75°C was found in 6F-PAI-2 using dynamic mechanical analysis (DMA). Measurement of the sorption coefficient at this temperature, however, did not affect the linearity of the natural log of sorption versus 1/T or the trends in ΔH_s between the different penetrants calculated using either the 3 temperature point fit between 30 to 60°C, or the 4 temperature point fit from 30 to 75°C. Subsequent R^2 values were still 0.98 or greater for both 3 and 4 point fits as well. Furthermore, Costello also found the natural log of *S* versus 1/T relationship to be unaffected upon traversing a sub-T_g in 6FDA-6FpDA polyimide [9]. Because the discovery of a transition in 6F-PAI-2 was made after 6F-PAI-1 and 2 were measured from 30 to 75°C, 6F-PAI-3, which was the last polyamide-imide studied, was only measured up to 60°C in order to avoid confusion. To maintain consistency in the calculation of ΔH_s and E_p between 6F-PAI-1, 2 and 3, the sorption enthalpies and permeation activation energies in all three materials were fit and calculated between 30 and 60°C. Repeat measurements on the same film for the different polymers generated very similar values for the transport properties, even after approaching the sub-T_g transition beginning at 75°C in 6F-PAI-2. This indicates that aging related volume relaxation did not occur in any of the materials. The 4 temperature point fits and the ΔH_S and E_p values obtained from such fits can be found in Appendix B. The correlation coefficients and standard deviations of the fits were calculated using the "LINEST" program in Microsoft Excel. The procedure for using this function is given in the reference [10] . Standard deviations are reported with the sorption and activation energies.

6.2. Analysis of 6FDA Polyamide-imides

6.2.1. Sorption Enthalpies

Figure 6.2 shows the sorption coefficients for CO_2, CH_4 and H_2S in 6F-PAI-1,2 and 3 as a function of temperature. The enthalpy of sorption divided by the gas constant, ($\Delta H_S/R$), is the negative slope of the plot of ln(S) vs. 1/T. The sorption enthalpy, ΔH_S, is tabulated in Table 6.2. As can be observed in the plots, the solubility vs. temperature response for all polyamide-imides is linear with 1/T, indicating that the temperature dependence of the sorption coefficient follows van't Hoff type behavior with constant ΔH_S over the temperature range from 30 to 60°C. Additionally, the sorption coefficient for all penetrants in all materials decreases with increasing temperature, indicating that gas sorption in these materials is an exothermic process.

Table 6.2: Sorption enthalpies for the 6F-PAI series at 40 psia.

ΔH_s (kJ/mol)	*6F-PAI-1*	*6F-PAI-2*	*6F-PAI-3*
CH_4	-22 ± 0.02	-22 ± 0.91	-20 ± 2.2
CO_2	-18 ± 2.2	-15 ± 0.54	-17 ± 1.3
H_2S	-15 ± 1.6	-12 ± 0.29	-16 ± 1.6

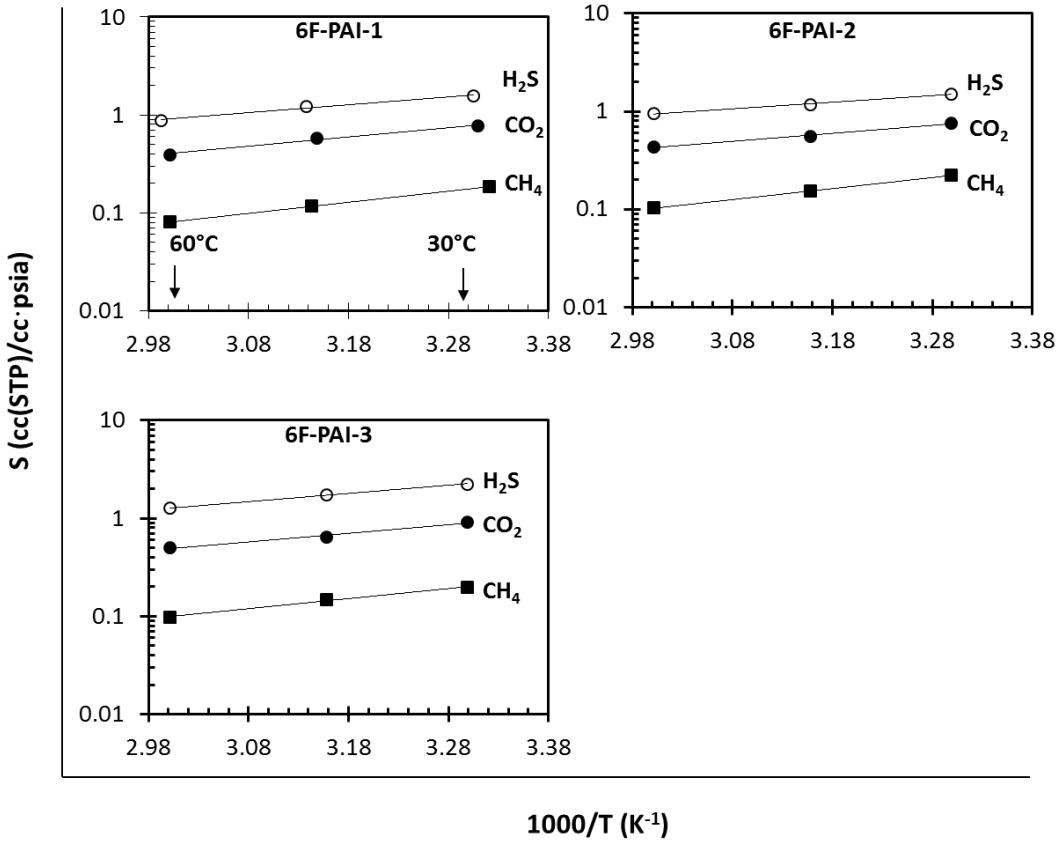

Figure 6.2: Temperature dependence of the sorption coefficients in the 6F-PAI series.

In the past, researchers have shown good correlation of the magnitude of ΔH_S with penetrant critical temperature, suggesting that the enthalpy of sorption depends mainly on the "condensation" enthalpy. However, the order of increasing critical temperature for the penetrants in Table 6.2 goes as follows: CH_4 (190 K) < CO_2 (303 K) < H_2S (373 K). As can be seen in Figure 6.2 and Table 6.2, the order of increasing (more exothermic) sorption enthalpy is the exact opposite. Therefore, the data suggests that the sorption enthalpy in the 6F-PAI series depends on additional factors other than gas condensability, such as the enthalpy of mixing. Higher (more exothermic) ΔH_S for CO_2 relative to H_2S in 6F-PAI-2 is likely due to higher (more endothermic) mixing enthalpy

for H_2S, which is believed to be due to differences in the proportions of sorbed H_2S in the Henry's and Langmuir environments. Because the Henry's region is more densely packed, creation of a molecular scale gap requires energy, as opposed to a Langmuir microvoid, where preexisting "holes" available for gas sorption occur. Therefore, different proportions of penetrant sorbed into each environment between different species can result in different sorption energetics. As will be shown in section 6.2.2, H_2S has a much higher fraction of its total sorbed concentration at 40 psia sorbed into the Henry's region than does CO_2, which may contribute to lower (less exothermic) sorption enthalpy for H_2S. This will be discussed in more detail in the next section.

The sorption enthalpy for both CO_2 and H_2S is less exothermic in less fluorinated 6F-PAI-2 relative to 6F-PAI-1. While contrary to the effect of fluorine on the heat of mixing for H_2S argument, the less exothermic ΔH_s for 6F-PAI-2 may reflect lower *ffv* in the less fluorinated matrix. Lower fluorine concentration was hypothesized to increase the interaction energy for H_2S in the more intrinsic heat of mixing contribution to ΔH_S in 6F-PAI-2 and 3, however this does not appear to be the case for 6F-PAI-2. For 6F-PAI-3, both CO_2 and H_2S sorption enthalpy is actually more negative than in 6F-PAI-2, which again, is unexpected based on an endothermic heat of mixing argument because sorption was remarkably lower in 6F-PAI-3 relative to 6F-PAI-2 as was shown in Chapter 5. The difference in enthalpy for 6F-PAI-3 compared to 6F-PAI-1 is less significant considering the uncertainty limits. These complicated and generally inconclusive results were the cause of considerable attention in this work, and they are believed to occur due to different proportions of CO_2 and H_2S, as well as CH_4 populating the Henry's and Langmuir environments to different extents between the three different polymers.

Therefore, we do not wish to over speculate the differences in ΔH_S between the different materials. These issues will be further discussed in section 6.2.2.

Perhaps the most surprising result from the sorption enthalpies shown in Table 6.2 is the clear observation that the sorption enthalpy change for CH_4 is more negative than both CO_2 and H_2S in all three polyamide-imides. This result cannot be explained by simple condensability or heat of mixing arguments, as CH_4's lower condensability would presumably result in the least exothermic heat of condensation. Moreover, the lack of strong interactions would not be expected to promote mixing in the densely packed regions. In order to validate and probe the CH_4 sorption versus temperature data, a number of tests were performed. Because CO_2 and H_2S were tested after CH_4, thermally induced membrane conditioning, such as volume relaxation from the initial S_{CH4} vs. temperature run was checked to verify that no artifact affected subsequent experiments performed on the same film. However, N_2 sorption was measured at 35°C after each temperature program for each gas, and was shown to be nearly identical after each run. Also, repeat measurements of S_{CH4} vs. temperature gave consistent values for both S_{CH4} and ΔH_S. These results indicate the absence of thermally induced membrane conditioning. To further probe CH_4's unusual sorption enthalpy, its sorption coefficient was measured at each temperature for at least 24 hours as opposed to the normal 8 hour run time. A comparison of ΔH_S calculated from the 24 hour run with the normal 8 hour run time showed nearly identical ΔH_S, thus the issue of not reaching equilibrium was also ruled out. As will be discussed in section 6.3, the sorption enthalpies for 6FDA-6FpDA and 6FDA-IpDA polyimides that are measured in this work are consistent with those reported by others in the literature, indicating the reliability of the sorption

equipment used in our study. Hence, the above discussion suggests that the unusual CH_4 sorption enthalpies measured for the 6F-PAI series in this dissertation are real and not due to experimental error such as temperature or volume calibrations. A hypothesis for the unusual trend as well as an experiment to test it will be discussed in the next section.

6.2.2 Hypothesis Regarding Anonymously Exothermic CH_4 Sorption Enthalpy

In section 6.2.1, an unusual trend in CH_4's sorption enthalpy was observed, which suggested that the sorption of CH_4 in the 6F-PAI polymers is more exothermic than CO_2 and H_2S. Such a result is quite surprising considering CO_2 and H_2S's higher tendency for condensation, which is inferred by their critical temperatures. This trend in ΔH_S for CH_4 was *not* observed in similar 6FDA based *polyimides*, as these materials demonstrated the often observed correlation of increased ΔH_S with higher penetrant critical temperature. Based on this finding, it was concluded that the trend in sorption enthalpy for CH_4 in the polyamide-imides is not due to experimental error. Instead, we postulate that this trend stems from differences in material properties, specifically, chain packing in the equilibrium domains.

Upon closer inspection of the CO_2, CH_4 and H_2S concentration isotherms in the polyamide-imides shown in Chapter 5, a significant difference in penetrant concentration in the "equilibrium packed" regions can be observed between CH_4 and CO_2/H_2S. The discrepancy is reflected through extremely low values for the Henry's Law parameter, k_D, for CH_4 in 6F-PAI-2 and 3 relative to CO_2 and H_2S. In other words, at the pressure where the temperature dependence of the sorption coefficient was measured (40 psia), the concentration of CH_4 in the densely packed environments is very low compared to its

concentration sorbed into the Langmuir sites. This difference between dissolved and Langmuir concentration is not as high for CO_2 or H_2S. Therefore, at 40 psia, a much higher fraction of total CH_4 concentration exists in lower energy Langmuir microvoids compared to the higher energy densely packed regions. Thus, the ratio of CH_4 concentration in the dense, Henry's type environments to Langmuir environments, which is essentially the equilibrium constant for the local partitioning of penetrant between the two types of sites, is lower than CO_2 and H_2S. The fractions of concentration in the Henry's and Langmuir regions for 6F-PAI-1,2 and 3, as well as the local equilibrium constant for dual-mode sorption site partitioning were calculated from the dual-mode parameters and are shown in Table 6.3. Additionally, the concentration in the Langmuir region as a function of pressure in the polyamide-imides was predicted using the dual-mode parameters given in Chapter 5, and is compared to the experimentally measured total concentration also as a function of pressure. These plots are show in Figure 6.3.

Table 6.3: Concentration fractions in the dissolved (*D*) and Langmuir (*H*) regions at 40 psia and 35°C. K^{EQ} is the equilibrium constant for the local equilibrium established for penetrant concentration in the dissolved to Langmuir regions.
*The parameters for 6F-PAI-3 are not shown, as the dual-mode parameters in this material could only be estimated crudely due to the low curvature observed.

	6F-PAI-1			6F-PAI-2		
	CH_4	CO_2	H_2S	CH_4	CO_2	H_2S
f_D	0.15	0.19	0.33	$2x10^{-3}$	0.07	0.35
f_H	0.85	0.80	0.66	0.99	0.93	0.65
K^{EQ}	0.17	0.24	0.5	$2x10^{-3}$	0.07	0.53

As can be seen in Figure 6.3, at 40 psia, the difference between the measured total concentration and the predicted *Langmuir concentration* is negligible for CH_4, while the discrepancy between the two concentrations becomes increasingly evident for CO_2 and then H_2S. This trend is particularly pronounced for CH_4 in 6F-PAI-2, where there is essentially no difference between the measured total concentration and the predicted Langmuir concentration. This tendency for CH_4 to sorb primarily in the low energy microvoids is further evidenced by the K^{EQ} values shown in table 6.3. For CH_4, K^{EQ} is lower than it is for CO_2 and H_2S in both 6F-PAI-1 and 2. In 6F-PAI-2, the equilibrium constant is an order of magnitude lower for CH_4 than it is for the other two gases. Therefore, at 40 psia, CH_4 likely partitions itself primarily into the excess microvoid volume, rather than the more densely packed polymer chains associated with Henry's type sorption, and only a small fraction of dissolved CH_4 concentration will exist in equilibrium with its Langmuir concentration. Because a greater fraction of CO_2 and H_2S is sorbed into the densely packed regions for both 6F-PAI-1 and 2, the sorption enthalpy for these two penetrants appears to be less exothermic than CH_4, as these more densely packed sites require more energy for penetrant dissolution. In fact, for each material, sorption enthalpy becomes less exothermic with increased K^{EQ} shown in Table 6.3. Therefore, H_2S, which is the *most* condensable out of the three gases, shows the *least* exothermic sorption enthalpy. Hence, a clear correlation appears to exist between penetrant dissolution in the higher energy Henry's type regions and decreasing total sorption enthalpy.

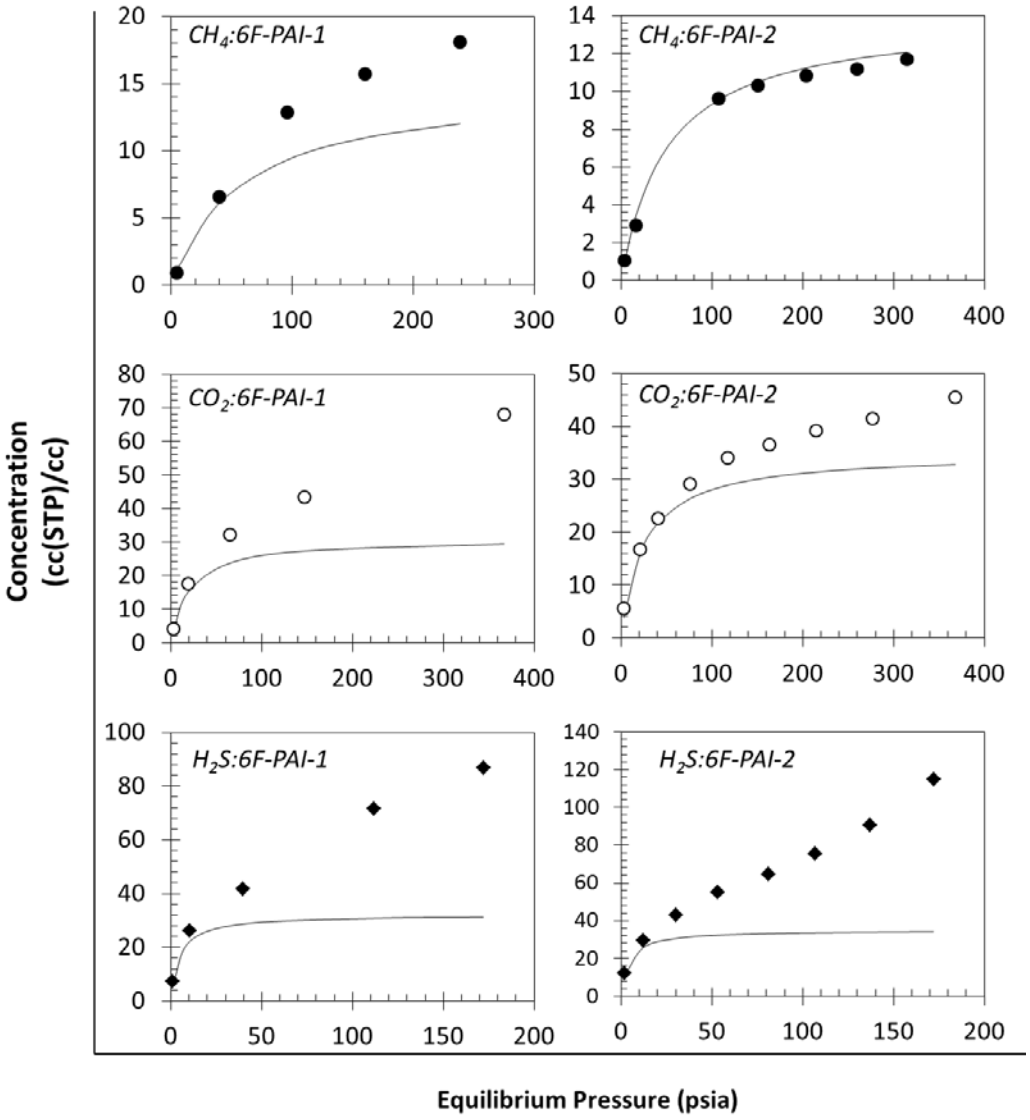

Figure 6.3: Total experimentally measured concentrations (dots) and predicted Langmuir concentration (solid lines) at 35°C for 6F-PAI-1 and 2. 6F-PAI-3 is not shown, however, it shows similar behavior as 6F-PAI-2.

It is hypothesized that greater condensability in H_2S and CO_2 as well as H_2S's polar nature affords these penetrants increased ability to mix into the densely packed regions of the polymer matrix. Indeed, such penetrant sorption described by Henry's Law often shows a positive correlation with penetrant condensability [6, 7]. As such, in polymers with relatively low values of k_D, as was shown for the 6F-PAI series in Chapter

5, large gases of low condensability, such as CH_4, tend to have low sorption capacity in such densely packed environments. Indeed, if this is true, then a larger gas relative to CH_4 with similar condensability should also show an apparent more exothermic sorption enthalpy relative to CO_2 and H_2S. Tetrafluoromethane (CF_4), which is only slightly more condensable than CH_4 (T_C=227 K) but has a critical volume of 139.6 *cc/mol*, is an ideal probe for testing this hypothesis. The temperature dependence of CF_4's sorption coefficient will be discussed in Section 6.2.3.

As will be shown in the 6FDA *polyimide* data in section 6.3, such non-conventional trends in sorption enthalpy do not occur in these materials. The reason this trend in CH_4's sorption enthalpy is observed in the polyamide-imides and not the polyimides may be due to a smaller difference in the local Henry's to Langmuir concentration equilibrium constants between CH_4, CO_2 and H_2S in the polyimides. This can be observed in Table 6.4.

Table 6.4: Dissolved and Langmuir concentration fractions and equilibrium constants representing the ratio of dissolved to Langmuir concentrations at 35°C and 40 psia for 6FDA-6FpDA.

	CH_4	CO_2	H_2S
f_D	0.14	0.12	0.36
f_H	0.86	0.88	0.64
K^{EQ}	0.16	0.14	0.56

The dual-mode parameters for CO_2 and H_2S were measured in this work, while CH_4 concentration fractions were estimated from dual-mode parameters fit from Costello's data [1]. A reasonable agreement between CO_2 sorption in 6F-6F measured in

our work and Costello's work was obtained, thus the dual-mode parameters for CH_4 measured in her work should provide a good prediction of CH_4 concentration fractions at our sorption pressure of 40 psia. Unfortunately, accurate parameters for CH_4 in 6F-Ip could not be obtained from the available literature data.

The data in Table 6.4 show very similar equilibrium constants for CO_2 and CH_4. This suggests that these penetrants have similar proportions of total concentration sorbed into each type of sorption site. Therefore, a comparison of their sorption enthalpies at 40 psia is more meaningful. On the other hand, a much greater difference in K^{EQ} was observed between CO_2 and CH_4 in the polyamide-imides. Therefore, the sorption enthalpies in the 6F-PAI series are likely not as meaningful in terms of comparing the effects of lower free volume and fluorine concentration on ΔH_S. As such, we will use the sorption enthalpy data in these polyimides to test our hypothesis regarding fluorine concentration on ΔH_S for H_2S.This will be discussed in the final section in this chapter.

Due to a lack of detailed characterizations of the sorption and transport properties of these complex polyamide-imides in the literature, the unusual sorption enthalpy trends outlined in the previous discussion were difficult to foresee. Additionally, 6F-PAI-2 and 3 have only been synthesized in our lab. Because of time constraints, additional measurements to characterize the sorption enthalpy of CO_2, CH_4, and H_2S in these materials could not be performed. In the future, it would much more fruitful to measure the temperature dependencies of the dual-mode parameters in order to decouple the energetics associated with hole filling in the Langmuir modes and penetrant dissolution in the densely packed regions. As Chapter 5 demonstrated, the structure of the diamine in the polyamide-imides had a more significant impact on sorption in the densely packed

regions than the Langmuir microvoids. The enthalpy change associated with k_D may be able to more appropriately capture the effect of increased chain packing and lower fluorine concentration on penetrant sorption in the "equilibrium" chain packing regions. Despite the rather inconclusive 6F-PAI sorption enthalpies presented in section 6.2.1, the trends in the polyimides which will be subsequently discussed *are consistent with our hypothesis* that H_2S sorption is more dependent on intermolecular interactions. In order to further test our hypothesis regarding the non-intuitive exothermic sorption enthalpy for CH_4 in the polyamide-imides, CF_4 sorption was measured as a function of temperature, the results of which are presented next.

6.2.3. Testing of Hypothesis Regarding Anomalously Exothermic CH_4 Sorption Enthalpy

Merkel and coworkers showed that the activity based sorption coefficient, which represents S or k_D multiplied by the penetrant vapor pressure, decreases with increasing penetrant critical volume [6]. They concluded that differences in size and condensability were mainly responsible for sorption differences between various penetrants. Therefore, when sorption is normalized for penetrant condensability, the sorption coefficient decreases with penetrant size. Tetrafluoromethane, with a critical temperature of 228.15 K, is slightly more condensable than CH_4 (T_c=190.15 K). However, CF_4 has a higher critical volume than CH_4, (139.6 versus 99.2 cc/mol). Merkel showed that the activity based Henry's Law parameter for CF_4 in poly(1-trimethylsilyl-1-propyne) (PTMSP) was lower than CH_4. They attributed this lower activity based sorption for the perfluorocarbon to its large size, which impedes its dissolution into the densified regions of the polymer. As PTMSP has a fractional free volume of 0.29, it is one of the highest free volume,

glassy polymers in existence. Therefore, because such size limited sorption for CF_4 was shown in PTMSP, this effect is expected to be much more pronounced in a much lower free volume material such as the polyamide-imides used in this work.

According to our original hypothesis, low free volume in the Henry's region in the 6F-PAI series, as inferred from very low k_D shown in Chapter 5 limits the sorption of large gases of low condensability in the densely packed portions of the polymer. Because sorption in the Langmuir microvoids requires less energy than the densely packed environments, such large gases tend to partition in the Langmuir microvoids, which are presumed to have lower (less endothermic) enthalpies of mixing. This causes the sorption enthalpy of these gases to appear more exothermic compared to smaller, more condensable gases that have a greater fraction of total concentration sorbed into the higher energy, dense regions. In accordance with this proposed phenomena, CF_4 is expected to appear to show the *most exothermic* sorption enthalpy in the polyamide-imides out of all penetrants studied. To further demonstrate that this phenomena is due to a complex interplay between penetrant size and condensability, Xe sorption was also measured as a function of temperature. Xenon (V_c=118 cc/mol), is larger than CH_4 but much more condensable, (T_c=289.65 K). Because k_D in a given material often scales with penetrant condensability, it follows then that Xe's sorption in the Henry's region should be higher than CH_4 at 40 psia, and its sorption enthalpy is expected to correlate with its critical temperature. As such, ΔH_S for Xe is expected to be lower (less exothermic) than CO_2 and H_2S.

As a control, CF_4 sorption was also measured in 6FDA-6FpDA (6F-6F) polyimide, the structure of which is given in Chapters 4 and 5. Additionally, its physical

properties are tabulated in Table 6.7 in the proceeding section. Because 6F-6F is not as densely packed as the polyamide-imides, it showed similar proportions of Henry's to Langmuir concentration amongst CH_4 and CO_2 in Table 6.4, indicating size and condensability excluded dissolution in the Henry's region is not a factor in this material as it was for the *amide-imides*. Therefore, CF_4 is expected to show the *least exothermic* sorption enthalpy out of all gases measured in 6F-6F.

Figure 6.4 compares CF_4 sorption vs. temperature between the various gases for 6F-PAI-2 and 6F-6F.

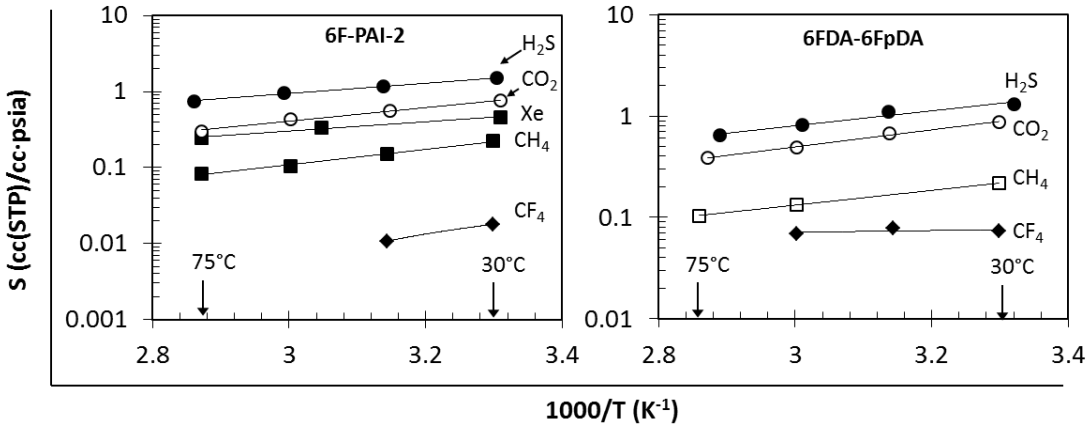

Figure 6.4: Temperature dependence of the sorption coefficient in 6F-PAI-2 and 6F-6F at 40 psia.

It is apparent in Figure 6.4 that CF_4 sorption in 6F-6F shows the lowest temperature dependence. Conversely, in 6F-PAI-2, CF_4 sorption appears to be the strongest function of temperature. Because the absolute value of CF_4's sorption coefficient in 6F-PAI-2 was so low, sorption at temperatures higher than 45°C was subject to significant deviation and was therefore concluded to be insignificant. Hence, its sorption enthalpy was calculated based on the sorption values at 30 and 45°C. The linear correlation between the sorption

coefficient at these temperatures results in the highest slope. The sorption enthalpy for CF_4 in 6F-PAI-2 and 6F-6F as well as Xe in 6F-PAI-2 are given in Table 6.5

Table 6.5: CF_4 and Xe sorption enthalpy in 6F-PAI-2 and 6F-6F at 40 psia.

ΔH_s (kJ/mol)	*6F-PAI-2*	*6F-6F*
CF_4	-27	-1.6
Xe	-12	--

As expected, because of its large size and low condensability, CF_4 likely sorbs predominantly into the Langmuir sites. As such, ΔH_S for the perfluorocarbon in 6F-PAI-2 appears to be the most exothermic out of all gases tested in this work. For Xe, its enthalpy of sorption is less exothermic than both CO_2 and H_2S, which is consistent with its lower critical temperature. The Henry's parameter for Xe is likely higher than it is for CH_4 and CF_4, and the value of K^{EQ} is probably similar to CO_2 and H_2S. These results suggest that the highly exothermic ΔH_S values obtained for CH_4 are due to a combination of its low condensability and large size, which causes sorption at 40 psia to occur largely into the preexisting glassy microvoids

The sorption enthalpy for CF_4 in 6F-6F is also in accordance with our hypothesis. Due to its larger size and low condensability compared to CO_2 and H_2S, CF_4 shows the lowest (least exothermic) sorption enthalpy and is practically independent of temperature.

These results support our hypothesis regarding such unusually high (exothermic) sorption for CH_4 compared to CO_2 and H_2S in the polyamide-imides. In general, k_D for

CO_2 and CH_4 is much lower in the polyamide-imides compared to the polyimides. Therefore, at low pressures, CH_4, which has low tendency to sorb based on its low condensability and low polarizability, partitions into the low heat of mixing Langmuir microvoids to a greater extent relative to the more densely packed and higher heat of mixing Henry's type environments in the polyamide-imides. Because CO_2 and H_2S are much more condensable and polar/polarizable, they have increased portions in the more densely packed, higher heat of mixing regions. This leads to an apparent sorption enthalpy for CH_4 that appears to be more exothermic than CO_2 and H_2S due to the higher fraction of CH_4 sorbed into the low energy sites. This stark contrast in ratios of Henry's to Langmuir concentrations between CH_4 and CO_2/H_2S is not observed in the polyimides, as was shown in Tables 6.3 and 6.4. Therefore, a comparison of their sorption enthalpies is more meaningful in terms of the weighting that each sorption site contributes to the overall enthalpy of sorption.

In summary, the presence of two idealized sorption environments in glassy polymers can complicate the analysis of sorption enthalpies due to different energetics associated with the two types of sites. To properly decouple the enthalpy change associated with sorption in the two domains, the temperature dependencies of the dual-mode parameters should be measured; however, this much more rigorous and extensive work was not possible in the time available. According to our original hypothesis regarding the difference between CO_2, CH_4 and H_2S sorption in materials with varying fluorine content, it is hypothesized that ΔH_S associated with k_D would be less exothermic for CO_2 and CH_4 in 6F-PAI-2 and 3 relative to 6F-PAI-1 due to increased chain packing. Because of lower fluorine concentration in 6F-PAI-2 and 3, ΔH_S associated with the

temperature dependence of k_D is expected to become more exothermic relative to 6F-PAI-1 for H_2S.

6.2.4. Comparison of Permeation Activation Energy in the 6F-PAI Family

The permeability vs. temperature plots for 6F-PAI are shown in Figure 6.5. Table 6.6 contains the permeation activation energies for these materials. Due to the anomalous sorption enthalpies shown for these polyamide-imides, the interpretation of the subsequent activation energies of diffusion, E_D, are not useful in terms of our hypothesis regarding the reversed H_2S/CH_4 diffusion selectivity that was shown in section 6.1. Instead, the E_D values in the easier to understand polyimides will be used to test our hypothesis. The activation energies of diffusion in the polyamide-imides are given for reference in Appendix B. In accordance with the trends reported by others [1,6,7], the permeation activation energies in the 6F-PAI series increase with size of the penetrant. Because in general diffusion is an activated process (endothermic), and $|E_D| > |\Delta H_S|$ for all gases in most conventional polymeric materials, permeation activation energy is weighted more heavily by E_D. Thus, permeation is an activated process which increases with temperature. This behavior is shown in 6F-PAI-1,2 and 3.

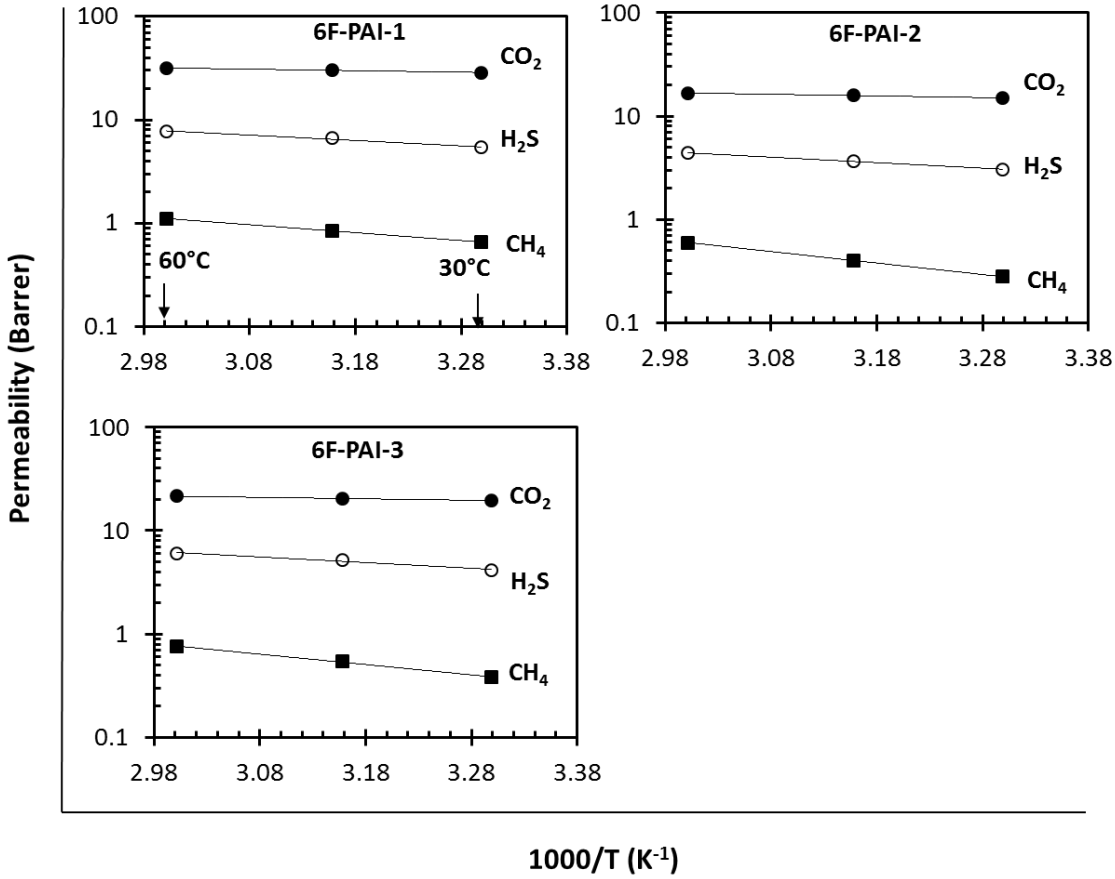

Figure 6.5: Temperature dependence of the permeability coefficients in the 6F-PAI series at 40 psia.

Table 6.6: Activation energies of permeation for the 6F-PAI series at 40 psia.

ΔE_P (kJ/mol)	*6F-PAI-1*	*6F-PAI-2*	*6F-PAI-3*
CH_4	15 ± 0.30	21 ± 0.40	19 ± 0.19
CO_2	2.9 ± 0.032	3.1 ± 0.12	2.7 ± 0.27
H_2S	9.8 ± 0.63	10 ± 0.012	11 ± 0.66

Comparison of E_P between 6F-PAI-1,2 and 3 shows that only E_P for CH_4 in 6F-PAI-2 and 3 increased relative to 6F-PAI-1. The permeation activation energy for CO_2

and H_2S is not significantly different between the three materials. This result is consistent with the CO_2/CH_4 and H_2S/CH_4 permselectivities reported in Chapter 5, where an increase in permselectivity for both gas pairs was shown in 6F-PAI-2 and 3 relative to 6F-PAI-1. It follows then that permselectivity, which is determined by the difference in E_P between a given gas pair, will be a stronger function of temperature in 6F-PAI-2 and 3. The temperature dependence on the permselectivities is discussed in the next paragraph.

The permeation selectivities versus temperature plots for the 6F-PAI series are shown in Figure 6.6.

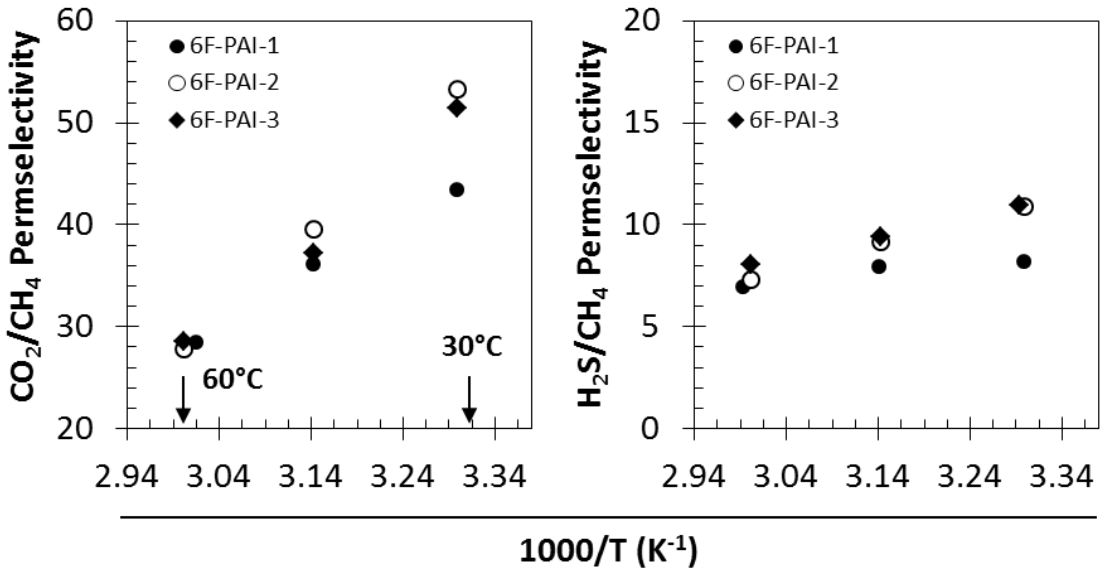

Figure 6.6: Permselectivity versus temperature for CO_2/CH_4 and H_2S/CH_4 in the 6F-PAI series at 40 psia.

As shown in Figure 6.6, CO_2/CH_4 and H_2S/CH_4 permselectivity in 6F-PAI-2 and 3 show greater dependence on temperature relative to 6F-PAI-1 in accordance with their

higher ΔE_P values. For the H_2S/CH_4 pair, 6F-PAI-1 shows only a marginal decrease in permselectivity, and is consistent with lower ΔE_P compared to 6F-PAI-2 and 3. In general, the lower fluorinated polyamide-imides 6F-PAI-2 and 3 are more selectivity for both gas pairs compared to 6F-PAI-1, and the temperature dependence of both selectivities in the former materials is a stronger function of temperature. For all materials, H_2S/CH_4 permselectivity shows lower temperature dependence than does CO_2/CH_4 permselectivity, and is consistent with lower mobility selectivity for the H_2S/CH_4 pair, as mobility differences are the primary mechanism for selective permeation of one gas relative to another in glassy polymers. Therefore, higher temperatures will be less detrimental to the H_2S/CH_4 permselectivity compared to CO_2/CH_4.

6.3. Analysis of 6FDA Polyimides

6.3.1. Physical Properties

Because uncrosslinked polyimides such as 6FDA-6FpDA (6F-6F) and 6FDA-IpDA (6F-Ip) are vulnerable to penetrant induced plasticization at low feed pressures, they are not appropriate for aggressive gas separations such as CO_2 and H_2S from natural gas. However, small changes in the fluorine concentration in the polymer backbone can provide valuable information on the effect of physiochemical interactions on the gas transport properties. The only difference between these two materials arises from the replacement of CF_3 groups in 6F-6F with CH_3 groups in 6F-Ip. Such a subtle change to the backbone allows one to more easily identify its effect on the membrane physical and transport properties. The structure of 6F-6F was presented in Chapters 4 and 5. The

molecular structure of 6F-Ip is shown in Figure 6.7. The physical properties of both materials are given in Table 6.7. The cohesive energy density, solubility parameter, and dielelectric constant were predicted from group contribution methods as given in the reference [13].

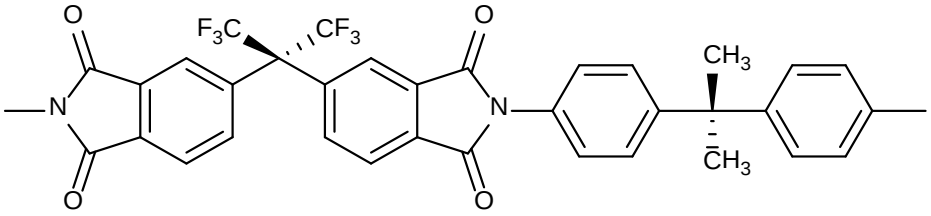

Figure 6.7: Molecular **s**tructure of 6FDA-IpDA.

Table 6.7: Physical properties of 6FDA based polyimides. T_g and *FFV* for 6FDA-IpDA were adapted from Coleman et al. [14].

	T_g (°C)	*CED (J/cc)*	δ ($J^{1/2}/cc^{3/2}$)	*Dielectric constant*	*[F] (mmol/cc)*	*FFV*
6FDA-6FpDA	320	450	21.2	3.3	23.66	0.17
6FDA-6IpDA	310	500	22.4	3.3	12.8	0.16

In general, introduction of bulky groups, such as CF_3, along the polymer main chain disrupt chain packing and increase free volume, which is similar to the effect that was shown in the 6F-PAI series in Chapter 5. It follows then that CO_2 sorption is lower in 6F-Ip compared to 6F-6F. The sorption isotherms are given in Figure 6.8. Replacement of CF_3 groups with CH_3 results in significantly lower fluorine concentration along the polymer backbone, which correlates with higher *CED*. This can be attributed to lower

free volume in 6F-Ip, which increases the force of attraction between the polymer chains per unit volume of polymer.

In the absence of specific polymer-penetrant interactions, gas sorption depends mainly on penetrant condensability. For a given penetrant, the sorption coefficient in different materials tends to vary with polymer free volume. Higher free volume materials can accommodate more penetrant. This is reflected in the concentration isotherms for 6F-6F and 6F-Ip, which are given in Figure 6.8. Higher CO_2 sorption is shown in higher free volume 6F-6F, and this higher sorption is particularly pronounced at elevated pressures, where penetrant gas saturates the Langmuir regions and sorption occurs mainly by dissolution into the densely packed environments. Consequently, k_D for CO_2 is higher in 6F-6F compared to 6F-Ip. Langmuir capacity is lower in 6F-Ip, which is likely due to the effect of the smaller CH_3 groups compared to CF_3 in 6F-6F. The bulky CF_3 groups along the main chain in 6F-6F disrupt equilibrium chain packing to a greater extent, thus, higher amounts of excess free volume become trapped into the polymer matrix. Aside from free volume effects, CO_2's higher sorption in 6F-6F may also be due to more favorable interactions with the C-F groups in 6F-6F. Teja et al. suggested that the lone pair electrons of the fluorine atom can interact with CO_2 in a Lewis acid/base type of interaction, with CO_2 participating as the Lewis acid [15]. The dual-mode parameters for the CO_2 and H_2S concentration isotherms shown in Figure 6.8 are given in Table 6.8.

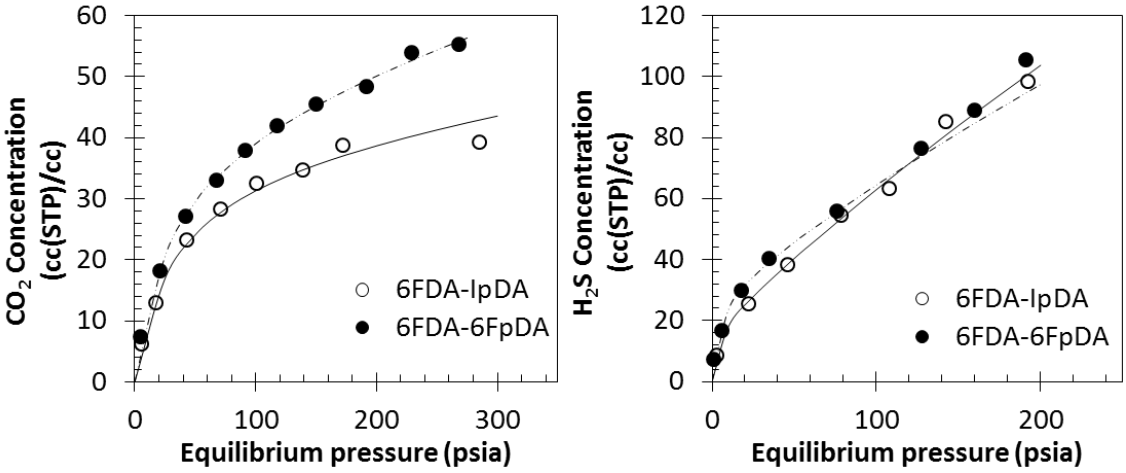

Figure 6.8: CO_2 and H_2S concentration vs. pressure isotherms at 35°C in 6FDA-6FpDA and 6FDA-IpDA. The solid lines represent dual-mode fits to the data.

Table 6.8: Dual-mode parameters at 35°C for CO_2 and H_2S in 6FDA-6FpDA and 6FDA-6IpDA.

	6FDA-6FpDA		*6FDA-6IpDA*	
	CO_2	H_2S	CO_2	H_2S
k_D *(cc(STP)/cc·psia)*	0.08	0.38	0.04	0.5
C_H' *(cc(STP)/ccpolymer)*	41.4	30.19	36.6	18.8
b (psia-^{1})	0.03	0.19	0.03	0.2

Similar to the trend shown in the 6F-PAI series in Chapter 5, H_2S sorption is nearly the same in both higher (6F-6F) and lower (6F-Ip) free volume materials despite lower CO_2 sorption in 6F-Ip. A closer look at Figure 6.8 and Table 6.8 reveals an increase in the Henry's constant for H_2S in 6F-Ip, whereas C_H' for H_2S is lower in the same material. Therefore, enhanced H_2S sorption capacity relative to CO_2 capacity in 6F-Ip can be attributed to higher sorption in the densely packed environments. Such higher

H_2S sorption in the Henry's type environments in less fluorinated materials is similar to what was observed in the 6F-PAI series as shown in Chapter 5. It appears that fluorine concentration along the polymer backbone mainly affects dissolution of H_2S in the more packed regions relative to the excess free volume microvoids. This picture seems reasonable, as sorption in packed environments requires more energy for polymer penetrant mixing relative to sorption in a packing defect. Thus, intermolecular forces, which can affect the polymer penetrant interaction energy, have a greater impact on penetrant mixing in the more closely packed regions. Indeed, in the previously cited article by Merkel et al., the most striking difference between fluorocarbon and hydrocarbon penetrant solubility occurred in rubbery PDMS, which is devoid of any non-equilibrium packing defects. Additionally, the difference in sorption between the two types of penetrants in glassy polymers was more apparent with increasing pressure, indicating that at very low pressures, sorption into packing defects provides a relatively nonspecific site for penetrant sorption that is mainly controlled by penetrant size and condensability [6]. Thus, lower fluorine concentration in 6F-Ip likely affects H_2S polymer-penetrant interactions to a greater extent in the more densely packed regions of the polymer, thereby increasing its sorption relative to less polar CO_2. If such polymer-penetrant mixing is more energetically favorable, it should be reflected by a more exothermic sorption enthalpy for H_2S in 6F-Ip relative to 6F-6F. The sorption enthalpy data will be discussed next.

6.3.2. Comparison of Sorption Enthalpies in 6FDA Polyimides

Figure 6.9 depicts the temperature dependence of CO_2, CH_4 and H_2S sorption coefficients in 6F-6F and 6F-Ip at 40 psia. The sorption coefficients were plotted against 1/T in accordance with the van't Hoff expression. All plots show good linearity, confirming adherence to van't Hoff behavior with a constant enthalpy over the temperature range from 30 to 75°C. The sorption enthalpy, which represents the slope of the plot of *S* vs. 1/T divided by the gas constant, R, is given in Table 6.9.

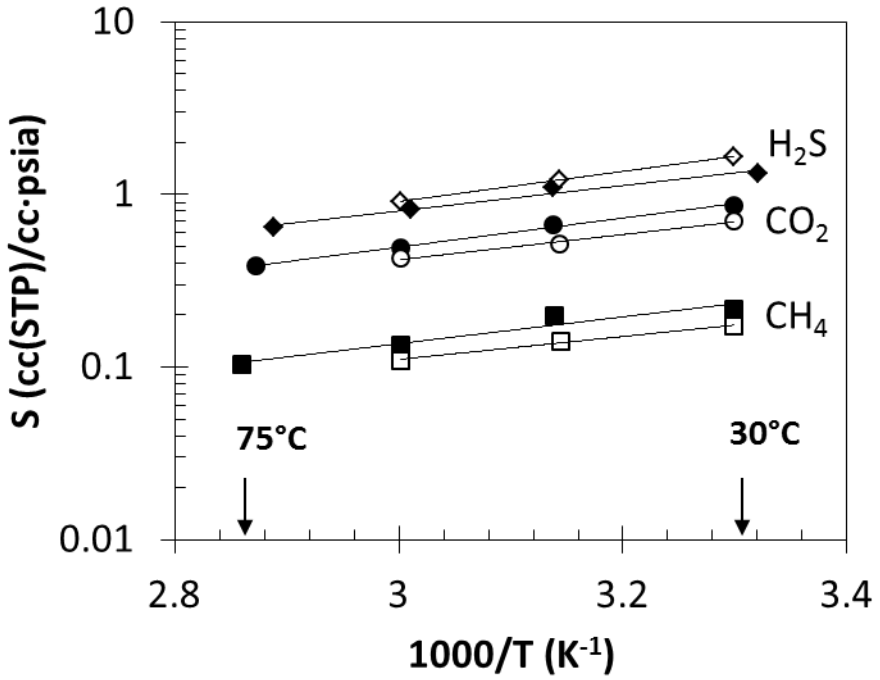

Figure 6.9: Temperature dependence of CO_2, CH_4 and H_2S sorption coefficients in 6FDA-6FpDA (**Filled symbols**) and 6FDA-IpDA (**Open Symbols**). Sorption coefficients were measured at ~40 psia.

Table 6.9: Enthalpy of sorption for 6FDA-6FpDA and 6FDA-6IpDA at ~40 psia.

ΔH_s (kJ/mol)	*6FDA-6FpDA*	*6FDA-IpDA*
CH_4	-14 ± 0.56	-13 ± 1.1
CO_2	-16 ± 0.78	-14 ± 1.4
H_2S	-14 ± 1.8	-17 ± 0.27

The sorption enthalpies for CO_2 and CH_4 in 6F-6F shown in Table 6.9 are in agreement with the values reported by Costello [9]. Comparison of the CO_2 and CH_4 values between 6F-6F and 6F-Ip demonstrates that gas sorption for these penetrants in lower free volume 6F-Ip is in general less exothermic than it is in higher free volume 6F-6F. For higher *CED* density in 6F-IpDA, as shown in Table 6.7, more energy is needed to open up the polymer chains in order to accommodate a penetrant. A similar trend was shown by Kim et al., who compared 6FDA-DAF to 6F-Ip [16]. 6FDA-DAF is a much more open structure relative to 6F-Ip. He showed slightly more exothermic sorption enthalpies for N_2, CO_2 and CH_4 in higher free volume 6FDA-DAF.

The trend in the H_2S sorption enthalpy shown in Table 6.9 and Figure 6.9 is opposite to what is shown for CO_2 and CH_4. That is, the heat of sorption for H_2S is *more exothermic* in lower free volume 6F-Ip, and supports our earlier hypothesis that H_2S sorption is more dependent on polymer-penetrant intermolecular interactions. Thus, lower unfavorable heat of mixing between H_2S and the polymer matrix of 6F-Ip may offset some of the work required to dilate the more tightly packed polymer chains in 6F-Ip, and H_2S sorption becomes more exothermic in the lower fluorinated material. Indeed, the Hildebrand solubility parameter for H_2S is 22.4, which is almost identical to the value

shown for 6F-Ip in table 6.7. This suggests that the intermolecular forces between like molecules (polymer-polymer and penetrant-penetrant) are similar to forces between unlike molecules (polymer-penetrant) in lower fluorinated 6F-Ip.

An interesting trend in 6F-6F is that the sorption enthalpy for H_2S does not correlate with penetrant critical temperature, as is usually the case with CO_2, CH_4, O_2, and N_2. Such a correlation is shown in Figure 6.10-A. Data from Costello's work on 6F-6F is also shown in Figure 6.10-A in order to obtain a more significant correlation. The sorption enthalpies in 6F-Ip are also correlated with critical temperature, and are given in Figure 6.10-B. Sorption enthalpy for N_2 in 6F-Ip was gathered from Kim's data [16], while the enthalpy in 6F-Ip for the other gases was measured in our work.

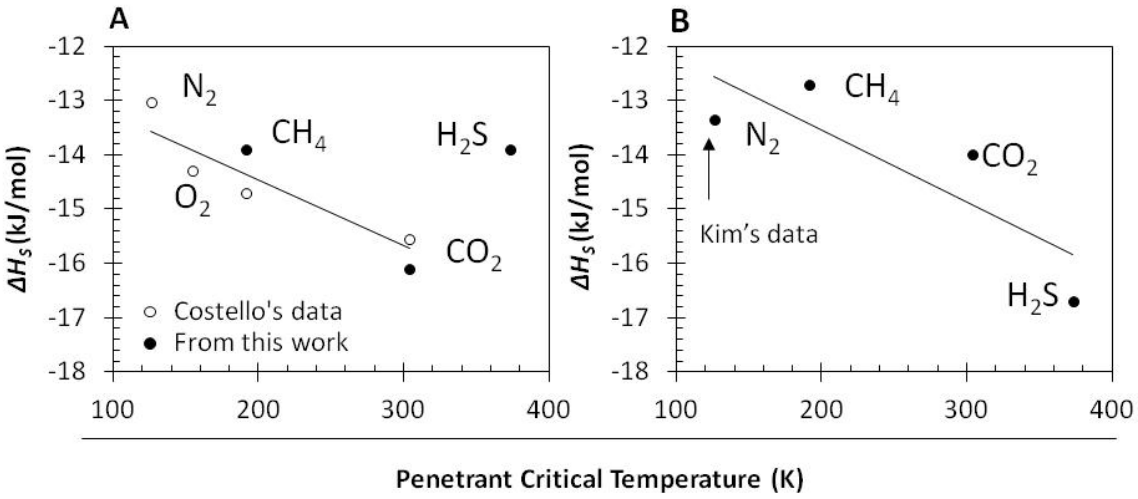

Figure 6.10: Sorption enthalpy vs. penetrant critical temperature in **A)** 6FDA-6FpDA and **B)** 6FDA-IpDA. Additional data for 6FDA-6FpDA and N_2 in 6FDA-IpDA was obtained from Costello's and Kim's thesis [1, 11].

For most gases, the enthalpy of mixing term is low compared to the enthalpy of "condensation", and the sorption enthalpy depends mostly on gas condensability. This is

the reason that CH_4 sorption is usually more exothermic than N_2 despite the fact that it has a larger critical volume. The enthalpy of sorption for H_2S in Figure 6.10-A is anomalously low (less exothermic) considering its critical temperature. In fact, its sorption enthalpy is not significantly different than that of CH_4. Because H_2S and CH_4 have similar critical volumes of approximately 99 cc/mol, the fact that they have similar total sorption enthalpy despite a much larger difference in critical temperature (ΔT_c=183 K) compared to the difference between N_2 and CH_4 (ΔT_c=37 K) suggests that the enthalpy of mixing for H_2S and the polymer in 6F-6F is considerably less favorable than it is for CH_4.

On the other hand, H_2S's sorption enthalpy in 6F-Ip correlates well with its critical temperature, which is shown in Figure 6.10-B. The enthalpy for N_2 in this figure, which was adapted from Kim's thesis, is anomalously exothermic; even more so than the enthalpy of CO_2 measured in the same work. This issue is not discussed in his thesis, however, it may be related to the phenomena behind the unusually more exothermic CH_4 sorption enthalpy in the 6F-PAI series in our work. A more meaningful correlation for 6F-Ip sorption vs. critical temperature would require more data points than what is presented in Figure 6.10-B, however the available sorption enthalpy data for 6F-Ip is limited. Nevertheless, the two correlations in Figure 6.10 suggest that the energetics of H_2S sorption are more dependent on intermolecular interactions with the polymer than are other less polar penetrants such as CO_2, CH_4, O_2 and N_2.

6.3.3. Analysis of Permeation and Diffusion Activation Energies in 6FDA Polyimides

The temperature dependence of the permeation coefficients was obtained from the slope of the plot of the ln(permeability) vs. 1/T, which is shown in Figure 6.11. The permeation activation energies for 6F-6F and 6F-Ip are tabulated in Table 6.10. The diffusion activation energies were calculated from Equation 6.3, and are also given in Table 6.10.

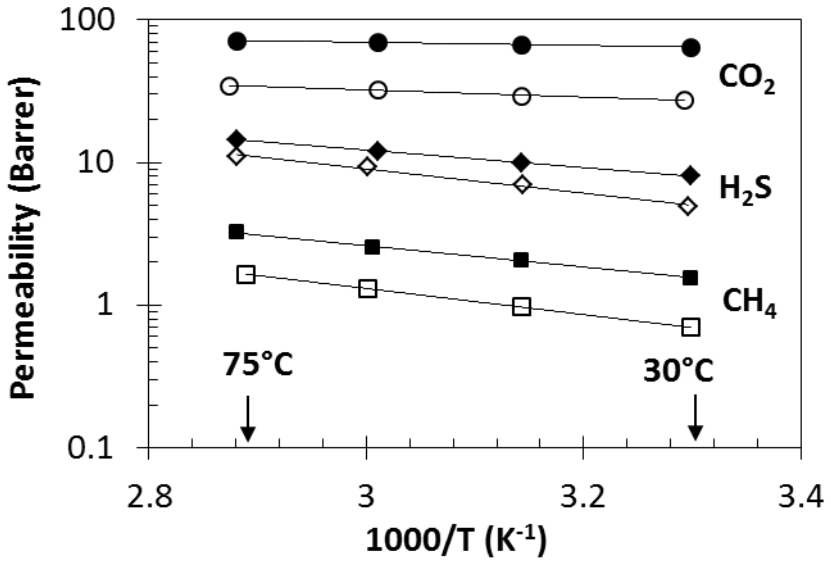

Figure 6.11: Temperature dependence of CO_2, CH_4, and H_2S permeability in 6F-6F (**Filled symbols**) and 6F-Ip (**Open symbols**).

Table 6.10: Permeation and diffusion activation energies in 6FDA-6FpDA and 6FDA-IpDA at 40 psia.

ΔE_P (kJ/mol)	*6FDA-6FpDA*	*6FDA-IpDA*
CH_4	14 ± 0.49	18 ± 0.27
CO_2	2.1 ± 0.10	5.0 ± 0.39
H_2S	12 ± 0.080	16 ± 1.3
ΔE_D (kJ/mol)		
CH_4	28 ± 1.5	30 ± 2.8
CO_2	18 ± 1.2	19 ± 2.4
H_2S	26 ± 3.3	33 ± 2.7

Analysis of the permeability vs. 1/T plots reveals increasing permeability with temperature, demonstrating that the activation energy of permeation is positive for all penetrants. As with the polyamide-imides, this activation energy increases with the size of the penetrant molecule. As such, CH_4 permeability shows the highest dependence on temperature. Carbon dioxide, the smallest molecule of the three, shows the smallest dependence on temperature. Hydrogen sulfide, whose kinetic diameter is intermediate between the two, shows permeation activation energy between CO_2 and CH_4. These trends are consistent with those shown by other authors, and demonstrate that gas permeation in these two materials is weighted more heavily by penetrant diffusion.

A comparison of the permeation activation energies between 6F-6F and 6F-Ip reveals lower E_P for all three gases in higher free volume 6F-6F. In general, such lower activation energies in 6F-6F can be attributed to both lower diffusion activation energies

as well as more exothermic sorption enthalpies. Greater disruptions to chain packing and lower *CED* reduce the energy required for polymer chain gap openings, thus, less energy is required for penetrant transport.

According to our earlier hypothesis regarding the unexpectedly reversed H_2S/CH_4 diffusion selectivity, more energy is needed for H_2S to overcome polymer-penetrant interactions prior to execution of a diffusive jump. This prediction is supported by the H_2S and CH_4 diffusion activation energies shown in Table 6.10, which shows higher E_D for H_2S compared to CH_4 in 6F-Ip. This is consistent with 6F-Ip's H_2S/CH_4 diffusion selectivity of less than 1. This interesting result is consistent with H_2S's higher ΔH_S value in 6F-Ip compared to 6F-6F. Because E_D for H_2S increased in 6F-Ip relative to 6F-6F to the greatest extent compared to CO_2 and CH_4, while only H_2S sorption enthalpy increased in the former material, these results certainly support, but do not prove, the our hypothesis that H_2S's diffusivity is closely linked in with its solubility.

For 6F-6F, E_D for CH_4 is slightly higher than E_D for H_2S. The H_2S/CH_4 diffusion selectivity for this material of 0.68 shown in Table 6.1 suggests that H_2S's diffusion activation energy should be higher than CH_4's. However, the data in Table 6.10 do not reflect this. The diffusivities obtained in Table 6.1 were obtained by the time-lag method. Diffusivities measured using this technique can be suppressed by penetrant immobilization in the low energy Langmuir sorption sites. According to the derivation of the dual-mode permeability model in Chapter 2, only a mobile fraction, *F*, of molecules sorbed into such microvoids contributes to the overall penetrant flux. It is likely that increased sorption of H_2S in such microvoids causes a greater portion of molecules to become trapped in these microvoids as compared to CH_4. Thus, this retardant diffusion of

H_2S can lead to longer time lags and hence lower apparent H_2S diffusivities compared to CH_4. Additionally, the mobility factor, *F*, for H_2S, is expected to be lower than it is for CH_4, as is the case for most condensable gases compared to relatively non-condensable ones. Others have demonstrated lower values of *F* for gases with higher condensability [17]. In, conclusion the less than unity H_2S/CH_4 diffusion selectivity observed in all of the polymers discussed in this project may be due to a combination of polymer-penetrant interactions, which increases the activation energy of H_2S relative to CH_4, and dual-mode effects, which tend to cause greater immobilization of H_2S molecules in the excess free volume microvoids.

6.3.4. Selectivity Dependence on Temperature in the Polyimides

6.3.4.1. Temperature Dependence of 6FDA Polyimide Sorption Selectivity

The temperature dependence of the sorption selectivities for H_2S/CH_4 and CO_2/CH_4 in the polyimides is shown in Figure 6.12. As can be observed, CO_2/CH_4 sorption selectivity shows only a minor decrease with increasing temperature up to 75°C. This is due to CO_2's more exothermic heat of sorption compared to CH_4. At most, however, only a 6.5% decrease in selectivity is observed, which occurs in 6F-6F. Furthermore, both 6F-6F and 6F-Ip show almost identical CO_2/CH_4 sorption selectivities as well as a similar temperature dependence of this selectivity. For these two similar materials, CO_2/CH_4 sorption selectivity is more dependent on the gas properties, such as condensability, rather than material properties such as free volume and polymer-penetrant interactions.

The H_2S/CH_4 sorption selectivity for 6F-Ip in Figure 6.12-B shows a similar trend of decreasing selectivity with higher temperature. However, the difference in sorption enthalpy between H_2S and CH_4 is greater than CO_2 and CH_4, thus a 13% decrease in H_2S/CH_4 selectivity occurs in 6F-Ip. For 6F-6F, the sorption selectivity is essentially unchanged up to 75°C. This is due to similar heats of sorption for H_2S and CH_4 in this material as a result of its higher fluorine concentration. These results suggest that an increase in temperature is likely to be more detrimental to H_2S/CH_4 sorption selectivity than for the CO_2/CH_4 pair. However, in highly fluorinated materials such as 6F-6F, the sorption selectivity for H_2S/CH_4 may not be significantly affected due to similar heats of sorption between the two penetrants. This is presumed to be the result of more unfavorable intermolecular interactions between the highly fluorinated polymer matrix and H_2S.

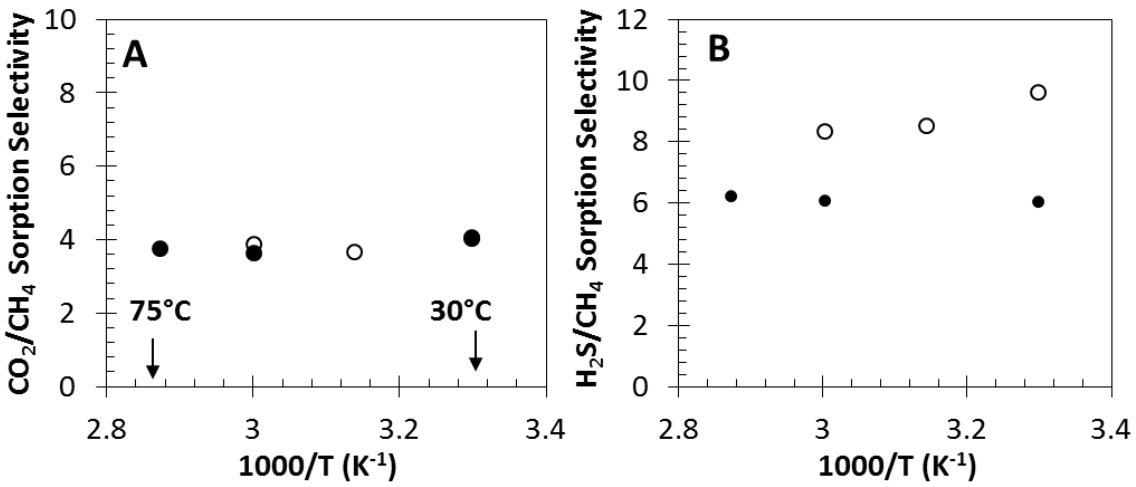

Figure 6.12: Temperature dependence of **A)** CO_2/CH_4 and **B)** H_2S/CH_4 sorption selectivity in 6F-6F (**Closed symbols**) and 6F-Ip (**Open Symbols**).

6.3.4.2. Temperature Dependence of 6FDA Polyimide Diffusion and Permselectivity

The diffusion selectivities for both CO_2/CH_4 and H_2S/CH_4 as a function of temperature are shown in Figure 6.13. As can be observed, the CO_2/CH_4 selectivity shows a much stronger dependence on temperature, which is consistent with higher ΔE_D compared to the H_2S/CH_4 pair. A significant decrease in CO_2/CH_4 diffusion selectivity for both 6F-6F and 6F-Ip suggests that in these materials, increases in temperature will be highly detrimental to CO_2/CH_4 permselectivity, as is the case with most glassy polymers.

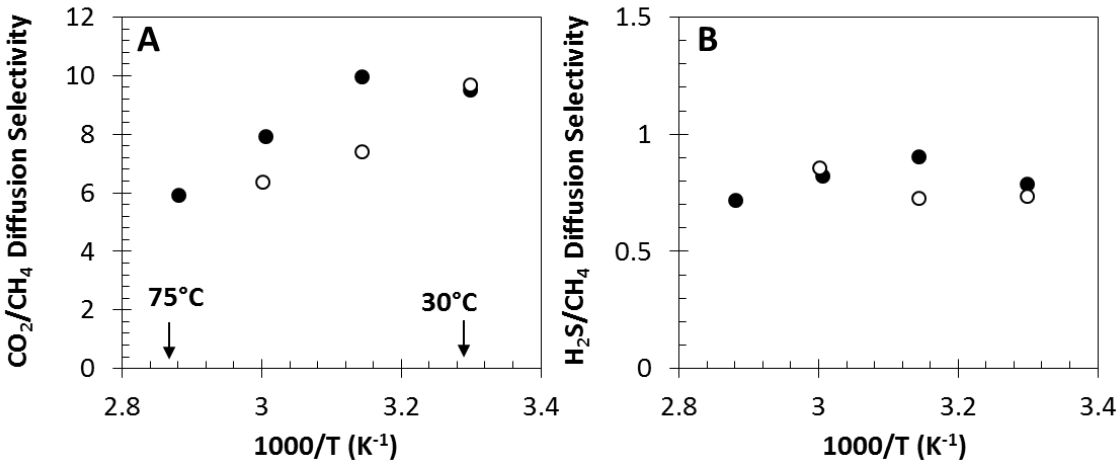

Figure 6.13: Diffusion selectivities at 40 psia for **A)** CO_2/CH_4 and **B)** H_2S/CH_4 in 6FDA-6FpDA (**Closed Symbols**) and 6FDA-IpDA (**Open symbols**).

For both 6F-6F and 6F-Ip, a much lower dependence on temperature is observed for H_2S/CH_4 diffusion selectivity. At 30°C, diffusion selectivity is approximately 0.80 for both materials, which is in good agreement with that predicted by time-lag measurements shown in Table 6.1. At higher temperatures, diffusion selectivity in 6F-Ip actually increases, which is consistent with H_2S's higher E_D in this material. On the other hand, H_2S/CH_4 diffusion selectivity in 6F-6F is essentially unchanged, which is due to the fact

that E_D for H_2S and CH_4 are the same. Based on these results, it can be concluded that higher temperatures do not affect the H_2S/CH_4 mobility selectivity to a great extent therefore, permselectivity in glassy polymers for this gas pair will likely be less susceptible to temperature induced decreases as it is for the CO_2/CH_4 pair.

It is interesting to note that H_2S/CH_4 diffusion selectivity is much less than one in 6F-6F, however, E_D for these two gases is essentially the same. The enthalpy of sorption values for this gas pair in 6F-6F are also very similar. As proposed in section 6.3.3, lower H_2S *diffusivities* compared to CH_4 in 6F-6F may be the result of H_2S partial immobilization in the low energy Langmuir sorption environments rather than lower frequency of activated polymer chain gap openings as is typically envisioned to control a so called diffusion jump. The mobility factor, *F*, as well as the temperature dependencies of the Langmuir and Henry's diffusivities, D_H and D_D respectively, can provide additional insight into mobility within the dual-modes. This information could help decouple the effects of chain mobility controlled diffusivity, which would be reflected in D_D, and penetrant trapping in Langmuir holes, as interpreted through D_H. In order to obtain these parameters, one would need to determine the pressure dependence of H_2S's permeability. However, 6F-6F's susceptibility to plasticization at low pressures makes it difficult to obtain such a relationship due to an upswing in permeability at low pressure.

On the other hand, in lower fluorinated 6F-Ip, the diffusion activation energy is higher for H_2S than it is for CH_4. This correlates with an increase in the heat of sorption for H_2S relative to its sorption enthalpy in higher fluorinated 6F-6F. These results suggest that H_2S diffusivity in lower fluorinated 6F-Ip may be hindered by more favorable polymer-penetrant intermolecular forces. Such forces are envisioned to increase the

energy barrier beyond what is required for a thermally activated "packet" of concomitant free volume to form between the polymer chains. The results of this section show that, in general, polymer membranes cannot achieve a molecular sieving effect on the H_2S/CH_4 gas pair, and development of materials targeted for this separation should focus on a solubility approach.

The temperature dependence of the permselectivities in 6F-6F and 6F-Ip are shown in Figure 6.14.

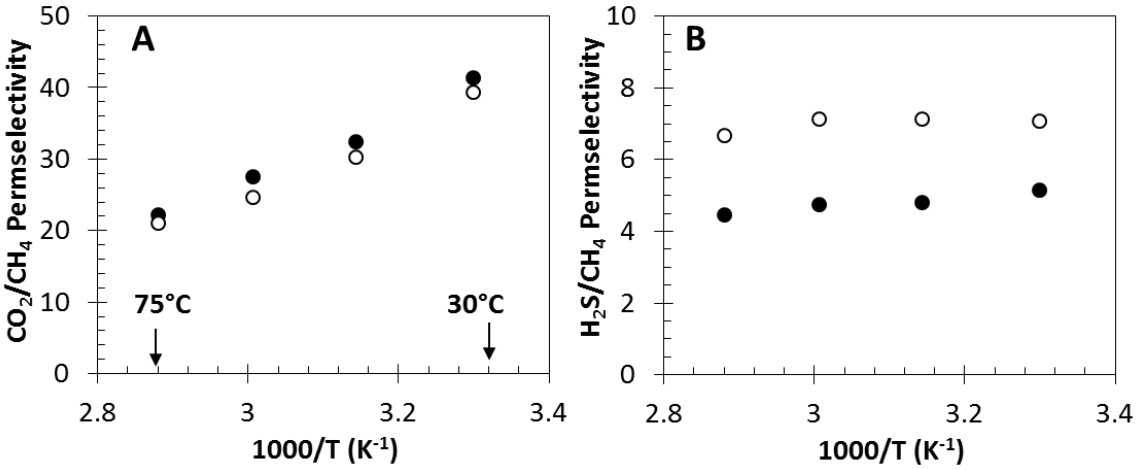

Figure 6.14: Permselectivity vs. temperature at 40 psia for **A)** CO_2/CH_4 and **B)** H_2S/CH_4 in 6FDA-6FpDA (**Closed circles**) and 6FDA-6IpDA (**Open circles**).

Due to the larger dependence of the permselectivity on the diffusion selectivity compared to sorption selectivity for the CO_2/CH_4 pair, the temperature dependence of the CO_2/CH_4 permselectivity is controlled by its diffusion selectivity's response to increasing temperature. As such, CO_2/CH_4 permselectivity in Figure 6.14-A decreases sharply with increasing temperature. The effect of temperature on the H_2S/CH_4 permselectivity is much lower in both 6F-6F and 6F-Ip. Due to very similar H_2S and CH_4 sorption enthalpies and diffusion activation energies in 6F-6F, permselectivity shows only a minor

reduction with higher temperature. For 6F-6F, the loss in permselectivity can be attributed to a small loss in diffusion selectivity as was shown in Figure 6.13-B. In 6F-Ip, the loss in solubility selectivity that was shown in Figure 6.12 is slightly offset by a small increase in diffusion selectivity, and H_2S/CH_4 permselectivity is nearly constant over 30 to 75°C, decreasing by only about 5%.

These interesting results highlight the differences between H_2S and CO_2 transport in polymer membranes. As demonstrated in the previous sections, CO_2/CH_4 permselectivity is controlled by mobility differences between the two penetrants. Thus, tailoring of membrane structure should focus on controlling free volume and chain mobilities. On the other hand, H_2S/CH_4 permselectivity is controlled entirely by solubility differences between H_2S and CH_4. Although H_2S is smaller than CH_4 based on kinetic diameter, it shows no diffusive advantage over CH_4 in any of the materials tested in this work. A combination of polymer-penetrant intermolecular interactions, which H_2S must overcome prior to executing a diffusive jump, as well as partial immobilization of H_2S molecules in glassy microvoids, contribute to an H_2S/CH_4 mobility selectivity for this pair that is less than 1 in all materials, both rubbery and glassy, that were tested in this work. Thus, membrane development targeting higher H_2S selectivity should improve upon solubility selectivity.

6.4. Conclusion

The temperature dependencies of permeation, diffusion, and sorption for CO_2, CH_4 and H_2S were measured in the 6F-PAI series, as well as in a series of structurally similar 6FDA based polyimides. For CH_4 in the 6F-PAI materials, very low sorption in

the densely packed regions resulted in an apparent heat of sorption that appeared to be more exothermic than CO_2 and H_2S because CH_4 partitioned primarily into the low energy Langmuir sites. The permeation activation energies were also measured independently, and were consistent with trends observed by others. That is, activation energy was positive and increased with kinetic diameter of the gas, demonstrating the permeability coefficient's higher dependence on diffusion.

For the similar 6FDA based *polyimides*, the sorption enthalpy for H_2S was *more exothermic* in less fluorinated 6FDA-IpDA (6F-Ip) compared to 6FDA-6FpDA (6F-6F), whereas CO_2 and CH_4 sorption enthalpy were *less exothermic* in the former material compared to the latter. These results support our hypothesis that H_2S sorption depends more on intermolecular interactions than does the sorption of CO_2 and CH_4. Furthermore, the activation energy of diffusion, E_D, for H_2S was higher than CH_4 in 6FDA-IpDA, while E_D for H_2S was lower than CH_4 in more fluorinated 6FDA-6FpDA. Higher E_D for H_2S in 6FDA-IpDA is consistent with its H_2S/CH_4 diffusion selectivity of less than 1. The less than unity H_2S/CH_4 diffusion selectivity in 6F-6F, however, cannot be interpreted simply from differences in diffusion activation energy. The reversed diffusion selectivity in 6F-6F is believed to be due to partial immobilization of H_2S in the glassy microvoids, which reduces the effective diffusion coefficient for H_2S relative to CH_4. As a result of similar diffusion activation energies in 6FDA-6FpDA, H_2S/CH_4 diffusion selectivity showed almost no dependence on temperature up to 75°C. For 6F-Ip, diffusion selectivity was slightly *increased* due to H_2S's higher diffusion activation energy relative to CH_4. As a result, H_2S/CH_4 permselectivity was only marginally reduced in both polyimides at

temperatures up to 75°C, which is in marked contrast to the highly temperature dependent CO_2/CH_4 permselectivity.

In summary, H_2S/CH_4 diffusion selectivity in polymeric materials is in general limited to values near unity or below due to a combination of H_2S immobilization in the Langmuir sorption sites and a higher activation barrier due to more favorable interactions between H_2S and the polymer chains. Additionally, H_2S sorption capacity appears to depend more on intermolecular interactions with the polymer than does CO_2 and CH_4. Therefore, the selective removal of H_2S from natural gas is mostly a thermodynamic separation, and efforts aimed at advanced separation materials should focus on such rather than targeting a kinetic separation.

6.5. References

[1] L. M. Costello, "Temperature Dependence of Gas Sorption and Transport Properties," *PhD Dissertation,* University of Texas at Austin, Austin, Texas, (1994).

[2] B. Meares, "The Diffusion of Gases Through Polyvinyl Acetate, *Journal of the American Chemical Society,***76** (13), 3415-3422, (1954).

[3] Z.-K. Xu, M. Böhning, J. Springer, N. Steinhauser, R. Mülhaupt, "Gas transport properties of highly fluorinated polyamideimides," *Polymer*, **38** (3), 581–588, (1997).

[4] T. Mohammadi, M. T. Moghadam, M. Saeidi, and M. Mahdyarfar, "Acid Gas Permeation Behavior Through Poly (Ester Urethane Urea) Membrane," *Society*, pp. 7361–7367, 2008.

[5] K. Ghosal and B. D. Freeman, "Gas separation using polymer membranes: an overview," *Polymers for Advanced Technologies*, **5** (11), 673–697, (1994).

[6] T. C. Merkel, V. Bondar, K. Nagai, B. D. Freeman, "Sorption and Transport of Hydrocarbon and Perfluorocarbon Gases in Poly(1-trimethylsilyl-1-propyne), *Journal of Polymer Science: Part B: Polymer Physics*, **38,** 273-296, (2000).

[7] T. C. Merkel, V. Bondar, K. Nagai, B. D. Freeman, “Hydrocarbon and Perfluorocarbon Gas Sorption in Poly(dimethylsiloxane), Poly(1-trimethylsilyl-1-propyne), and Copolymers of Tetrafluoroethylene and 2,2-Bis(trifluoromethyl)-4,5- difluoro-1,3-dioxole,” *Macromolecules*, **32** (2), 370–374, (1999).

[8] T. C. Merkel and L. G. Toy, “Comparison of Hydrogen Sulfide Transport Properties in Fluorinated and Nonfluorinated Polymers,” *Macromolecules*, **39** (22), 7591–7600, (2006).

[9] L. M. Costello and W. J. Koros, “Effect of structure on the temperature dependence of gas transport and sorption in a series of polycarbonates,” *Journal of Polymer Science Part B: Polymer Physics*, **32** (4), 701–713, (1994).

[10] D. C. Harris, *Quantitative Chemical Analysis, Sixth edition*, (W.H. Freeman and Company, New York, New York, 2003).

[11] G. R. Husk, T.-H. Kim, W.J. Koros, "Temperature Effects on Gas Permselection Properties in Hexafluoro Aromatic Polyimides," *Journal of Membrane Science*, **46**, 43-56, (1989).

[12] S.P. Chen, J.A.D. Edin, "Fickian Diffusion of Alkanes Through Glassy Polymers: Effects of Temperature, Diffusant Size, and Polymer Structure, *Polymer Engineering and Science*, **20** (1), 40-50, (1980).

[13] D.W. Van Krevelen, *Properties of Polymers*, (Elsevier Science B.V., Amsterdam, The Netherlands, 1990).

[14] M. R. Coleman and W. J. Koros, “The transport properties of polyimide isomers containing hexafluoroisopropylidene in the diamine residue,” *Journal of Polymer Science Part B: Polymer Physics*, **32** (11), 1915–1926, (1994).

[15] A. Kasturirangan and A. S. Teja, “Correlation of Cloud Points in CO_2+fluorinated Polymer Systems †,” *Journal of Chemical & Engineering Data*, **55** (10), 4385–4389, (2010).

[16] T.-H. Kim, “Gas Sorption and Permeation In a Series of Aromatic Polyimides,” *PhD dissertation*, University of Texas at Austin, Austin, Texas, (1988).

[17] R. Wang, C. Cao, T-S. Chung, “A critical review on diffusivity and the characterization of diffusivity of 6FDA–6FpDA polyimide membranes for gas separation,” *Journal of Membrane Science*, **198** (2), 259–271, (2002).

CHAPTER 7

MIXED GAS SEPARATION CHARACTERIZATIONS

7.1 Introduction

In accordance with the general theme of this project, mixed gas testing is an extremely important technique for determining how a membrane material might perform under more industrially realistic conditions. While useful in characterizing the intrinsic separation properties under ideal conditions, pure gas measurements often overstate how well a material may perform for a given separation. In multicomponent feed conditions, especially at high total pressures as occurs at a natural gas well-head, the actual selectivity of a membrane is usually lower than the ideal selectivity estimated from pure gas measurements. Competitive sorption can reduce the sorption coefficient of the more permeable component, thereby reducing the fast gas permeability and ultimately the selectivity relative to pure gas values. Additionally, plasticization effects can cause considerable selectivity drops due to increasing permeability of all of the feed components. Because CH_4 does not cause plasticization, the effect of CO_2 and H_2S induced plasticization on its permeability cannot be assessed using pure gas conditions. Therefore, in order to truly say a material is high performance, it is necessary to determine how its selectivity holds up under conditions that more closely resemble a real industrial separation for a given gas pair. For natural gas separations, these conditions include high pressures (800 psia or greater) and concentrations of CO_2 and H_2S that are similar to what may be found in an actual natural gas well.

As many materials in the literature have been characterized using binary feeds composed of CO_2 and CH_4, we will first present the mixed gas permeation results for 6F-PAI-2 and 3 using a 50/50 CO_2/CH_4 feed stream. Similar conditions were used to test the

separation performance of 6F-PAI-1 in Chapter 4. As will be shown, the results for all three polyamide-imides are quite promising in comparison to current industrial materials such as CA. Based on the relatively lower pure gas H_2S plasticization resistance in 6F-PAI-2 and 3, only 6F-PAI-2 was chosen out of these two materials for additional permeation tests using ternary feeds containing H_2S.

The bulk of this chapter will discuss the effects of H_2S concentration on the separation performance 6F-PAI-1 and 2 and compare them to Pebax®, a representative highly H_2S selective rubbery polymer. As previously discussed in Chapter 2, the total acid gas separation factor, which is shown in Equation 7.1, will be used as a figure of merit to compare total selectivity for CO_2 and H_2S over CH_4 between glassy and rubbery polymers.

$$SF_{TAG} = \left(\frac{y_{H2S} + y_{CO2}}{y_{CH4}} \right)_{perm} \Big/ \left(\frac{y_{H2S} + y_{CO2}}{y_{CH4}} \right)_{feed} \tag{7.1}$$

To test the effect of H_2S concentration on the total acid gas selectivity, the following two ternary composed feeds will be used: **(1)** An H_2S "lean" feed consisting of 5/45/50 $H_2S/CO_2/CH_4$ and **(2)** An H_2S "rich" feed consisting of 20/20/60 $H_2S/CO_2/CH_4$. In the H_2S lean feed, the H_2S flux relative to CO_2 will be low, therefore, SF_{TAG} will be more heavily weight by the relative permeation rates of CO_2 and CH_4. For the H_2S rich feed, the difference in the relative CO_2 and H_2S permeation rates will be much lower than in the lean feed. In such a case, SF_{TAG} is expected to become a stronger function of the relative H_2S and CH_4 fluxes. Therefore, higher H_2S selectivity is presumed to be more desirable in the H_2S "rich" feed streams, and the rubbery polymers may show better total acid gas selectivities. In the H_2S lean feeds, it is more desirable to have higher CO_2/CH_4

selectivity, and as such, glassy polymers are hypothesized to show better total acid gas selectivity factors. The ternary gas permeation testing will be presented in section 7.3 of this chapter, while the binary CO_2/CH_4 permeation results for 6F-PAI-2 and 3 will be discussed next.

7.2. Characterization of 6F-PAI-2 and 6F-PAI-3 using Binary CO_2/CH_4 Feed

To compare the separation performance of 6F-PAI-2 and 3 to 6F-PAI-1 in the absence of H_2S, a 50/50 CO_2/CH_4 feed stream was used. As CO_2 partial pressure in a real natural gas well can be well above 400 psia, the use of 50% CO_2 feed allows us to reach CO_2 partial pressures that are similar to what may be encountered in natural gas well [1,2]. Also, it has been well documented that such high CO_2 pressures can cause significant plasticization in many glassy polymers which otherwise show high ideal selectivity.

6F-PAI-2 and 3 dense film membranes were fabricated as described in the previous chapters. The CO_2 permeability and CO_2/CH_4 permselectivity versus pressure for both materials are shown in Figure 7.1.

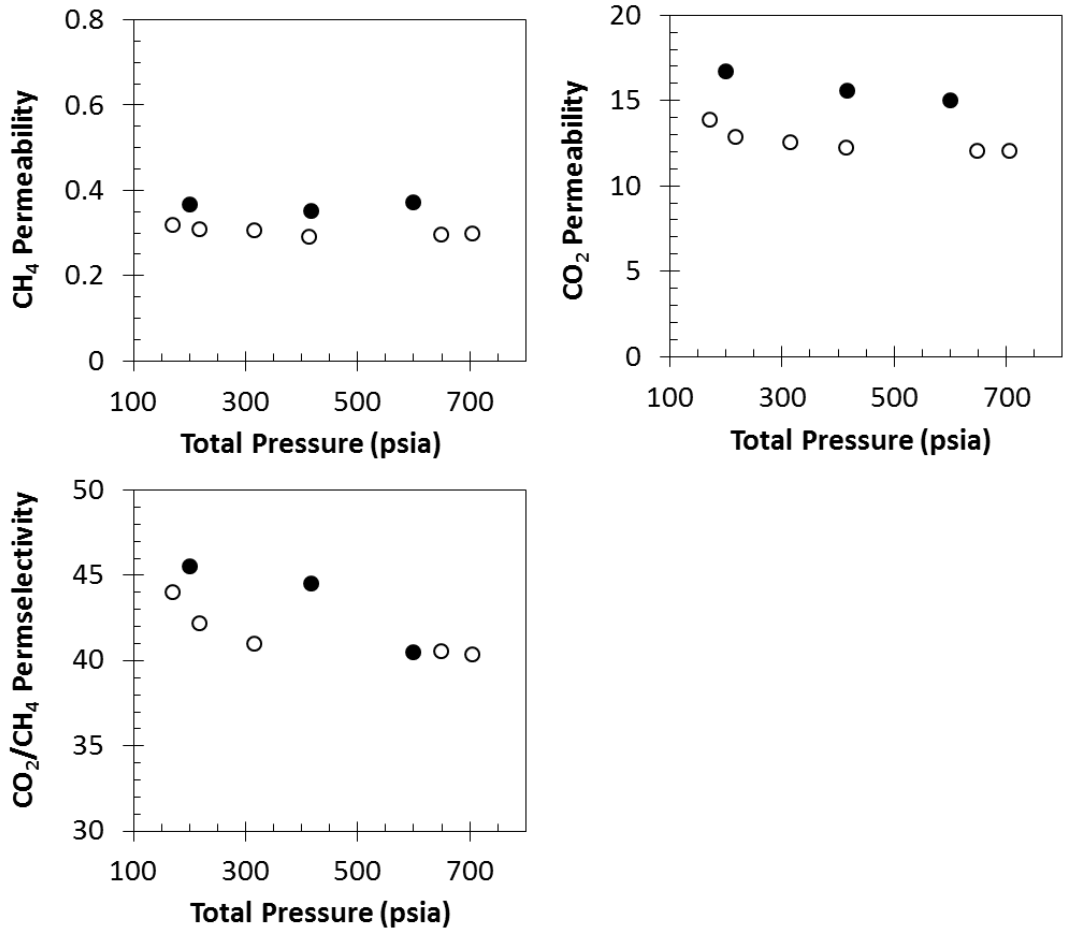

Figure 7.1: CO_2 and CH_4 50/50 mixed gas permeability and CO_2/CH_4 permselectivity in 6F-PAI-2 **(open symbols)** and 6F-PAI-3 **(closed symbols)**.
Units of permeability are Barrer.

As be seen in the Figure 7.1, both materials show high selectivity (40 or greater) throughout the entire pressure range. The decrease in selectivity with pressure shown for both materials coincides with decreasing CO_2 permeability with pressure as shown in 7.1-B. This reduction in CO_2 permeability is due to decreasing solubility with pressure as its Langmuir sorption capacity reaches saturation. For 6F-PAI-3, an upswing in CH_4 permeability is shown near 600 psia total pressure. This indicates the onset of plasticization. As a result, a sharp decrease in the permselectivity is shown at 600 psia. Because CO_2 permeability in 6F-PAI-3 is constant with pressure, the increase in CH_4 permeability is likely due to small, localized increases in chain mobility which increase

CH_4's diffusivity. This result highlights the importance of mixed gas testing. Recalling from Chapter 5, CO_2 permeability in the *pure gas* isotherm of 6F-PAI-3 was stable up to ~380 psia, which suggests plasticization in mixed gas testing will not occur until equivalent partial pressures are reached. However, CH_4 permeability in Figure 7.1-A begins to increase at a lower CO_2 *partial pressure* between 200 and 300 psia. Increasing concentrations of CO_2 can cause subtle increases in local segmental chain mobilities, which can have a greater effect on the diffusivity of the larger penetrant.

On the other hand, 6F-PAI-2 shows stable CH_4 permeability up to 750 psia total feed pressure. The CO_2/CH_4 permselectivity is ~40 at this pressure, which is roughly 20% below its ideal selectivity of 50 at 35 psia. As this material is uncrosslinked, such high selectivity under these conditions is quite promising. Most uncrosslinked pure polymer materials plasticize at lower pressures. For instance, under the same feed conditions, CA becomes plasticized near 390 psia total pressure, and its CO_2/CH_4 selectivity falls below 25 [3].

Because 6F-PAI-3 showed lower CO_2 plasticization resistance than 6F-PAI-2 based on Figure 7.1, it was not chosen for ternary gas permeation testing. Mixed gas testing in the presence of H_2S was only performed on 6F-PAI-1 and 2, as these materials showed better CO_2/CH_4 mixed gas performance. Furthermore, as demonstrated in Chapter 5, 6F-PAI-2 showed enhanced CO_2 plasticization suppression relative to 6F-PAI-1, however, its H_2S plasticization resistance appeared to be slightly lower than more fluorinated 6F-PAI-1. As such, a comparison between the two materials will show the effect that fluorine concentration has on the H_2S mixed gas separation performance.

7.3. Characterization of Mixed Gas Separation Performance in 6F-PAI-2 in the Presence of H_2S

Figure 7.2 shows the mixed gas CO_2, H_2S, and CH_4 permeability isotherms versus total feed pressure for 6F-PAI-2 using the H_2S "rich" feed composed of 20/20/60 $H_2S/CO_2/CH_4$.

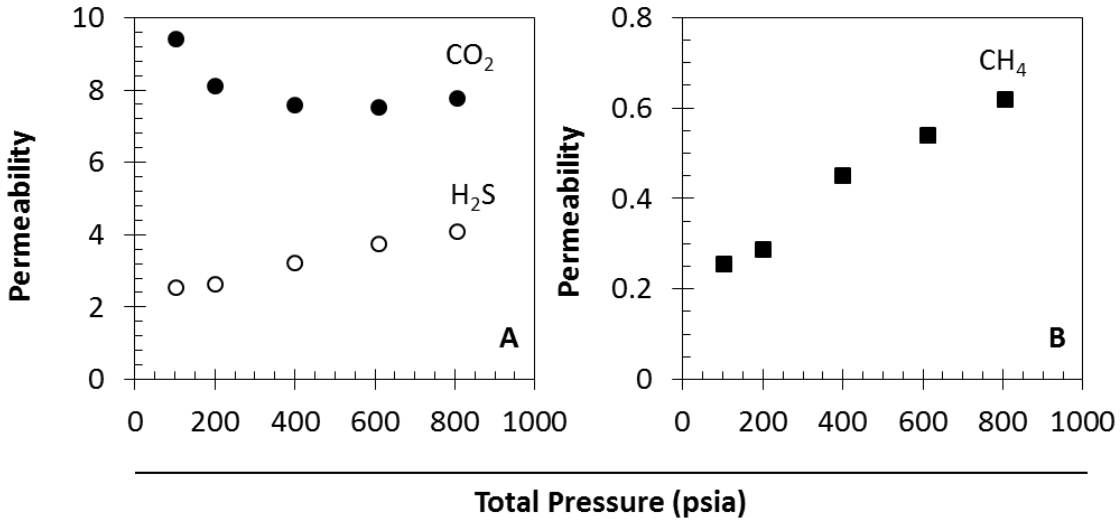

Figure 7.2: CO_2 and H_2S **(A)** and CH_4 **(B)** mixed gas permeability isotherms at 35°C. *Units of permeability are Barrer.*

As the data in Figure 7.2 demonstrate, the mixed gas separation performance in 6F-PAI-2 is significantly impacted in an undesirable manner in the presence of H_2S. This is signified by continual increase in both CH_4 and H_2S permeability throughout the entire pressure range. Carbon dioxide permeability, on the other hand, decreases up to approximately 600 psia, where beyond this pressure, CO_2 permeability also starts to increase. Because CO_2 displays the typical dual-mode response to increasing pressure up to 600 psia, the increase in CH_4 and H_2S are likely due to localized increases in chain mobility which only affect the larger gases, similar to the behavior shown in the binary feeds in the previous section. As CO_2's kinetic diameter is smaller than both H_2S and

CH_4 (3.3 versus 3.6 and 3.8 Å, respectively), such small scale increases in segmental chain mobility may not significantly affect its diffusivity until higher concentrations of CO_2 and H_2S in the membrane are reached.

Figure 7.3 shows the effect of increasing H_2S and CH_4 permeability on the CO_2/CH_4 and H_2S/CH_4 permselectivities.

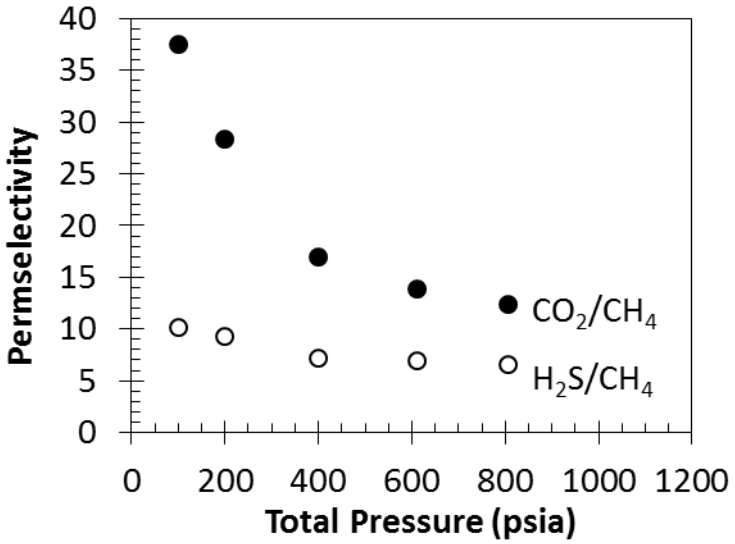

Figure7.3: CO_2/CH_4 **(filled circles)** and H_2S/CH_4 **(open circles)** permselectivity versus pressure for 6F-PAI-2 at 35°C.

As can be observed, a serious loss in CO_2/CH_4 permselectivity of over 50% coincides with the increase in CH_4 permeability. Permselectivity for H_2S/CH_4 decreases to a much lower extent, which is due to the accompanied increased in H_2S permeability with pressure. Considering 6F-PAI-2's very stable and highly selective mixed gas performance using a binary CO_2/CH_4 feed as shown in Figure 7.1, H_2S appears to have a significantly deleterious impact on 6F-PAI-2's separation performance. While these results are not very promising in terms of the overarching goal of this work, which is to develop highly robust materials for CO_2 *and* H_2S separation from natural gas, they are

very interesting and provide potentially useful information for future efforts aimed at material development for such a separation.

In order to verify that the results shown in Figure 7.3 were due to the presence of H_2S and not simply an experimental artifact, the membrane was degassed and evacuated for approximately one month while other permeation experiments were run, then reloaded into the permeation cell for additional mixed gas testing. A binary feed containing only CO_2/CH_4 at a composition of 50/50 was then applied to the upstream and a permeability isotherm was measured in a similar manner as has been used for all mixed gas testing in this work. Figures 7.4 and 7.5 show CO_2 and CH_4 permeability and CO_2/CH_4 permselectivity, respectively, versus pressure for the "H_2S conditioned" film.

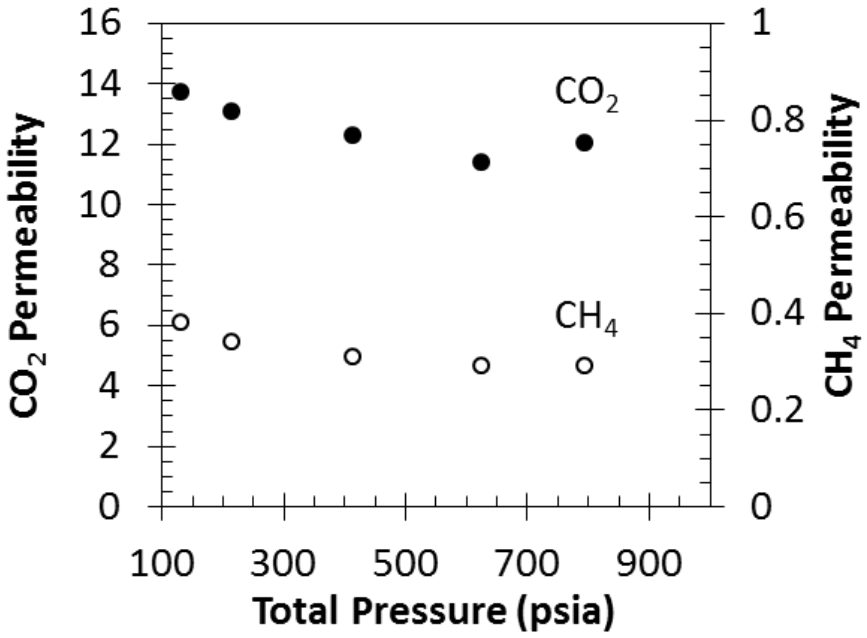

Figure 7.4: CO_2 and CH_4 permeability versus pressure in 6F-PAI-2 on the "H_2S conditioned" film using a 50/50 CO_2/CH_4 feed at 35°C.
Units of permeability are Barrer.

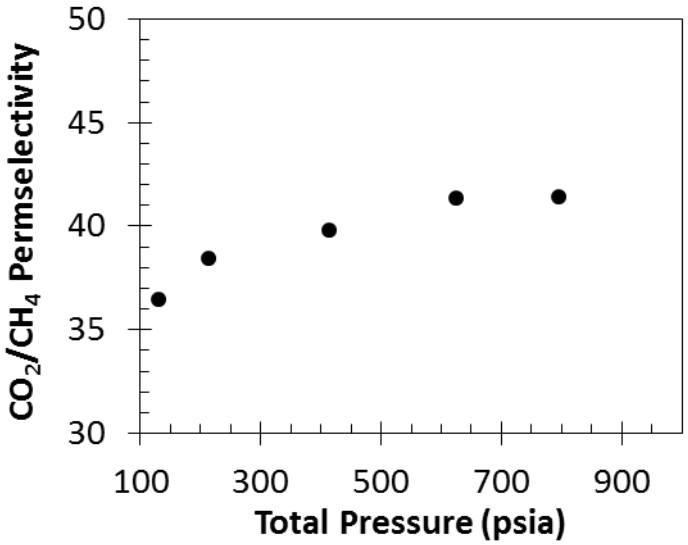

Figure 7.5: CO_2/CH_4 permselectivity in 6F-PAI-2 on the "H_2S conditioned" film using 50/50 CO_2/CH_4 feed at 35°C.

As can be observed in Figures 7.4 and 7.5, the permeability and selectivity behavior with increasing pressure is consistent with that of an unplasticized membrane. That is, both CO_2 and CH_4 permeability decrease continually with increasing pressure, which is characteristic of a so called dual-mode response with pressure in glassy polymers in the absence of plasticization. Therefore, the results shown in Figure 7.3 are in fact due to the presence H_2S, which has a significant plasticizing effect on the less fluorinated 6F-PAI-2. Due to such swelling, the transport properties at low pressures in the conditioned film are slightly different compared to the unconditioned film exposed to the same 50/50 CO_2/CH_4 binary feed shown in section 7.2. Methane permeability in the conditioned film is slightly higher at low feed pressures relative to its mixed gas permeability of 0.31 Barrer in the unconditioned film. Carbon dioxide permeability is not significantly different between the conditioned and unconditioned films. As such, CO_2/CH_4 permselectivity at 200 psia total feed pressure in the conditioned film is 37, which is much lower than its value of 44 at 200 psia shown for the unconditioned film. Rapid removal of H_2S during depressurization can "lock" in H_2S induced polymer chain

dilations, thereby increasing permeability in membranes exposed to such high activity penetrants.

The important result shown in Figures 7.4 and 7.5 is the fact that both CO_2 and CH_4 permeability decreased over the entire pressure range, which is in accordance with dual-mode sorption behavior of an unplasticized film. With this decrease, CH_4 permeability in the conditioned film at high pressures approaches its high pressure limit in the unconditioned film of 0.30 Barrer, indicating that H_2S did cause a small but permanent dilation in free volume. However, at very high pressures, when gas sorption occurs mainly in the Henry's type environments, CH_4 permeability in the unconditioned and conditioned films is the same. Similarly, the permselectivity in the conditioned film increases towards 40, which is the value shown in the unconditioned film in the high pressure limit. As such, 6F-PAI-2 still appears to maintain very good plasticization resistance against high CO_2 partial pressures even after prior exposure to H_2S and its plasticizing effect on the membrane. These results confirm that the crash in the separation performance of 6F-PAI-2 shown in Figures 7.2 and 7.3 was due to the presence of H_2S, and likely stems from enhanced sorption affinity, as was discussed in Chapter 6, of H_2S for the less fluorinated polymer structure.

These mixed gas permeation results are consistent with the results from Chapters 5 and 6, which demonstrated that H_2S likely has an increased affinity for materials with lower fluorine concentration. This enhances H_2S's swelling affect in polymer membranes even in materials which otherwise demonstrate exceptional CO_2 plasticization resistance, such as was shown for 6F-PAI-2. However, after removal of H_2S, the separation properties in 6F-PAI-2 showed only minor differences relative to their values in an "unconditioned" membrane under the same binary feed conditions. Additionally, 6F-PAI-2 retained excellent stability against high CO_2 partial pressures as well as an attractive CO_2/CH_4 permselectivity of ~40 at 800 psia. Therefore, 6F-PAI-2 may not be suitable for

applications involving H_2S, however, it does show very good separation performance in the absence of H_2S.

7.4. Characterization of 6F-PAI-1 using Ternary Gas Feeds Containing H_2S

7.4.1. Prediction of Sorption Reductions in 6F-PAI-1 Exposed to Ternary Gas Feeds

In accordance with the dual-mode sorption formalism outlined in Chapter 2, the presence of a second component, B, can reduce the sorption of component A by effectively lowering component A's Langmuir sorption term. This can be predicted using the dual-mode sorption model by including the terms $b_B f_B$, where b_B is the Langmuir affinity constant of B and f_B is its partial fugacity, into the denominator of the Langmuir portion of component A's sorption coefficient. The effect of additional components on A's sorption can also be predicted by including the appropriate Langmuir affinity constants and partial fugacities of said components into the denominator of A's Langmuir sorption term. Figure 7.6 compares the experimentally measured pure gas sorption coefficient isotherms in 6F-PAI-1 to sorption predictions from the dual-mode model using H_2S "lean" and "rich" feed streams, which were described in the introduction to this chapter.

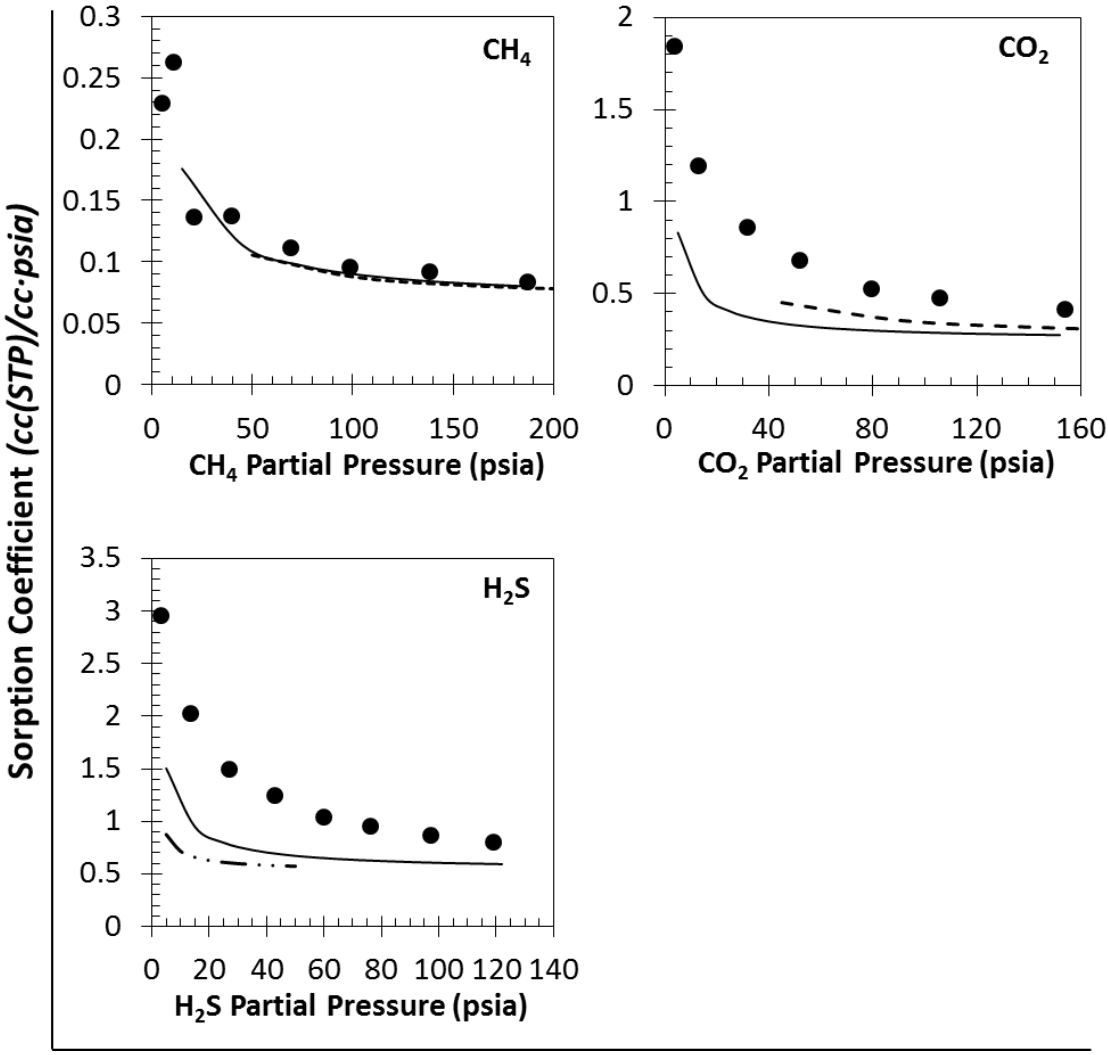

Figure 7.6: Experimental pure gas **(closed circles)** sorption coefficients compared to dual-mode model predictions using H_2S "rich" **(solid line)** and H_2S "lean" **(dashed line)** feed streams at 35°C. The H_2S "rich" feed is composed of 20/20/60 $H_2S/CO_2/CH_4$. The H_2S "lean" feed is composed of 5/45/50 $H_2S/CO_2/CH_4$.

The predicted sorption coefficients for both CO_2 and H_2S in the ternary composed feed streams are reduced relative to their pure gas values. Carbon dioxide's sorption coefficient is more depressed in the H_2S "rich" feed compared to the "lean" feed. This is due to higher H_2S concentration which can sorb into the Langmuir sites, thereby reducing CO_2's Langmuir sorption term to a greater extent than conditions where H_2S concentration in the feed is much lower relative to CO_2, as it is in the lean feed. Because

of such lower CO_2 capacity in the Langmuir regions, S_{CO2} approaches its more constant, high pressure asymptotic value, which tends towards its k_D value, at lower CO_2 partial than it does in the pure gas feeds. This signifies that total CO_2 sorption reaches its mostly constant Henry's value at lower partial pressures. Similar behavior in S_{CO2} is demonstrated in the H_2S "lean" feed. However, S_{CO2} is higher in the lean feed. This is due to "less competition" with H_2S for the Langmuir sorption sites as a result of lower H_2S concentration in the feed.

The effect on the varying component concentrations on the H_2S sorption coefficient is similar to CO_2, however, S_{H2S} is more significantly reduced in the H_2S "lean" feed compared to the "rich" feed. The reason for these reductions in S_{H2S} are similar to what was previously described for S_{CO2} in the preceding paragraph. For both feed conditions, S_{CO2} and S_{H2S} will likely be lower than their pure gas values, while such depression in sorption will be greater for the component with lower a *bf* term relative to the other condensable component.

Methane's sorption coefficient is predicted to be only marginally lower in the presence of CO_2 and H_2S. This is due to its low Langmuir capacity relative to the more condensable penetrants. The sorption predictions as just discussed will be used to help interpret the mixed gas permeabilities in the following section.

7.4.2. Analysis of Ternary Mixed Gas Permeabilities in 6F-PAI-1

The ternary mixed gas permeability isotherms as a function of total feed pressure for CO_2 and CH_4 in both the H_2S "rich" and H_2S "lean" feeds are shown in Figure 7.7. The CO_2/CH_4 and H_2S/CH_4 permselectivities will be discussed in section 7.4.3.

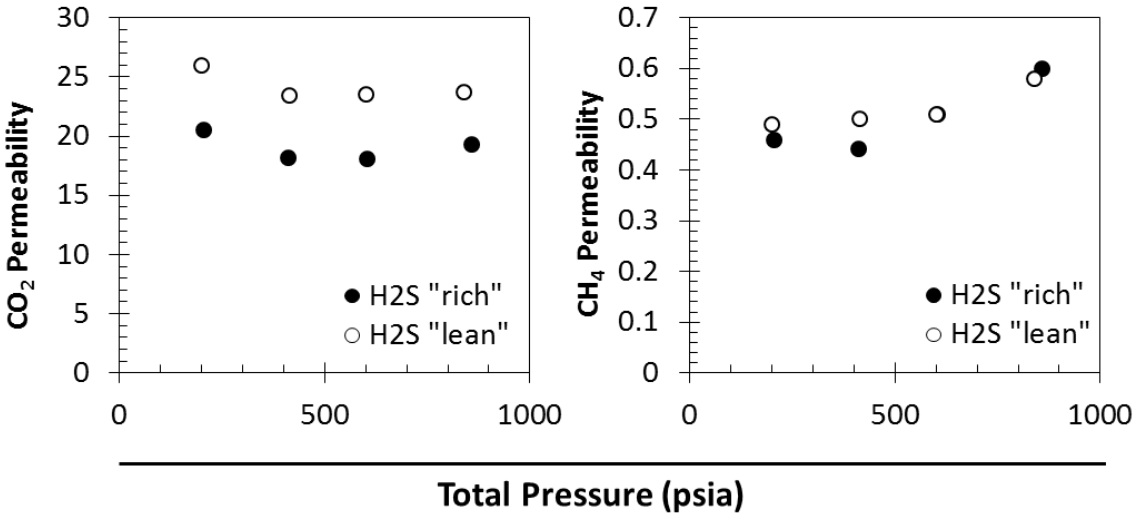

Figure 7.7: CO_2 and CH_4 permeability versus total feed pressure for H_2S "rich" and "lean" feeds. The H_2S "rich" feed is composed of 20/20/60 $H_2S/CO_2/CH_4$. The H_2S "lean" feed is composed of 5/45/50 $H_2S/CO_2/CH_4$.
Permeability is given in units of Barrer

In accordance with its predicted sorption behavior, CO_2 permeability is more significantly depressed in the H_2S rich feed, and decreases with pressure until a minimum is reached around 600 psia. At pressures beyond this minimum, an upswing in CO_2 permeability occurs, indicating that plasticization begins to affect CO_2. For the H_2S lean feed, CO_2 permeability reaches a minimum around 600 psia and subsequently appears constant up to 850 psia.

The effect of H_2S concentration on CH_4 permeability is much less pronounced than what is shown for CO_2, which is consistent with the predicted effect on CH_4's sorption coefficient shown in Figure 7.6. This is due to CH_4's low Langmuir sorption capacity and affinity compared to CO_2 and H_2S. In the H_2S rich feed, the effect of increasing total pressure appears to cause an increase in CH_4 permeability around 400 psia, which is lower than the total pressure that was shown to induce the upswing in CO_2 permeability. This is presumably due to a localized but significant increase in segmental chain mobility, which has a greater effect on the diffusion coefficient of larger kinetic

diameter CH_4. In the H_2S lean feed, CH_4 permeability is stable up to 600 psia. At higher pressures, an upswing in permeability signifying the onset of plasticization occurs. These results underscore the importance of analyzing CH_4's permeability during mixed gas testing, as CO_2 permeability suggests that plasticization does not occur until higher pressures. In general, the results in Figure 7.7 demonstrate the greater plasticizing effect of H_2S. In the H_2S rich feed, the onset of plasticization occurs around 400 psia, which equates to a total acid gas partial pressure of 160 psia as well as total acid gas concentration of 64 *cc(STP)/cc*, of which H_2S represents 66%, or 42 *cc(STP)/cc*, of the total acid gas concentration, while CO_2's concentration is 22 *cc(STP)/cc.* The total acid gas partial pressure and concentration is the sum of CO_2 and H_2S partial pressures and CO_2 and H_2S concentration sorbed into the membrane as predicted by the dual-mode sorption model, respectively. In the H_2S lean feed, the onset of plasticization occurs near 600 psia total feed pressure, which equates to a higher total acid gas partial pressure of 300 psia as well as higher total acid gas concentration of 77 *cc(STP)/cc*, of which H_2S represents 18%, or 14 *cc(STP)/cc* and CO_2 concentration is 63 *cc(STP)/cc.* In other words, H_2S concentration sorbed in the membrane at the plasticization pressure in the rich feed is lower than CO_2 concentration sorbed into the membrane at the point of plasticization in the lean feed. This is also consistent with the pure gas plasticization isotherms shown in Chapter 5, where all materials become plasticized below 80 psia H_2S pressure, while much higher CO_2 pressures, which were generally above 360 psia, were shown to induce plasticization. It can be concluded then that H_2S has much greater tendency to plasticize polymers than does CO_2.

The H_2S permeability isotherms for the H_2S rich and lean feeds are shown in Figure 7.8.

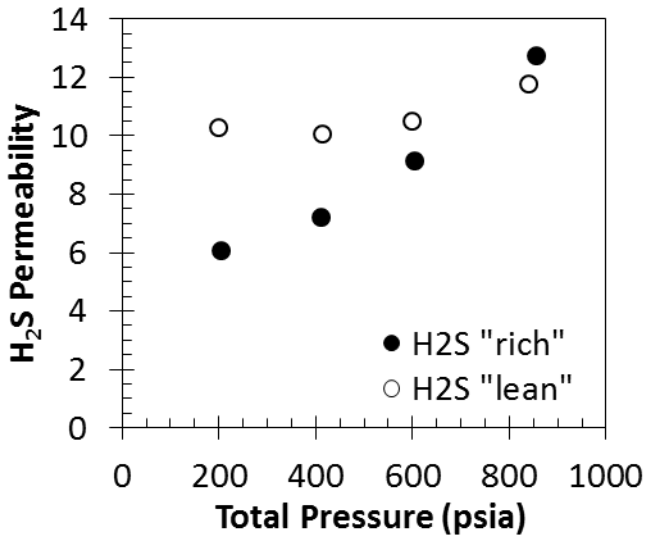

Figure 7.8: Mixed gas H_2S permeability versus total feed pressure in 6F-PAI-1 at 35°C. The H_2S "rich" feed is composed of 20/20/60 $H_2S/CO_2/CH_4$. The H_2S "lean" feed is composed of 5/45/50 $H_2S/CO_2/CH_4$.

The effect of H_2S composition in the feed on the permeability of H_2S is opposite to what is shown for CO_2 and CH_4. That is, H_2S permeability in the rich feed is lower relative to that in the lean feed. This result is not consistent with the sorption predictions shown in Figure 7.6, as S_{H2S} in the lean feed was predicted to be lower due to more CO_2 in the feed which "competes" for the unrelaxed free volume packets. Intuitively, H_2S permeability would also be expected to be lower in the lean feed. One possible explanation may be that in the H_2S lean feed, suppression of its sorption coefficient relative to the rich feed appears to be much more pronounced at very low pressures. This suggests that H_2S's Langmuir capacity is lower in the lean feed. Therefore, $D_{eff}(C)$, which is the concentration dependent effective or local diffusion coefficient, may be higher in the H_2S lean feed because at a given H_2S partial pressure, a much higher fraction of H_2S sorbed into the membrane will be "dissolved" in the more mobile, equilibrium packed regions. Indeed, using the dual-mode parameters, the ratio of Henry's to Langmuir concentrations were predicted, and are shown in Figure 7.9. Additionally, the apparent diffusion coefficients for H_2S were calculated from the relation $D = P / S$ in the pure and mixed

gas permeability and sorption isotherms. The apparent diffusivities are given in Table 7.1.

Table 7.1: Apparent H_2S diffusivities in various feed conditions at 35°C. For the mixed gas feeds, D_{H2S} in the lean feed was calculated based on its permeability at 200 total psia and the predicted *S* in the lean feed at an equivalent partial H_2S pressure of 10 psia. For the H_2S rich feed, D_{H2S} was calculated from H_2S permeability at 200 psia in the rich feed and *S* in the rich feed predicted at an equivalent partial pressure of 40 psia. For the pure gas feed, D_{H2S} was calculated based on experimentally measured *P* and *S* at ~30 psia.

	D_{H2S}^{app} $(x10^8)$
H_2S "lean"	0.89
H_2S "rich"	0.39
Pure gas	0.24

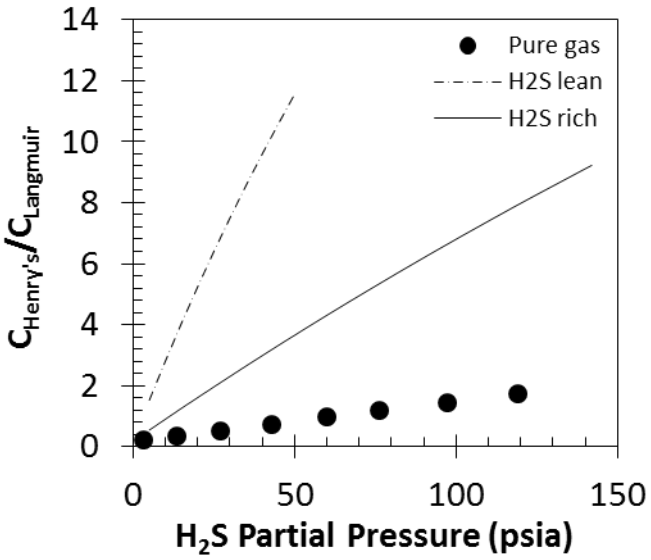

Figure 7.9: Ratio of H_2S Henry's to Langmuir concentration in 6F-PAI-1 at 35°C in various feed streams. The solid dots are based on experimentally measured pure gas sorption data. The H_2S "rich" feed is composed of 20/20/60 $H_2S/CO_2/CH_4$. The H_2S "lean" feed is composed of 5/45/50 $H_2S/CO_2/CH_4$.

As suggested, the apparent diffusivity in the lean feed is essentially double that in the rich feed. The apparent diffusivity in the rich feed is also higher than it is in the pure gas feed, although the difference is much smaller compared to the lean feed. This is consistent with very similar H_2S permeabilities at 40 psia H_2S partial pressure in the rich feed and H_2S pure gas permeability at 30 psia, which is ~6 Barrer. Furthermore, as can be observed in Figure 7.9, the Henry's concentration relative to Langmuir is much higher in the H_2S lean feed. In fact, the lower the ratio of Henry's to Langmuir concentration, the lower is the apparent diffusivity. Higher Henry's to Langmuir ratios likely translates to a higher C_m. The mobile concentration, or C_m, is the effective mobile concentration that contributes to the permeation flux. With increasing H_2S concentration in the equilibrium packed regions, the effective diffusivity is presumed to be less dependent on concentration since a greater fraction of H_2S exists in Henry's sites, which are characterized by constant and higher diffusivity than for the population in the Langmuir sites, even in the absence of plasticization. Such behavior is consistent with H_2S permeability in the lean feed, which is shown to be fairly constant with pressure up to 600 psia total feed pressure in Figure 7.8. The increase in permeability at higher pressures signifies plasticization, as both CH_4 and H_2S permeability become increasing functions of pressure beyond this point.

Hydrogen sulfide permeability in the rich feed in Figure 7.8 shows much stronger dependence on total pressure. Between 200 and 400 psia, an increase in H_2S permeability is shown despite a constant CH_4 permeability. This is likely due to an increase in its effective diffusivity, since at low pressures it may have a greater fraction sorbed into the less mobile Langmuir sites as is suggested by Figure 7.9. As pressure increases from 200 to 400 psia, additional H_2S sorbs into the more mobile Henry's regions, which may also cause the effective diffusivity to increase. The diffusion coefficient in glassy polymers is

usually an increasing function of sorbed concentration even in the absence of plasticization. The general form of the concentration dependence of the local or effective diffusivity for penetrants in glassy polymers is depicted in Figure 7.10.

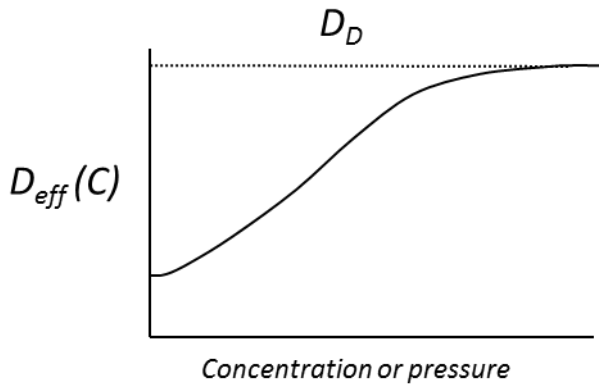

Figure 7.10: Depiction of concentration dependence of the local or effective diffusivity in glassy polymers.

As can be observed, the effective diffusivity is lower than the concentration independent Henry's diffusivity, which is represented in Figure 7.10 by D_D. The reason for such depression in D_{eff} is that at low pressures, a higher fraction sorbs into the Langmuir packing defects. Penetrants sorbed into these domains have lower mobility than penetrant in the Henry's, or dissolved domains. With increasing pressure and consequently sorbed concentration, a greater proportion of penetrant sorbs into the Henry's regions, therefore the mobility of the total sorbed concentration increases. At very high pressures, and in the absence of plasticization, D_{eff} approaches an asymptotic limit which is characterized by the concentration independent Henry's mode diffusion coefficient. Therefore, at high pressures, when sorption occurs primarily in the Henry's environments, penetrant diffusivity becomes mostly independent of concentration.

The initial increase in H_2S permeability in the rich feed between 200 and 400 psia is not presumed to be caused by plasticization since CH_4 permeability is mostly constant through this same pressure range. At higher pressures, CH_4 permeability shows an

upswing typical of plasticization, and similarly, H_2S permeability appears to increase more rapidly compared to its increase between 200 and 400 psia. Slight concavity to the permeability axis is also shown in H_2S permeability with increasing pressure beyond 400 psia, which takes the form of penetrant diffusivity versus pressure in a swollen or plasticized media. Beyond 600 psia, all three penetrants likely "feel" the effect of plasticization, and the permeabilities for all three penetrants increase with pressure.

In summary, it appears that H_2S transport may be more highly dependent on the differences in penetrant transport in the so-called dual-mode environments that are characteristic of glassy polymers. When H_2S concentration is more significantly reduced due to much higher relative concentrations of a secondary condensable component, as is the case in the lean feed, its Langmuir capacity is presumably much lower relative to pure gas conditions. As such, H_2S partitions itself primarily into the higher mobility "equilibrium" packed regions, which results in higher transport permeability compared pure gas as well as mixed gas conditions when H_2S composition in the feed is higher or similar to the second condensable component. Therefore, the pressure dependence of H_2S permeability in single and multi-component feeds appears to be highly dictated by the balance between the sorption reductions and concentration dependent diffusivity as a result of dual-mode transport effects.

7.4.3. Analysis of Mixed Gas Selectivity in 6F-PAI-1 Exposed To Ternary Gas Feeds

Figure 7.11 shows the CO_2/CH_4 permselectivity versus total feed pressure for the H_2S rich and lean feeds.

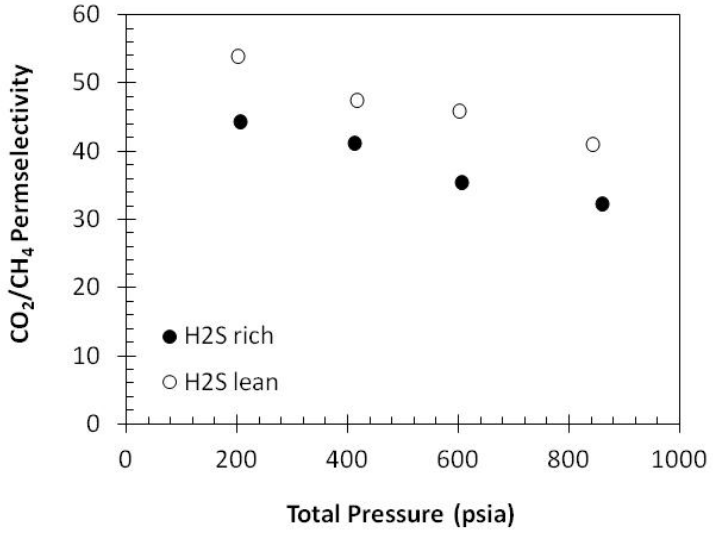

Figure 7.11: CO_2/CH_4 permselectivity in 6F-PAI-1 versus total feed pressure at 35°C. The H_2S "rich" feed is composed of 20/20/60 $H_2S/CO_2/CH_4$. The H_2S "lean" feed is composed of 5/45/50 $H_2S/CO_2/CH_4$.

Permselectivity in 6F-PAI-1 exposed to the H_2S lean feed is higher relative to the rich feed. This is due to smaller reductions in CO_2 permeability in the lean feed relative to the rich feed. Selectivity in both feed streams decreases with pressure to a similar extent in accordance with decreasing CO_2 permeability with pressure. Even in the H_2S rich feed, selectivity is maintained at an attractive value of above 30. In the H_2S lean feed, selectivity at 850 psia is similar to its ideal selectivity of ~43. These promising results suggest that even in such aggressive conditions, 6F-PAI-1 is able to maintain a competitive, and in fact much better, separation performance relative to current industrial materials such as CA, which suffers dramatically in the presence of only CO_2 at even modest partial pressures of 200 psia [3].

The H_2S/CH_4 permselectivity is shown in Figure 7.12.

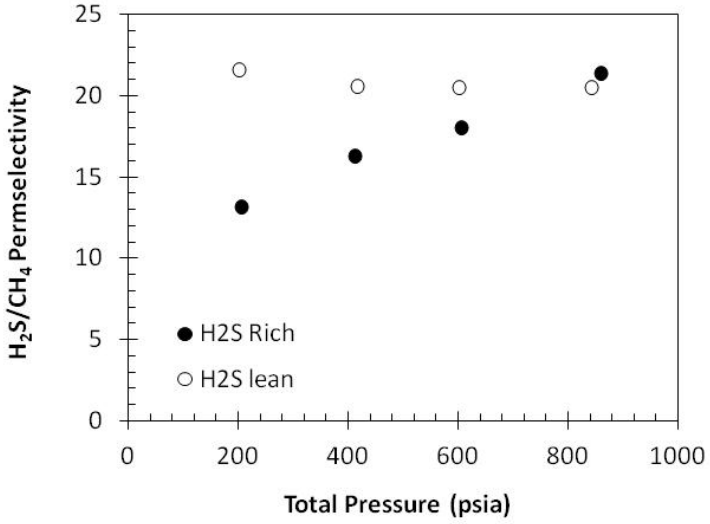

Figure 7.12: H_2S/CH_4 permselectivity in 6F-PAI-1 versus total feed pressure at 35°C. The H_2S "rich" feed is composed of 20/20/60 $H_2S/CO_2/CH_4$. The H_2S "lean" feed is composed of 5/45/50 $H_2S/CO_2/CH_4$.

Similar to the CO_2/CH_4 selectivity behavior, H_2S/CH_4 selectivity is higher in the lean feed, and is due to higher H_2S permeability in the lean feed relative to the rich feed. However, in this case, such higher permeability is likely due to a higher effective diffusivity for H_2S. Consistent with the H_2S and CH_4 permeability behavior with pressure in the lean feed, selectivity is mostly constant throughout the entire pressure range. Additionally, this selectivity is twice as high as its ideal selectivity of ~8, and is believed to be due to the higher H_2S diffusivity in the lean feed as a result of a higher mobile concentration. This is supported by the apparent diffusivities in Table 7.1 as well as the concentration ratios given in Figure 7.9.

In the H_2S rich feed, H_2S/CH_4 permselectivity at low total pressure is slightly higher than its ideal selectivity of 8. This is due to reduced CH_4 permeability in the rich feed as CO_2 and H_2S can "out compete" low solubility CH_4 for the fixed number of Langmuir microvoids. With increasing pressure, a continual increase in H_2S/CH_4 permselectivity occurs in accordance with H_2S's permeability versus pressure behavior in the rich feed. Interestingly, even though CH_4 permeability in the rich feed is also an

increasing function of pressure beyond 400 psia, selectivity still continues to rise. This is due to faster increasing H_2S permeability, which is presumably caused by the combined result of increased *Deff* at low pressures *as well as* increased segmental chain mobility at higher pressures, both of which are believed to cause a more rapid increase in H_2S diffusivity relative to CH_4. These results further demonstrate the difference between H_2S and CO_2 permeability, as H_2S appears to be much more dependent on dual-mode sorption and diffusion effects because of its high sorption capacity.

As will be shown in the final section of this chapter, the high separation performance of 6F-PAI-1 towards high pressure feed streams containing CO_2 and H_2S translates to similarly promising total acid gas selectivity compared to Pebax®. In the next section, the permeabilities and binary selectivities in Pebax® will be analyzed using pure gas conditions as well as mixed gas conditions using the same H_2S rich and lean feeds. In the final section of this chapter, 6F-PAI-1 and Pebax® will be analyzed using the total acid gas selectivity factor.

7.5. Characterization of the Separation Performance in Pebax®

7.5.1. Pure Gas Sorption and Permeation Analysis

Because rubbery polymers are devoid of “permanent” microvoid packing defects, their transport properties are generally constant in the absence of penetrant induced swelling. As such, k_D, which is the sorption coefficient in rubbers, and diffusivity are also constant in the absence of swelling and do not depend on the presence of additional components [2, 3]. This is demonstrated in the pure gas sorption coefficients for CO_2 and CH_4 versus pressure, which are shown in Figure 7.13. The sorption coefficients were measured in Pebax® using a pressure decay technique as has been done with all materials in this work.

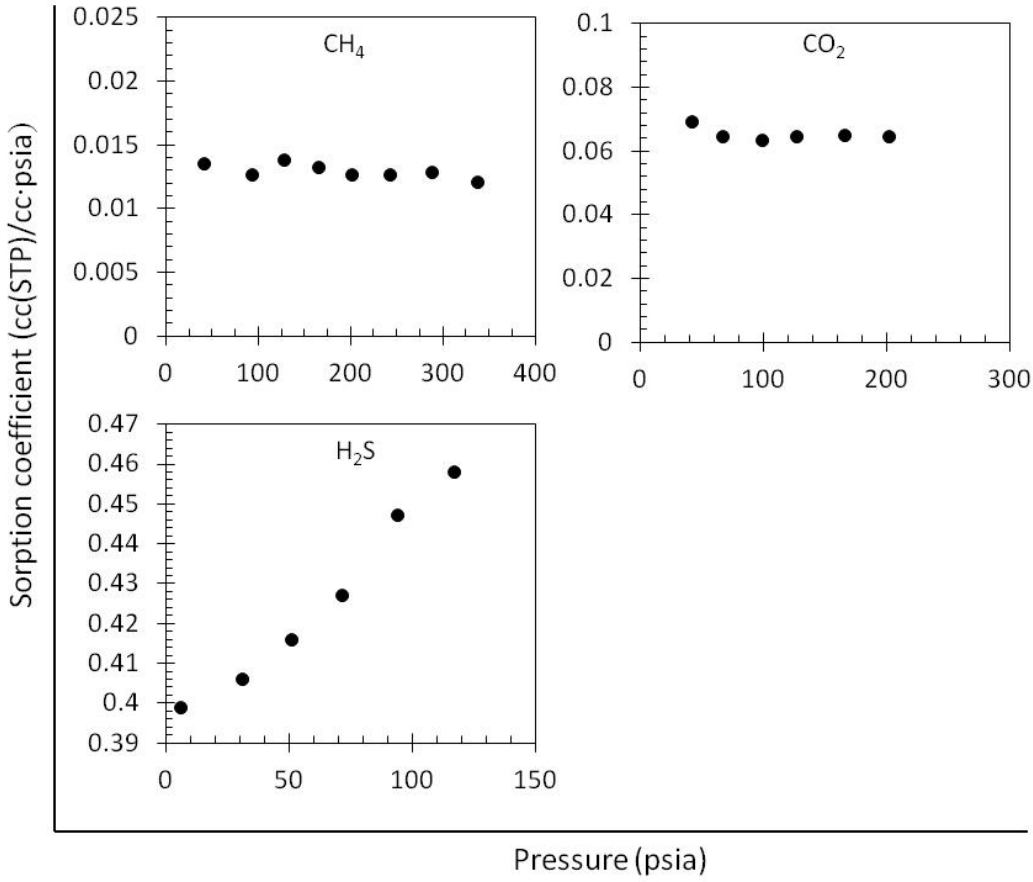

Figure 7.13: Experimentally measured sorption coefficients versus equilibrium pressure in Pebax® at 35°C.

The sorption coefficient for CO_2 and CH_4 are independent of pressure, indicating the absence of penetrant induced swelling. In contrast, H_2S sorption increases continually with pressure, indicated swelling induced by the highly polar and condensable H_2S. Due to this swelling tendency, H_2S permeability is also highly pressure dependent. The pure gas permeabilities for H_2S, CH_4, and CO_2 in Pebax® are shown in Figure 7.14.

In accordance with its pressure independent sorption coefficient, CH_4 permeability is also constant with pressure. This is shown in Figure 7.14. Interestingly, CO_2 permeability increases with pressure, albeit to a much lower extent than does the permeability of H_2S. The increase in CO_2 permeability is inconsistent with its sorption

behavior shown in Figure 7.13. Because CO_2's sorption coefficient was constant over similar pressure ranges, the permeability increase indicates an increase in CO_2's diffusion coefficient. This suggests that CO_2 also has a swelling effect on Pebax®, although to a much lower extent than H_2S.

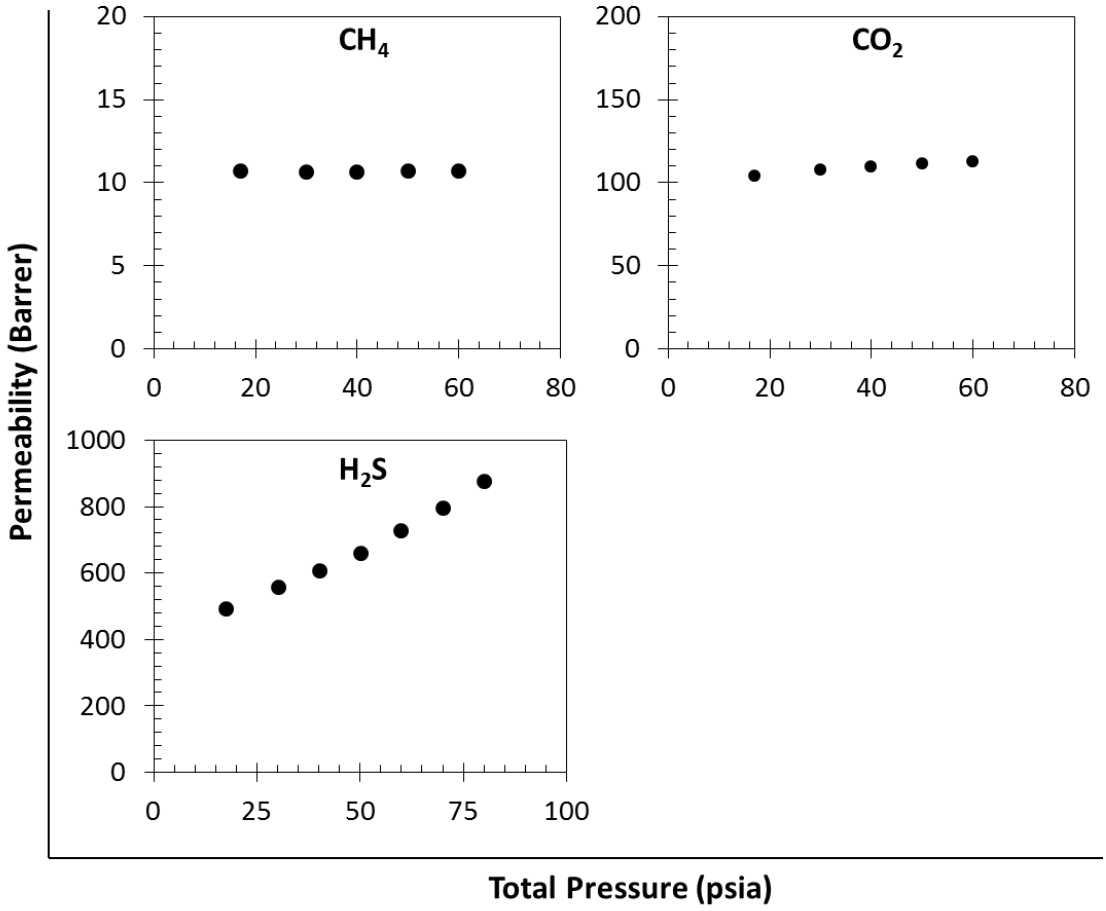

Figure 7.14: Pure gas permeability versus pressure isotherms in Pebax® at 35°C.

Similar to H_2S's sorption coefficient, H_2S permeability is also a strong function of pressure, which is likely due to an increase in both the diffusion and sorption coefficients. Based on these pure gas results, the transport properties of H_2S and CO_2 in Pebax® appear

to be increasing functions of pressure. It is expected then that CH_4's permeability in the presence of these components will also depend on pressure, which may undermine permselectivity in mixed gas feeds. However, as discussed in Chapter 2, plasticization has been shown to increase selectivity of condensable components over less condensable ones due to an increase in the more condensable component's sorption coefficient as plasticization sets in. These issues will be addressed in the remainder of this chapter.

7.5.2. Characterization of Separation Performance in Pebax® using Ternary Gas Feeds

The mixed gas separation performance in Pebax® was characterized using the same H_2S rich and lean feeds as previously discussed. Figure 7.15 shows the CH_4, CO_2 and H_2S mixed gas permeabilities versus pressure for the different ternary gas feeds.

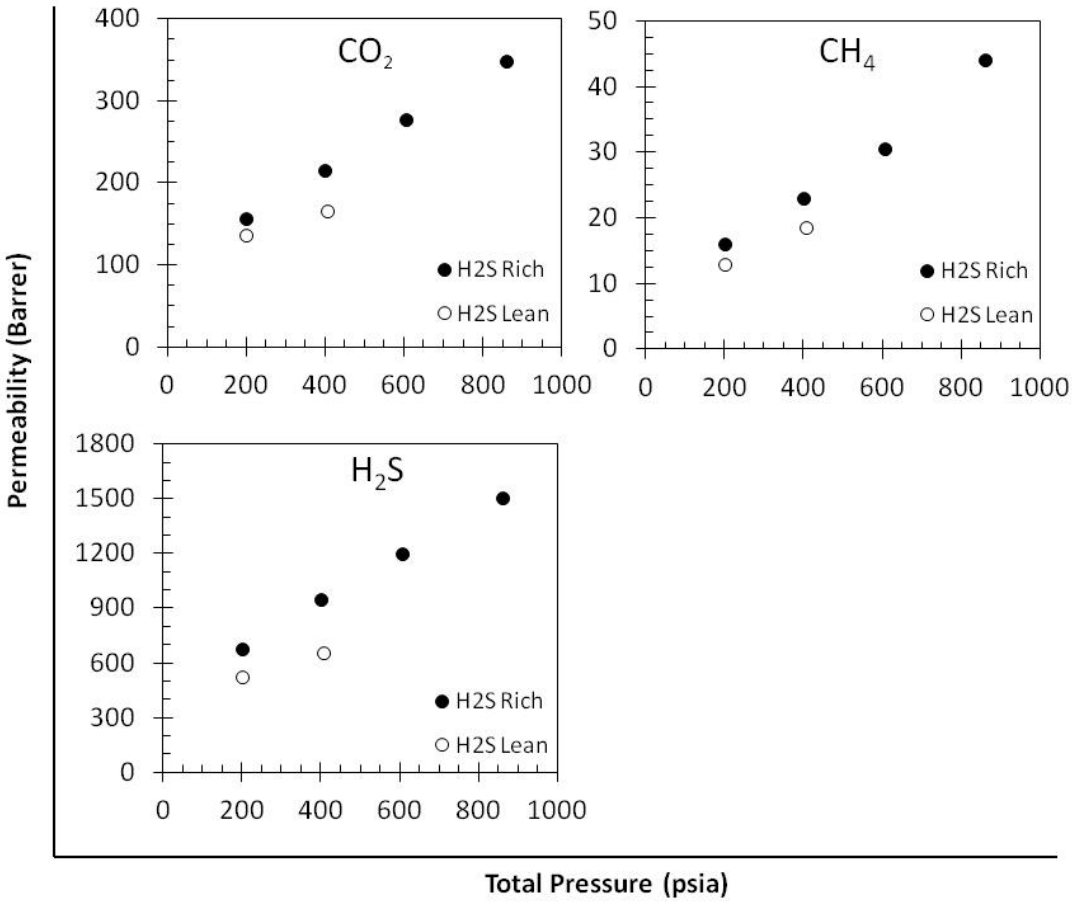

Figure 7.15: Mixed gas permeability versus total feed pressure for Pebax® at 35°C. The H_2S "rich" feed is composed of 20/20/60 $H_2S/CO_2/CH_4$. The H_2S "lean" feed is composed of 5/45/50 $H_2S/CO_2/CH_4$.

The mixed gas permeabilities for all components are higher in the H_2S rich feed, and is consistent with higher H_2S concentration in this feed. Such higher concentrations easily induce segmental scale increases in the polymer chains, as suggested by the pure gas H_2S sorption and permeability isotherms. Additionally, the permeabilities for all components in both feed streams increase substantially with pressure, with the extent of the increase being slightly lower in the lean feed. In the higher H_2S concentration feed, all permeabilities increase by over 100% at 850 psia. These results demonstrate the striking contrast between permeability in glassy and rubbery polymers in the presence of high

activity components. In general, the presence of such components causes the permeability of all penetrants in rubbery polymers to become strong functions of pressure due to increases in polymer chain mobility. As such, more CH_4 may be lost in the downstream due to such a substantial increase in its permeability. The effect of increasing penetrant fluxes on the selectivities for CO_2/CH_4 and H_2S/CH_4 in Pebax® are given in Figure 7.16.

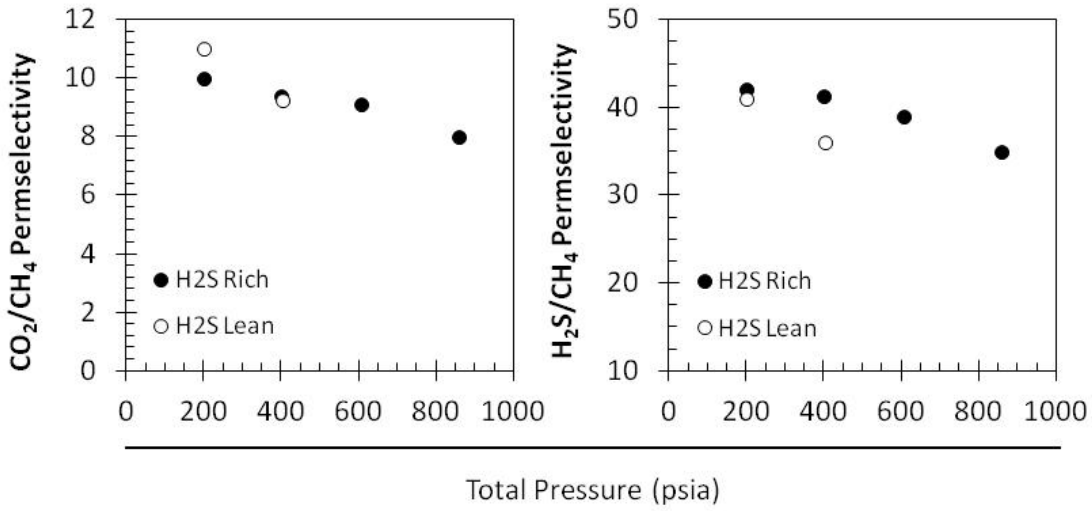

Figure 7.16: CO_2/CH_4 and H_2S/CH_4 permselectivities versus total feed pressure in Pebax® at 35°C. The H_2S "rich" feed is composed of 20/20/60 $H_2S/CO_2/CH_4$. The H_2S "lean" feed is composed of 5/45/50 $H_2S/CO_2/CH_4$.

As can be observed in Figure 7.16, both CO_2 and CH_4 permeability appear to be affected by H_2S concentration to the same extent, as CO_2/CH_4 selectivity is the same for both feed streams. It should be pointed out that CO_2/CH_4 selectivity in Pebax® in both feeds is less than 50% of the value shown for 6F-PAI-1 subjected to the same feed streams in Figure 7.11, even in the high pressure limit of 850 psia for the H_2S rich feed. Such higher selectivity is due to rubbery polymers' very low diffusion selectivity. As was shown in Chapter 6, CO_2/CH_4 diffusion selectivity in Pebax® at 35 psia and 35°C is 1.3.

Consequently, CO_2/CH_4 permselectivity in Pebax® is due almost exclusively to sorption selectivity, which is ~7.8 based on its ideal permselectivity of 11. Based on the CO_2/CH_4 selectivity decrease shown for both feed conditions in Figure 7.16, which tends towards a value slightly below 8, all mobility selectivity in Pebax® appears to diminish. Therefore, permselectivity in both feeds depends mostly on sorption selectivity, which is not a very strong function of polymer chain swelling. As such, it does not appear that the CO_2/CH_4 selectivity in Pebax® will benefit from plasticization, and Pebax® does not appear to be a very useful polymer membrane material for natural gas separations involving CO_2 as the primary contaminant of interest. This will be further discussed in the final section of this chapter, which compares Pebax® and 6F-PAI-1's performance based on the total acid gas selectivity.

Consistent with its CO_2/CH_4 selectivity, H_2S/CH_4 selectivity in Pebax® is similar in both feed conditions. As well, H_2S/CH_4 selectivity decreases continually with feed pressure in both feeds. This is likely the result of a further decrease in the already very low, and less than 1, H_2S/CH_4 diffusion selectivity. As Figure 7.13 demonstrated, H_2S's sorption is a strong increasing function of H_2S partial pressure. Because H_2S/CH_4 permselectivity decreases in Figure 7.16, the presumed increase in H_2S solubility in the mixed gas conditions does not appear to affect H_2S/CH_4 permselectivity. Although H_2S/CH_4 selectivity for both feed conditions in Figure 7.16 is almost double that shown for 6F-PAI-1, which was between 11 and 22, such higher selectivity in Pebax® has only a small effect on the total acid gas selectivity as will be shown in the next section. Based on these results, Pebax® is not appropriate for strictly binary CO_2/CH_4 separations, and its

use in membrane based acid gas sweetening should be limited to conditions where H_2S is the predominant component in the acid gas feed.

7.6. Total Acid Gas Selectivity Comparison between 6F-PAI-1 and Pebax®

As previously outlined in Chapter 2, our proposed total acid gas selectivity factor, SF_{TAG}, quantifies the removal efficiency of both CO_2 *and* H_2S relative to CH_4. The equation for calculating SF_{TAG} is shown in Equation 7.1.

$$SF_{TAG} = \left(\frac{y_{H2S} + y_{CO2}}{y_{CH4}} \right)_{perm} \Big/ \left(\frac{y_{H2S} + y_{CO2}}{y_{CH4}} \right)_{feed} \tag{7.1}$$

As H_2S concentration in the feed increases, more of the permeate gas in the downstream side of the membrane will be composed of H_2S. Because rubbery polymers have higher H_2S/CH_4 selectivities, as shown in Figure 7.16, each mole of H_2S that permeates through the membrane will result in a corresponding lower amount of CH_4 permeate into the downstream compared to glassy polymers. Because SF_{TAG} will become increasingly dependent on the mole fraction of H_2S in the downstream as H_2S concentration increases in the upstream, such higher H_2S/CH_4 selectivity is expected to yield higher SF_{TAG} for the highly H_2S selective rubbers. Contrarily, as H_2S concentration in the feed is reduced to below CO_2's feed concentration, the composition of the permeate product will become increasingly composed of CO_2, and the permeate term in equation 7.1 will be weighted more heavily by y_{CO2}. As glassy polymers have much higher CO_2/CH_4 selectivities compared to rubbers, less CH_4 will be lost in the downstream per mole of CO_2 permeated,

therefore, SF_{TAG} is expected to be higher for glassy polymers. Higher SF_{TAG} means that less CH_4 will be lost in the downstream per mole of total acid gas permeated (CO_2+H_2S).

Figure 7.17 compares SF_{TAG} between 6F-PAI-1 and Pebax® for the H_2S rich and lean feeds.

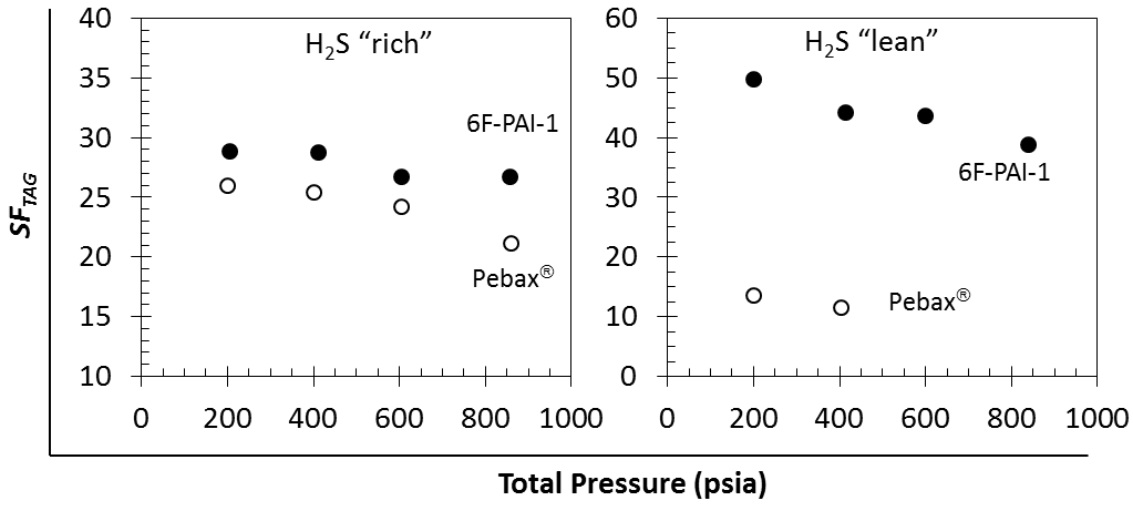

Figure 7.17: Comparison of the total acid gas separation factor versus pressure between 6F-PAI-1 and Pebax® at 35°C. The H_2S "rich" feed is composed of 20/20/60 $H_2S/CO_2/CH_4$. The H_2S "lean" feed is composed of 5/45/50 $H_2S/CO_2/CH_4$.

As can be seen in Figure 7.17, SF_{TAG} is higher in 6F-PAI-1 in both feed streams compared to Pebax®. Moreover, in the H_2S lean feed, the difference in selectivity between the glassy and rubbery polymers is significantly different. This is in accordance with our hypothesis as outlined in the beginning of this chapter. Such higher selectivity for 6F-PAI-1 in the lean feed is due to an increase in both its CO_2/CH_4 and H_2S/CH_4 selectivity relative to the H_2S rich feed. The reasons for such increases in the binary selectivities were discussed in section 7.4.

Interestingly, SF_{TAG} for Pebax® in the rich feed is only about 1.9 times higher than it is in the lean feed. Based on Equation 7.1, for a given permeate composition in the

numerator of the equation, SF_{TAG} in the rich feed will always have a 1.67x advantage over SF_{TAG} in the lean feed because the denominator in Equation 7.1 is smaller in the rich feed. As such, higher SF_{TAG} for Pebax® in the rich feed is mostly due to the lower denominator and not improved ratios of H_2S and CO_2 mole fractions relative CH_4 in the permeate term of Equation 7.1. This is also supported by the binary selectivities shown in Figure 7.16, as selectivities for both gas pairs were very similar between the rich and lean feeds. This also demonstrates the concentration dependence of SF_{TAG}, where if one wishes to be ultra-rigorous, a true cause and effect relationship of varying H_2S concentration relative to CO_2 should keep CH_4 constant, therefore the denominator of Equation 7.1 will be the same for different H_2S and CO_2 composed ternary feeds. Nevertheless, SF_{TAG} for 6F-PAI-1 is higher in the lead feed despite having a higher denominator compared to the rich feed. Therefore the improvement in SF_{TAG} for 6F-PAI-1 as H_2S concentration decreases and CO_2 concentration increases is in fact due to higher ratios of CO_2 and H_2S mole fractions relative CH_4 in the permeate term of Equation 7.1. The mole fractions of CH_4 in the permeate stream (downstream side of the membrane) are plotted against total feed pressure in Figure 7.18 for both feed conditions, and support the trends just discussed.

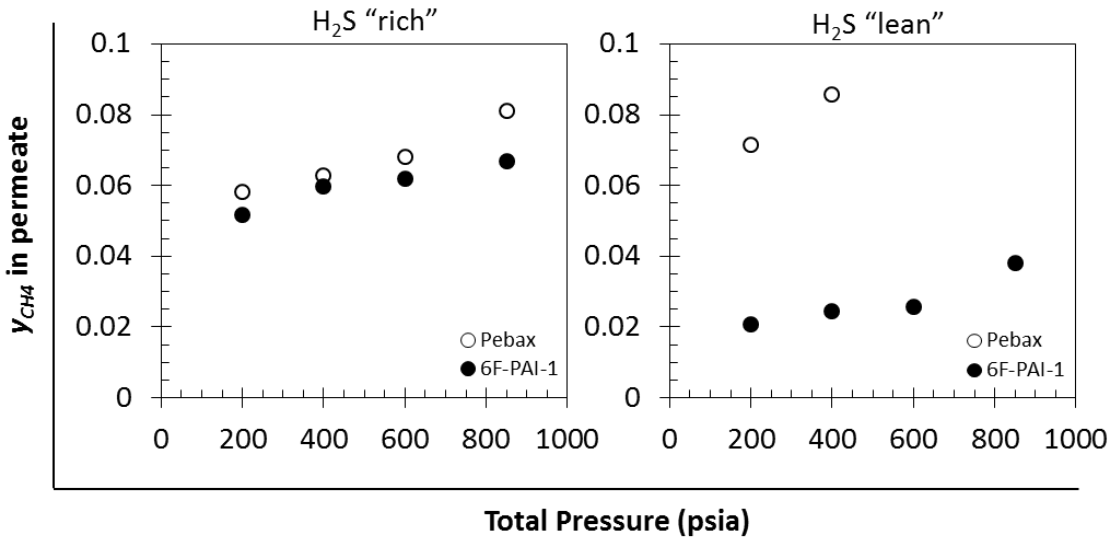

Figure 7.18: CH_4 fraction in the permeate versus total pressure for 6F-PAI-1 and Pebax®.

In the H_2S lean feed, significantly less CH_4 is lost in the permeate stream for 6F-PAI-1 compared to Pebax® under the same feed conditions. Additionally, as discussed above, CH_4 *permeate composition* in the lean feed in 6F-PAI-1 is about half of what it is for 6F-PAI-1 in the rich feed, demonstrating that the improvement in SF_{TAG} in the lean feed does correlate to better separation performance. For Pebax®, CH_4 permeate composition is only slightly lower in the rich feed than in the lean feed. This supports our previous claim that higher SF_{TAG} for Pebax® in the rich feed is mostly due to a smaller denominator in Equation 7.1. Even though H_2S concentration is higher in the rich feed relative to the lean feed, the ratio of H_2S/CH_4 mole fractions in the permeate does not improve to an appreciable extent relative to the lean feed, because the increase in H_2S flux across the membrane as a result of higher H_2S feed composition is accompanied by a corresponding increase in CH_4 due to membrane swelling. Therefore, SF_{TAG} in Pebax® does not improve for these feed conditions. However, 6F-PAI-1, higher CO_2 concentrations in the lean feed results in a substantial increase in the ratio of CO_2/CH_4 mole fractions in the

permeate because 6F-PAI-1 is not plasticized until much higher pressures, and therefore, becomes much more selectivity as CO_2 concentration in the feed increases.

These results demonstrate greater stability and higher selectivity in glassy 6F-PAI-1 compared to rubbery Pebax®. In order to more appropriately compare the effect of various H_2S and CO_2 concentrations in the feed on the separation performance, CH_4 composition in the feed should be held constant while varying the other two components. Nevertheless, the preceding results certainly support our hypothesis that glassy polymers, specifically highly stable materials such as fluorinated 6FDA based polyamide-imides, will show better total separation efficiency for acid gas sweetening compared to the primarily H_2S selective rubbery materials. Moreover, glassy polymers appear to result in appreciably less amounts of CH_4 loss in the downstream when CO_2 composition in the feed is much higher than H_2S, which is usually the case in most acid gas natural gas reserves[1, 6].

7.7. Conclusion

This chapter demonstrated high mixed gas separation performance in the 6FDA polyamide-imides which have been the focal point of this project. The polyamide-imides with lower fluorine concentration, namely 6F-PAI-2 and 3, however, are unlikely suitable for separations involving H_2S, as lower fluorine concentration along the backbone proved to dramatically reduce the separation properties of 6F-PAI-2. In more simple binary feed conditions containing only CO_2 and CH_4, 6F-PAI-1 and 2 show plasticization resistance up to 400 psia CO_2 partial pressure, and show selectivities for CO_2 over CH_4 of ~35 and 40, respectively. These results are particularly promising as these materials do not require crosslinking. Additional testing, such as long term stability tests at high mixed gas feed pressures would be useful for further characterization and development of these materials under realistic feed conditions.

Due to higher fluorine concentration in the polymer backbone, 6F-PAI-1 showed much better stability against feeds containing H_2S. Compared to a highly H_2S selectivity rubbery material, 6F-PAI-1 demonstrated higher total acid gas selectivity in feeds containing both low and similar concentrations of H_2S relative to CO_2. These results suggest that the more CO_2 selective glassy polymers will have a higher total separation efficiency in conditions where H_2S concentration in the feed is similar or lower than CO_2. This claim was further supported by analysis of CH_4's mole fraction in the permeate stream, which showed that $y_{CH4,perm}$ for 6F-PAI-1 was at or below the upper threshold of what is generally considered an acceptable composition of CH_4 lost in the downstream in an industrial natural gas separation unit [1]. In summary, glassy polymers, specifically highly fluorinated 6FDA based polyamide-imides, represent a competitive platform of polymer materials for membrane separations due to their good intrinsic stability against highly interacting feed components as well as high CO_2/CH_4 and total acid gas selectivity factors.

7.8. References

[1] R. W. Baker and K. Lokhandwala, "Natural Gas Processing with Membranes: An Overview," *Industrial & Engineering Chemistry Research*, **47** (7), 2109–2121, (2008).

[2] A. Bos, I.G.M. Pünt, M. Wessling, H. Strathmann, "Plasticization-resistant glassy polyimide membranes for CO_2/CO_4 separations," *Separation and Purification Technology*, **14** (1–3), 27–39, (1998).

[3] A. Y. Houde, B. Krishnakumar, S. G. Charati, S. A. Stern, "Permeability of Dense (Homogeneous) Cellulose Acetate Membranes to Methane, Carbon Dioxide, and Their Mixtures at Elevated Pressures," *Journal of Applied Polymer Science*, **62** (13), 2181–2192, (1996).

[4] R.E. Kesting and A.K. Fritzsche, *Polymeric Gas Separation Membranes*, (John Wiley & Sons, Inc., New York, 1993).

[5] W. S. Winston Ho and K. K. Sirkar, *Membrane Handbook*, (Chapman and Hall, London, England, 1992). W. Ho, *Membrane Handbook*. .

[6] A. Rojey, C. Jaffret, *Natural Gas, Production Processing Transport*, (Editions Technip, Paris, France, 1997).

CHAPTER 8

CONCLUSIONS AND RECOMMENDATIONS

8.1. Summary and Conclusions

Over the past decade, membrane based gas separations have gained traction in industry as an attractive alternative to traditional thermally based separations due to their potential to offer lower operational and capital expenditures, greater ease of operation and lower environmental impact. As membrane research evolves, new state-of-the-art membrane materials as well as processes utilizing membranes will likely be developed. Therefore, their incorporation into existing thermally based units as a debottlenecking step or as a stand-alone separation unit is expected to become increasingly more common. Specifically for natural gas, utilization of smaller, more remote natural gas wells will require the use of less equipment intensive and more flexible separation technologies, which precludes the use of traditional, more capital and equipment intensive thermally based units. The use of membranes is, however, not without challenges. Perhaps the most important hurdle to overcome in membrane development for natural gas purification is the ability to maintain high efficiency in the presence of harsh feed components such as CO_2 and H_2S. Additionally, as this project has demonstrated, achievement of similarly high selectivity for *both* CO_2 and H_2S is challenged by the different factors that control their transport through membranes. However, as others have suggested and shown, as well as what has been demonstrated in this project, when CO_2 is the primary contaminant of interest, high CO_2/CH_4 selectivity is more important.

In this dissertation, polyamide-imides were shown to offer high selectivity and moderate permeability under high pressure mixed gas feed conditions. In Chapter 4, it was shown that a combination of interchain hydrogen bonding as well as intermolecular charge transfer interactions likely contributes to such high stability against aggressive feed conditions. Furthermore, it was found that H_2S permeability as well as H_2S/CH_4 permselectivity in glassy polymers is always much lower than CO_2 permeability and its selectivity over CH_4. Perhaps most surprising, such low permselectivity is in part due to a reversed H_2S/CH_4 diffusion selectivity. Therefore, the backbone of the starting polyamide-imide material was modified by incorporating packing inhibiting diamines over the *amide bond.* The rationale behind such modifications was to increase H_2S permeability through higher diffusivity, and because H_2S/CH_4 diffusion selectivity was already less than 1, such increased diffusivities were not expected to affect overall permselectivity.

Chapter 5 showed that the trends in the transport properties of the new, modified polymers, 6F-PAI-2 and 6F-PAI-3, were exactly opposite to what was expected—that is, permeabilities of all gases decreased relative to the original material, 6F-PAI-1. The diamines used in the two new polymers were chosen because they have been shown by past researchers to disrupt chain packing and increase permeabilities when incorporated over an *imide*. However, incorporation of such diamines over the *amide* bond in the polyamide-imides used in this project actually lowered the permeabilities of all gases, and this was attributed to increased chain packing. Therefore, the same methodology used to increase permeabilities in polyimides does not appear to apply when said methodologies are adapted to amide bonds. Despite lower permeabilities, selectivities for both gas pairs, increased in the new materials. Hydrogen sulfide solubility in 6F-PAI-2 and 3 was also enhanced relative to CO_2 and CH_4 sorption, which were both reduced relative to the original material. Less fluorine concentration in the new materials likely reduced the extent of non-ideal H_2S-fluorine interactions. Interestingly, H_2S plasticization

resistance was lower in the new, less fluorinated polymers despite having showed similar, and for 6F-PAI-2, markedly increased CO_2 plasticization resistance compared to the original, more fluorinated 6F-PAI-1. Perhaps the most revealing observation was that Torlon®, one of the most intrinsically CO_2 plasticization resistance polymers known, also showed similarly low H_2S resistance compared to the highest fluorinated polyamide-imide used. Torlon® also happens to be non-fluorinated. Therefore, fluorine concentration along the polymer backbone appears to have a profound impact on H_2S solubility and subsequently, swelling resistance of the polymer towards H_2S.

Chapter 6 attempted to quantify the effect of fluorine concentration on the heat of sorption for H_2S, as well as elucidate the unusually low H_2S/CH_4 diffusion selectivity by measuring diffusion activation energies. For all three polyamide-imides, the heat of sorption became increasingly *less* exothermic with increasing penetrant condensability. This trend, which defies conventional wisdom and understanding of gas sorption in polymers, was found to be caused by different proportions of each penetrant sorbing into the two idealized sorption domains, as each domain presumably involves different heats of mixing. This trend was not observed in the more conventional polyimides, with the reason being that, in general, the Henry's Law sorption term is much higher in these materials compared to the polyamide-imides. Therefore, because of such low Henry's Law sorption in the more tightly packed polyamide-imides, the larger and less condensable the penetrant, the greater is the fraction of said penetrant sorbed into the non-equilibrium, low energy packing defects compared to the more densely packed Henry's Law type regions. It is concluded then that the separate enthalpy changes associated with each type of idealized sorption domain in glassy polymers would provide a more meaningful determination of the effect of intermolecular interactions on H_2S sorption.

Analysis of the sorption enthalpy in the *polyimides* did reveal more exothermic sorption enthalpy for H_2S in the lower fluorinated structure relative to the higher

fluorinated one. With such an increase, the activation energy of H_2S diffusion was also shown to be larger (more endothermic) than CH_4 in the less fluorinated polyimide, which supports our hypothesis that more favorable polymer-penetrant interactions between H_2S and the less fluorinated polymer matrix would increase the energy barrier that must be overcome prior to execution of a diffusion jump. For the more fluorinated polyimide, H_2S sorption enthalpy and diffusion activation energy were very similar to CH_4. The similarity in these sorption enthalpies was the most striking considering H_2S is significantly more condensable than CH_4. On this basis, fluorine concentration appears to cause non-ideal polymer penetrant interactions with H_2S. Finally, since CH_4 and H_2S had similar diffusion activation energies in the higher fluorinated polyimide, the fact that the diffusion selectivity for H_2S/CH_4 in this material is less than 1 suggests that additional factors, such as partial immobilization of H_2S in the Langmuir microvoids, contributes to such low diffusion selectivity. In general then, H_2S/CH_4 diffusion selectivity in polymeric materials will likely always be close to unity or below due to the factors just discussed. Therefore, selective removal of H_2S from CH_4 should focus primarily on a solubility based separation.

In the final chapter of this dissertation, the mixed gas separation performance was characterized using binary CO_2/CH_4 feeds and ternary $H_2S/CO_2/CH_4$ feeds. Both 6F-PAI-1 and 2 displayed mixed gas CO_2/CH_4 selectivities of 35 and 40 respectively, at CO_2 partial pressures above 400 psia. Due to less fluorine concentration in 6F-PAI-2, this material became significantly plasticized in the ternary feeds containing H_2S at even low total pressures. Higher fluorinated 6F-PAI-1 displayed much better stability against the ternary feeds, and showed a CO_2/CH_4 selectivity of 35 or greater at 800 psia total feed pressure in both high and low H_2S (relative to CO_2) feed concentrations. Compared to Pebax®, a highly H_2S selective rubbery polymer, 6F-PAI-1 showed higher total acid gas selectivity in both high and low (relative to CO_2) H_2S feed concentrations. Such higher selectivity was significantly more pronounced in the feed containing 5/45/50

$H_2S/CO_2/CH_4$ relative to the feed containing 20/20/60 $H_2S/CO_2/CH_4$, indicating that glassy polymers, specifically highly fluorinated materials with high intrinsic selectivity and stability against high acid gas partial pressures will outperform rubbery materials in conditions where CO_2 is the primary contaminant of interest.

In summary, this project has demonstrated that polyamide-imides based on packing inhibiting structural units, such as CF_3 groups, have the potential to offer high mixed gas selectivity with adequate permeabilities under high operating pressures. Also, glassy polymers will likely never achieve H_2S/CH_4 permselectivities as high as their CO_2/CH_4 selectivity due to the selectivity of H_2S being entirely thermodynamically controlled, as glasses separate mainly by diffusion differences. However, in conditions where CO_2 concentration in the process gas feed is similar or much higher than H_2S, maintaining high CO_2/CH_4 selectivity is more important. As such, glassy polymers, specifically highly fluorinated materials, may be able to operate as an efficient and robust separation material for acid gas streams containing low to high amounts of CO_2 and low to moderate concentrations of H_2S.

8.2. Recommendations for Future Research

8.2.1. In-depth investigation of thermal annealing effect on 6F-PAI-1

While the sorption, diffusion, XRD and fluorescence data supported the idea that 6F-PAI-1 underwent a non-densification based physical aging mechanism at higher annealing temperatures, the exact changes to the polymer microstructure are still not well understood. If the pendent methyl group ortho to the N-C *imide* bond was in fact impeding conjugation over this bond and therefore disrupting intermolecular pi-pi stacking in the unannealed state, some additional experiments could provide further verification of this hypothesis. For instance, synthesis of 6FDA-3ABA diacid *without* the pendent ortho group and comparison of the solution state UV-vis spectra of this diacid

monomer to the regular methylated 6FDA-3ABA that was used could reveal whether conjugation over the imide bond was in fact reduced due to steric interactions between the methyl group of the benzoic acid moiety and carbonyl groups of the dianhydride. This non-methylated 6FDA-3ABA is shown below and compared to methylated 6FDA-3ABA that was used in the polyamide-imides in this work.

Methylated 6FDA-3ABA

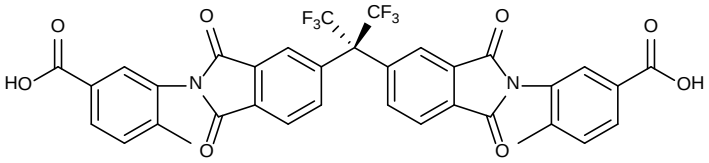

Non-methylated 6FDA-3ABA

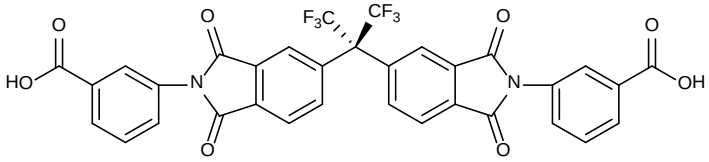

Also, qualitative observations, such as a darker, more yellow color in the solid-state of the non-methyl containing 6FDA-3ABA monomer would provide evidence of a more conjugated and planar structure that can pack adjacent monomer units together more efficiently. Additionally, determination of the solubility of methylated and non-methylated 6FDA-3ABA in common solvents of low to high polarity would reveal qualitative information regarding how planar and thus how well the solid monomer units pack together. Non-planarity around the imide bond induced by steric interactions of the methyl group should disrupt such packing of monomer units, and therefore, non-methylated 6FDA-3ABA would be expected to have lower solubility in low boiling solvents, while methylated 6FDA-3ABA should have increased solubility in low boiling solvents.

Similarly, non-methylated 6FDA-3ABA could be polymerized with 6FpDA, and dense film membranes could be formed and annealed using the same conditions as

discussed in Chapter 4. If the non-methlyated 6FDA-3ABA containing polymer did indeed have less sterically hindered planarity around the imide bond, it would be expected to show greater CTC formation in films annealed at lower temperatures relative to 6F-PAI-1 at the same annealing temperature due to a potentially more planar backbone. Finally, if densification based physical aging, namely simple free volume reduction and increased density is shown in non-methylated 6F-PAI-1, strong evidence would exist that the non-conventional annealing response observed in methylated 6F-PAI-1 was due to the effect of the pendent methyl group.

More direct, albeit more complex techniques such as positron annihilation spectroscopy (PALS) would provide valuable information regarding free volume and free volume distribution changes to the annealed polymer films. Dynamic mechanical analysis (DMA) could also be used to help probe sub-T_g transition changes that are characteristic of localized segmental chain mobilities such as flipping of a phenyl ring around its principle axis. Together, these techniques could provide more direct evidence of free volume rearrangement and chain mobility reductions as was hypothesized to occur in thermally annealed 6F-PAI-1.

8.2.2. Further characterization of the differences between the microstructures of 6F-PAI-1,2 and 3

Similar to what was just outlined for 6F-PAI-1, additional characterization of the differences in chain packing between 6F-PAI-1, 2 and 3 may help to clarify some still not well understood trends observed between the different materials. For instance, CO_2 and CH_4 sorption was remarkably lower in 6F-PAI-3 compared to 6F-PAI-1 and 2, however, diffusivities in 6F-PAI-3 were higher than 6F-PAI-2 and only marginally lower than 6F-PAI-1. To probe this, PALS could again be used to examine the free volume distribution in these materials. 6F-PAI-3 is expected to show considerably lower free volume compared to 6F-PAI-1 and 2, however, the distribution of free volume packets available

for diffusion may be more interconnected in 6F-PAI-3, thus providing more interconnected pathways for diffusion jumps. Additionally, localized chain mobilities which are believed to have influence on gas diffusivity, such as the flipping motion of phenyl ring around its axis, could be probed using DMA by determining the temperatures of the sub-T_g transitions in these materials. As 6F-PAI-1 and 3 showed similar extents of charge transfer formation, these transitions may occur at similar temperatures, while for 6F-PAI-2, increased charge transfer formation is expected to increase the activation energy of this transition, therefore shifting a sub-T_g transition to higher temperatures. This would help to explain the reason behind lower diffusivities but similar to higher free volume, as inferred by its higher sorption capacity for CO_2 and CH_4, in 6F-PAI-2 relative to 3.

8.2.3. Additional Mixed Gas Characterization

As was demonstrated briefly in Chapter 4, 6F-PAI-1 also showed good plasticization resistance towards high pressure feeds containing toluene. Both 6F-PAI-1 and 2 should be further tested using various concentrations of toluene in CO_2/CH_4 mixed gas feeds. 6F-PAI-3, which showed lower mixed gas plasticization resistance in Chapter 7, is not as useful of a material for additional high pressure feed gas testing. As hydrocarbon contamination has been shown to cause significant reductions, and sometimes permanent alterations to membrane performance, it is important to determine how 6F-PAI-1 and 2 perform under increasing concentrations of toluene contamination and whether such exposure causes permanent damage to their separation performance. Other contaminants relevant to natural gas separations that would be fruitful to test include heptane and ethylene glycol.

Similarly, long term exposure to high pressures of CO_2 can cause subtle but serious reductions in selectivity due to drifts in permeability with time. These drifts can be induced by high partial pressures of CO_2. Therefore, long term stability against high

mixed gas feed conditions and high CO_2 partial pressures will provide useful information regarding 6F-PAI-1 and 2's performance under even more realistic operating conditions.

Since the ternary feeds used to test 6F-PAI-2 in Chapter 7 were composed of a relatively high H_2S concentration, it may still perform well if H_2S concentration is very low. As stated in Chapter 1, H_2S concentration generally ranges from ppm levels to 5-10% in most conventional gas wells. The information in Chapter 7 provided strong evidence that glassy polymers may be more appropriate for conditions where CO_2 concentration is similar to or higher than H_2S. On this basis, it would be useful to test even more realistic feed compositions, such as 5/20/75 $H_2S/CO_2/CH_4$, as well as CO_2 concentrations ranging between 10-50% and H_2S in ppm levels.

8.2.4. Analysis of the temperature dependencies of the dual-mode parameters

As was determined in Chapter 6, the enthalpy of sorption associated with "hole-filling" in the Langmuir regions and "dissolution" in the Henry's regions would provide more useful information regarding the effect of fluorine concentration on H_2S's sorption enthalpy. Alternatively, one could measure the total sorption enthalpy, as was done at 40 psia in this project, at higher pressures, for instance above 100 psia, where gas sorption most likely occurs in the Henry's regions. It has been shown by past researchers that gas dissolution in the "equilibrium" domains is more dependent on intermolecular interactions, as opposed to the relatively less-discriminant excess free volume packing defects. However, H_2S plasticizes most materials below 80 psia partial pressure. Therefore, the temperature dependencies on the dual-mode parameters appear to be the best route for a more meaningful interpretation of the effect of fluorine concentration on H_2S sorption. In a similar manner, the activation energies of the Langmuir and Henry's diffusivities, D_H and D_D, respectively, may be able to better elucidate the reasons behind such unusually low and reversed H_2S/CH_4 diffusion selectivity. Since D_D is characteristic of the more conventional interpretation of penetrant diffusivity controlled by the size and

frequency of polymer chain gap openings, its activation energy may be more appropriate for testing our hypothesis regarding H_2S's anonymously low diffusivity relative to CH_4.

8.2.5. Potential polymer modifications

Since ortho methyl group steric interactions over the *amide* bond did not achieve the desired permeability enhancements in 6F-PAI-2 and 3, pendent groups ortho to the *imide* bond could be incorporated into the benzoic acid moiety. This modification would be analogous to the effect that ortho methyl groups in DAM and TmPDA connected polyimides have on increasing permeability in the 6FDA based *polyimides* as was discussed in Chapter 5. The structure of the amino-methyl-benzoic acid monomer could be altered by using similar monomers as shown below:

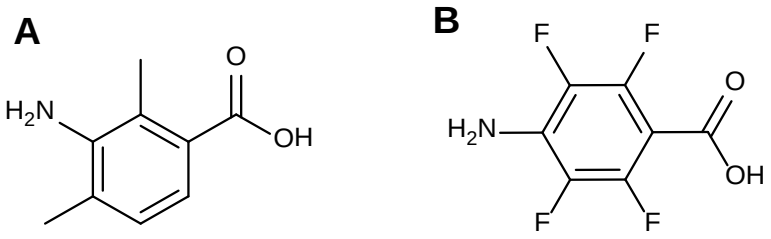

Unfortunately, monomer A does not currently appear to be commercially available. However, monomer B is, and in fact, attempts to synthesize a polymer based on this monomer were made. This acid was reacted with 6FDA dianhydride to produce the intermediate diacid, however, this diacid was found to have very low solubility in NMP, and in order to completely dissolve it for polymerization, an extremely dilute solution in NMP was necessary. Subsequent polymerization with the diamine was therefore unsuccessful, which was presumably due to the very dilute conditions. Additional co-solvent mixtures containing NMP and a perfluorinated solvent may help to circumvent this problem. As a bonus, if the 6FDA diacid formed with monomer B could be

polymerized with 6FpDA, the higher fluorine concentration in the subsequent polymer may provide additional stabilization against high H_2S partial pressures.

In a similar methodology, since the effect of incorporating DAM into the amide bond of 6F-PAI-2 was shown to enhance its CO_2 plasticization resistance but lower its H_2S plasticization, fluorinated diamines with a similar structure as DAM may help to bolster its stability against H_2S. However, it is not known whether such monomers are readily available.

As a final corollary, if one wishes to pursue the more conventional and more well understood crosslinkable 6FDA-DAM:DABA polyimide copolymers for acid gas separations, its stability against H_2S could also be improved by incorporating fluorinated versions of the diol crosslinkers shown below.

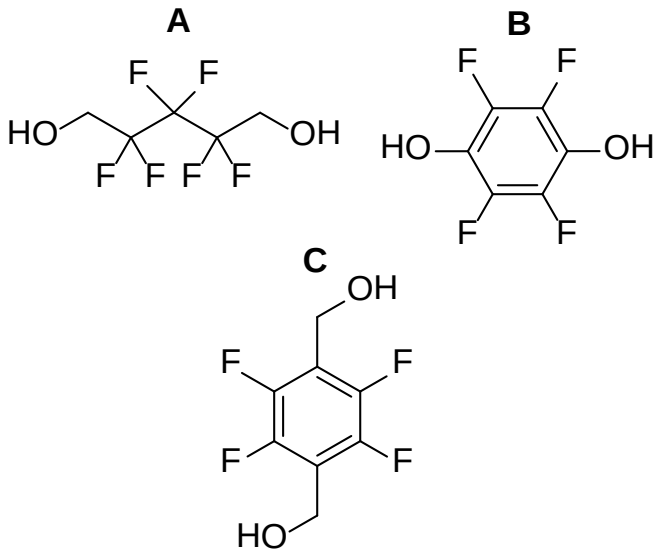

If the primary contaminant of interest is CO_2, incorporation of such monomers should not reduce total acid gas selectivity since CO_2/CH_4 selectivity is often preserved if not increased by incorporation of bulky and rigid units such as fluorine moieties into the polymer. In order to increase the low reactivity of the phenol moiety in monomer B for

nucleophilic substitution with the carboxylic acid of DABA, a base such as sodium hydroxide could be used to increase the nucleophilicity of the phenol.

APPENDIX A

CALCULATION OF COMPRESSIBILITY FACTORS

The compressibility factor is a measure of the deviation of a gas from ideal behavior. For natural gas mixtures and gas/condensate mixtures, the Peng Robinson Equation of State is often used to calculate the compressibility factors and fugacity coefficients [1].

In terms of pressure, the PR EOS is given by the following expression:

$$P = \frac{RT}{v-b} - \frac{a(T)\alpha}{v(v+b)+b(v-b)} \tag{A.1}$$

where P, T, R, and *v* represent the system pressure, temperature, universal gas constant, and volume, respectively. The PR cubic expression for Z then becomes:

$$Z^3 - (1-B)Z^2 + (A - 3B^2 - 2B)Z - (AB - B^2 - B^3) = 0 \tag{A.2}$$

where $A = \frac{a\alpha P}{R^2T^2}$, $B = \frac{bP}{RT}$, and $Z = \frac{Pv}{RT}$.

Applying Equation A.1. at the critical temperature, α in the above expressions is equal to unity, and the following relationships hold:

$$a(T_c) = 0.45724\frac{R^2T_c^{\,2}}{P_c}, b(T_c) = 0.07780\frac{RT_c}{P_c}, Z_c = 0.307$$

a and *b* are thus merely functions of penetrant critical parameters.

At temperatures other than the critical temperature, α in Equation A.1 and in the expression for A is no longer equal to 1, and *a* becomes a function of the system temperature as shown in A.3.

$$a(T) = a(T_c) \cdot \alpha(T_r, \omega) \tag{A.3}$$

where

$$\alpha = \sqrt{1 + \kappa(1 - T_r^{1/2})} \tag{A.4}$$

$$\kappa = 0.37464 + 1.54226\omega - 0.026992\omega^2 \tag{A.5}$$

b is still only a function of the critical temperature, and is equal to the expression given previously. T_r in Equation A.4 is the reduced temperature. The acentric factor, ω, is a constant for a given penetrant and is tabulated in many thermodynamic tables [2]. It is said to be a measure of the non-sphericity (centricity) of molecules. The compressibility factor at a given temperature and pressure, is calculated iteratively from Equation A.2. Critical parameters and acentricity factors for CO_2, CH_4, and H_2S are tabulated below in Table A.1.

The fugacity coefficients used in the permeability calculations were also calculated from the PR EOS. For a ternary mixture containing components *i*, *j* and *k*, the mixture fugacity of component *k* is calculated using Equation A.6 [1]:

$$\ln\left(\frac{f_k}{y_k P}\right) = \frac{b_k}{b_m}(Z-1) - \ln(Z-B) - \frac{A}{2\left(\sqrt{2}\right)B}\left(\frac{2\sum_i y_i a_{ik}}{a_m} - \frac{b_k}{b_m}\right) \cdot \ln\left(\frac{Z+2.41B}{Z-0.414B}\right) \tag{A.6}$$

P is the total system pressure. f_k and y_k are the fugacity and mole fractions, respectively, of component k in the mixture. b_k is as defined earlier, and only depends on the critical temperature of component k. Z is the compressibility factor as given in Equation A.2.

a_m and b_m are the mixture parameters, and are defined by the following mixing rules:

$$a_m = \sum_i \sum_j x_i x_j a_{ij} \tag{A.7}$$

$$b_m = \sum_i x_i b_i \tag{A.8}$$

where

$$a_{ij} = (1-\delta_{ij}) a_i^{1/2} a_j^{1/2} \tag{A.9}$$

δ_{ij} is an empirically determined binary interaction coefficient between components i and j. a_m and b_m are also used in Equation A.2 instead of the simple pure component values of a and b for calculation of the compressibility factor of the mixture. The binary interaction parameters for CO_2, CH_4, and H_2S are given in Table A.2.

For the pure component fugacity, Equation A.6 reduces to Equation A.10.

$$\ln\frac{f}{P} = Z - 1 - \ln(Z-B) - \frac{A}{2\left(\sqrt{2}\right)B}\ln\left(\frac{Z+(1+\sqrt{2})B}{Z+(1-\sqrt{2})B}\right) \tag{A.10}$$

Z, *B*, *P*, and *f* are as defined earlier.

Table A.1: Critical parameters and acentric factors for CO_2, CH_4, and H_2S [2, 3].

Species	T_c (K)	P_c (Bar)	ρ_c (mol/L)	ω
H_2S	373.15	89.997	10.19	0.1
CH_4	190.564	45.992	10.139	0.01142
CO_2	304.13	73.773	10.6249	0.2234
Xe	289.65	37.43	8.475	0
CF_4	227.5	37.39	7.163	0.0969

Table A.2: Binary interaction parameters applicable temperature ranges. Values were obtained from Nishiumi et al. [4].

System	Temperature Range (K)	δ_{ij}
H_2S-CO_2	221-353	0.106
H_2S-CH_4	277-344	0.081
CO_2-CH_4	199-283	0.152

The compressibility factors for Xe were calculated by a generalized form of the Redlich/Kwong equation of state as given by Equation A.11. This relation is the basis for the two parameter theorem of corresponding states, which states that all gases compared at the same reduced temperature and pressure have similar compressibility and will deviate from non-ideality to about the same extent [2].

$$Z = \frac{1}{1-h} - \frac{4.9340}{T_r^{1.5}} \cdot \left(\frac{h}{1+h} \right) \tag{A.11}$$

$$h = \frac{0.08664\, P_r}{Z T_r} \tag{A.12}$$

These equations are arranged for a convenient iterative solution for the calculation of Z.

For simple, spherical gases, such as Xe, Kr and Ar, Equations A.11 and A.12 can be used without significant deviation from experimental data. However, for non-spherical gases, much improvement results when the acentric factor, as described previously, is introduced. The correlation for Z for non-spherical gases is defined by Equation A.13.

$$Z = 1 + B^o \frac{P_r}{T_r} + \omega B^1 \frac{P_r}{T_r} \tag{A.13}$$

where $B^o = 0.083 - \frac{0.422}{T_r^{1.6}}$ and $B^1 = 0.139 - \frac{0.172}{T_r^{4.2}}$.

The acentric factor is usually tabulated [2], however, it can also be calculated from Equation A.14.

$$\omega = -1.0 - \log(P_r^{SAT})_{T_r=0.7} \tag{A.14}$$

P_r^{SAT} is the reduced vapor pressure measured at T_r=0.7. The calculated acentric factor for CF_4 based on Equation A.14 is given in Table A.1. For simple, spherical molecules, ω=0. It is important to note that Equation A.13 is only applicable over low to moderate pressures where Z is linear with P_r. For gases with T_r >1, Z is linear up to P_r almost equal to 1. For T_r <1, Z increasingly deviates from linearity at P_r below 0.4.

.

References

[1] D.-Y. Peng and D. B. Robinson, “A New Two-Constant Equation of State,” *Industrial & Engineering Chemistry Fundamentals*, **15** (1), 59–64, (1976).

[2] M. Abbott, J.M. Smith, H.C. Van Ness, *Introduction to Chemical Engineering Thermodynamics, 6th Edition*, (McGraw-Hill Education, New York, New York, 2004).

[3] J.P. O'Connell, B.E. Poling, J.M. Prausnitz, *The Properties of Gases and Liquids, 5th Edition,* (McGraw-Hill, New York, New York, 2001).

[4] H. Nishiumi, T. Arai, "Generalization of the Binary Interaction Parameter of the Peng-Robinson Equation of State By Component Family, *Fluid Phase Equilibria,* **42**, 43-62, (1988).

APPENDIX B

4 TEMPERATURE POINT FITS TO SORPTION AND PERMEATION ACTIVATION ENERGY

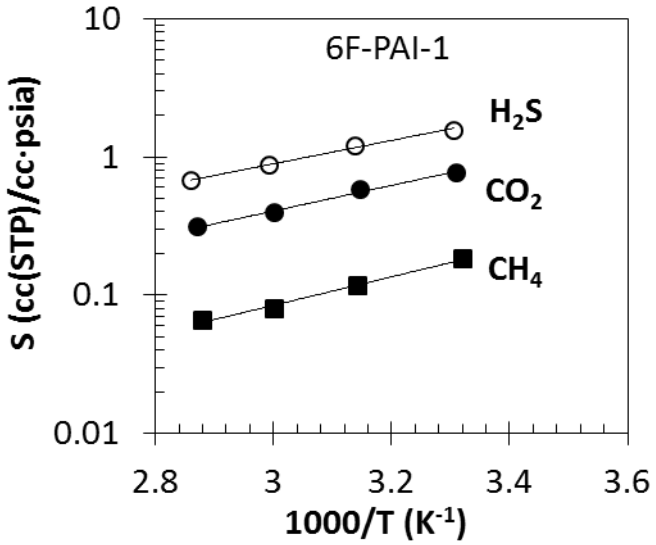

Figure B.1: 4 temperature point fit to 6F-PAI-1 sorption versus temperature plots.

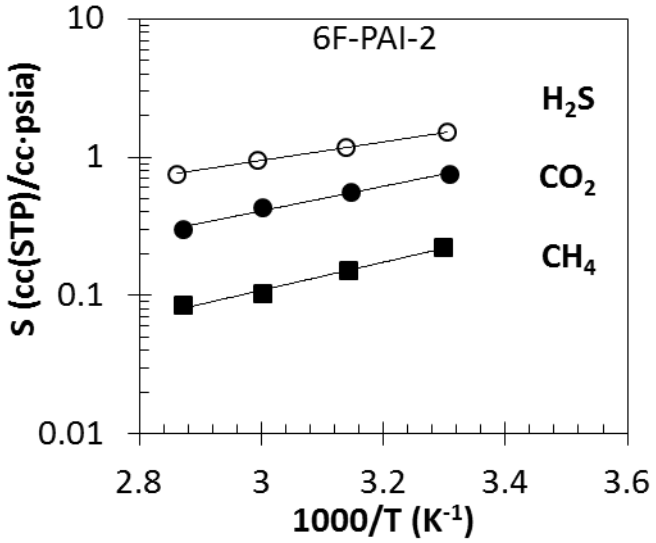

Figure B.2: 4 temperature point fit to 6F-PAI-2 sorption versus temperature plots.

Table B.1: Sorption enthalpies in 6F-PAI-1, 2 obtained using the 4 temperature point fits in Figures B.1 and B.2. *6F-PAI-3 was only measured at temperatures of 30, 45 and 60°C. It is included as a reference.

ΔH_s (kJ/mol)	*6F-PAI-1*	*6F-PAI-2*	**6F-PAI-3*
CH_4	-20 ± 1.3	-19 ± 1.4	-20 ± 2.2
CO_2	-18 ± 1.0	-17 ± 1.2	-17 ± 1.3
H_2S	-16 ± 0.91	-13 ± 0.35	-16 ± 1.6

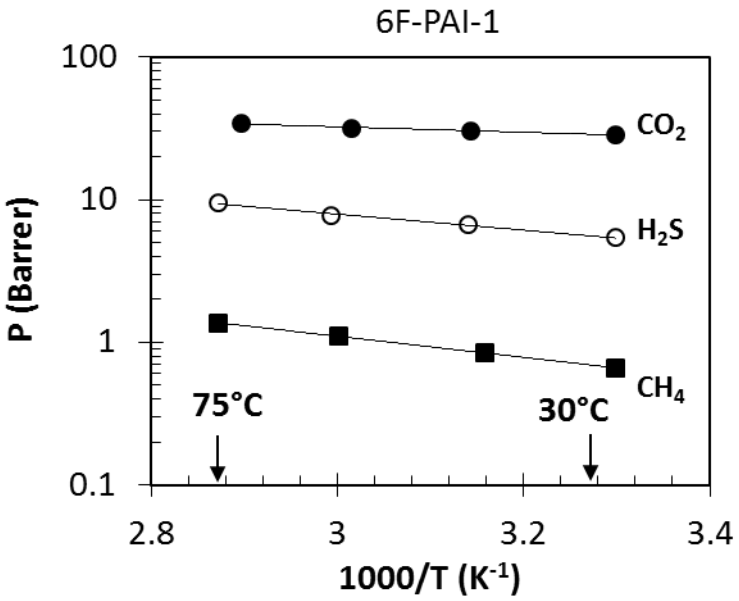

Figure B.3: 4 temperature point fit for permeability versus 1000/T in 6F-PAI-1.

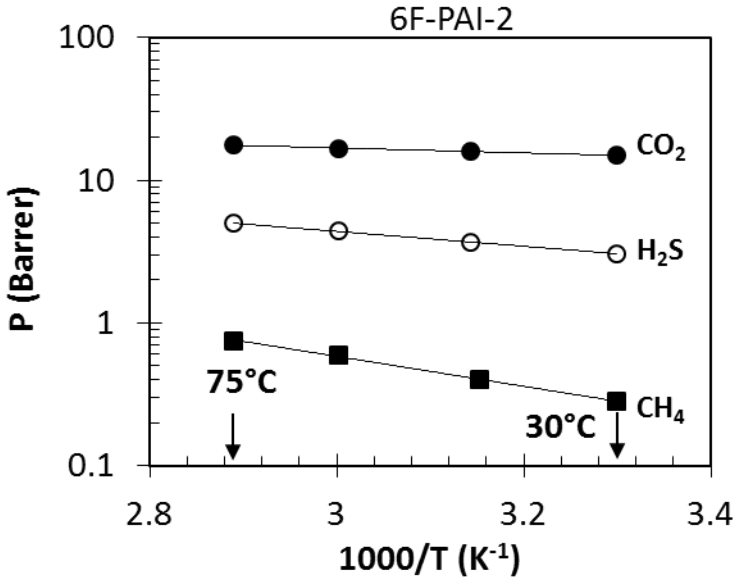

Figure B.4: 4 point temperature fit for permeability versus 1000/T in 6F-PAI-2.

Table B.2: Permeation activation energies in 6F-PAI obtained from the 4 temperature point fits shown in Figure B.3 and B.4. *6F-PAI-3 was only measured at temperatures of 30, 45 and 60°C. It is included as a reference.

ΔE_P (kJ/mol)	*6F-PAI-1*	*6F-PAI-2*	**6F-PAI-3*
CH_4	14 ± 0.33	20 ± 0.79	19 ± 0.19
CO_2	3.7 ± 0.49	3.3 ± 0.17	2.7 ± 0.27
H_2S	11 ± 0.72	10 ± 0.13	11 ± 0.66

Table B.3: Diffusion activation energies in 6F-PAI obtained from $E_D = E_P + \left|\Delta H_S\right|$ using the ***3*** temperature point fits to the natural log of permeation and sorption versus 1/T plots.

ΔE_D (kJ/mol)	*6F-PAI-1*	*6F-PAI-2*	*6F-PAI-3*
CH_4	36 ± 0.75	39 ± 1.0	39 ± 2.2
CO_2	21 ± 2.2	18 ± 1.0	20 ± 1.3
H_2S	25 ± 3.0	23 ± 0.80	27 ± 1.4

Table B.4: Diffusion activation energies in 6F-PAI obtained from $E_D = E_P + \left|\Delta H_S\right|$ using the ***4*** temperature point fits to the natural log of permeation and sorption versus 1/T plots. *6F-PAI-3 was only measured at temperatures of 30, 45 and 60°C. It is included as a reference.

ΔE_D (kJ/mol)	*6F-PAI-1*	*6F-PAI-2*	**6F-PAI-3*
CH_4	34 ± 2.5	39 ± 3.2	39 ± 2.2
CO_2	22 ± 3.1	20 ± 1.8	20 ± 1.3
H_2S	27 ± 2.3	23 ± 0.68	27 ± 1.4

Vita

Justin Tyler Vaughn was born in Denver, Colorado, on the 13th day of August, year 1985. Shortly after his birth, his family moved back closer to his father's roots in St. Clairsville, Ohio. A gem of a small town in the heart of coal-country, also referred to as "paradise on the hill-top," St. Clairsville rests about 10 miles west of the picturesque Ohio-West Virginia Border. Justin spent his entire childhood and high-school years in this area of Ohio affectionately referred to as Appalachia. Upon graduating high-school in 2004, Justin enrolled in The Ohio State University in Columbus, Ohio, home of the mighty Buckeyes. After dabbling in a number of different majors, he settled with a chemistry degree. By the time Justin was a 4th year undergraduate, he appreciated the underlying scientific theory of his studies, but yearned for a more applied approach to chemical science. He quickly realized he should have been a chemical engineer, but didn't want to change his major once again and eventually become a 6th year undergraduate student. In August 2008, Justin enrolled in graduate school at the Georgia Institute of Technology as a Doctor of Philosophy Candidate in the School of Chemical and Biomolecular Engineering, where he was lucky enough to be taken under the guidance of Dr. W.J. Koros. Upon defending his thesis in February 2013, Justin took a post-doctoral research assistant position again under the guidance of Dr. Koros, where he worked on carbon molecular sieve membranes. This time, however, no H_2S was involved. After his post-doctoral position, only time will tell where Justin will be…